A TEST OF CPT SYMMETRY BY MEASURING THE PHASE DIFFERENCE $\Phi_{00} - \Phi_{+-}$ IN THE NEUTRAL KAON SYSTEM

BY

BERNHARD SCHWINGENHEUER

JUNE, 1995

Enrico Fermi Institute

The University of Chicago

Dissertation

THE UNIVERSITY OF CHICAGO

A TEST OF CPT SYMMETRY BY MEASURING THE PHASE DIFFERENCE $\Phi_{00} - \Phi_{+-}$ IN THE NEUTRAL KAON SYSTEM

A DISSERTATION SUBMITTED TO
THE FACULTY OF THE DIVISION OF THE PHYSICAL SCIENCES
IN CANDIDACY FOR THE DEGREE OF
DOCTOR OF PHILOSOPHY

DEPARTMENT OF PHYSICS

BY

BERNHARD SCHWINGENHEUER

CHICAGO, ILLINOIS

JUNE, 1995

A TEST OF CPT SYMMETRY BY MEASURING THE PHASE DIFFERENCE $\Phi_{00} - \Phi_{+-}$ IN THE NEUTRAL KAON SYSTEM

BY

BERNHARD SCHWINGENHEUER

JUNE, 1995

Abstract

The FNAL experiment E773 measured the phase difference $\Phi_{00}-\Phi_{+-} = 0.62°\pm0.71°(\text{stat})\pm 0.75°(\text{syst})$ of the CP violating parameters η_{+-} and η_{00} from the interference in the decay of neutral kaons into two charged or neutral kaons downstream of a pair of regenerators. This result test CPT symmetry and shows no evidence for a violation.

ACKNOWLEDGMENTS

The analysis documented in this thesis is the common effort of many physicists. The apparatus was built over many years and data taking and data analysis would have been impossible without the support of the entire collaboration. I therefore want to thank every author for her/his contribution.

I enjoyed especially working with Pete Haas, Bill Hogan, John Matthews and Sunil Somalwar who helped me to understand the lead glass, and Bob Tschirhart who explained to me details of the detector while I was writing this thesis.

In Chicago, Elliott Cheu made important contributions to the analysis. I am especially in debt to my advisors Bruce Winstein and Roland Winston, whose guidance during my thesis work was paramount. Over the course of the past years our families have become friends.

More than anyone else I want to thank Roy Briere with whom I had many discussions and who, as he put it, did half of the work that led to this thesis.

Over the years I have become friends with many people, especially in Chicago. Because of their friendship it was a pleasant time for me and my family and I would like to thank all of them, without listing their names individually.

Schließlich möchte ich Silke danken, die immer ein erstaunliches Maß an Toleranz für den geleisteten Zeitaufwand gezeigt hat, insbesondere während der vielen Monate, die wir getrennt waren.

The E773 Collaboration

R.A. Briere, A.R. Barker, E. Cheu, L.K. Gibbons, D.A. Harris, G. Makoff,
K.S. McFarland, A. Roodman, B. Schwingenheuer, Y.W. Wah, B. Winstein, R. Winston
The Enrico Fermi Institute, The University of Chicago, Chicago, IL 60637

E.C. Swallow
Elmhurst College, Elmhurst, Illinois 60126,
and The Enrico Fermi Institute, The University of Chicago, Chicago, IL 60637

G.J. Bock, R. Coleman, M. Crisler, J. Enagonio, R. Ford, Y.B. Hsiung,
D.A. Jensen, E. Ramberg, R. Tschirhart, T. Yamanaka
Fermi National Accelerator Laboratory, Batavia, Illinois 60510

E.M. Collins, G.D. Gollin
University of Illinois, Urbana, Illinois 61801

P. Gu, P. Haas, W. P. Hogan, S.K. Kim, J.N. Matthews, S.S. Myung,
S. Schnetzer, S.V. Somalwar, G.B. Thomson, Y. Zou
Rutgers University, Piscataway, New Jersey 08855

TABLE OF CONTENTS

LIST OF TABLES

LIST OF ILLUSTRATIONS

CHAPTER 1

Introduction

This thesis describes the measurement of the phase difference $\Delta\Phi = \Phi_{00} - \Phi_{+-}$ of η_{+-} and η_{00} which measure the CP symmetry violation in the neutral kaon system. The difference is expected to be smaller than 0.1° if the weak interaction is invariant under the CPT transformation. Conversely, a $\Delta\Phi$ measurement significantly different from zero would clearly prove a violation of the CPT symmetry.

In the following sections I will briefly discuss the history of symmetry violations in the neutral kaon system, why $\Delta\Phi$ is expected to be small if CPT is conserved, and the method used to measure the phase difference in our experiment E773 at Fermilab.

1.1 Symmetries

Symmetries play a fundamental role in all areas of physics. In classical mechanics for example the lagrangian is best written in term of generalized coordinates which are chosen according to the symmetry properties of the system. In quantum mechanics the solution of the Schrödinger equation will depend on the specific symmetries. If the hamilton operator commutes with the parity operator P then the eigenfunctions of the hamilton operator will also be eigenfunctions of P, i.e. they are symmetric or antisymmetric. If on the other hand P symmetry is violated then the hamiltonian must contain terms that transform as a scalar

and terms that transform as a pseudo-scaler. Symmetries are therefore closely related to the structure of a theory.

CPT is the product of the charge conjugation operator C, the parity operator P and the time reversal operator T. Until the 1950s physicists assumed that all fundamental interactions are invariant under C, P and T. It was therefore a surprise when three experiments, whose results were published within two weeks, showed that the weak interaction violates parity [Wu 57, Garwin 57, Friedman 57]. These experiments were suggested by Lee and Yang to resolve the τ-θ problem [Lee 56]. The experiments also proved that the charge conjugation symmetry was violated provided CPT is conserved [Lee 57].

In 1964 Christenson, Cronin, Fitch and Turley found that the product of C and P is also violated in the weak decay of neutral kaons [Christenson 64]. Until today the neutral kaon system is the only instance where CP violation has been observed and even now, more than 30 years after the discovery, the origin of CP violation is still unknown in the sense that we do not know whether the standard model describes CP violation correctly or whether new interactions play a role.[1]

What did these four physicists observe? The K^0 and $\bar{K}^0$ are the mass eigenstates produced by the strong interaction. They both can decay into the same final state, e.g. two pions. Therefore the K^0 and $\bar{K}^0$ will mix through the process $K^0 \rightarrow 2\pi \rightarrow \bar{K}^0$ [Gell-Mann 55]. The eigenfunctions of the weak decay will therefore be linear combinations

$$K_S = aK^0 + b\bar{K}^0 \tag{1.1}$$

$$K_L = cK^0 + d\bar{K}^0 \tag{1.2}$$

If CP is a good quantum number and if we choose the phase convention $CP\ K^0 = \bar{K}^0$ then the physical states are the symmetric and antisymmetric combination

$$K_S = K_1 \equiv (K^0 + \bar{K}^0)/\sqrt{2}; \qquad CP = +1 \tag{1.3}$$

$$K_L = K_2 \equiv (K^0 - \bar{K}^0)/\sqrt{2}; \qquad CP = -1 \tag{1.4}$$

In this case the decay $K_S \rightarrow 2\pi$ is allowed since $CP\,(2\pi) = +1$. K_L will decay into 3 body

[1] The value of ϵ'/ϵ for instance has not been measured and calculated precisely enough to test the standard model.

final states. This is suppressed by phase space and the life time of K_L is therefore much longer (by a factor of 580). Thus the index L stands for long lived.

Christenson, Cronin, Fitch and Turley found however that about 0.2% of the K_L decay into two charged pions, i.e. violate CP. Later, the interference between K_S and K_L decays into $\pi^+\pi^-$ was observed [Fitch 65]. This proved that there was no additional neutral particle in the final state which would have changed the interpretation of the experiment.

What about the CPT symmetry? In the 1950s the so called CPT theorem was proven [Lüders 54, Jost 57, Pauli 55, Sachs 87, Streater 64]: Every local field theory with the ingredients hermiticity and Lorentz invariance conserves CPT. [2] This theorem states a strong theoretical bias since the requirements are very general. In particular, the standard model satisfies the conditions. [3]

CPT violating theories must violate at least one of the conditions. In string theories for example the interactions are nonlocal due to the dimension of the strings. For some classes of strings however this is not sufficient to cause a violation of the CPT invariance of the action. Instead, the CPT invariance of the ground state is questionable because the higher-dimensional Lorentz invariance might be broken [Kostelecky 94]. In a different model the quantum mechanical description for the neutral kaon system was altered to allow for the evolution of pure states into mixed states [Ellis 92, Huet 95]. This change was motivated by the break down of unitarity at the event horizon of a black hole (Hawking radiation) [Hawking 75]. [4] Non of the mentioned theories make good predictions about the size of CPT violating effects currently. The symmetry violation occurs however at mass scales comparable to the Planck mass and the effects are very small at low energies.

Experimentally, no CPT violation has been observed. One can check the symmetry by comparing the masses, lifetimes, electric charges and magnetic moments of particles and their antiparticles. If CPT is conserved they are equal. Table 1 lists the current status

[2] To prove the theorem the action $S = \int d^4x L$ has to be invariant under CPT. From Lorentz invariance L contains scalar, pseudo scalar, vector, axial vector and tensor terms with contracted Lorentz indices. All terms of L need to be normal-ordered. The proof shows that the transformation properties of all possible combinations conserve CPT. Since T is anti-hermitian L must be replaced by $L + L^*$, i.e. L is hermitian.

[3] Reference [Kobayashi 92] points out that the proof of the CPT theorem makes uses of properties of asymptotic states. Since quarks and gluons are not free the theorem might not be applicable to QCD.

[4] For a recent reference of CPT violation in the context of quantum gravity see [Strominger 93].

Table 1. CPT tests through comparison of mass, life time, magnetic moment and electric charge of particle and anti-particle. Listed are the differences of the measurements for particle and anti-particle over the averages. From CPT conservation all numbers are expected to be zero. Upper limits are for 90% C.L. All numbers are taken from [PDG 94] and [Gabriele 95] (for the proton-antiproton mass difference).

	mass	life time	magnetic moment	charge
electron	$< 4 \cdot 10^{-8}$		$(-0.5 \pm 2.1) \cdot 10^{-12}$	$(1 \pm 4) \cdot 10^{-8}$
muon		$(2 \pm 8) \cdot 10^{-5}$	$(-2.6 \pm 1.6) \cdot 10^{-8}$	
charged pion	$(2 \pm 5) \cdot 10^{-4}$	$(5.5 \pm 7.1) \cdot 10^{-4}$		
charged kaon	$(6.5 \pm 18) \cdot 10^{-5}$	$(11 \pm 9) \cdot 10^{-4}$		
neutral kaon	$< 9 \cdot 10^{-19}$			
proton	$(5 \pm 11) \cdot 10^{-10}$		$(-2.6 \pm 2.9) \cdot 10^{-3}$	$(1 \pm 2) \cdot 10^{-5}$
neutron	$(9 \pm 5) \cdot 10^{-5}$			

of some of these tests. The neutral kaon system is especially sensitive for studying CPT symmetry using the interference between K_L and K_S decays. This interference occurs because of the small mass difference $(m_L - m_S)/m_L \approx 10^{-15}$ (see equation 1.57) which originates from second order weak transitions. CPT violating effects will be small at low energies but compared to a second order weak amplitude these effects might be detectable. In addition, CP violation has only been observed in the neutral kaon system, which makes the neutral kaons a premier place to look for CPT symmetry violating effects.

1.2 Phenomenology

Many review articles have been written in the last decade over the CP and CPT symmetry violation in the neutral K- and B-meson system which reflects the large interest in this topic (see for example [Barmin 84, Cronin 81, Nakada 93, Sachs 87, Winstein 93]). Unfortunately, there are many different conventions in the literature once CPT violation amplitudes are considered, or the way Barmin *et al.* put it: "Although from the theoretical-technical point of view this analysis boils down to the multiplication and addition of complex numbers, nevertheless, as it will be seen below, twenty years were not enough to settle all the detail

of CPT-violating phenomenology. Surely this paper will not be the final one."[Barmin 84]. One of the first analysis of the data (especially using the first measurement of η_{00}) without the assumption of CPT invariance was done in reference [Schubert 70].

In the following discussion I will follow the conventions of Barmin et al. (1984) and Nakada (1993). The weak interaction will be treated as a small perturbation of the strong and electromagnetic forces. The phases of the K^0 and the $\bar{K}^0$ states are therefore arbitrary since the strong interaction does not transform one state into the other.

$$CP\,|K^0\rangle = e^{i\theta_{cp}}|\bar{K}^0\rangle, \tag{1.5}$$

$$CP\,|\bar{K}^0\rangle = CP(e^{-i\theta_{cp}}CP\,|K^0\rangle) = e^{-i\theta_{cp}}|K^0\rangle. \tag{1.6}$$

θ_{cp} is therefore arbitrary and so is the phase of K^0. [5] The time reversal operator is anti-hermitian. Since the kaon has no spin we find

$$T\,|K^0\rangle = e^{i\theta_T}(|K^0\rangle)^*,\ T\,|\bar{K}^0\rangle = e^{i\bar{\theta}_T}(|\bar{K}^0\rangle)^*. \tag{1.7}$$

where the * denotes complex conjugation and θ_T and $\bar{\theta}_T$ are again arbitrary phases.[6] If CP and T commute it follows that

$$2\theta_{cp} = \bar{\theta}_T - \theta_T. \tag{1.8}$$

The time evolution of K^0 and $\bar{K}^0$ in the Wigner-Weisskopf approximation can be described by a Schrödinger equation

$$\frac{d}{dt}\begin{pmatrix} K^0(t) \\ \bar{K}^0(t) \end{pmatrix} = \Lambda \begin{pmatrix} K^0(t) \\ \bar{K}^0(t) \end{pmatrix} \tag{1.9}$$

with Λ being a non-hermitian 2×2 matrix. Λ can be written as the sum of two hermitian matrices $\Lambda = M - \frac{i}{2}\Gamma$. M is called the mass matrix and Γ is called the decay matrix.

In the following the hamilton operator H_M and H_Γ which determine the matrices M and Γ are assumed to be hermitian, i.e. $H_{M,\Gamma} = H^\dagger_{M,\Gamma}$.[7] For the remainder of this section

[5] After deriving some interesting facts about observables in case of T, CP and CPT violation we will set $\theta_{cp} = 0$.

[6] In a more formal way $T\,|K^0\rangle = U\,K\,|K^0\rangle$ with U being a unitary operator and K being the complex conjugation operator defined in references [Sachs 87, Wigner 32].

[7] If H_M or H_Γ would not be hermitian their eigenvalues would be complex and consequently transition probabilities would vary with time.

I will write H instead of $H_{M,\Gamma}$. If CPT symmetry is conserved,[8] i.e. $CPT\,H\,(CPT)^{-1} = H$ we find

$$\begin{aligned}\langle K^0|H|\bar{K}^0\rangle &= [CPT\,|K^0\rangle]^\dagger\,CPT\,H\,(CPT)^{-1}\,CPT|\bar{K}^0\rangle \\ &= e^{i(-2\theta_{cp}-\theta_T+\bar{\theta}_T)}(\langle\bar{K}^0|H|K^0\rangle)^* \\ &= (\langle\bar{K}^0|H|K^0\rangle)^* \end{aligned} \tag{1.10}$$

and

$$\begin{aligned}\langle\bar{K}^0|H|\bar{K}^0\rangle &= [CPT\,|\bar{K}^0\rangle]^\dagger CPT\,H\,(CPT)^{-1}\,CPT|\bar{K}^0\rangle \\ &= (\langle K^0|H|K^0\rangle)^* = \langle K^0|H^\dagger|K^0\rangle \\ &= \langle K^0|H|K^0\rangle \end{aligned} \tag{1.11}$$

If CP is a good quantum number:

$$\begin{aligned}\langle\bar{K}^0|H|\bar{K}^0\rangle &= [CP\,|\bar{K}^0\rangle]^\dagger CP\,H\,(CP)^{-1}\,CP|\bar{K}^0\rangle \\ &= \langle K^0|H|K^0\rangle \end{aligned} \tag{1.12}$$

and

$$\begin{aligned}\langle\bar{K}^0|H|K^0\rangle &= [CP\,|\bar{K}^0\rangle]^\dagger CP\,H\,(CP)^{-1}\,CP|K^0\rangle \\ &= e^{i2\theta_{cp}}\langle K^0|H|\bar{K}^0\rangle = e^{i2\theta_{cp}}(\langle\bar{K}^0|H^\dagger|K^0\rangle)^* \\ &= e^{i2\theta_{cp}}(\langle\bar{K}^0|H|K^0\rangle)^* \end{aligned} \tag{1.13}$$

Finally, if T is conserved

$$\begin{aligned}\langle\bar{K}^0|H|K^0\rangle &= [T\,|\bar{K}^0\rangle]^\dagger T\,H\,(T)^{-1}\,T|K^0\rangle \\ &= e^{i(\theta_T-\bar{\theta}_T)}(\langle\bar{K}^0|H|K^0\rangle)^* \end{aligned} \tag{1.14}$$

From above equations it follows for the matrix Λ:

$$\begin{aligned} T \text{ conserved}: &\quad |M_{12}-\tfrac{i}{2}\Gamma_{12}| = |M_{12}^*-\tfrac{i}{2}\Gamma_{12}^*| \\ CP \text{ conserved}: &\quad |M_{12}-\tfrac{i}{2}\Gamma_{12}| = |M_{12}^*-\tfrac{i}{2}\Gamma_{12}^*|,\ M_{11}=M_{22},\ \Gamma_{11}=\Gamma_{22} \\ CPT \text{ conserved}: &\quad M_{11}=M_{22},\ \Gamma_{11}=\Gamma_{22} \end{aligned} \tag{1.15}$$

[8] Note that CPT does not have a quantum number since it is an anti-hermitian operator.

If therefore the mass or lifetime differ for K^0 and $\bar{K}^0$ CP and CPT are violated and if M_{12}/Γ_{12} is not real CP and T are violated. After deriving these results the phase convention $\theta_{cp} = \theta_T = \bar{\theta}_T = 0$ will be used for the rest of this chapter.

For the next steps it is convenient to change the basis from K^0 and $\bar{K}^0$ to the CP eigenstates $K_{1,2} = (K^0 \pm \bar{K}^0)/\sqrt{2}$. Λ becomes

$$\Lambda = \frac{1}{2}\begin{pmatrix} \Lambda_{11}+\Lambda_{22}+\Lambda_{12}+\Lambda_{21} & \Lambda_{11}-\Lambda_{22}-(\Lambda_{12}-\Lambda_{21}) \\ \Lambda_{11}-\Lambda_{22}+(\Lambda_{12}-\Lambda_{21}) & \Lambda_{11}+\Lambda_{22}-(\Lambda_{12}+\Lambda_{21}) \end{pmatrix} \tag{1.16}$$

$$\equiv \begin{pmatrix} \lambda_S & \Delta(\lambda_S-\lambda_L)-\epsilon(\lambda_S-\lambda_L) \\ \Delta(\lambda_S-\lambda_L)+\epsilon(\lambda_S-\lambda_L) & \lambda_L \end{pmatrix} \tag{1.17}$$

Since CP violation is a small effect the off-diagonal elements of this matrix are small in this basis and to first order in the off-diagonal elements the eigen values are

$$\lambda_S = \frac{1}{2}(\Lambda_{11}+\Lambda_{22}+\Lambda_{12}+\Lambda_{21}) = m_S - \frac{i}{2}\Gamma_S \tag{1.18}$$

$$\lambda_L = \frac{1}{2}(\Lambda_{11}+\Lambda_{22}-(\Lambda_{12}+\Lambda_{21})) = m_L - \frac{i}{2}\Gamma_L \tag{1.19}$$

and the eigenvectors are

$$K_S = K_1 + (\epsilon+\Delta)K_2 \tag{1.20}$$

$$K_L = (\epsilon-\Delta)K_1 + K_2 \tag{1.21}$$

with

$$\epsilon = \frac{1}{2}\frac{\Lambda_{12}-\Lambda_{12}}{\lambda_S-\lambda_L} = \frac{\mathrm{Im}M_{12} - \frac{i}{2}\mathrm{Im}\Gamma_{12}}{i\Delta m - \Delta\Gamma/2} \tag{1.22}$$

$$\Delta = \frac{1}{2}\frac{\Lambda_{11}-\Lambda_{22}}{\lambda_S-\lambda_L} = \frac{1}{2}\frac{i(M_{11}-M_{22})+(\Gamma_{11}-\Gamma_{22})/2}{i\Delta m - \Delta\Gamma/2} \tag{1.23}$$

$$\Delta m = m_L - m_S \tag{1.24}$$

$$\Delta\Gamma = \Gamma_S - \Gamma_L \tag{1.25}$$

From equation 1.15 it follows that $\epsilon \neq 0$ results in CP and T violation while CPT symmetry is conserved. Sometimes the symbol ϵ_T is therefore used instead of ϵ. Δ is CP and CPT violating, and T conserving. A different notation is therefore ϵ_{CPT} instead of Δ.

Next, ϵ and Δ have to be related to measurable quantities in $\pi\pi$ decays. For the decay into two pions the measurable CP violating quantities are:

$$\eta_{+-} = \frac{A(K_L \to \pi^+\pi^-)}{A(K_S \to \pi^+\pi^-)} \tag{1.26}$$

$$\eta_{00} = \frac{A(K_L \to \pi^0\pi^0)}{A(K_S \to \pi^0\pi^0)} \tag{1.27}$$

Because of the strong interaction (the electromagnetic interaction effects are much smaller) the two pions in the final state will rescatter. This can be described by a final state phase shift which will not depend on the initial state. Since the isospin is conserved by the strong interaction the phase shifts δ_0 and δ_2 for the isospin $I = 0$ and $I = 2$ states, respectively, will be different in general.

We can write the decay amplitudes as

$$Amp(K^0 \to |2\pi; I = k\rangle) = M_k e^{i\delta_k} \tag{1.28}$$

$$Amp(\bar{K}^0 \to |2\pi; I = k\rangle) = \bar{M}_k e^{i\delta_k} \tag{1.29}$$

with $k = 0, 2$. The amplitudes M_k and $\bar{M}_k$ are the weak decay amplitudes only:

$$M_k = \langle 2\pi; I = k|H_w|K^0\rangle,\ \bar{M}_k = \langle 2\pi; I = k|H_w|\bar{K}^0\rangle \tag{1.30}$$

If CPT symmetry is conserved by the weak hamiltonian H_w we find

$$M_k = (CPT|2\pi; I = k\rangle)^\dagger\ CPT\ H_w\ CPT^{-1}\ CPT|K^0\rangle \tag{1.31}$$

$$= (\langle 2\pi; I = k|H_w|\bar{K}^0\rangle)^* = (\bar{M}_k)^* \tag{1.32}$$

Here $CP|2\pi\rangle = |2\pi\rangle$ and $T|2\pi\rangle = (|2\pi\rangle)^*$ have been used since the pions have no spin and T reverses the momenta of the outgoing pions which is the same as complex conjugation for plane waves.

With the last result it is natural to decompose the decay amplitudes in a CPT conserving part A_k and CPT violating part B_k:

$$Amp(K^0 \to 2\pi; I = k) = (A_k + B_k)e^{i\delta_k} \tag{1.33}$$

$$Amp(\bar{K}^0 \to 2\pi; I = k) = (A_k^* - B_k^*)e^{i\delta_k} \tag{1.34}$$

Using this decomposition one finds

$$Amp(K_1 \to 2\pi, I=k) = \sqrt{2}(\mathrm{Re}A_k + i\mathrm{Im}B_k)e^{i\delta_k} \quad (1.35)$$

$$Amp(K_2 \to 2\pi, I=k) = \sqrt{2}(\mathrm{Re}B_k + i\mathrm{Im}A_k)e^{i\delta_k} \quad (1.36)$$

Since $Amp(K_1 \to 2\pi, I=k)$ is CP conserving $\mathrm{Re}A_k$ and $\mathrm{Im}B_k$ are CP conserving while $\mathrm{Im}A_k$ and $\mathrm{Re}B_k$ parameterize direct CP violation, i.e. CP violation in the decay amplitude.

To calculate η_{+-} using above results we need the decomposition of the 2π state into isospin states:

$$|\pi^+\pi^-\rangle = \sqrt{\frac{2}{3}}|2\pi; I=0\rangle + \sqrt{\frac{1}{3}}|2\pi; I=2\rangle \quad (1.37)$$

$$|\pi^0\pi^0\rangle = -\sqrt{\frac{1}{3}}|2\pi; I=0\rangle + \sqrt{\frac{2}{3}}|2\pi; I=2\rangle \quad (1.38)$$

$$(1.39)$$

For η_{+-}:

$$\eta_{+-} = \frac{A(K_L \to \pi^+\pi^-)}{A(K_S \to \pi^+\pi^-)} = \frac{A(\,(\epsilon-\Delta)K_1 + K_2 \to \pi^+\pi^-)}{A(\,(K_1 + (\epsilon+\Delta)K_2 \to \pi^+\pi^-)} \quad (1.40)$$

$$\approx \epsilon - \Delta + \frac{A(K_2 \to \pi^+\pi^-)}{A(K_1 \to \pi^+\pi^-)} \quad (1.41)$$

$$= \epsilon - \Delta + \frac{\sqrt{\frac{2}{3}}(\mathrm{Re}B_0 + i\mathrm{Im}A_0)e^{i\delta_0} + \sqrt{\frac{1}{3}}(\mathrm{Re}B_2 + i\mathrm{Im}A_2)e^{i\delta_2}}{\sqrt{\frac{2}{3}}(\mathrm{Re}A_0 + i\mathrm{Im}B_0)e^{i\delta_0} + \sqrt{\frac{1}{3}}(\mathrm{Re}A_2 + i\mathrm{Im}B_2)e^{i\delta_2}} \quad (1.42)$$

With the definitions

$$\omega = \frac{\mathrm{Re}A_2 + i\mathrm{Im}B_2}{\mathrm{Re}A_0 + i\mathrm{Im}B_0}e^{i(\delta_2-\delta_0)} \quad (1.43)$$

$$\epsilon' = \frac{1}{\sqrt{2}}\frac{\mathrm{Re}B_2 + i\mathrm{Im}A_2}{\mathrm{Re}A_0 + i\mathrm{Im}B_0}e^{i(\delta_2-\delta_0)} \quad (1.44)$$

$$a = \frac{\mathrm{Re}B_0 + i\mathrm{Im}A_0}{\mathrm{Re}A_0 + i\mathrm{Im}B_0} \quad (1.45)$$

we get

$$\eta_{+-} = \epsilon - \Delta + \frac{\sqrt{\frac{2}{3}}(\mathrm{Re}B_0 + i\mathrm{Im}A_0)e^{i\delta_0} + \sqrt{\frac{1}{3}}(\mathrm{Re}B_2 + i\mathrm{Im}A_2)e^{i\delta_2}}{\sqrt{\frac{2}{3}}(\mathrm{Re}A_0 + i\mathrm{Im}B_0)e^{i\delta_0}(1+\omega/\sqrt{2})} \quad (1.46)$$

$$= \epsilon - \Delta + \frac{a+\epsilon'}{1+\omega/\sqrt{2}} \approx \epsilon - \Delta + a - a\omega/\sqrt{2} + \epsilon' \quad (1.47)$$

Here we have used the experimental fact that $\omega \approx 1/22$ and ϵ' are small. For η_{00} a similar computation gives

$$\eta_{00} = \epsilon - \Delta + \frac{a - 2\epsilon'}{1 - 2\omega/\sqrt{2}} \approx \epsilon - \Delta + a + 2a\omega/\sqrt{2} - 2\epsilon' \tag{1.48}$$

From our definitions Δ, a, ω and ϵ' have CPT violating contributions. Before we go on analyzing these contributions lets consider the case that CPT symmetry is conserved. With the common convention of the K^0 phase [Wu 64, Schubert 70]

$$\mathrm{Im}A_0 = 0. \tag{1.49}$$

Then $\eta_{+-} \approx \epsilon + \epsilon'$ and $\eta_{00} \approx \epsilon - 2\epsilon'$. ϵ' being different from zero is therefore equivalent to $Amp(K_2 \to \pi\pi) \neq 0$, i.e. direct CP violation. The current experimental data for $|\epsilon'/\epsilon| \approx \mathrm{Re}(\epsilon'/\epsilon)$ are conflicting since the E731 result is $(7.4 \pm 5.9) \cdot 10^{-4}$ [Gibbons 93b] and the NA31 result is $(23 \pm 6.5) \cdot 10^{-4}$ [Barr 93]. On the basis of these numbers one can not draw any conclusion about the origin of CP violation. In particular, the superweak model [Wolfenstein 64] which predicts $\epsilon' = 0$ is not ruled out.

For the difference of η_{00} and η_{+-} we find from equations 1.47 and 1.48 and using above phase convention

$$\eta_{00} - \eta_{+-} = -3(\epsilon' - a\omega/\sqrt{2}) \approx \frac{-3}{\sqrt{2}} \frac{\mathrm{Re}A_0(\mathrm{Re}B_2 + i\mathrm{Im}A_2) - \mathrm{Re}B_0\mathrm{Re}A_2}{\mathrm{Re}A_0(\mathrm{Re}A_0 + i\mathrm{Im}B_0)} e^{i(\delta_2 - \delta_0)} \tag{1.50}$$

Here quadratic terms in the CPT violating amplitudes B have been neglected. Experimentally, the phases of η_{+-} $(43° - 44°)$ and of $ie^{i(\delta_2 - \delta_0)}$ $(48° \pm 4°$, [Chell 93]) are very similar. We can therefore split $\eta_{00} - \eta_{+-}$ in a part that is parallel and perpendicular to η_{+-}: Since CPT violating amplitudes are small, i.e. $|\mathrm{Im}B_0| \ll |\mathrm{Re}A_0|$:

$$(\eta_{00} - \eta_{+-})_{\|} = \frac{-3}{\sqrt{2}} \frac{\mathrm{Im}A_2}{\mathrm{Re}A_0} \tag{1.51}$$

$$(\eta_{00} - \eta_{+-})_{\perp} = \frac{-3}{\sqrt{2}} \frac{\mathrm{Re}A_0\mathrm{Re}B_2 - \mathrm{Re}B_0\mathrm{Re}A_2}{\mathrm{Re}A_0(\mathrm{Re}A_0 + i\mathrm{Im}B_0)} \tag{1.52}$$

The parallel component depends only on the CPT conserving amplitudes. Note that both terms in $(\eta_{00} - \eta_{+-})_{\perp}$ and $\Delta - a$ (in equation 1.47) are purely CPT violating. Therefore all observables in the 2π decay modes are the sum of two CPT violating amplitudes and it is not possible to prove that CPT symmetry is conserved from these decay modes alone. Only the opposite is possible: assume that CPT symmetry is conserved, i.e. $\Delta = B_k = 0$, and check the resulting predictions. This is discussed in the next section.

1.3 Predictions

If CPT symmetry is conserved we find $\eta_{00} - \eta_{+-} = -3\epsilon'$ and

$$\Delta\Phi = \Phi_{00} - \Phi_{+-} = 3\mathrm{Im}(\epsilon'/\epsilon) < 3 \cdot 10^{\circ}\,\mathrm{Re}(\epsilon'/\epsilon) \approx 0.03. \tag{1.53}$$

Here the above mentioned results for $\mathrm{Re}(\epsilon'/\epsilon) \approx 10^{-3}$ and the phase difference $(\delta_2 - \delta_0)$ have been used. A first prediction if CPT holds is therefore $\Delta\Phi \approx 0$.

Since ϵ' is parallel to ϵ if CPT symmetry is conserved, the phases of η_{+-} and ϵ are very close. Recall that the definition of ϵ is

$$\epsilon = \frac{1}{2}\frac{\mathrm{Im}M_{12} - \frac{i}{2}\mathrm{Im}\Gamma_{12}}{i\Delta m - \Delta\Gamma/2} \tag{1.54}$$

While M_{12} describes the mixing through any virtual intermediate state Γ_{12} describes the mixing in the decay matrix by the weak interaction.

$$\Gamma_{12} = 2\pi \sum_f \langle K^0|H_w|f\rangle\langle f|H_w|\bar{K}^0\rangle\, \delta(m - E_f) \tag{1.55}$$

where f denotes any common final state like $|2\pi; I = 0\rangle$, $|2\pi; I = 2\rangle$, $\pi^+\pi^-\gamma$, $\pi l\nu$ (semileptonic decays), $\pi^+\pi^-\pi^0$, $3\pi^0$ and modes with more than 3 particles in the final state.

To the imaginary part of Γ_{12} the term with $f = |2\pi; I = 0\rangle$ does not contribute because of our phase convention (A_0 is real) and the $f = |2\pi; I = 2\rangle$ term is suppressed by ϵ'. Our experiment also measured CP violation in the radiative decay mode which is parameterized similar to the $\pi\pi$ modes by the ratio $\eta_{+-\gamma}$ of the violating to conserving amplitudes. We found $\eta_{+-\gamma}$ to be consistent with η_{+-} [Matthews 95a]. Thus, the contributions of $f = \pi^+\pi^-\gamma$ to Γ_{12} will have the same phase as the one from the $\pi^+\pi^-$ channel. The contributions from the semileptonic channels to Γ_{12} would violate the $\Delta S = \Delta Q$ rule and are therefore expected to be very small. The $f = 3\pi$ terms are suppressed by $\Gamma_L/\Gamma_S = 1/580$ relative to the 2π terms provided CP violation in the 3π mode ($\eta_{3\pi}$) is similar to $\eta_{2\pi}$ as the mixing matrix suggests. Contributions from final states with more than 3 bodies are suppressed by the small branching ratios. Combining all arguments one expects the imaginary part of Γ_{12} to be very small. As a second prediction if CPT holds we get that

$$\Phi_{+-} = \Phi_\epsilon \approx \Phi_{sw} = \tan^{-1}\left(\frac{2\Delta m}{\Delta\Gamma}\right) \tag{1.56}$$

Experimentally, the bounds on CP violation in 3π decays and on $\Delta S \neq \Delta Q$ amplitudes are not very stringent. For a recent analysis of the existing data see reference [Nakada 93].

The measurement of $\Delta\Phi$ is the topic of this thesis while the measurements of Φ_{+-} and Φ_{sw} are discussed in Roy Briere's thesis [Briere 95b]. These results are accepted for publication [Schwingenheuer 95]. Our above mentioned measurement of $\eta_{+-\gamma}$ is the thesis topic of John Matthews [Matthews 95b].

1.4 Experimental Technique

To determine Φ_{+-} and $\Delta\Phi$ the phase of the interference between the decays $K_L \to \pi\pi$ and $K_S \to \pi\pi$ into charged and neutral pions need to be measured. There are several different experimental techniques which effectively differ in the way the initial quantum state is prepared [Adler 93, Buchanan 92, Carosi 90]. In our experiment K^0s or $\bar{K}^0$s are produced by the strong interaction of a 800 GeV proton beam with a Beryllium target. Far away from the target (120 m = 27 K_S lifetimes for an average 80 GeV kaon) the K_S component of the beam has decayed.

The K_L beam then traverses a regenerator. At the downstream face the kaon amplitude is a coherent superposition of K_L and K_S: $|K_L\rangle + \rho|K_S\rangle$ with ρ being the regeneration amplitude for forward scattering. This is the initial state used in our analysis. ρ depends on the composition and length of the regenerator and the kaon momentum. Using equation 1.27 the decay rate downstream of the regenerator is:

$$\begin{aligned} R(|K_L\rangle + \rho|K_S\rangle \to \pi\pi) &\propto |\eta e^{-i(m_L - \frac{i}{2}\Gamma_L)\tau} + \rho e^{-i(m_S - \frac{i}{2}\Gamma_S)\tau}|^2 \\ &= |\eta|^2 e^{-\Gamma_L \tau} + |\rho|^2 e^{-\Gamma_S \tau} + \\ &\quad 2|\eta||\rho| e^{-\frac{1}{2}(\Gamma_L + \Gamma_S)\tau} \cos(\Delta m \tau + \Phi_\rho - \Phi_\eta). \end{aligned} \tag{1.57}$$

with τ being the proper time of the kaon. If ρ is known one can extract the phase of η from the interference term. How ρ is determined in our experiment is explained in the following section. Fig. 1 shows an example of the decay distribution.

The apparatus used in E773 was essentially the same as for E731 which took data in the previous fixed target run. E731 had two K_L beams and one of them was intercepted by a

regenerator. Since the phase information is in the interference term two regenerators were employed in the E773 experiment, one in each beam. Both beams could therefore be used to fit for the phases. It turned out that this method had one important disadvantage: there was no K_L beam in the experiment to predict the kaon energy spectrum incident on the regenerators. Thus two parameters were floated in the fit to compensate for our ignorance (see chapter 8). The statistical and systematical error especially in our determination of Φ_{+-} was compromised because of this.

Alternatively, the interference can be measured close to the kaon production target with $K^0 \approx (K_S + K_L)/2$ and $\bar{K}^0 \approx (K_S - K_L)/2$ decays. Since the interference has opposite sign for K^0 and $\bar{K}^0$, the relative production probability (called dilution factor) has to be known [Carosi 90]. In the CPLEAR experiment the neutral kaons are produced by $p\bar{p}$(at rest) $\rightarrow K^-\pi^+K^0$ or $K^+\pi^-\bar{K}^0$. The flavor of the neutral kaon can therefore be tagged by the charge of the kaon.

Naturally, all methods have advantages and disadvantages. Instead of comparing the different experiments I will briefly mention the main characteristics of our method. Only $\Phi_\rho - \Phi_\eta$ can be extracted from the interference term. For the phase difference $\Phi_{00} - \Phi_{+-}$ the regeneration phase drops out but for our measurement of Φ_{+-} we have to extract Φ_ρ from our data. In addition kaons scatter diffractively in the regenerator which needs to be simulated. Our analysis proofs however that these problems can be solved and our measurements for $\Delta\Phi$ and Φ_{+-} are currently the most precise ones (see chapter 11).

1.5 Regeneration

The regeneration of K_S when a K_L beam traverses material has first been predicted and observed in the 1950s [Pais 55, Good 61]. Since then this phenomenon was studied in many experiments. Reference [Kleinknecht 73] is a review article on this subject. This section describes the basic principles of the regeneration amplitude and outlines how we determined ρ in our experiment.

The elastic scattering amplitude for the $K^0$and $\bar{K}^0$ nucleon scattering are called $f(E, p_T^2)$ and $\bar{f}(E, p_T^2)$, respectively. In general f and $\bar{f}$ are different because of the different quark

contents of K^0 and $\bar{K}^0$. If a $K_L \approx K^0 - \bar{K}^0$ scatters in a thin regenerator the amplitude becomes:

$$f\,K^0 - \bar{f}\,\bar{K}^0 = \frac{f+\bar{f}}{2}(K^0 - \bar{K}^0) + \frac{f-\bar{f}}{2}(K^0 + \bar{K}^0) \quad (1.58)$$

$$= f_{22}K_L + f_{21}K_S \quad (1.59)$$

with $f_{22} = (f+\bar{f})/2$ and $f_{21} = (f-\bar{f})/2$. Thus after the regenerator the kaon amplitude is a *coherent* sum of K_L and ρK_S with $\rho \propto f_{21}$.

Of special importance is the forward scattering. The incoming K_L oscillates with the frequency $m_L c^2/\hbar$. At some length l within the regenerator scattering to a K_S occurs with some phase shift $e^{i\phi}$. [9] Afterwards the K_S oscillates with the frequency $m_S c^2/\hbar$. Since the frequency difference Δm is small for our regenerator length and kaon momentum, the phase of the K_S amplitude at the downstream face of the regenerator does not depend on the depth where the scattering occurs.[10] Therefore all phases add *coherently* and ρ is proportional to the number of scattering centers N.

For diffractive scattering by an angle θ with

$$\theta^2 > \frac{2\hbar}{Lp} + \frac{2m_K \Delta m\, c^2}{p^2} \approx \frac{4\cdot 10^{-16}}{Lp[m\,GeV/c]} + \frac{3.5\cdot 10^{-15}}{p^2[GeV^2/c^2]} \quad (1.60)$$

the scattering centers add *incoherently* because the path length the kaon travels from the scattering to the downstream face of the regenerator depends on the scattering center position and because this position can be measured in principle. The decay rate from diffractively regenerated K_S is then $|A|^2 \propto N$. Since the decay rate for coherently regenerated K_S was proportional to $|\rho|^2 \propto N^2$ the regeneration is strongly forward peaked. This forward peak is visible in Fig. 2 which shows the observed p_T^2 distributions in $\pi^+\pi^-$ decays.

By adding the spherical waves $f_{21}e^{ikr}/r$ from all scattering centers[11] one finds

$$\rho = 2\pi i N L \frac{f_{21}}{k}\,\frac{1 - e^{-L(\frac{1}{2}\Gamma_S - i\Delta m)/\gamma c}}{L(\frac{1}{2}\Gamma_S - i\Delta m)/\gamma c} \quad (1.61)$$

[9] The question whether the kaon energy or kaon momentum is conserved in the process of regeneration is discussed in reference [Lipkin 95].

[10] For kaon energies larger than 20 GeV and a regenerator length $L = 1.2$ m the phase difference due to the different frequencies is smaller than $(\Delta m\, L\, m_k)/(c\,E) = 30°$. The geometric factor in the formula for ρ will correct for this effect.

[11] $\vec{r}$ is the vector between the scattering center and the downstream face of the regenerator.

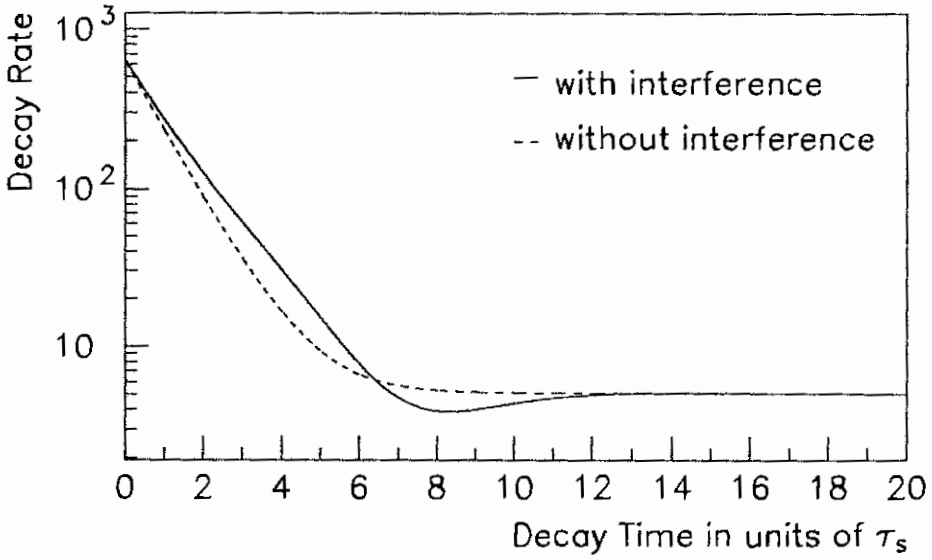

Figure 1. Decay distribution of $K_L + \rho K_S$ into $\pi\pi$.

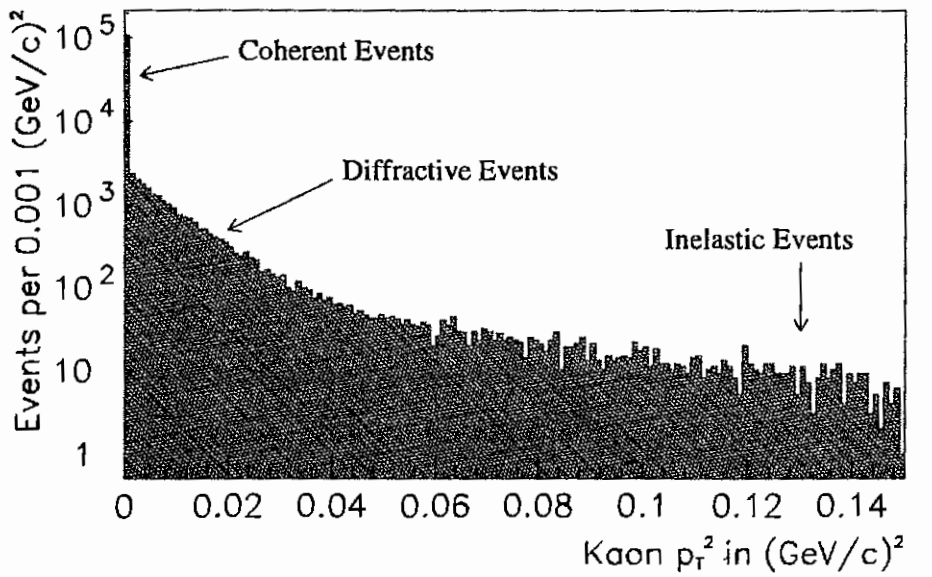

Figure 2. Data p_T^2 distribution for $\pi^+\pi^-$ decays. Coherently regenerated events reconstruct with a $p_T^2 < 250$ (MeV/c)^2, a quarter of the first bin. Diffractively regenerated kaons scatter off the entire nucleus and have a much steeper slope than inelastically regenerated kaons which scatter off single nucleons. Shown is the DR beam (see chapter 2) distribution.

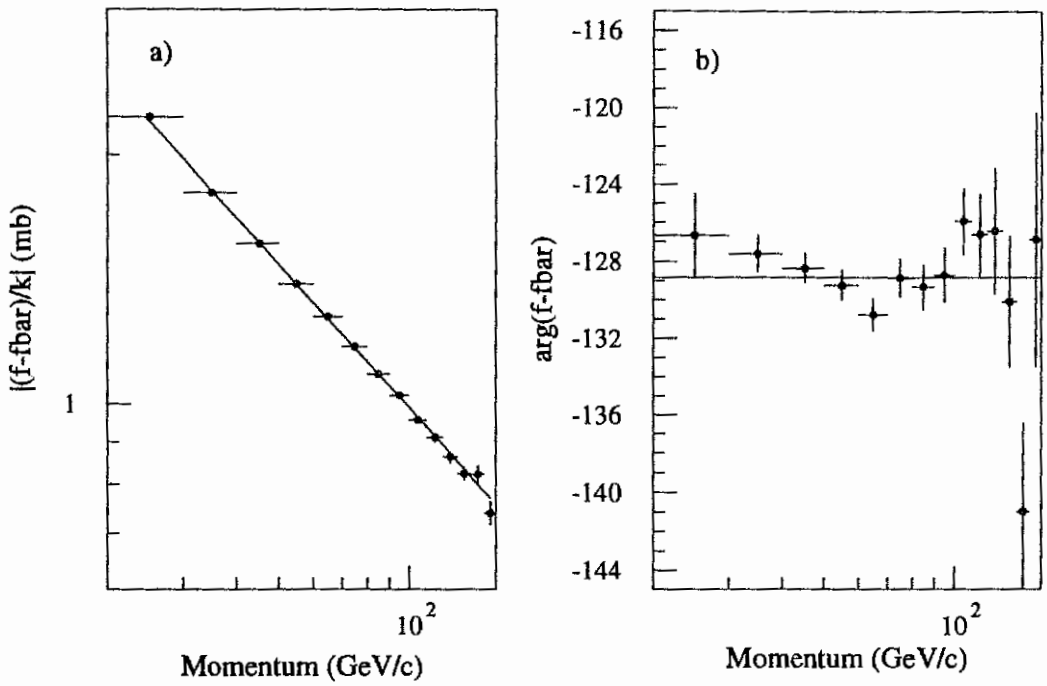

Figure 3. Magnitude of $|f-\bar{f}|/k$ and the phase of $(f-\bar{f})/k$ versus the kaon momentum. All phases and magnitudes are extracted from a simultaneous fit to the $\pi^+\pi^-$ data. The errors are therefore correlated.

The last term in this equation is called the geometric factor and is due to the propagation of the K_S amplitude within the regenerator. This factor is 1 for a short regenerator.

For our phase measurements we need to determine $\rho\,(f_{21})$ from our data. Experimentally, the size of f_{21}/k as a function of the kaon momentum ($p = \hbar k$) is well described by a power law $f_{21}/k \propto p^{\alpha}$. Many experiments in the past as well as this experiment have seen this behavior (see Fig. 3 in this thesis and Fig. 5 in reference [Gibbons 93b]).

Regeneration (by the strong interaction) can be described in terms of meson exchange. The meson has to have charge conjugation quantum number $C = -1$ (like the ρ and ω) since the K_L and K_S have nearly opposite C quantum numbers. For carbon, an isoscalar nuclei, only the ω contributes because of isospin conservation in the strong interaction. Regge theory then predicts the observed power law behavior of $|f-\bar{f}|/k \propto p^{\alpha}$ [Briere 95b]. If one assumes that the scattering amplitudes f and $\bar{f}$ are analytic functions of the kaon momentum, dispersion relations can be used to calculate the real parts if the imaginary parts are know with the Kramers-Kronig relation [Jackson 75] or the phase can be extracted from

the magnitude [Briere 95a, Kleinknecht 94]. For a power law behavior the phase of $(f-\bar{f})/k$ is $-\pi(2+\alpha)/2$ with α being the power law exponent. Therefore α and $|f-\bar{f}|/k$ at a fixed momentum determine the regeneration amplitude.

In practice there are corrections to the single power law behavior. Our regenerator is made out of $CH_{1.1}$ and regeneration off hydrogen is mediated by the ρ and the ω meson, thus a second power law for the ρ with a different α has to be added. This is however a small correction [Briere 95a, Briere 95b] and in the fit to the data the measured regeneration off hydrogen is taken from reference [Bock 79].

In addition, the kaon can scatter multiple times in the nucleon which results in the so called elastic screening correction. A numerical analysis of this correction shows however that the main effect is a shift of the power law coefficient α whereas the power law behavior is almost unchanged [Briere 95a, Briere 95b]. Because of the analyticity constraint the phase of f_{21} is still determined correctly. The regeneration off carbon was therefore parameterized by a single power law modified by the screening correction, a complex function of the momentum. In the fit to the data we float the power law coefficient α and the absolute value of regeneration amplitude at 70 GeV/c, $|(f-\bar{f})/k|_{70\ GeV}$ (see chapter 8).

CHAPTER 2

Beamline and Detector

During the last 5 years 14 Ph.D. thesis have been written (including this one) about measurements performed by our group. The experiments were E731, E773 and E799. The main difference between the three setups was the number of regenerators employed (one in E731, two in E773 and none in E799). Therefore, the common parts of the detectors have been well documented already. Here, I will focus on detector elements specific to E773 and important to this analysis.

2.1 The Beamline

The Fermilab TEVATRON accelerator provides an 800 GeV/c proton beam to the fixed target experiments. The beam is delivered in spills of 23 sec length every minute. Each spill is divided in 'buckets' of 1.3 nsec length and 19 nsec separation. An RF signal with this timing provided by the accelerator was used in coincidence with other signals in the trigger. In our experiment the protons hit a beryllium target with the dimensions of $3.2 \times 3.2 \times 3600$ mm^3. The position and size of the proton beam at the target was monitored using a small wire chambers (SWIC) 3 m upstream of the target. The integrated intensity varied between 10^{12} and $2.5 \cdot 10^{12}$ protons per spill.

Fig. 4 shows the fractional uptime of the accelerator per day during our data taking. The eight day period where this fraction is zero corresponds to a downtime of the accelerator. Averaged over all days but excluding the long downtime, the accelerator was up 69% of the

time. If the downtime is also averaged in the uptime drops to 59%. The second interesting question is: how often were data written to tape when there was beam. This fraction per day is shown in Fig. 5. The average was about 72%. One important reason for such a low uptime were constant problems with the data acquisition system which could not be fixed during the run. In total, only 43% of the time did we write data to tape.[1]

Neutral kaons produced in the horizontal plane at an angle of 4.9 mrad relative to the proton direction point towards our apparatus. The beamline is shown in Fig. 6. At $z = 15$ m a collimator with two holes splits the beam in the y (vertical) direction. In total there are 6 collimators and slabs to define the size and position of the upper and lower beams. Positions and tilts are known from a survey and by comparing the beam profiles between data ($K \to \pi^+\pi^-$ decays) and a simulation (see chapter 7.7). The size of the beams was 8×8 cm^2 at $z = 180$ m.

Magnets downstream of slabs and collimators swept charged particles away. A beryllium absorber (51 cm long) increased the kaon to neutron flux. A lead absorber (7.6 cm long) removed photons in the beams. The two regenerators of different length were employed, one in each beam. To keep the kaon flux after the regenerators similar a beryllium absorber (called shadow absorber in Fig. 6) of 46 cm length (about 0.9 K_L interaction length) was placed in the beam with the shorter regenerator. At the detector the beams consisted mainly of kaons and neutrons with similar fluxes.

In our coordinate system, the z axis connects the target with the center of the lead glass (see Fig. 7), the $+y$ direction is upwards and the x axis is horizontal with $\vec{e}_x = \vec{e}_y \times \vec{e}_z$. Because of the boost along the z direction from the primary protons, the longitudinal dimensions of the detector are much bigger than the radial dimensions. The apparatus extends between 115 m and 190 m in z and has almost circular symmetry with the radial dimension increasing with the distance from the target up to 1.2 m. Main elements of the detector were the two regenerators, the vacuum decay region, the charged spectrometer and the electromagnetic calorimeter. Furthermore, there were 12 photon vetoes at different

[1] The accelerator was called 'up' if the total number of protons exceeded $3 \cdot 10^{11}$ per spill (typically $15 \cdot 10^{11}$) or the number of MU2 hits exceeded $2 \cdot 10^6$ per spill (typically 10^6 when the beam stop in MC2 was closed and $4 \cdot 10^7$ when the beam stop was open). If the number of events written to tape was bigger than 3000 per spill (typically 14000), the detector was called 'up'.

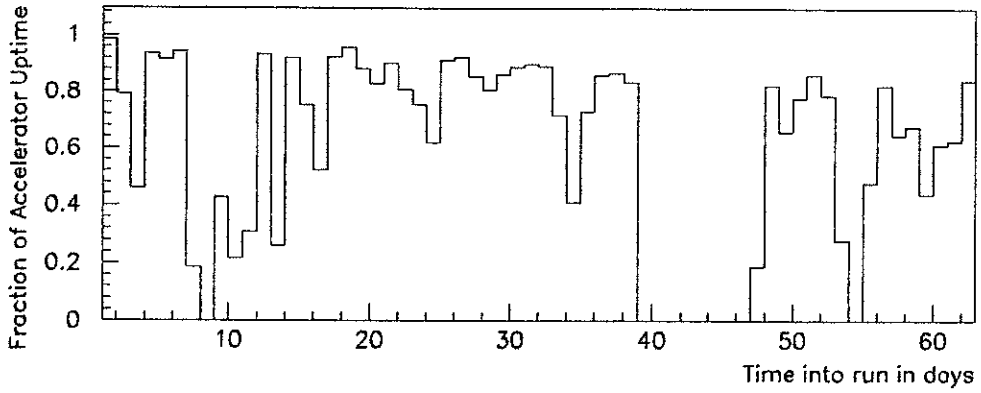

Figure 4. Fractional uptime of the accelerator per day. The 8 day period without data correspond to a down time of the accelerator.

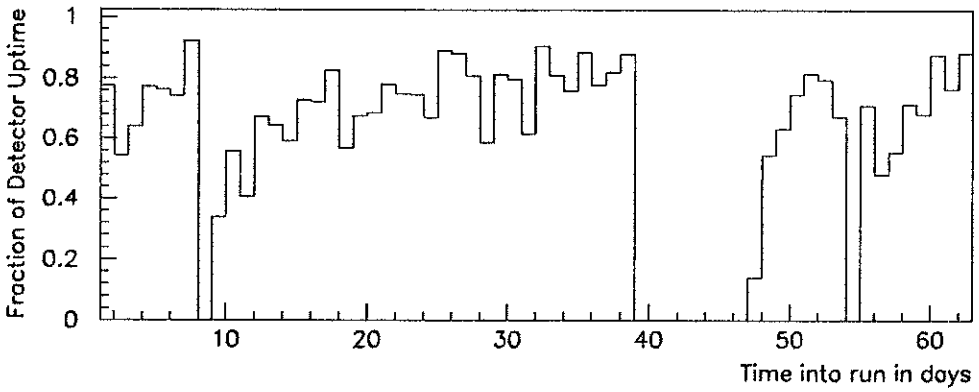

Figure 5. Ratio of the number of spills when data were written to tape over the number of spills beam was delivered.

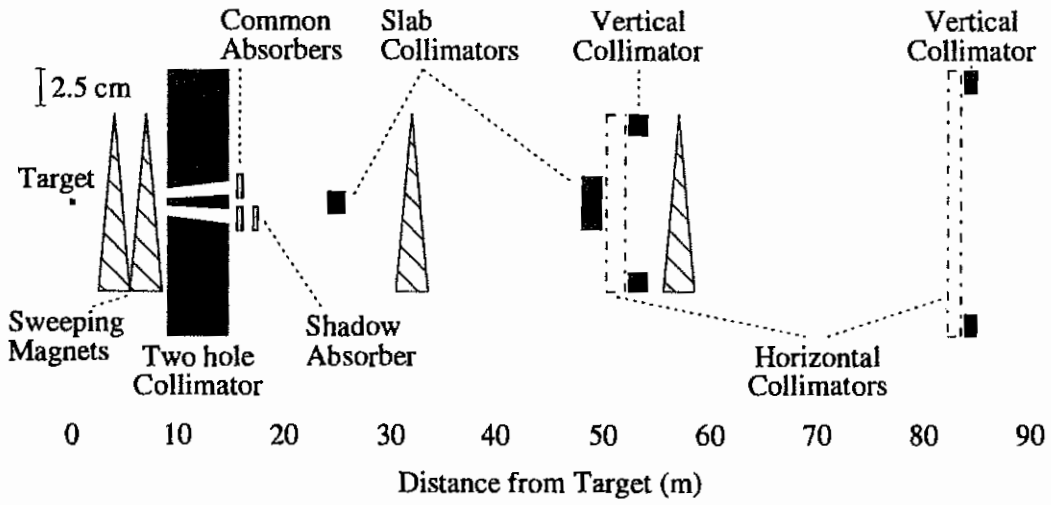

Figure 6. Schematic of the E773 beamline.

positions, trigger hodoscopes, a hadrons shower veto and a muon veto system. In the next sections these detector systems will be described.

2.2 The Regenerators

The regenerators are made out of plastic scintillator ($CH_{1.1}$ Pilot U, trademark NE Technologies). The upstream regenerator (UR) was located at $z = 117.14$ m and about 1.2 interaction length long. The downstream regenerator (DR) was located at $z = 128.40$ m and about 0.4 interaction length long. The 24 pieces for the DR were arranged as shown in Fig. 8. Each piece was 3.3 cm long in the beam direction and wrapped with 0.5 *mils* aluminized mylar and and 16 *mils* of tape. A more detailed description of the dimensions and the wrapping can be found in [Briere 95b]. The pieces were about 1.7 cm apart in z. The DR was fully active, i.e. every piece of scintillator was glued to two photo tubes. The anode signal was AC coupled to a pulse shaping amplifier. With an LRC network the recovery time of the signal was cut from 30 nsec to 20 nsec and the signal was then amplified and pulse shaped to compensate for the dispersion and attenuation of the 520 nsec long RG213 cable connecting the amplifier to the ADC. This delay is needed because of the trigger timing.

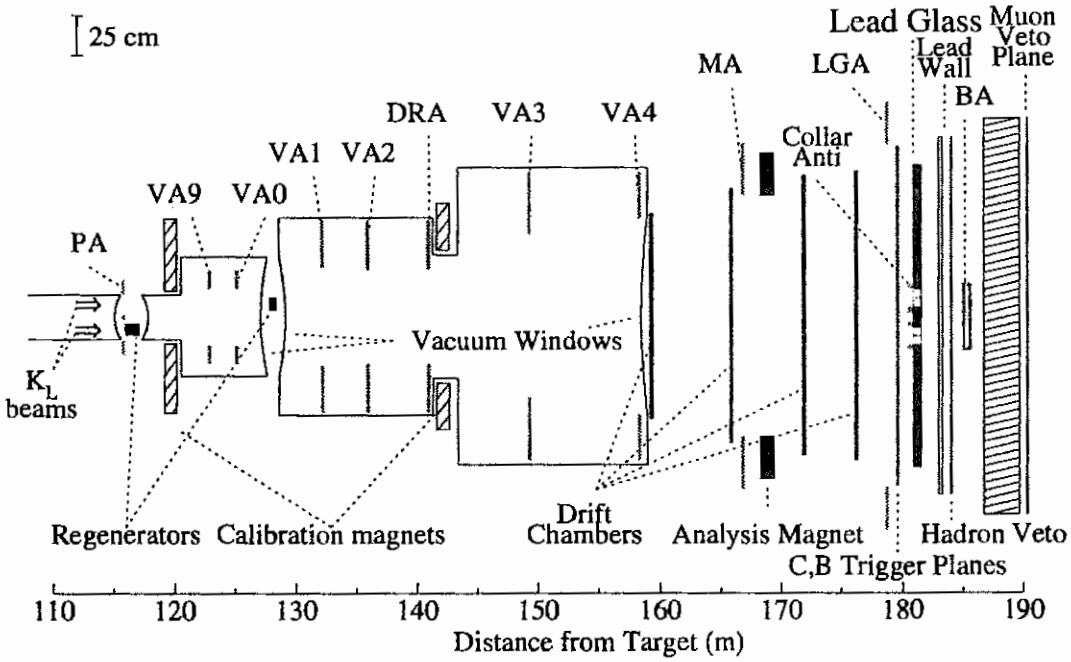

Figure 7. Schematic drawing of the E773 detector.

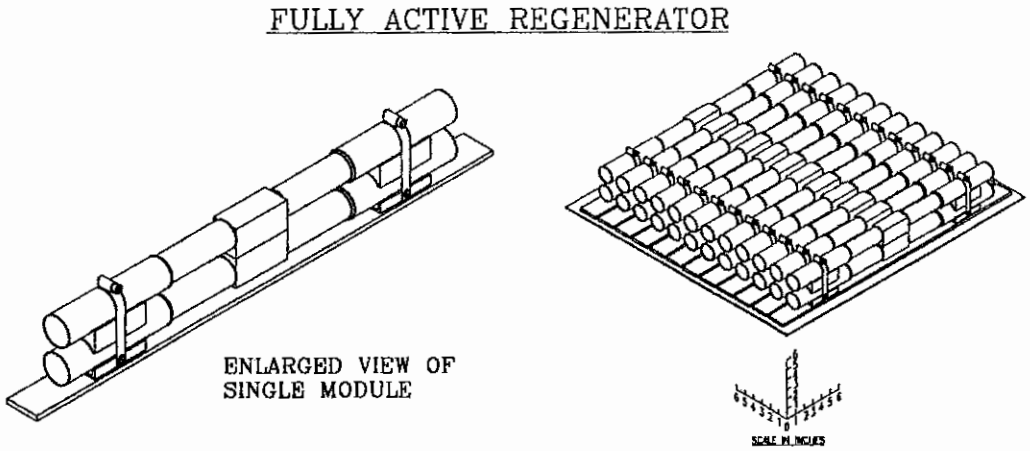

Figure 8. Schematic drawing downstream regenerator (DR).

In addition the amplifiers provided a fast signal for triggering purposes. The signals from the two most downstream pieces of the regenerator were discriminated with a threshold of 50% of the signal size from a minimum ionizing particle (MINI). If an inelastic interaction in the regenerator produced charged particles or photons which then converted, the event could be vetoed at the trigger level and an offline cut on all regenerator signals at 20% of MINI further reduced the background as discussed in chapter 5.2. For about 1% of the buckets the DR trigger signal was on (for typically $1.5 \cdot 10^{12}$ protons per spill).

The upstream regenerator (UR) was made out of 72 scintillator pieces arranged similarly to the DR. It was therefore three times as long but only partially instrumented. In every fourth row the two scintillator pieces were viewed by one photo tube each. There were no air gaps between the pieces and the wrapping for the blocks viewed by the PMTs was 0.5 *mils* aluminized mylar and 9 *mils* tape. A passive current splitter provided two signals: one for digitization and one for triggering. For the UR four of the channels were used in the trigger. Because of the higher beam intensity for the UR[2] and the lack of signal shaping and amplification, the offline cut was looser than for the DR (at 80% of MINI).

Both regenerators could be moved from one beam hole to the other. Once every minute they switched their positions to cancel differences between the two beams.

2.3 The Spectrometer

The charged tracks from $K \to \pi^+\pi^-$ were reconstructed in the spectrometer. It consisted of 4 drift chambers and a dipole magnet which provided a 200 MeV/c kick in the $+x$ direction. The size of the kick was chosen according to the maximum p_T of a pion ($\sqrt{0.25\, m_K^2 - m_\pi^2} \approx 0.21$ MeV/c). The chamber sizes increased with the distance from the target from 1.26×1.26 m^2 to 1.77×1.77 m^2.

Each chamber measures the x and y projection of the tracks with two wire planes. The drift cells have hexagonal geometry as shown in Fig. 9. The spacing between two signal wires in a plane is 1/2 inch. The second plane of signal wires is staged relative to the first one by half the wire spacing to resolve left-right ambiguities. The chambers were operated

[2]The DR beam was attenuated by the shadow absorber.

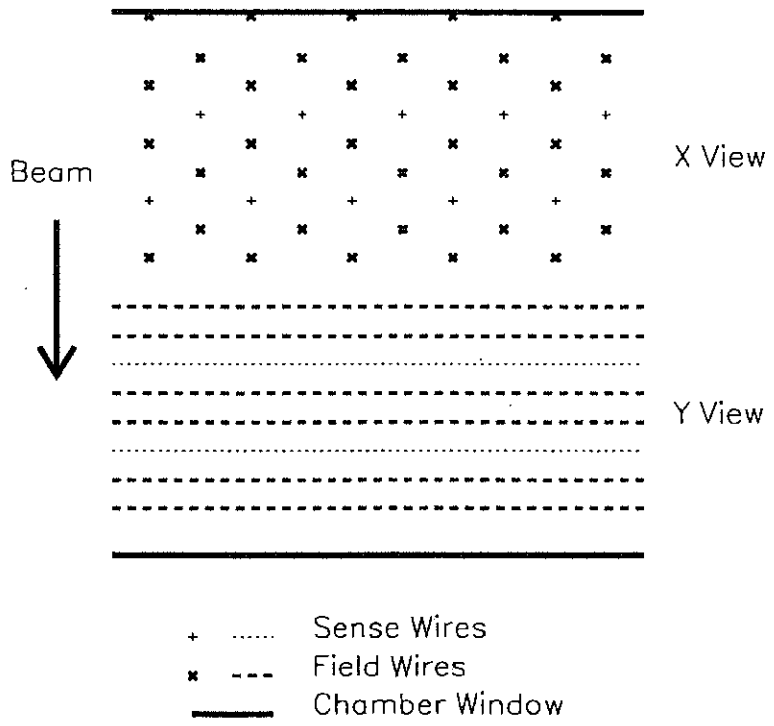

Figure 9. Schematic drawing of sense wire and field wire layout in a drift chamber.

at atmospheric pressure and the drift gas was a mixture of equal parts of Argon and Ethane with a 1% admixture of isopropal alcohol for quenching. The high voltage of the field wires was -2650 V. Off-spill (the time between spills) the voltage was lowered to 80% to reduce aging effects.

The pulses from the signal wires were amplified and discriminated at the chamber. Sixty meter long twisted-pair cables brought the logic outputs to time-to-digital converters (TDCs, LeCroy 4291B) and to "repeater boards" in the counting room. The TDCs measured the drift times with 1 nsec resolution while the repeater boards were part of the

level 2 charged mode trigger. The long delay time was needed for triggering. The TDCs were started by the wire hit and stopped by the level 1 trigger signal (common stop mode). The TDCs were inhibited after a level 1 trigger until the level 2 decision was made and the event was read out. This ensured that hits from a following bucket did not restart the TDC before the readout occurred. The ionization of the gas occurs in bursts about 300 μm apart along the path of the track. Since the drift velocity of 50 μm/nsec is much smaller than the track velocity the ionization occurring closest to the signal wire will arrive first. To block out later pulses which would restart the TDC the discriminator outputs were 250 nsec long.

A more detailed description of the chamber system can be found in reference [Briere 95b].

2.4 The Calorimeter

An array of 804 lead glass blocks (Schott F2 glass) served as electromagnetic calorimeter for the reconstruction of $K \to \pi^0\pi^0$ decays. This array was located downstream of the spectrometer at $z = 181$ m. Each block had a surface of 5.8×5.8 cm^2 and was 60.2 cm (= 18.7 radiation lengths) deep. It was wrapped with 0.5 mil aluminized mylar to optically separate the blocks. The array was almost circular with a radius of about 93 cm (see Fig. 10). No blocks were employed where the upper and lower beams passed through the array because of the high beam intensities. The array was kept in a light tight and air conditioned house.

In the lead glass electrons radiate photons and photons convert into electron-positron pairs. If these charged particles travel with a speed $\beta = v/c$ such that $n\beta > 1$ with $n \approx 1.6$ being the refractive index for lead glass, Çerenkov light is emitted at an angle $\cos\Theta_C = 1/n\beta$. The light was collected by a 10 stage Amperex 2202 photo tube with a bialkali cathode and a gain of about 10^5. The photo tube was pressure mounted to the glass block. Silicon gel in between was used to make optical contact. To reduce the nonlinear response of the lead glass due to light absorption (see chapter 4) a Wratten 2A filter was placed in the gel which absorbed light below 430 nm. The high voltage of the photo tubes was about 1200 V and set and controlled by a LeCroy 1440 system. A 1 Volt change caused

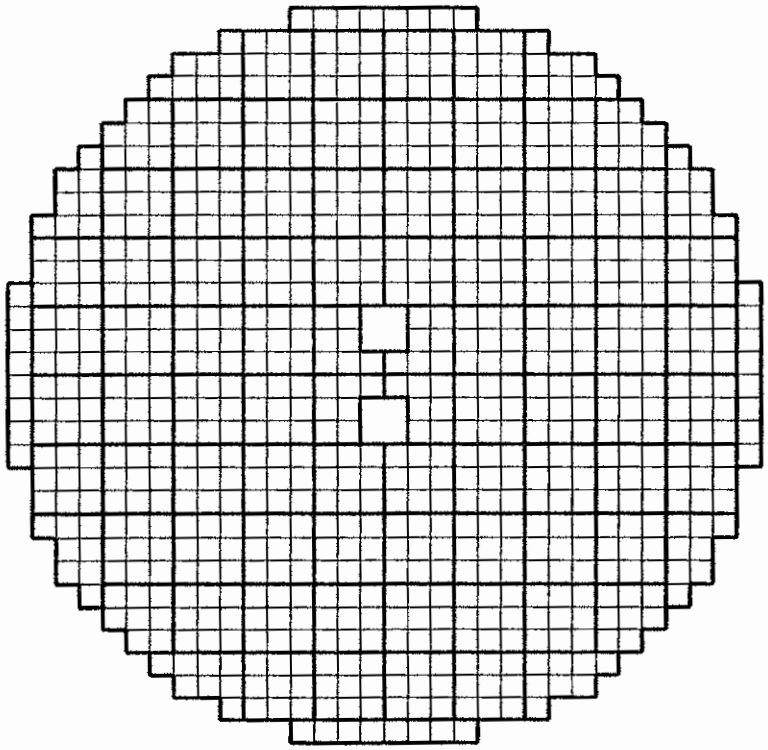

Figure 10. Front view of the Lead Glass array. Shown is the arrangement of the 804 blocks. The thick lines mark the blocks that belong to one adder channel.

a gain change of about 1%. The HV was stable to within a fraction of a volt during the run and the voltages were adjusted from time to time to adjust for the changing response of the blocks due to radiation damage and curing (see below).

The damage increased with the amount of radiation. Especially blocks close to the beams were damaged and twice through our 3 month of running we cured [Patterson 90] these blocks with UV light from a 400 W mercury vapor lamp.

The PMT signal was split. 87.5% of it was brought to the analog-digital converter (ADC)

in the counting room through a 80 m RG58 cable. Through a capacitive coupling this signal was also available to a hardware cluster finder (HCF). Once a level 1 trigger decision was made, the HCF digitized the energy in each block with a 30 MHz 6 bit flash ADC and compared the energy with a preloaded threshold (in our case 1 GeV). Thus for each of the 804 blocks 1 bit was loaded into the cluster finder boards and every connected island of blocks above threshold was counted as one hardware cluster. Note that the definition of a cluster used in the reconstruction later will be different.

The ADCs used to reconstruct the block energies were LeCroy 1885N. This is a dual range ADC with 12 bits precision. The 96 input channels per board were digitized by one ADC chip. Each input signal was split 80%/10%/10% by a voltage divider. Two parts (the 80% and a 10% part, which corresponded to the low and high range signals, respectively) were integrated with a gate width of 150 nsec.[3] The resulting high to low range gain difference was 8 which increased the dynamic range to 15 bits.

The 96 high and low range signals were then voltage multiplexed to a comparator, which decided to digitize the low or the high range signal. If the low range charge was above 175 pC (about 3600 counts) the high range charge was digitized. The actual voltage digitized is the difference between the high or low range voltage and a bias voltage. This method compensates for temperature effects. To produce the bias voltage a bias current was integrated simultaneously to the signal. After the event was digitized all capacitors discharged to ground until the next gate was received. There was one FET switch to drain the input signals and one for the bias charges. These switches had a small resistance which caused a decay time for the two signals. Depending on the integration rate of the ADC, i.e. the beam intensity, the reset times varied. The amount of residual charge therefore depended on the running conditions and because of the two FET switches involved, the effect can have either signs. This effect is expected to be the same for all 96 channels of an ADC module and was observed in the data (see Fig. 23). Section 5.1 describes the method we used to correct for this "pedestal shift".

The long gate width relative to the promptness of the Çerenkov light was necessary

[3]The remaining 10% were not used in our experiment.

because of the dispersion of the RG58 cable and the scintillation light component of the lead glass signal.

Ten ADCs were used in our experiment. They were read out with a LeCroy 1821 module. At this stage the pedestals for all channels were subtracted and a readout threshold of $\geq$ 6 counts (= 30 MeV) was applied.[4] Off-spill, special pedestal events were taken for the low and high range and once every minute the average of the pedestals was calculated and downloaded into the 1821 module.

The remaining 12.5% of the PMT signal was added together with that of 8 neighboring blocks. This adder signal (see Fig. 10) was digitized with a short gate width of 30 nsec.[5] Since the block energies were digitized with a 150 nsec gate, energy out of time relative to the trigger will affect the reconstructed energy but not the adder energy and, by comparing the two, accidental activity in the array could be identified. Part of all adder signals were also summed to give the total energy of the array. The comparison of the total energy with a threshold of about 25 GeV was part of the level 1 trigger.

To stabilize the cathode current of the PMTs and thus the gain of the tubes, the blocks were illuminated by an LED. The LED light was distributed by optical fibers to the front of each block. On-spill and off-spill we took flasher events to monitor the array. In those events the light of a flash lamp was distributed through the same fibers to each block and the PMT signal was then digitized. Gain changes could be traced with these events quickly.

2.5 The Trigger Hodoscopes

Between the last chamber and the lead glass we used two scintillator planes, call the B and C banks, to trigger on charged tracks. The scintillators with 1 cm thickness gave fast signals whereas the chamber drift times were too slow to be used for level 1 triggering. The C bank was segmented horizontally in 24 counters, 12 east and 12 west of the centerline of the detector. The B bank was segmented vertically, 15 counters above and 15 counters below the centerline. Each counter covered an area of about 0.1×1 m^2. Each of the 54

[4]For accidental events no pedestal subtraction was performed.

[5]The time separation between buckets was 19 nsec.

signals was discriminated at 0.5 MINI and used in the trigger. For the B bank the individual signal sizes were also digitized.

The logical OR of the discriminator signals from the upper 16 counters of the C bank is called CUP while the combination from the lower 16 counters is called CDOWN. Note that there is an overlap of counters for CUP and CDOWN because the two beams were separated vertically and the same signals could be used to trigger on decays in either beam. The logical OR of the discriminator outputs of the 16 easternmost B bank counters is called BEAST and the combination of the 16 westernmost counters is called BWEST. Other logical combinations used in the trigger were 1B, 1C, 2B and 2C for one or two B or C bank counters firing. There was no overlap between the individual counters of the banks and the separation was about 1 mm. These cracks were mapped out using data and the map was used in the detector simulation.

For part of the run there were two more trigger planes in the middle of the decay volume at 141 m, called T and V. The two planes were segmented horizontally or vertically in 6 counters and were 2 mm thick in total. All signals were discriminated and digitized. The logical OR of the discriminator outputs from the T bank and from the V bank were used in the level 1 decision. After a level 2 trigger upgrade was implemented, T and V were physically removed. The first part of the data will be referred to as data set 1 and the part after the removal will be referred to as data set 2 for the rest of this thesis. The decay region for charged tracks used in the final fit was extended by 14 m for set 2. For measuring the interference this was extremely useful.

2.6 The Photon Vetoes

To detect charged and neutral particles outside the spectrometer and calorimeter 12 detector components at different z positions, with different geometry and different specifications were employed (see Fig. 7). In the following each of them will be described briefly.

The scintillator pieces of the **PA** were arranged around the upper and lower beams just upstream of the UR at $z = 116$ m. The logical OR of all discriminated signals was used in the trigger.

The vetoes **VA9** and **VA0** were located between the two regenerators at z=123 m and z= 125 m. They consisted of a layer of scintillator in the front and a lead-lucite sandwich detector in the back. The light was read out by photo tubes. The shape of the vetoes was rectangular with a 9.5 cm by 17.2 cm hole in the middle for the beam and the decay particles to pass through. The scintillators were in veto as part of the trigger while the sandwich signals were digitized and used in the off-line analysis.

The vetoes **VA1** and **VA2** were at z = 132 m and z = 136 m. They consisted of a layer of scintillator in the front followed by two lead-lucite sandwich detector of 3 radiation length each. Their shape was circular with an inner hole of radius 30 cm. The scintillator signal was used in the trigger while the sandwich signals were digitized and used off-line.

Another veto system was **DRA** at z = 141 m. It consisted of a scintillator and a lead-scintillator component. Both signals were digitized and the scintillator signal was used for triggering. This veto had a rectangular inner hole of 50 × 60 cm^2 and was used to define the outer acceptance edge of the T and V trigger hodoscopes.

The vetoes **VA3** and **VA4** were at z =149 m and z = 158 m. They were identical with VA1 except that the inner hole radii increased to 50 and 60 cm, respectively.

The **MA** was just upstream of the magnet and employed to detect particles hitting the iron yoke. The build-up was scintillator followed by a lead-lucite sandwich. The scintillator signal was again used in the trigger and the lead-lucite signal was digitized and used off-line.

The **LGA** was 2 m upstream of the lead glass, circular in shape and with an inner radius of 91 cm. The LGA is a lead-lucite sandwich detector. The signal was digitized and discriminated. The ADC information was used off-line while the discriminator output was used in the trigger.

The **CA** was mounted a few centimeters in front of the lead glass. Its purpose was to detect particles hitting the glass very close to the beam holes. In that case a large portion of the electromagnetic shower is lost in the beam holes and the energy reconstruction is poor. With the CA covering the inner half of the blocks next to the two holes these events could be vetoed. The CA also defined a sharp acceptance edge. Because of the two holes the CA consisted of two identical modules, each being made out of a layer of copper, followed by a layer of lead and a layer of scintillator, in total 8.1 radiation length. Eight PMTs read

out the light. Each signal is digitized and the analog sum is discriminated and used in the trigger.

Particles that went though the beam holes in the lead glass were detected by the **BA**. It is located 3 m downstream of the glass and made out of 48 lead-lucite sandwich layers, which adds to 28 radiation length (1.3 interaction length). Because of the high rate in the beam holes the lucite is segmented vertically or horizontally. The BA signals from the last third of the layers are added to the BA3 signal while all other signals are added to the BA12 signal. Both signals were discriminated and digitized. Electromagnetic showers deposited almost all their energy in the first 2/3 of the BA while hadronic showers will deposit energy in the back as well. The logical combination BA12 and not BA3 was part of the trigger and additional cuts were made on the BA12 and BA3 energies offline.

The coverage for particles even with the 12 photon vetoes is not hermetic. To fill one hole a ring out of iron was added 30 cm upstream of the C bank. The inner radius was 85 cm and the outer radius was 93 cm. The idea was that photons would convert in the iron ring and the conversion products would then be detected in the hodoscope. It turned out however that many hits in the hodoscopes came from accidental activity or from backsplash of lead glass showers. Therefore only a very loose cut was made on the B and C bank activity in the neutral mode analysis.

2.7 The Hadron Veto

The lead glass was 18.7 radiation length long. A wall of lead bricks 2 meters downstream added another 21 radiation length. Electromagnetic showers were therefore contained in the combination. Hadronic showers however were not, since the glass and wall correspond to only 3 interaction length. A scintillator bank downstream of the wall, called **MU1**, detected charged particles produced in hadronic showers. If the analog sum of all signals was bigger than 5 MINI the MU1 trigger bit was set. This was used in veto in the neutral mode trigger.

2.8 The Muon Veto

Downstream of all other components there was a muon filter consisting of 3.2 m of steel and a scintillator bank, called **MU2**, which was used to veto muons from $K_L \to \pi\mu\nu$ decays. Each of the 34 scintillator signals was discriminated and the logical OR of all discriminator outputs was used in the trigger. Hadrons were stopped in the filter of 19 interaction length while muons above 7 GeV/c would penetrate it.

2.9 The Trigger

For the two decay modes of interest, $\pi^+\pi^-$ and $\pi^0\pi^0$, two different trigger requirements were used. In addition, several triggers for calibration events and "accidental" events were used. The trigger changed between data sets 1 and 2.

The trigger for each type consisted of a deadtimeless level 1 trigger, making a decision every bucket (19 nsec) from fast scintillator or calorimeter signals and a slower level 2 trigger (up to 20 μsec). The dead time of the experiment was however not determined by the decision time of the trigger but rather by the event readout and digitization time which was about 700 μsec. The dead time was typically 55 % which resulted in a 700 Hz data taking rate, about 14000 events per 23 sec spill.

The logic modules used were standard CAMAC or NIM modules except for the charged mode level 2 trigger for set 2, which was implemented in custom made FASTBUS boards.

2.9.1 The Charged Mode Trigger

For the two body decay $K \to \pi^+\pi^-$, the two tracks will be symmetric about the center of the beam upstream and downstream of the magnet. This is not the case for the dominant three body decay modes $\pi e\nu$, $\pi\mu\nu$ and $\pi^+\pi^-\pi^0$. The purpose of the trigger was therefore to find two track events and to discriminate against three body decays. Muons were identified and vetoed at the level 1. Electrons could only be identified offline.

The level 1 trigger used the following combination of logical signals for data set 1:

$$L1 = 2B \cdot 2C \cdot BEAST \cdot BWEST \cdot CUP \cdot CDOWN \cdot (T + V) \cdot RF \cdot VETO \qquad (2.1)$$

and for data set 2:

$$L1 = 2B \cdot 2C \cdot BEAST \cdot BWEST \cdot CUP \cdot CDOWN \cdot RF \cdot VETO \qquad (2.2)$$

with

$$\begin{aligned} VETO \;=\; & \overline{UR} \cdot \overline{DR} \cdot \overline{PA} \cdot \overline{VA9} \cdot \overline{VA0} \cdot \overline{VA1} \cdot \overline{VA2} \\ & \cdot \overline{DRA} \cdot \overline{VA3} \cdot \overline{VA4} \cdot \overline{MA} \cdot \overline{LGA} \cdot \overline{MU2} \end{aligned} \qquad (2.3)$$

The signal names like '2B' are explained above. The coincidence of the B and C bank at z= 178 m and T and V at z= 141 m for set 1 ensured that most events passing level 1 were from kaon decays, i.e. there was almost no correlated random activity in the two sets of hodoscopes (see Fig. 40). For set 2 the lever arm from the two hodoscopes was missing which caused the level 2 input rate to increase by a factor of 5. Most of the level 1 triggers in the experiment were charged mode triggers and in order to enhance the fraction of neutral mode events, charged mode was prescaled by a factor of 2 for the second data set.

The level 2 trigger used the drift chamber hits to further improve the fraction of two track events and to discriminate against three body decays. For set 1 the OR of all hits east and west of the center line (in the x view) was formed for all four chambers. The level 2 trigger was the logical AND of these 8 combinations.

For data set 2, the ORs of hits from 16 drift chamber wires were formed (all wires within 10 cm). These ORs were the input to custom made FASTBUS boards. Because of the finer granularity relative to the logic used for data set 1, cuts on the track angles could be made. Further details and the rejection rates for the two level 2 triggers are explained in reference [Briere 95b].

No requirement on the lead glass was made for charged mode triggers. However the hardware cluster finder was started. It injected some charge on the input lines which affected the digitized lead glass energy because of the capacitive coupling of the HCF. Since electrons from charged mode $\pi e \nu$ decays were used to calibrate the lead glass it was advantageous to bias electrons and photons the same way.

2.9.2 The Neutral Mode Trigger

The final state of $K \rightarrow \pi^0\pi^0$ consists of four photons. Since the Çerencov light is prompt the total energy ETOT deposited in the lead glass could be triggered on for every bucket, i.e. at level 1. The threshold was set to about 25 GeV. All other signals used at the level 1 were scintillator signals to veto on tracks or photons missing the active regions of the detector. The level 1 logic for data set 1 was

$$\mathrm{L1} = \mathrm{ETOT} \cdot \overline{\mathrm{V}} \cdot \cdot(\overline{\mathrm{BA12}} + \mathrm{BA3}) \cdot \mathrm{RF} \cdot \mathrm{VETO} \tag{2.4}$$

For set 2 $\overline{\mathrm{V}}$ could no longer be used. The logic was instead

$$\mathrm{L1} = \mathrm{ETOT} \cdot \cdot(\overline{\mathrm{BA12}} + \mathrm{BA3}) \cdot \overline{\mathrm{PA}} \cdot \overline{\mathrm{DRA}} \cdot \mathrm{RF} \cdot \mathrm{VETO} \tag{2.5}$$

Here, VETO is defined as

$$\begin{aligned} \mathrm{VETO} \;=\; & \overline{\mathrm{CA}} \cdot \overline{\mathrm{MU1}} \cdot \overline{\mathrm{UR}} \cdot \overline{\mathrm{DR}} \cdot \overline{\mathrm{VA9}} \cdot \overline{\mathrm{VA0}} \cdot \overline{\mathrm{VA1}} \cdot \overline{\mathrm{VA2}} \\ & \cdot \overline{\mathrm{VA3}} \cdot \overline{\mathrm{VA4}} \cdot \overline{\mathrm{MA}} \cdot \overline{\mathrm{LGA}} \cdot \overline{\mathrm{MU2}} \end{aligned} \tag{2.6}$$

In level 2, a cut on the number of clusters found by the HCF was made. Events with four or more than five clusters were accepted. The level 1 rate for neutral mode was typically 10^5 triggers per spill (before dead time) and the HCF rejection was about a factor of 15.

2.9.3 Calibration Triggers

Additional triggers existed for pedestal events and flasher events. Both have been mentioned above and are only listed here for completeness.

2.9.4 The Accidental Trigger

The high rate environment of our detector and the long drift and integration times of the chamber and the glass made it necessary to estimate the activity in the detector from out-of-time buckets. This accidental activity effected especially the reconstructed glass energies and some cuts used in the neutral mode analysis. To get a random snap shot of the detector

no detector signal could be used for triggering. Instead a scintillator telescope far upstream of the detector (at $z = 40$ m) was used. The telescope pointed back to the target with an angle of 90 mrad relative to the beamline and consisted of 3 scintillator pieces. A muon produced at the target could therefore fire all scintillators but had no change to end up in the detector. The trigger was the coincidence between all scintillator signals and the accelerator RF.

The activity in the telescope was proportional to the proton intensity in the buckets at lower intensities (see Fig. 11). Above $2 \cdot 10^{12}$ protons per spill the trigger rate increases faster. The activity in the detector as measured by the number of interactions in the DR was proportional over a wider range of beam intensities (see Fig. 12). A similar behavior was observed in E799 (see [McFarland 94]) but no explanation is know. Despite of this question, the accidental events were very important to the acceptance calculation and modeled the random activity in the detector quite well. This will be discussed in chapter 7.5.

About 1.5% of the events written to tape were accidental events. The ADCs were not pedestal subtracted and no sparsification was done.

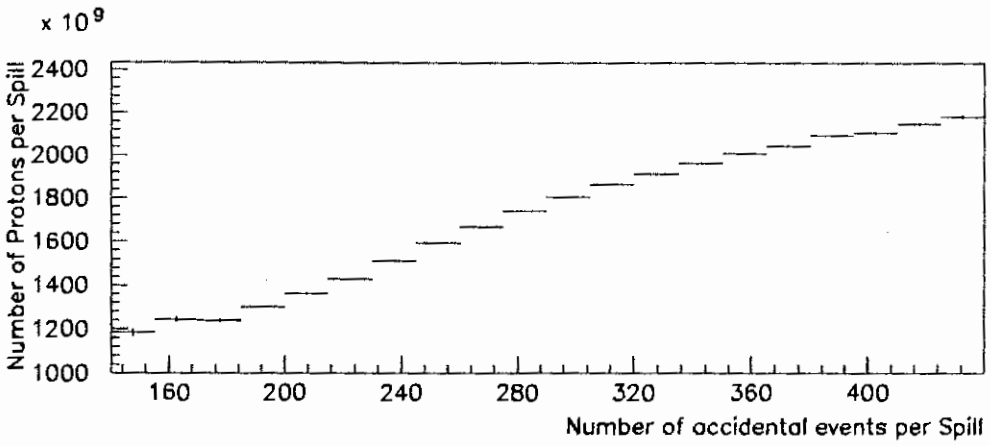

Figure 11. Total number of protons per spill versus number of accidental triggers. The number of triggers is prescaled by a factor of about 400.

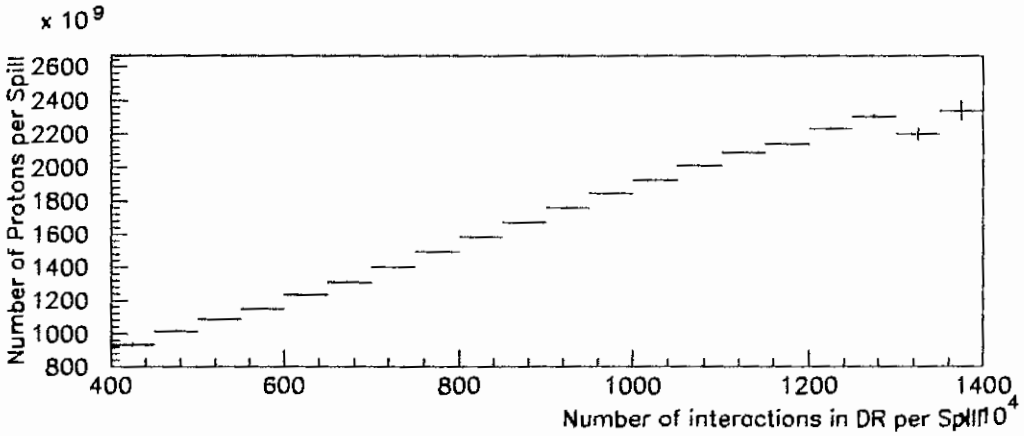

Figure 12. Total number of protons per spill versus number of interactions in the DR.

CHAPTER 3

Spectrometer Calibration and Aperture Determination

The drift chambers and the magnet were used to reconstruct charged tracks. Its calibration is described in detail in [Briere 95b]. Here the basic steps and principles are discussed.

For the magnet the absolute field strength needed to be measured since it defines the absolute momentum scale for charged tracks. This scale then determines the mean of the reconstructed $\pi^+\pi^-$ mass. Since the kaon mass is known very well (at the $6 \cdot 10^{-5}$ level), the argument can be turned around to fix the absolute momentum scale, i.e. the momentum scale was chosen such that the mean reconstructed $\pi^+\pi^-$ mass was equal to the kaon mass. The mean $\pi^+\pi^-$ mass was stable throughout the run except for two small shifts after repairs of the magnet power supply. The relative field strength across the surface of the magnet was measured for E731 and the same field map was used in this analysis.

The drift chamber calibration comprised of the determination of the chamber positions, the relative timing offsets between the arrival times of the drift chamber wire signals, and the drift time - drift distance relation. For the chamber simulation in the Monte Carlo the hit efficiency of the wires and the resolution of the chambers needed to be measured.

First, the timing offsets were determined which were caused by different propagation delays along the 60 m cables connecting the drift chambers to the TDCs and by different delays for the stop signals of the TDCs. Fig. 13 shows the raw TDC distribution for hits on intime tracks. Because of the common stop mode of the TDC, hits from tracks close to

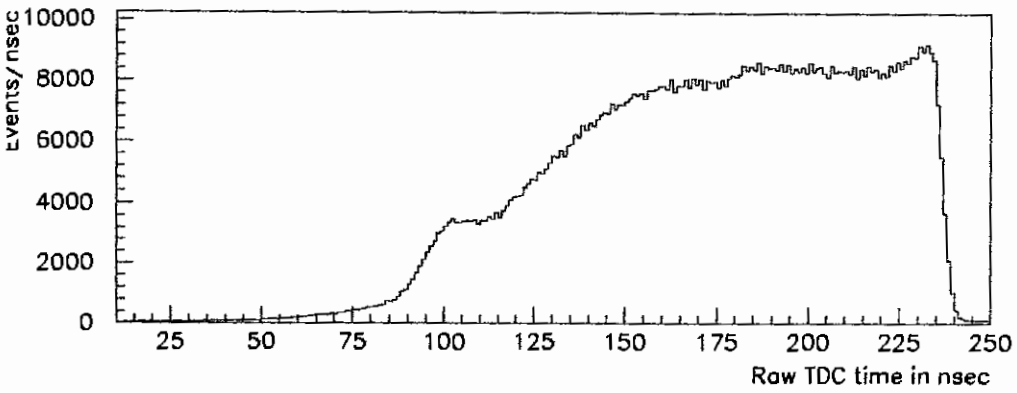

Figure 13. Raw drift time distribution from hits on intime tracks.

a wire have a TDC value of about 240 nsec and cause the sharp edge in the distribution whereas longer drift times correspond to smaller TDC values. The position of this edge is different for every wire because of the mentioned delays. The relative timing among the wires of a plane was therefore measured by comparing the edge position of one wire to the edge of all wires. The χ^2 of the overlay of the two distributions in the region of the edge was calculated and by shifting the TDC distribution of the single wire in 1 nsec steps, the minimum in χ^2 was found. The minimum corresponded to the relative timing offset. This procedure was used iteratively and converged quickly. The wire timing offsets did not change during the run except for those of a few wires.

Next, the drift time - drift distance relation for each wire plane was determined. This relation was updated frequently to track changes in the drift chamber gas composition or environmental conditions. Two track events intime with the RF were selected. The TDC values for every plane were recorded. In case there was a missing hit in one plane, the TDC value of the missing hit was taken from a different event for which hits in both planes existed and the TDC value for the hit in the second plane was the same.

The track illumination of these events if folded onto one drift cell is very flat. Because of this and the wire 'efficiencies' of 100% (through the method of filling in TDC values for missing hits), the integral distribution of the TDC times maps to the drift time to drift

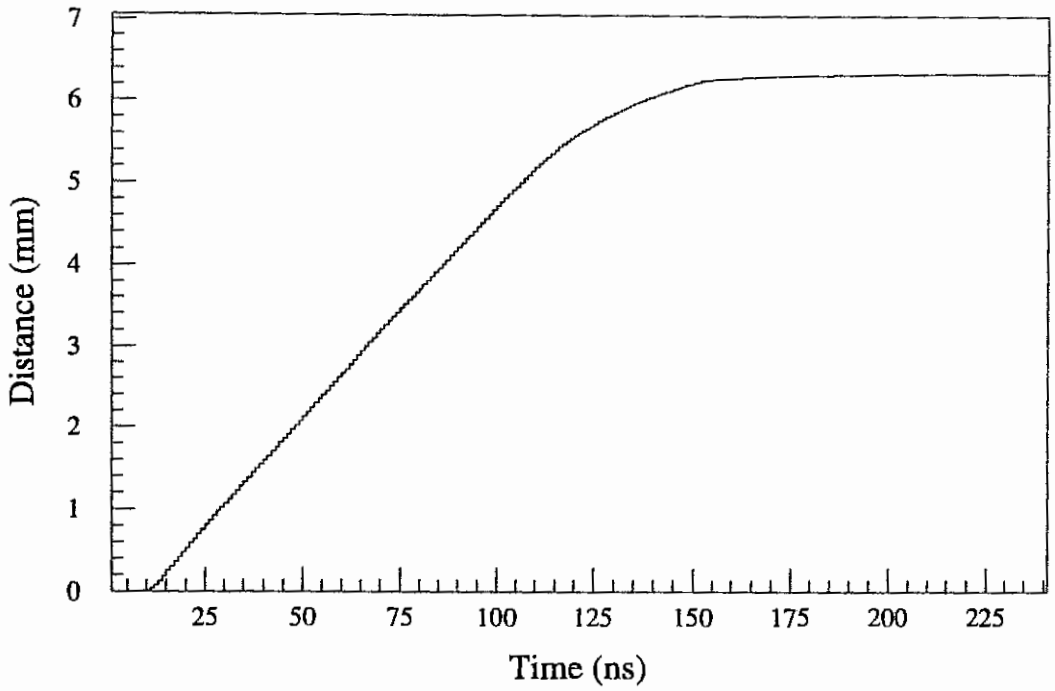

Figure 14. Example of a drift time - drift distance relation. Note the nonlinear behavior for large drift times.

distance relation $d(t)$:

$$d(t) = d_{cell} \frac{\sum_{t_0}^{t} N(t)}{\sum_{t_0}^{t_1} N(t)} \tag{3.1}$$

Here $d_{cell} = 6.35$ mm (the cell size), $N(t)$ is the TDC distribution, $t_0 = 249$ nsec and $t_1 = 10$ nsec. The reverse order in the summation is due to the common stop mode of the TDCs. Fig. 14 shows an example of $d(t)$.

Once the TDC offsets for all wires and the drift time - drift distance relations were determined the track positions in the chambers could be determined. To reconstruct the entire track the positions and rotations of the chambers needed to be determined. First the relative offsets, and rotations within the four drift chambers were measured.

In special runs taken about once a day the magnet was turned off and muons produced in the beam dump or target were recorded in the detector. Since the tracks did not bend and the z positions of the chambers were known from a survey, the track's (x, y) position at the second and third chamber were calculated with the information from the two outer chambers. The expected position can then be compared with the measured position and

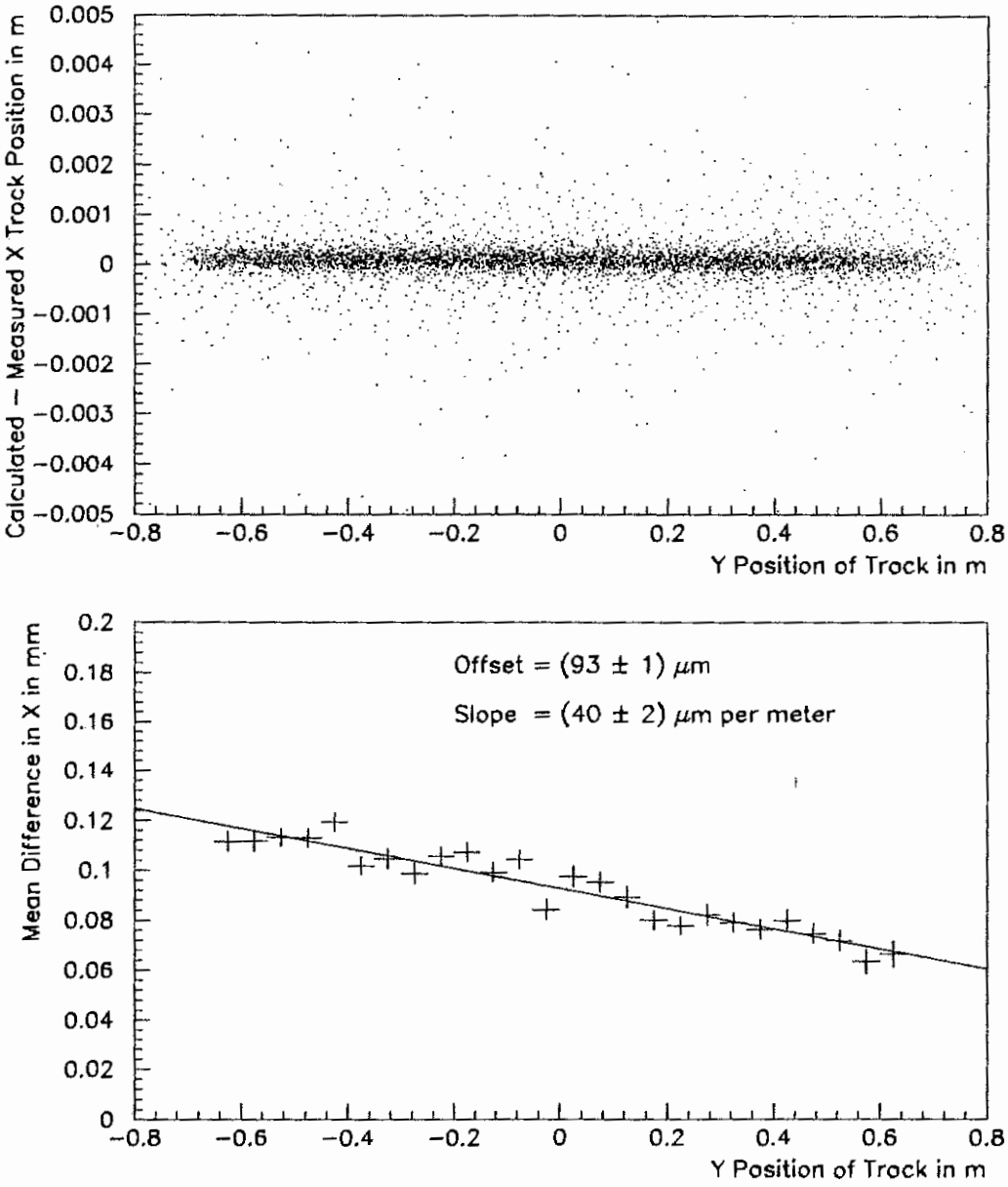

Figure 15. Scatter plot of the difference between the reconstructed and calculated x positions of tracks at chamber 2 as a function of the y track position. The lower plot shows for each slice in y the fitted mean and a fit of this distribution to a line.

the offsets and rotations of chambers 2 and 3 can be calculated relative to chambers 1 and 4. As an example, Fig. 15 shows a scatter plot of the difference between the expected and measured x position versus the y track position at the second chamber. In the calibration the scatter plot is sliced in small y intervals and the mean for each slice is fitted. The means for all slices are plotted in the lower part of the figure and this distribution is fitted to a line. The intercept is the x offset of this chamber and the slope is the rotation angle of the x plane wires.

This method determines the positions of the middle chambers relative to the outer chambers. If the last chamber is rotated relative to the first chamber by an angle θ, a cork-screw rotation of the chambers remains after the calibration: chambers two and three are rotated by angles $\theta_i = \theta(z_i - z_1)/(z_4 - z_1)$ relative to the first one. Here z_i is the z position of the ith chamber. To measure this rotation $K \rightarrow \pi^+\pi^-$ events were used since the two tracks in these events are planar. Let $\vec{a}_1$ ($\vec{a}_2$) be the vector connecting the hits of track 1 (2) from the first to the second chamber and let $\vec{r}_1$ ($\vec{r}_2$) be the vector between the two track positions at the first (second) chamber. Without a cork-crew rotation all four vector are in a plane and $\vec{r}_1$ and $\vec{r}_2$ are parallel, i.e. $\vec{r}_1 \times \vec{r}_2 = 0$. In case the cork-screw angle θ does not vanish we find:

$$\vec{a}_1 \cdot (\vec{r}_1 \times \vec{r}_2) = d|\vec{r}_1||\vec{r}_2| \sin\theta \tag{3.2}$$

with d being the separation between chambers 1 and 2. Thus the angle θ was measured by fitting a line to the $|\vec{r}_1 \times \vec{r}_2|$ versus $|\vec{r}_1||\vec{r}_2|$ distribution.

The cork-screw rotation was the last step of the internal alignment of the chambers. By comparing the cluster position and the extrapolated track position for electrons at the lead glass the offset and rotation of the chamber system relative to the glass was measured. Whereas the chambers were easily accessible and moved during the experiment the lead glass house did not move and the chamber positions were measured relative to it. Finally, the target position was found by tracing the kaons back to $z = 0$. The chamber locations were then adjusted such that the target was at the origin of our coordinate system.

At this point the chamber positions with respect to the detector coordinate system are measured. Tracks and kaons can be reconstructed. For the simulation of the drift chambers in the Monte Carlo the wire efficiencies and the position resolutions for all wire planes were

determined. From two track events we determined for every wire how often a track went by and the wire did not fire. The position resolution was taken from the width of the SOD distribution (sum of drift distances for a hit pair). Wire efficiencies were typically 99% and the plane resolutions were about 90 μm.

Another important input to the Monte Carlo were the transverse positions of limiting aperture in the experiment. The most important ones were the CA (in front of the lead glass) and the DRA (see section 2.6). Electrons from $K \rightarrow \pi e\nu$ decays were extrapolated to the z position of the apertures. Since the CA and DRA were active a tight cut on the energy deposited in these devices ensured that the electron did not hit them. Monte Carlo $K \rightarrow \pi e\nu$ were generated to simulate the position resolution of the electrons. In case the electron hit the CA or DRA in the simulation the event was discarded. By comparing the (x, y) position distributions between data and the Monte Carlo the size and offsets of the apertures were determined. This is shown in Fig. 16 for the CA aperture. The figure shows the data and Monte Carlo electron illuminations for two of the eight CA edges after the correct CA positions were used in the simulation. To determine the CA position the Monte Carlo distribution was shifted relative to the data and the overlay χ^2 was calculated as a function of the shift. The shift which minimized the χ^2 determined the CA position. Thus the location of the edge was determined to better than 100 μm (= half a bin width in Fig. 16). In chapter 10.2.3 we will consider the systematic effect on $\Delta\Phi$ caused by a shift in the edge by 1.5 mm.

The calibration and aperture measurements were pivotal to our understanding of the data and the detector simulation. Especially the good position resolution of the chambers and the precision of the calibration were a reliable basis for the analysis of $K \rightarrow \pi^+\pi^-$ and $K_L \rightarrow \pi e\nu$ decays and for the lead glass calibration. The latter will be discussed in the next chapter.

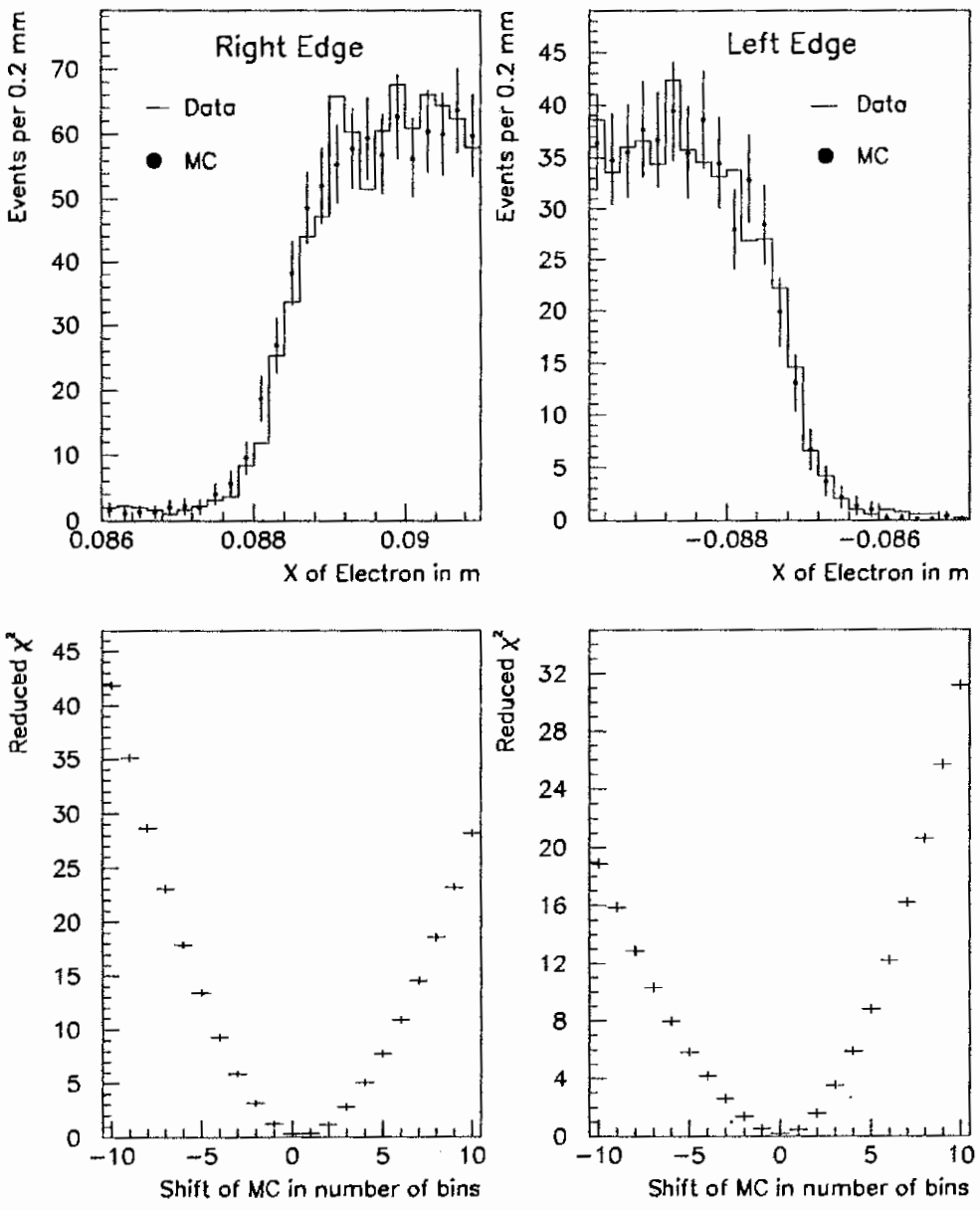

Figure 16. The CA edge illuminations for the left and right edge of the upper CA module. Shown are the data and Monte Carlo distributions. The bin width is 0.2 mm. The lower two plots show the reduced χ^2 of the overlays as a function of the the relative shift between the Monte Carlo and data distribution. The χ^2 is minimal for a shift of zero.

CHAPTER 4

Lead Glass Calibration

This chapter discusses the calibration of the lead glass array. Electrons from $K_L \to \pi e \nu$ decays collected simultaneously with the $K \to \pi^0\pi^0$ events were suitable for the calibration because of the large statistics and the momentum range. By comparing the cluster energy E to the momentum of the electron track p, which was well measured in the charged spectrometer, all calibration constants were determined. The analysis cuts required to select a clean electron sample are discussed in [Gibbons 93c]. This chapter discusses how the lead glass was calibrated once the electrons were selected.

The calibration constants needed to convert lead glass ADC counts to an energy are the gains of the photo multiplier tubes (PMT) and ADCs, the effective light absorption coefficients α and the "high range-low range" gain changes S of our dual range ADC. All three "constants" needed to be determined for every block and changes with time needed to be tracked.

The gain changes S were determined only once during the run since they depended on passive electronic elements of the ADC only and did not change. For different values of S, the gain and α were calibrated as described below and the χ^2 of a fit of the mean E/p versus p distribution to a constant was calculated. S was changed in 0.1% steps and the value that minimized the χ^2 determined S. The gain changes for all blocks were determined individually.

Because of the radiation damage, especially for blocks in the middle of the array, the absorption constant changed with time. Fig. 17 shows how the average light output changes

in flasher events after the blocks are irradiated by 20 and 46 hours of beam. For blocks in the center the light output dropped by about 1% per day. We therefore decided to do a full calibration for the blocks around the beam holes for every day of running.[1] With increasing distance from the holes and therefore decreasing radiation damage and electron sample size, the calibration was performed less often.

The position of the shower maximum t_{max} grows logarithmically with the shower energy. The fraction of light absorbed reduces therefore with energy causing a nonlinear response of the lead glass.[2] Understanding this nonlinearity was crucial for this analysis; it was reduced by adding the Wratten 2A filter in the silicon gel (see section 2.4). Obviously, one needs to know the nonlinear response function before the array can be calibrated. To study this the EGS4 Monte Carlo [Nelson 85] was used to generate electron clusters in the lead glass. The energies generated ranged from 0.25 GeV to 90.5 GeV, spaced logarithmically in energy. The number of clusters generated varied between 3200 for smaller energies and 210 for the largest.

Fig. 18 shows the EGS simulation of the light production $f(l, E)$ as a function of depth l into the block for 0.5 GeV, 4 GeV and 32 GeV showers. Plotted is the light output averaged over all clusters and for two single EGS events. One can see the shift of the position of the shower maximum with increasing cluster energy.

The total amount of light I as seen by the photo tube is reduced because of absorption. If the absorption per radiation length α' is uniform across the block, I is given by

$$I = g_0 E \int_0^L f(l, E) e^{-\alpha'(L-l)/\cos\Theta_C} \, \mathrm{dl} \tag{4.1}$$

Here, $L = 18.7$ X_0 is the total length of the block, Θ_C is the Çerenkov angle and g_0 is the amount of light reaching the cathode for a 1 GeV shower in case $\alpha' = 0$. $\alpha = \alpha'/\cos\Theta_C$ is called the effective absorption coefficient. For our experiment we found that α is typically 4% (see Fig. 21). f is normalized to one: $\int_0^\infty f(l, E)\mathrm{dl} = 1$.

The nonlinearity correction of the glass response $C(E, \alpha)$ was defined as:

[1] For previous experiments α was determined for larger time intervals and the change in light output between calibrations was corrected for with flasher events.

[2] This was compensated in part by the leakage out of the back of the array.

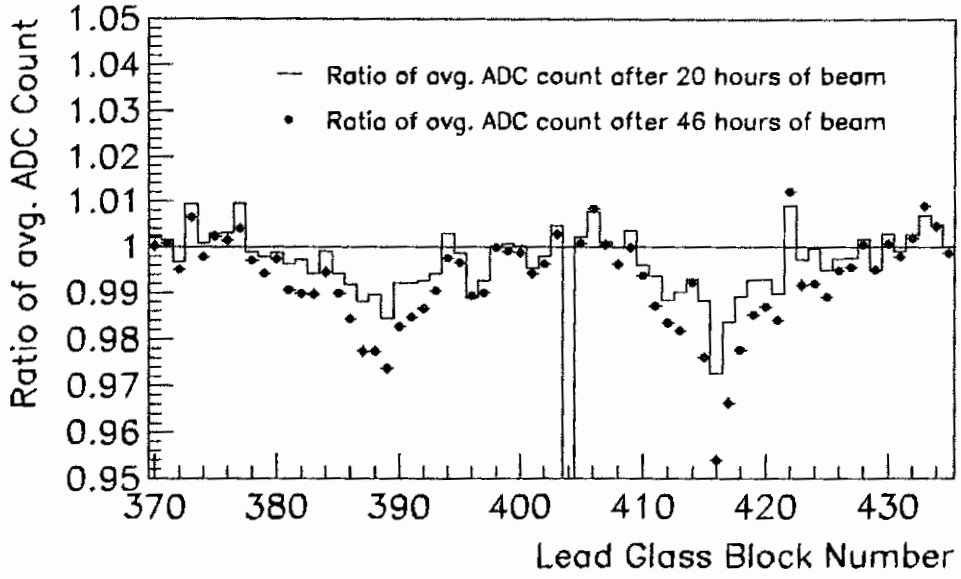

Figure 17. Ratio of the average light output (average ADC count per event) in flasher events after 20 and 46 hours of beam time relative to the light output before the irradiation. This fractional change in the average ADC count is plotted for the two central columns of lead glass blocks. The average number of protons per spill was about $1.8 \cdot 10^{12}$ during the 46 hour period. The blocks 387 to 390 and 415 to 418 are next to the beam holes. Blocks with numbers close to 374, 402 or 430 are at the outside of the array. There is no damage at the outside of the array and about a 1% drop in light output per day for blocks around the beam holes.

$$C(E,\alpha) = \left\langle \int_0^L f(E,l) e^{-\alpha(L-l)} \mathrm{dl} \right\rangle / c_1(\alpha) \tag{4.2}$$

The function $c_1(\alpha) = \exp(-\alpha(L - l_0))$ is close to the response of the glass to a 1 GeV shower and the average is taken over all EGS clusters generated for a given energy E. The empirical value for $l_0 = 5.157$. Thus $C(E,\alpha)$ is defined relative to the absorption of a 1 GeV cluster and the factor $c_1(\alpha)$ is absorbed in our definition of the gain. Because of the definition of $C(E,\alpha)$, the true energy E and the energy before the correction E_m are related by

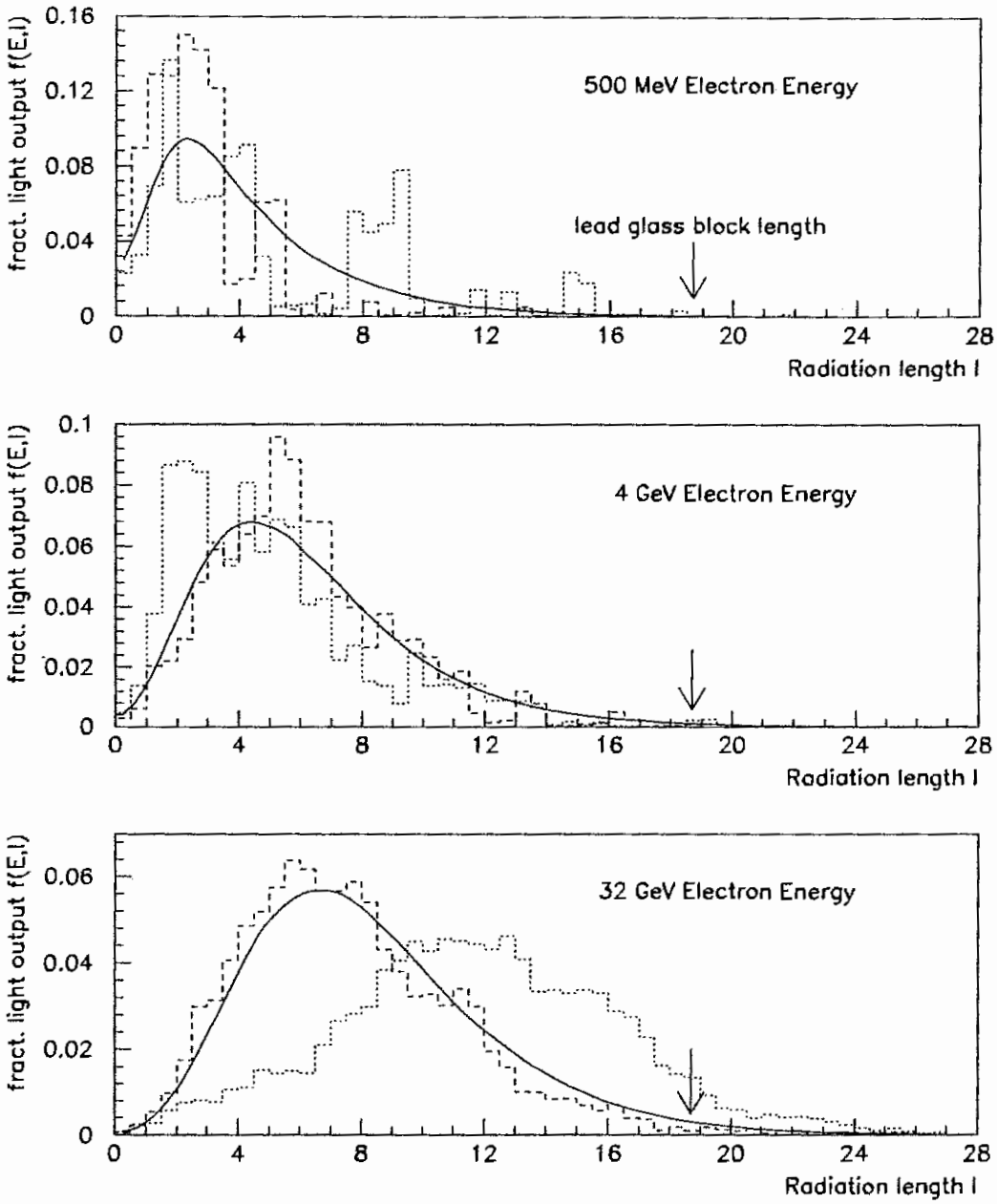

Figure 18. Longitudinal shower profiles for 500 MeV, 4 GeV and 32 GeV. The solid curve is the average over all EGS clusters. The dashed and the dotted distribution correspond to individual showers.

$$E = \frac{E_m}{C(E,\alpha)} \tag{4.3}$$

For our energy and α range this can be approximated by

$$E \approx E_m^{\beta} = E_m^{1.0053-0.9106\alpha} \tag{4.4}$$

In the calibration a least square fit of $\ln p$ versus $\ln E$ to a straight line was performed: $\ln p = a_0 + a_1 \cdot \ln E$. E was calculated using the current best value for the gain g_{old}, the absorption constant α_{old} and equation 4.3. Each electron used in the fit was weighted with the expected smearing from the momentum and cluster energy measurement. If g_{old} and α_{old} were determined correctly the fit would give a slope $a_1 = 1$ and an intercept $a_0 = 0$. If the fitted slope is different from one a better absorption coefficient α_{new} is calculated by using equation 4.4:

$$\alpha_{new} = \frac{1.0053}{0.9106} - a_1\left(\frac{1.0053}{0.9106} - \alpha_{old}\right) \tag{4.5}$$

If the intercept is different from zero a better gain g_{new} is given by

$$g_{new} = e^{-a_0}\, g_{old} \tag{4.6}$$

This is the basic concept used in the calibration. In practice some complications arose from the fact that an electromagnetic shower is not contained within one block. The fitted gain and absorption of a block therefore depended on those of the neighboring blocks. A cluster is defined as a 3×3 array of blocks with the central block energy being the maximum of the nine energies. The cluster energy is then

$$E = \left(\sum_{3\times3} \frac{n_i}{g_i}\right)/C(E,\alpha_c) \tag{4.7}$$

with $n_i(g_i)$ being the ADC count (gain) of block number i. α_c is the absorption of the central block. To calibrate a given block, all electron clusters for which this block was the central cluster were used. Rather than fitting for all 804 gains and all 804 absorptions at once, the calibration constants for only one block were determined in a step while those of the other blocks were held constant. This required an iterative procedure which converged after a few passes.

Unfortunately, equation 4.7 is not the whole story of how to convert ADC counts into cluster energies. There are several corrections applied to the cluster energies which are not specific to the calibration procedure and are therefore discussed in chapter 5.1.

Fig. 19 shows the E/p versus p distribution for the electrons used in the calibration. Overall, E/p is flat to a few tenths of a percent. There is however an increase of the mean E/p for higher momenta. Later we found that this increase is due to a mismeasurement of the high range gain changes S. The procedure described above did not always find the correct gain change. This can be seen in Fig. 20. The plotted E/p versus ADC count distribution shows no step at the transition between the low and high range for channel 262 but there is a step of about 0.4% for channel 264. The "high range - low range" gain change was therefore found correctly for channel 262 but it was off by 0.4% for channel 264.

There were two options of how to solve this problem: redo the entire calibration or scale the cluster energies such that the E/p distribution is flat after the scaling. Because of time constraints and the evaluation of the systematic error we chose the second option. Fig. 50 shows the E/p versus p distribution after the rescaling was done. In chapter 10.2.1 the systematic error on $\Delta\Phi$ from the lead glass simulation is discussed. To study the understanding of the nonlinear response cluster energies were rescaled by $(1 + 0.0004 \cdot E_{cluster})$. This nonlinearity is larger than the one seen in Fig. 19 which gives us confidence that any systematic effect of the mismeasurement of the gain change S is within our errors.

Fig. 21 shows the fitted values of the absorption coefficient and gains from an early and a late calibration for all 804 blocks. The increased radiation damage causes the the average absorption coefficient and gain to increase for the later calibration.

To summarize, even though some problems with the lead glass calibration remained in the final analysis, the systematic error estimate showed that the effect on $\Delta\Phi$ is within the assigned uncertainty of the glass simulation. In chapter 7.3 the agreement between the Monte Carlo and the data is discussed.

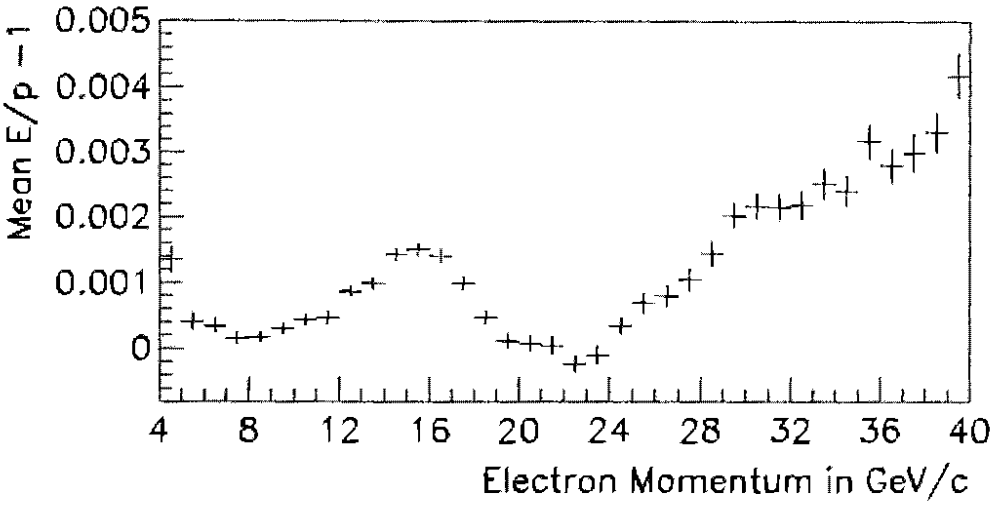

Figure 19. Mean E/p versus p for electrons used in the lead glass calibration before the rescaling described in the text.

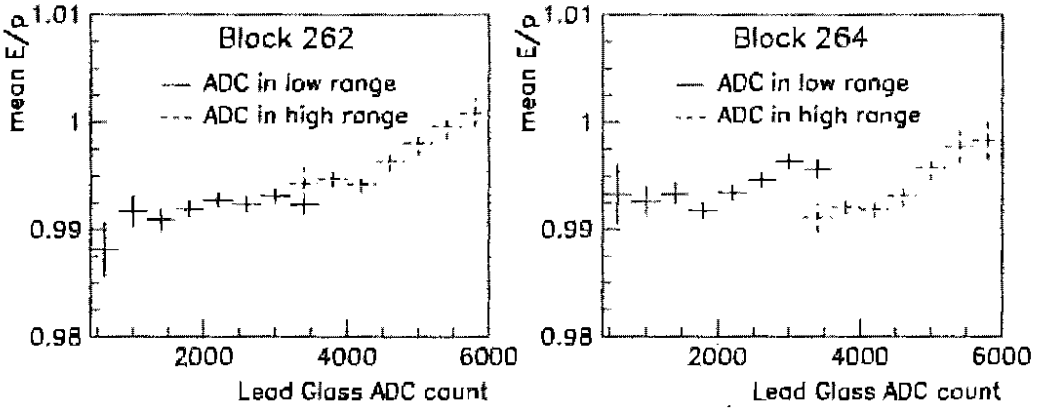

Figure 20. E/p versus ADC count for the high and low range. The high range ADC count was multiplied by the "high range - low range" gain difference.

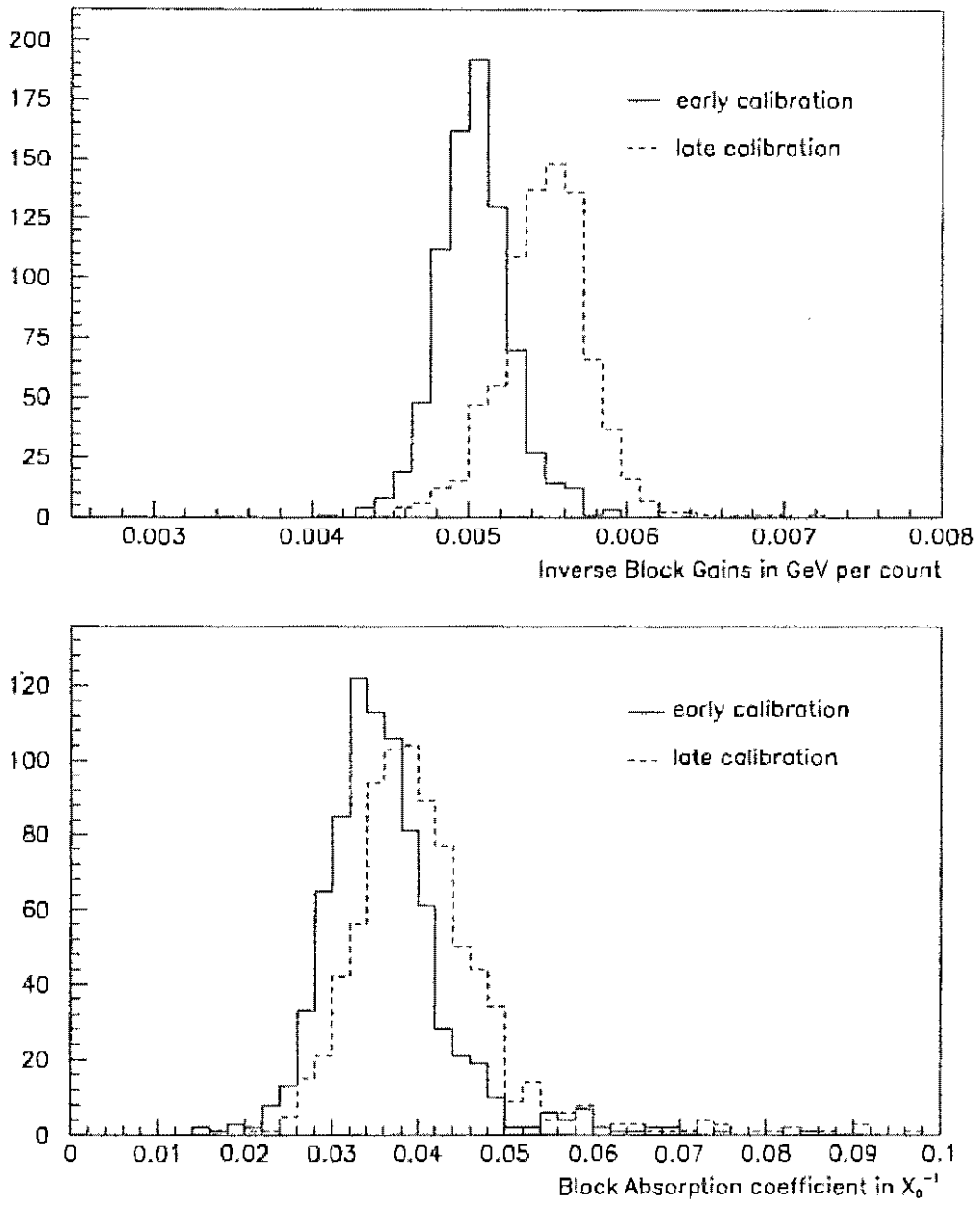

Figure 21. Distribution of fitted gains and absorption coefficients for a calibration early and late in the run. The shift in the mean gain by +9% for the later calibration is consistent with the increase in the average absorption by $0.48\% X_0^{-1}$ which causes light attenuation by about 8%.

CHAPTER 5

The Neutral Mode Analysis

The analysis of $K \to \pi^0\pi^0$ decays uses the lead glass to reconstruct the four photon energies and position. The glass calibration is explained in chapter 4. Here, all analysis steps needed to convert ADC counts into cluster energies and to reconstruct the kaon decay are described. Most of these methods have been used in the E731 analysis and are well documented in [Patterson 90, Gibbons 93c]. This chapter therefore summarizes the different steps and is more detailed in the parts specific to our experiment.

5.1 Cluster Energy and Position Reconstruction

The neutral mode trigger required four or more than five hardware clusters[1] and the total energy in the calorimeter had to be at least 25 GeV. The lead glass information available to reconstruct the event are the ADC counts of all blocks above the readout threshold and a map of all blocks with energy above the HCF threshold. The first step in the analysis is to find all clusters. Then, the cluster energies and positions are calculated. In this section each of these steps is discussed.

A cluster is an array of 3×3 lead glass blocks centered around a local maximum of energy. In the neutral mode analysis all blocks above the HCF threshold were used to find local maxima. Since the HCF ADC gate was only 30 nsec long this helped to identify intime photons. For the $K \to \pi^0\pi^0$ analysis events with four clusters were retained.

[1] A hardware cluster is an "island" of blocks above the HCF threshold of 1 GeV.

The energy reconstruction evolves in several steps. In the first step, the lead glass gains were used to calculate the raw cluster energy as defined by

$$E_{raw} = \sum_{i=1}^{9} \frac{\text{ADC count of block i}}{\text{gain of block i}} \tag{5.1}$$

was calculated. The sum is taken over the nine blocks of the 3×3 array.

Since the 3×3 arrays of two clusters can overlap the energy deposited in the shared block has to be split between the two clusters. For each of the clusters the expected fraction of cluster energy deposited in the shared block is calculated as a function of $\vec{r}_{cluster} - \vec{r}_{shared\ block}$. $\vec{r}_{cluster}$ is the cluster position and $\vec{r}_{shared\ block}$ is the position of the shared block. The two expected energies are scaled, such that the sum is equal to the observed block energy. After the splitting of the block energy both cluster energies and positions are recalculated and the sharing algorithm is applied again. The process stopped after three iterations.

The raw cluster energy was then corrected for different effects. The most important effect stems from light absorption in the lead glass blocks:

- The depth of the shower maximum grows logarithmically with the energy. The fraction of light absorbed decreases therefore with energy (see chapter 4). Since the gains are determined such that the mean E/p is equal to one[2] the size of the nonlinearity depends on the spread of the cluster energy and the absoption coefficient. The correction is typically $\pm 2.5\%$.

  The biggest range of cluster energies in a single block is from 2 GeV to 60 GeV. For a 60 GeV cluster the shower maximum is shifted by about 3.4 radiation length deeper into the block relative to a 2 GeV cluster. In E773, the light absorption for almost all blocks was smaller than 6% per radiation length (see Fig. 21). The ratio of light outputs between a 60 GeV and a 2 GeV cluster is therefore in the most extreme case approximately $e^{3.4 \cdot 0.06} = 1.23$.

- Photon showers have a different shower profile than electron showers. The photon converts inside the glass into an electron-positron pair, i.e. the effective block length

[2]The gains depend therefore on the spectrum of the electrons which is similar to the photon spectrum.

is reduced by the conversion depth t. The shower profile is then the sum of the electron and the positron profile. The nonlinearity correction for a photon shower is therefore different from that of an electron. Defining $C(E,\alpha,t)$ similar to $C(E,\alpha)$ (equation 4.2) as the electron nonlinearity correction for a block of length $L-t$

$$C(E,\alpha,t) = \left\langle \int_0^{L-t} f(E,l)e^{-\alpha(L-t-l)}\mathrm{dl} \right\rangle / c_1(\alpha) \tag{5.2}$$

we find for the average photon–electron correction $R(E,\alpha)$

$$R(E,\alpha) = \int_0^L \mathrm{dt} \int_0^1 \mathrm{dx}\, P(t,x)[xC(E,\alpha,t) + (1-x)C(\,(1-x)E,\alpha,t)] \tag{5.3}$$

with P(t,x) being the probability distribution for a photon to convert at depth t into an electron with energy fraction x and a positron with energy fraction $(1-x)$. P(t,x) is given by the Bethe-Heitler spectrum:

$$P(t,x) = (1+\frac{1}{42\zeta})^{-1}\, e^{-7/9t}(x^2+(1-x)^2+(\frac{2}{3}-\frac{1}{9\zeta})x(1-x)) \tag{5.4}$$

where ζ is the zeta-function. R varies between 0.95 and 1, which is a large correction considering that the average lead glass response needed to be understood at the 0.1% level.

The light output of a shower was measured with photo tubes and the tube signal was digitized. The following list mentions the effects that distort the measurement:

- For part of the run (in August 1991) temperatures were very high and the air conditioning was not working properly. As a consequence the temperature in the lead glass house varied by about 2 °C between day and night as shown in Fig. 22. The gain of the photo tubes changed by about 0.7% per degree Celsius. Since the temperature in the glass house was measured every minute this slope could have been used to correct for the gain change. However a better compensation was achieved by applying a time dependent correction factor. The correction was calculated by averaging E/p for electrons over 20 minutes.

- The readout threshold was > 5 counts. For lower cluster energies some of the blocks were below threshold and not read out. During E731 a special run, where no readout

threshold was applied, was taken and the amount of energy loss as a function of cluster energy and threshold was studied and tabulated. This table was then used in the analysis to account for blocks not read out.

- The ADC counts needed to be pedestal subtracted. The pedestals were extracted from pedestal events (see chapter 2.9.4), which were taken off-spill, i.e. during the time of the one minute beam cycle when no protons were delivered. On-spill the pedestal values shifted depending on the data taking rate. This is explained in chapter 2.4. The effect was similar for all channels of an ADC and depended on the digitization rate. Fig. 23 shows the average ADC count per block for accidental events[3] before and after a pedestal shift correction was applied. Visible is the common shift for all blocks digitized by one ADC as indicated in the figure for 3 of the 10 modules. The energy deposited in the outer channels of the lead glass array was negligible for these events. Eight of these channels per ADC module were therefore used to determine the pedestal shift as a function of the instantaneous rate of data taking. Two quantities were available as measures of this rate for each event: the time since the last level 2 trigger and the number of interactions in the downstream regenerator during a 100 μsec window before the event trigger. Fig. 24 shows the size of the correction per block for some of the ten modules as a function of these variables.

Two corrections were applied for missing energy:

- The electromagnetic shower was in general not contained in the 3×3 array of the cluster. The radial leakage was studied using a simulation and a correction of about 2.6% was applied, depending slightly on the cluster energy.

- In clusters where the central block is next to a beam hole or the outer edge of the array, not all blocks of the 3×3 array exist. For every missing corner block the energy was increased by 0.6% and for other missing blocks the increase was 1.1%.

One final correction was applied for photons that convert downstream of the last chamber. If the conversion occurs upstream or in the scintillator banks B and C the conversions

[3]Since accidental events were readout without a threshold and were taken simultaneously with the neutral mode data, the pedestal shift could be studied using these events.

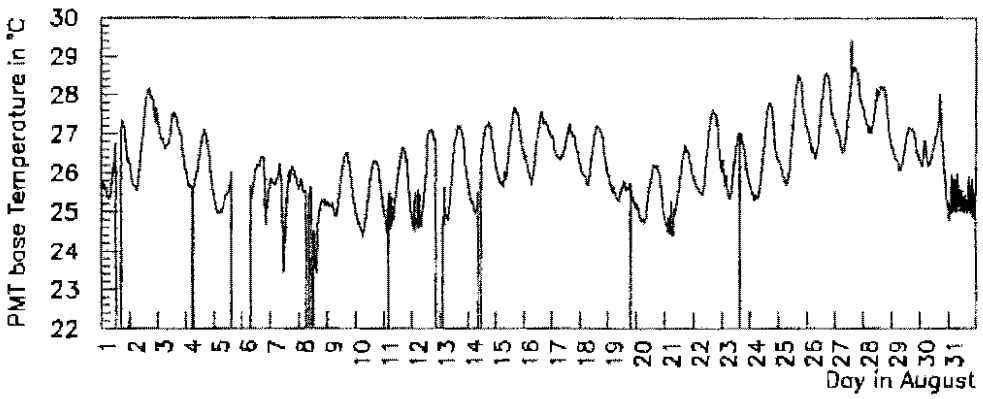

Figure 22. Temperature in the lead glass house for the month of August. The Temperature is averaged over 10 minutes. On the last day, the air conditioning was fixed.

can be detected by hits in the B bank.[4] In this case the cluster at the lead glass is not a photon cluster but the sum of two electron clusters which results in a different nonlinear response.

A hit in the B bank was however not always caused by a conversion. Low energy photons produced in an electromagnetic shower, especially those with an energy of about 2 MeV, where the absorption length is maximal, can traverse the lead glass backwards and hit the B bank scintillator. These backsplash photons arrive time delayed at the B bank relative to the photons from the kaon decay by at least twice the distance from the B bank to the lead glass, i.e. by at least 10 nsec. This is shown in Fig. 25. Events with a TDC time of about 44 nsec come from photon conversions (part c), while backsplash photons often do not match with clusters and arrive later (part b).

A correction of the photon cluster energy was therefore applied if at least one B bank counter had fired, the timing of the 1B trigger signal was consistent with being intime and if the position of the cluster and the B bank counter lined up. The cut on the 1B trigger TDC is necessary because the number of backsplash photons (and therefore the probability of firing a B bank latch) depended on the energy of the incident photon. The size of the

[4]The B bank is closer to the glass.

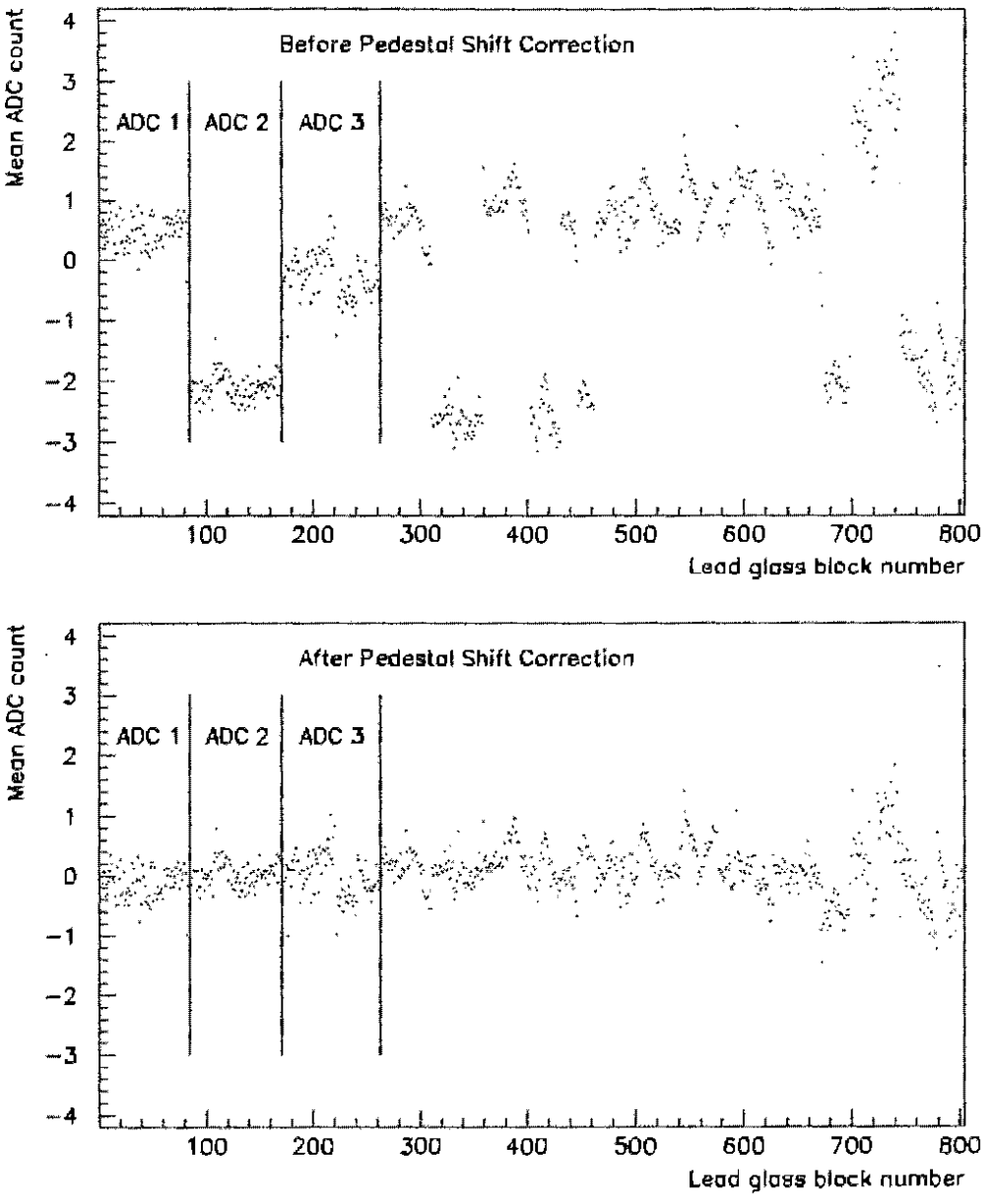

Figure 23. Average Lead Glass ADC count in accidental events as a function of block number before and after the pedestal correction was applied. The channels digitized by three of the ten ADCs are marked.

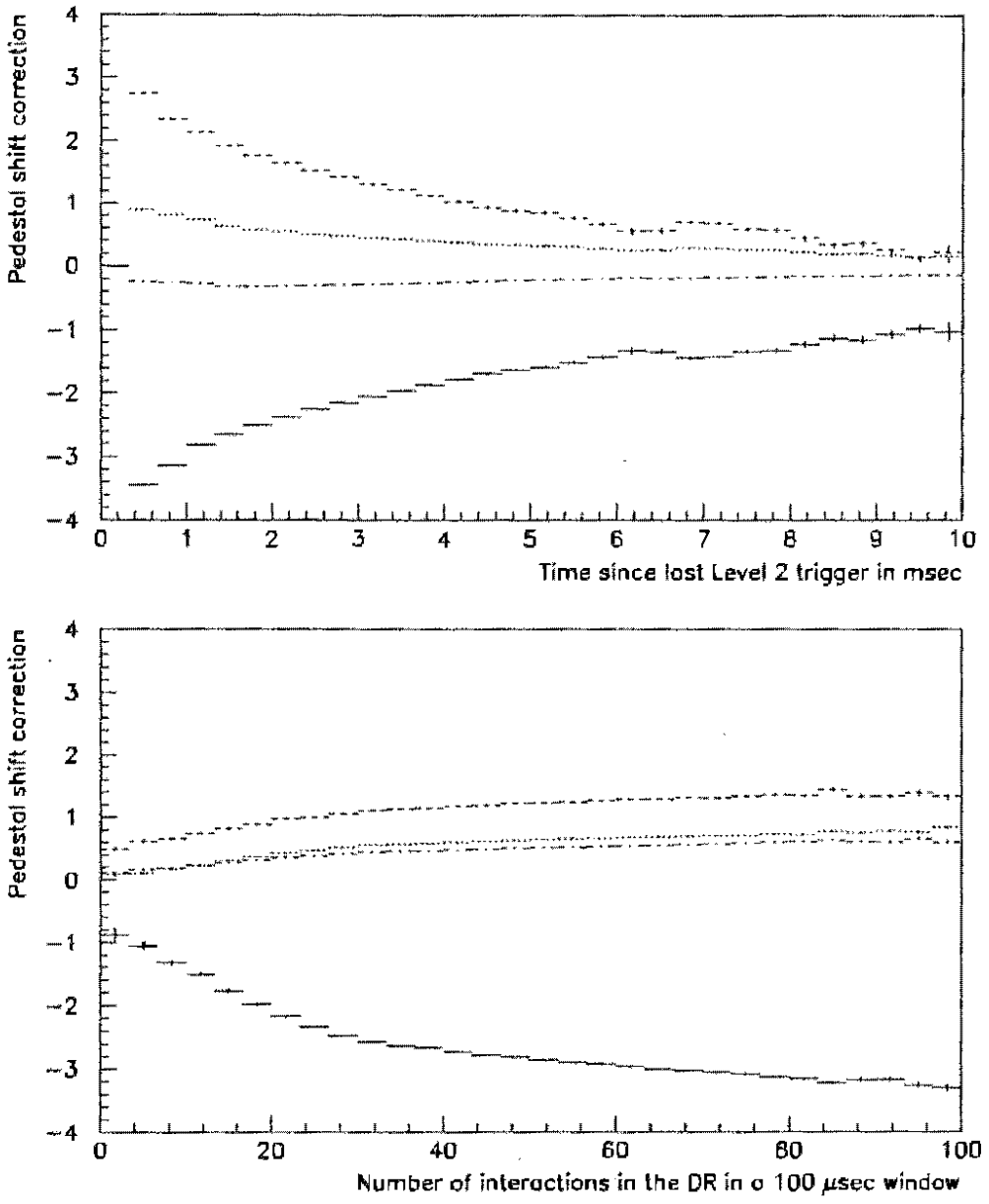

Figure 24. Size of the applied pedestal correction per block for some of the 10 ADC modules as a function of the two variables used to parameterize the digitization rate: the time since the last level 2 trigger and the instantaneous interaction rate in the DR.

conversion correction was studied with the Monte Carlo and depended on the absorption α. The correction factor was approximated by $(1.01 + 0.62 \cdot \alpha)$. About 38% of the $\pi^0\pi^0$ decays have at least one B bank latch on and about 1/3 of these latches fired because of backsplash photons.

To reconstruct the cluster position, the ratio of left column energy over middle column energy of the 3×3 array and the ratio of right column energy over middle column energy is calculated. The maximum of the two ratios, q, was used to reconstruct the x position. The distribution $N(q)$ of this ratio for clusters distributed uniformly across the surface of a block was measured with electrons. From the observed value of q in a given event the x position could then be extracted:

$$x = \frac{h}{2} \frac{\int_0^q N(q')\,\mathrm{d}q'}{\int_0^1 N(q')\,\mathrm{d}q'} \tag{5.5}$$

$h = 5.82$ cm is the size of a block. The reconstruction of the y cluster position uses the same method except q is then the ratio of the top or bottom row energy to the middle row energy.

This method determines the cluster position relative to the position of the edges of the central block. The positions of all block edges are known from measurements of the individual block dimensions and the order the blocks are stacked in the array. Thus the cluster position in the detector coordinate system was reconstructed. The position resolution was about 3 mm.

5.2 Event Reconstruction and Selection

The positions and energies of the four clusters from $K \to \pi^0\pi^0 \to \gamma\gamma\gamma\gamma$ were used to reconstruct the kaon energy and decay vertex. First, two of the photons were paired and, assuming a π^0 decay, the decay vertex was calculated using the small angle approximation:

$$m_{\pi^0}^2 = \frac{E_{\gamma 1} E_{\gamma 2} r_{12}^2}{z^2}; \tag{5.6}$$

$$E_{\gamma n} = \text{energy of } n\text{th photon}; \tag{5.7}$$

$$r_{nm} = \text{distance between } n\text{th and } m\text{th photon}; \tag{5.8}$$

$$z = \text{distance between decay point and calorimeter}. \tag{5.9}$$

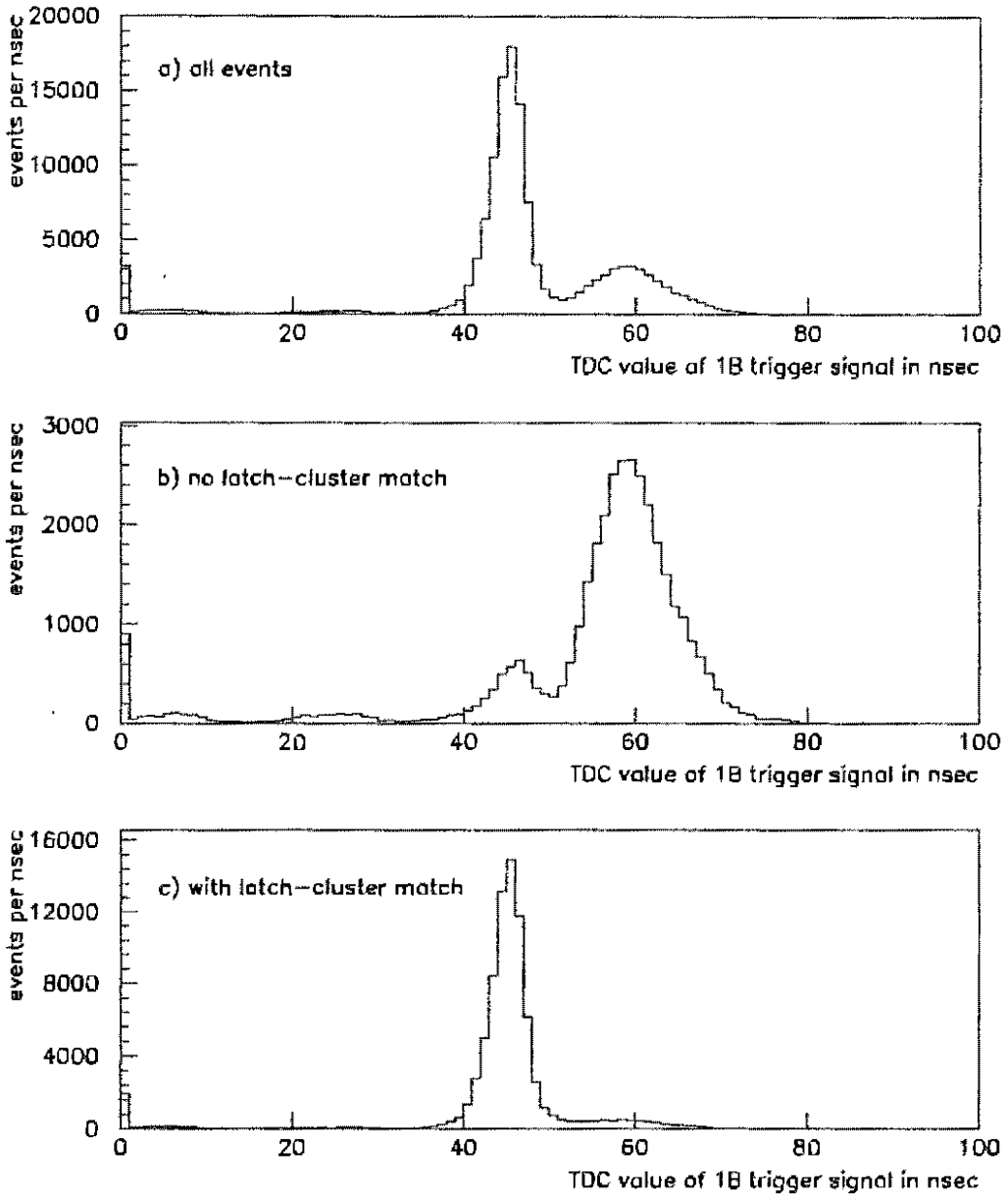

Figure 25. TDC distribution of the 1B trigger signal for neutral mode events. Shown is the distribution for all events with 1 B bank latch on (a), for events without a match between the cluster positions and the latch position (b) and for events where the cluster and latch position match (c). The latch firing in part (b) is mainly due to backsplash photons from the clusters since the latch fired late (TDC time > 50 nsec) while the latch in part (c) fired dominantly intime and is thus due to conversions.

The remaining two photons were also paired and a second decay vertex was calculated. In total, there are three different ways of pairing the four photons as shown in Fig. 26. For each pairing a χ^2 was calculated for the hypothesis that the two π^0 decay vertices agree. The best pairing χ^2 had to be smaller than 4 to keep the event and the weighted average z_{av} from this pairing gave the kaon decay vertex.

A second small angle approximation was then used to calculate the four photon mass.

$$m_{4\gamma}^2 = \frac{\sum_{n>m} E_{\gamma n} E_{\gamma m} r_{nm}^2}{z_{av}^2} \tag{5.10}$$

Thus the decay vertex and mass were calculated. The kaon energy was the sum of the four photon energies. Note that $m_{4\gamma}$ does not depend on the absolute energy scale of the calorimeter since z_{av} is proportional to the scale.

Sometimes the pairing with the best χ^2 was not the correct pairing. If therefore the second best pairing also had a $\chi^2 < 4$ and $m_{4\gamma}$ was within 14 MeV/c^2 of the kaon mass the event was rejected.

The phrase 'decay vertex' is used very loosely here. Measured was only the z position of the decay. The (x, y) positions can not be reconstructed. However, the kaon position at the plane of the glass can be calculated. This is simply the center of energy (x_c, y_c):

$$x_c = \frac{\sum_1^4 E_i x_i}{\sum_1^4 E_i}, \quad y_c = \frac{\sum_1^4 E_i y_i}{\sum_1^4 E_i} \tag{5.11}$$

with $x_i(y_i)$ being the $x(y)$ position of the ith cluster and E_i being its energy. Two important quantities in this analysis are the ring numbers relative to the center of the kaon beams in the upper and lower beam hole, (x_{upper}, y_{upper}) and (x_{lower}, y_{lower}). They are defined as:

$$\text{ring}_{upper} = 4\{\max(|x_c - x_{upper}|, |y_c - y_{upper}|)\}^2; \tag{5.12}$$

$$\text{ring}_{lower} = 4\{\max(|x_c - x_{lower}|, |y_c - y_{lower}|)\}^2. \tag{5.13}$$

The ring number is just the area of the smallest square around the beam center which contains the point (x_c, y_c). Since we know for each event whether the downstream regenerator was in the upper or lower beam hole the ring numbers can be renamed: if the upstream regenerator (UR) was in the upper position then the ring number relative to the upper hole was called UR ring number and the one relative to the lower hole DR ring number.

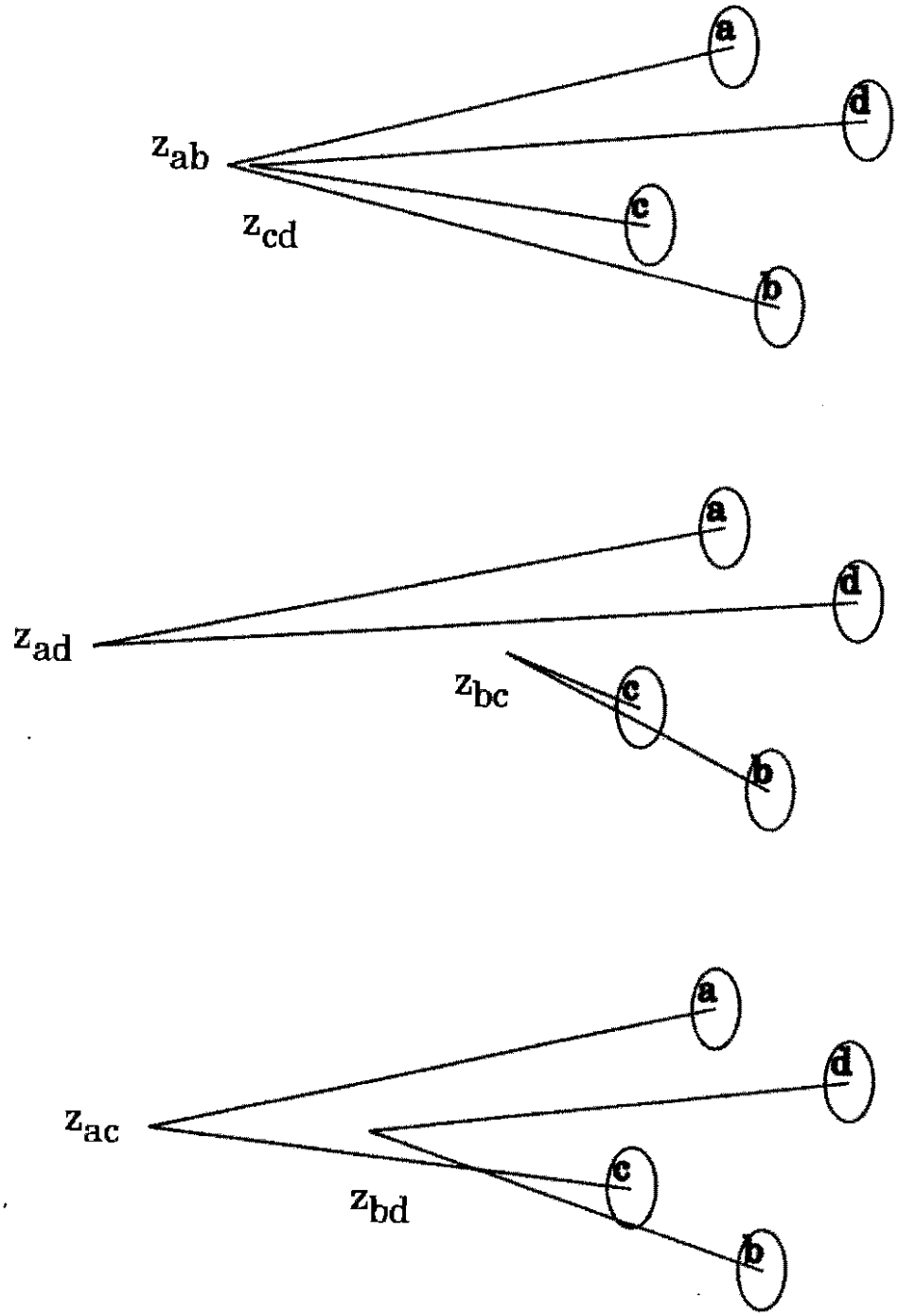

Figure 26. The z vertex reconstruction for $K \to \pi^0\pi^0$ decays. Drawn are the three possible pairings of four photons into two pairs. The two calculated z vertices for the first pairing give the best χ^2.

Fig. 31 shows these distributions for the two regenerators. Kaons that did not scatter will reconstruct within the beam profile of about 8×8 cm^2 and hence have small ring numbers. Events with high ring numbers result from diffractively or inelastically scattered kaons and are treated as background. A cut on the ring number at 120 cm^2 reduced this background. No event could have both ring numbers be smaller than 120 cm^2. Thus the event could be identified as coming from a kaon that traversed the UR or DR.[5]

If the mass $m_{4\gamma}$ was between 474 MeV/c^2 and 512 Mev/c^2 the event was kept. The $m_{4\gamma}$ distribution for neutral mode four cluster events before any analysis cut is made is shown in Fig. 27. The large background under the mass peak comes predominantly from $K_L \to \pi^0\pi^0\pi^0$ decays with two photons escaping detection.

A number of cuts have been applied to reduce this background, i.e. to detect the missing photons. The additional photons can miss the calorimeter and hit one of the photon vetoes. Fig. 28 shows the effect of the cuts on the photon veto energies. Displayed is the mass distribution before and after the cuts have been applied.

The clusters in the lead glass can overlap and therefore be counted as one cluster. A set of fusion cuts was developed to detect these cases. If the energy sum E_{side} of two neighboring blocks outside the 3×3 cluster was above $(0.8\text{GeV} + 0.0063 \cdot E_{cluster})$, the event was cut. Fig. 29 plots E_{side} for data and Monte Carlo with and without accidental overlays (see chapter 7.5 for accidental overlays). For the Monte Carlo events without overlays, only leakage of cluster energy outside of the 3×3 array contributes to E_{side} whereas in the other two samples accidental activity also adds to E_{side}. In E731 the acceptance was calculated without overlaying accidentals to the Monte Carlo and the applied cut was at 0.8 GeV, independent of the cluster energy. Since only high energy clusters could fail this cut in the Monte Carlo, a bias in the cluster energy spectrum was introduced. The was referred to as the '60 GeV' problem (see Fig. 94 in [Gibbons 93c]).

A second fusion cut ensured that the energy of the corner blocks of the 3×3 array was smaller than 50% of the energy of any of the two side blocks next to a corner block.

In a cluster, the middle column and the middle row contain typically most of the energy. The fraction of energy in the outer columns/rows is either smaller (when the photon hits

[5] In a small number of events the kaon scattered in one regenerator and its position at the glass was in the other beam. These are called crossover events.

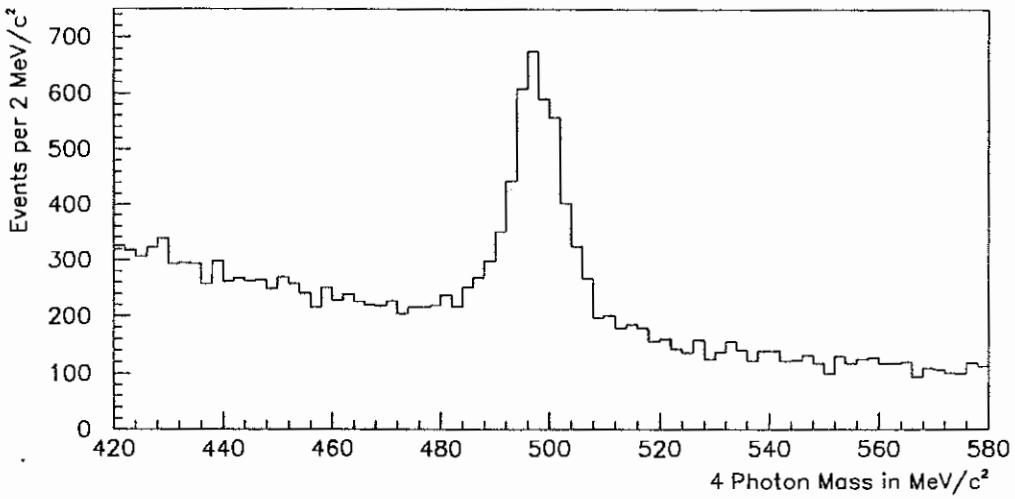

Figure 27. The reconstructed mass $m_{4\gamma}$ for neutral mode trigger events before any analysis cuts have been applied.

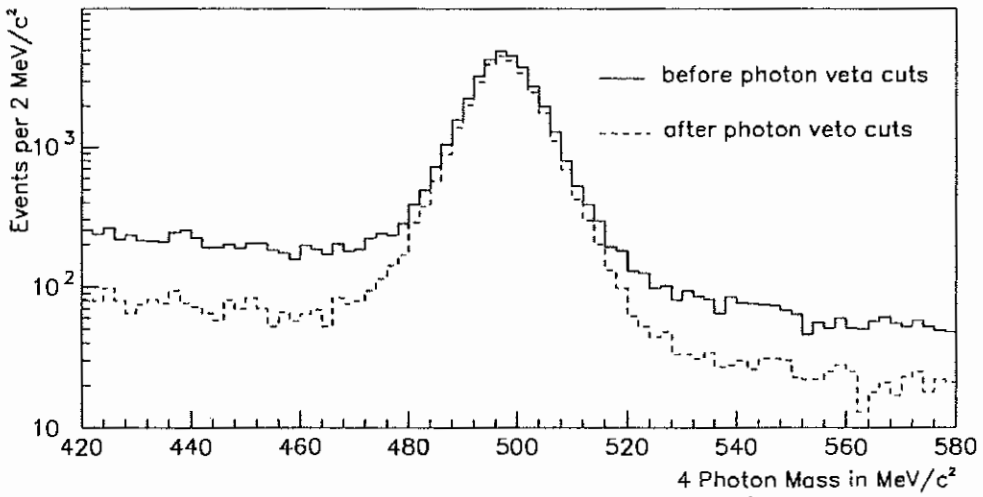

Figure 28. The reconstructed mass $m_{4\gamma}$ before and after cuts on energies deposited in the photon vetoes. All other cuts have been applied. Events with a reconstructed vertex between 136 m and 152 m are selected.

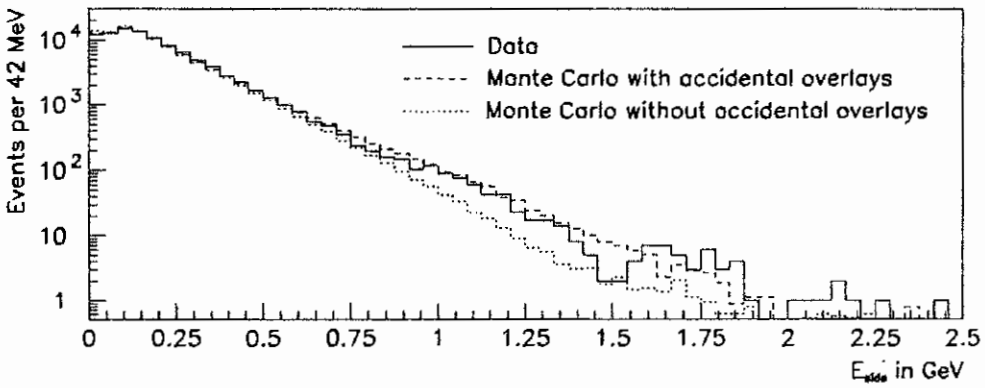

Figure 29. E_{side} for data and Monte Carlo with and without accidental overlays. E_{side} is defined in the text. Upstream regenerator events with a reconstructed decay vertex between 119.6 m and 125.9 m or between 130.9 m and 136 m were selected to reduce background from non-kaon decays. The data is not background subtracted.

the central block in the middle) or sizable in only one of the two outside columns/rows (when the photon hits the central block close to the edge). Therefore, as a third fusion cut, the event was discarded if bigger fractions of energy were deposited in both outside rows or columns.

The extra photons from $3\pi^0$ decays could be below the energy threshold of the HCF. Since there were many low energy clusters from accidental activity the direct search for these photons was infeasible. Instead, events were rejected if the intime energy (as determined by the ratio of adder to lead glass energy) of a block outside of the 5×5 array around the clusters was above 120 ADC counts (about 600 MeV).

Fig. 30 shows the effect of the three fusion cuts and the last cut on soft photons on the mass background. Plotted is the mass distribution before and after these cuts were made as final cuts.

Another class of background under the mass peak originated from interactions of the beam (kaons or neutrons) with the material in the beamline (regenerators, vacuum windows, air and, for data set 1, the hodoscope T+V). The decay vertex of these events reconstruct at the positions of the material and the pairing χ^2 distribution is similar to the one from

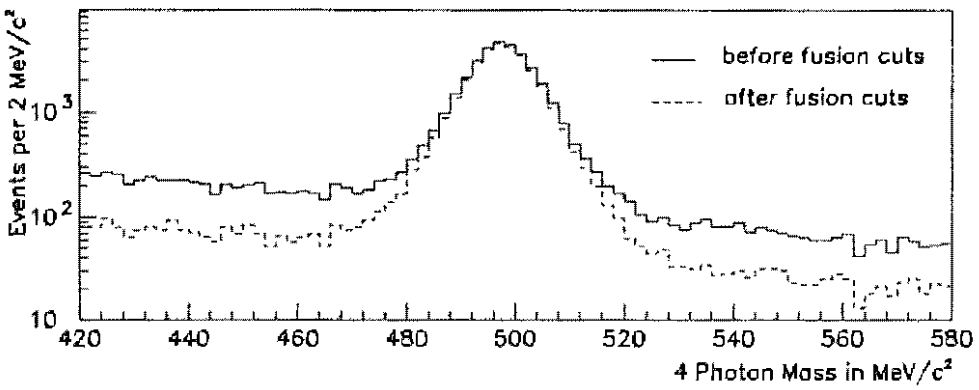

Figure 30. $m_{4\gamma}$ before and after the fusion cuts and the soft photon cut. All other cuts have been applied. Events with a reconstructed vertex between 136 m and 152 m are selected.

kaon decays. This is evidence that two neutral pions were produced in those interactions (rather than 4 random photons). Often charged particles are produced in these interactions as well. Therefore events with more than 8 B and C bank latches on or more than 10 drift chamber hit pairs with good sum of drift distances were rejected.

To further reduce this background, cuts were made on the digitized photo multiplier signals of the DR and UR at 20% and 80% of the signal size of a minimum ionizing particle, respectively. This cut also removed most of the kaons that scattered inelastically in the regenerators. Even though inelastic interactions were already vetoed at the trigger level these cuts improved the background rejection by more than a factor of 5 (see Fig. 31).

The nominal threshold for the HCF was at 1 GeV per block. A minimal cluster energy cut of 2.2 GeV ensured that the acceptance did not depend on the detailed simulation of this threshold in the Monte Carlo. In chapter 10.1 the dependence of $\Delta\Phi$ on the cut threshold will be discussed in detail. No cut on the maximal cluster energy was applied.

If a cluster results from an out-of-time photon the adder energy is smaller than the cluster energy because of the shorter ADC gate (see chapter 2.4). To reject these events the corresponding adder energy for every cluster was required to be at least 68% of the cluster energy.

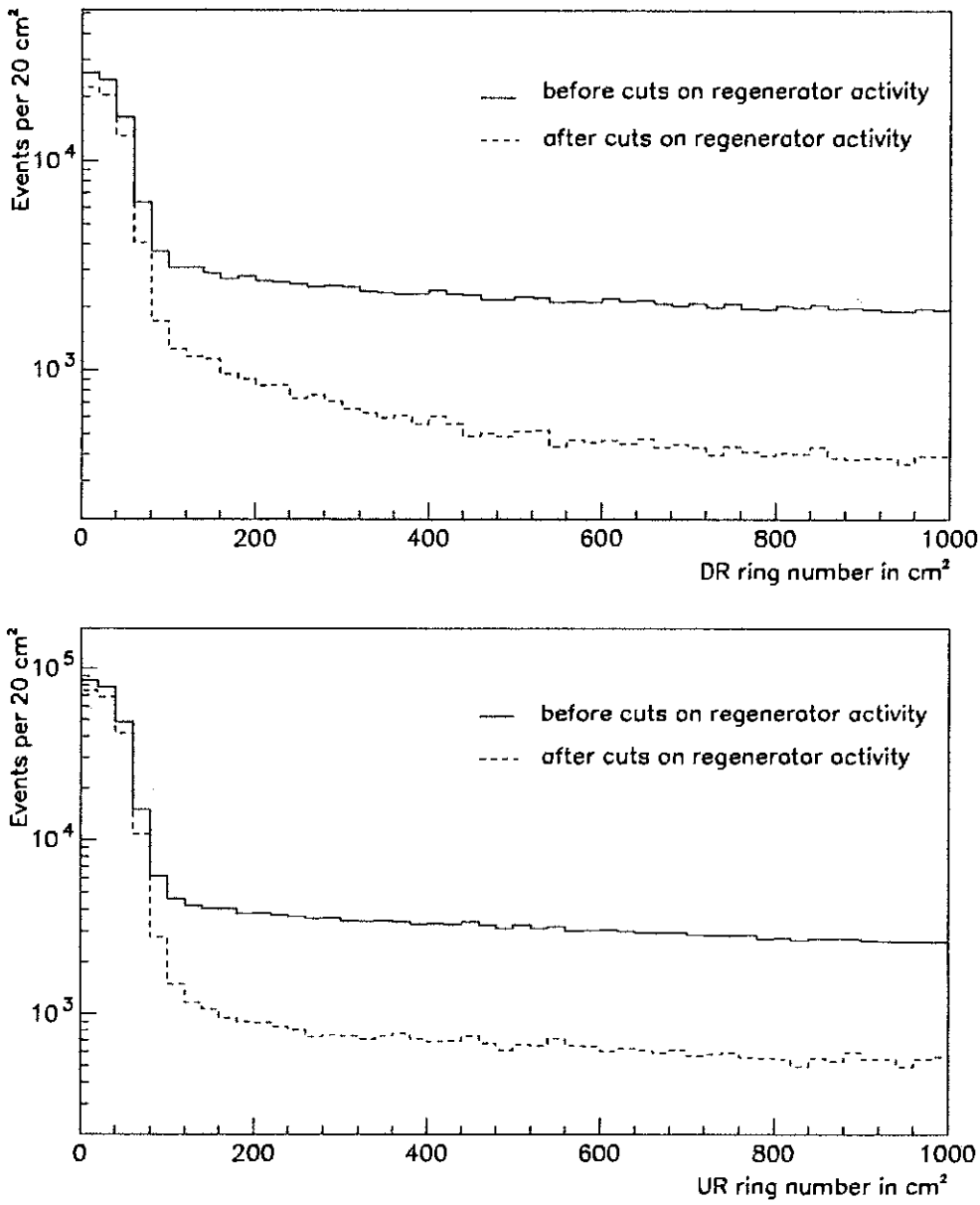

Figure 31. Ring number distributions with respect to the two regenerators (UR and DR) before and after the cut on activities in the regenerators. All other cuts have been applied. Events with a ring number smaller than 120 cm^2 are kept.

Some of the limiting apertures were not active: For the two photon vetoes between the UR and the DR, VA9 and VA0, the distance between the scintillator and the aluminum cover was about a centimeter and VA0 was a limiting aperture. The DR was mounted on an aluminum table which also turned out to be a limiting aperture. The iron ring just upstream of the C bank had an inner radius of 85 cm, much smaller than the 93 cm lead glass radius. Rather than trying to determine the amount of material and, more important, the positions and geometries of these apertures as inputs to the Monte Carlo a cut on the photon position at the different z locations was made, to ensured that photons could not hit any of them.

5.3 Background Subtraction under the Mass Peak

As mentioned in the previous section a number of cuts were employed to reduce the background to the coherent decays. This section describes how the remaining background was subtracted. First, the background under the mass peak from $K_L \to 3\pi^0$ decays and beam interactions was calculated. Then the background from scattered kaons was subtracted. The first step is described next.

The reconstructed decay vertices for beam interaction events coincide with the positions of material in the beam. In the vacuum decay region between the regenerators and vacuum windows, all events in the mass side bands were therefore from $K_L \to 3\pi^0$ decays where two photons escape detection.

To estimate the remaining background under the mass peak, a Monte Carlo was used. A detail description of this program can be found in chapter 7. Important for the $3\pi^0$ background simulation were the simulation of the HCF thresholds (see reference [Papadimitriou 90]) and the gains, resolutions and positions of the photon vetoes. The gains and resolutions were determined with muons produced in proton interactions in the target or beam dump and with $K_L \to \pi^+\pi^-\pi^0$ events where one of the photons hit a photon veto and the other one the lead glass. The energy and position of the photon hitting the veto could be reconstructed by assuming a kaon decay and calculating the π^0 momentum. The apertures

of the detector elements were taken from survey informations or from data as explained in chapter 3.

Our understanding of the $3\pi^0$ background simulation was checked by comparing the energy and decay vertex distributions of the mass side band events. In the vacuum decay region the Monte Carlo should reproduce the data. Fig. 32 and 33 show the overlays for the UR and DR beams. Data sets 1 and 2 have been added in these plots. The MC normalization is fixed to the number of data events between 140 m and 150 m. For data set 1 the region around T+V (140 m to 143 m) is excluded from the normalization calculation.[6]

The decay vertex distributions show that the background downstream of 134 m is described by the Monte Carlo. The additional background around 118 m and 128 m (close to the regenerator positions) is due to beam interactions. Only events downstream of 136 m entered the energy distribution plots. The Monte Carlo events were reweighted with a factor $(0.68 + 0.0043 \cdot E)$ with E being the sum of the four photon energies. The plots show the reweighted distributions which agrees well with the data. The systematic effect of the reweighting on $\Delta\Phi$ was studied and turned out to be small (see chapter 10.2.2). Therefore no attempt was made to find the origin of this discrepancy.

After the $3\pi^0$ background subtraction, the mass distribution in the side bands was flat. Therefore a linear interpolation was chosen to determine the beam interaction background under the mass peak.

Fig. 34 shows the mass distribution for the upstream and downstream regenerator beams after all cuts. Plotted are the data, the two contributions to the mass background and the sum of the backgrounds and the $K \to \pi^0\pi^0$ signal Monte Carlo. The mass distributions in the side bands are well described by the simulation. Note that the mass distribution of the signal Monte Carlo is shifted by about $+0.4$ MeV/c^2 relative to the data. This is due to the nonlinear response of the lead glass not being simulated correctly and will be discussed in more detail in chapter 10.2.1.

[6] Due to misreconstruction of $K \to \pi^0\pi^0$ events not all events in the side bands come from $3\pi^0$ decays. The misreconstruction rate was estimated with $2\pi^0$ Monte Carlo events and the normalization calculation included this effect.

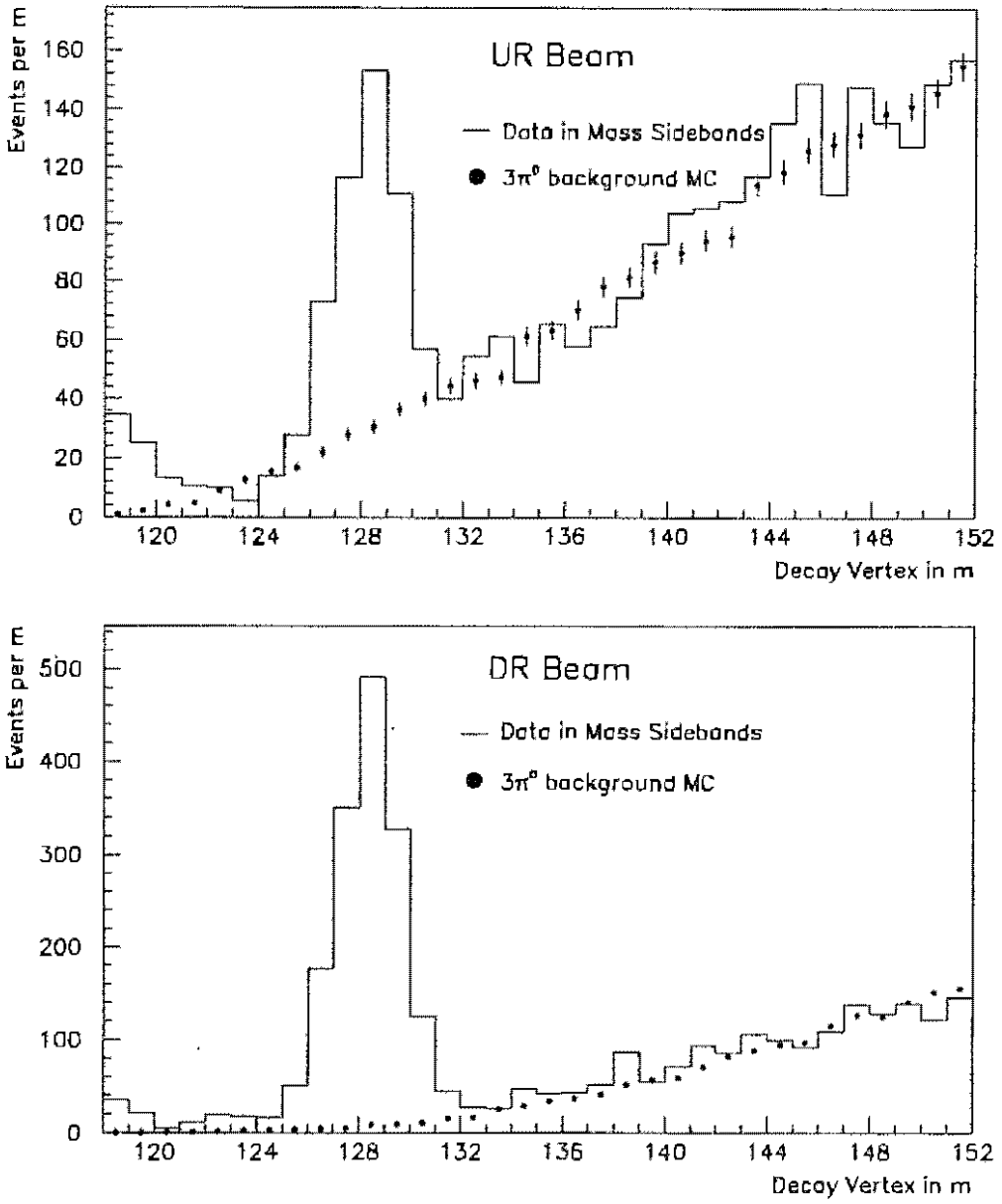

Figure 32. z distribution for events in the mass side bands (420 - 456 MeV/c^2 and 540 - 576 MeV/c^2). Plotted are the data and the Monte Carlo simulation of $K_L \rightarrow 3\pi^0$ background for the two regenerator beams.

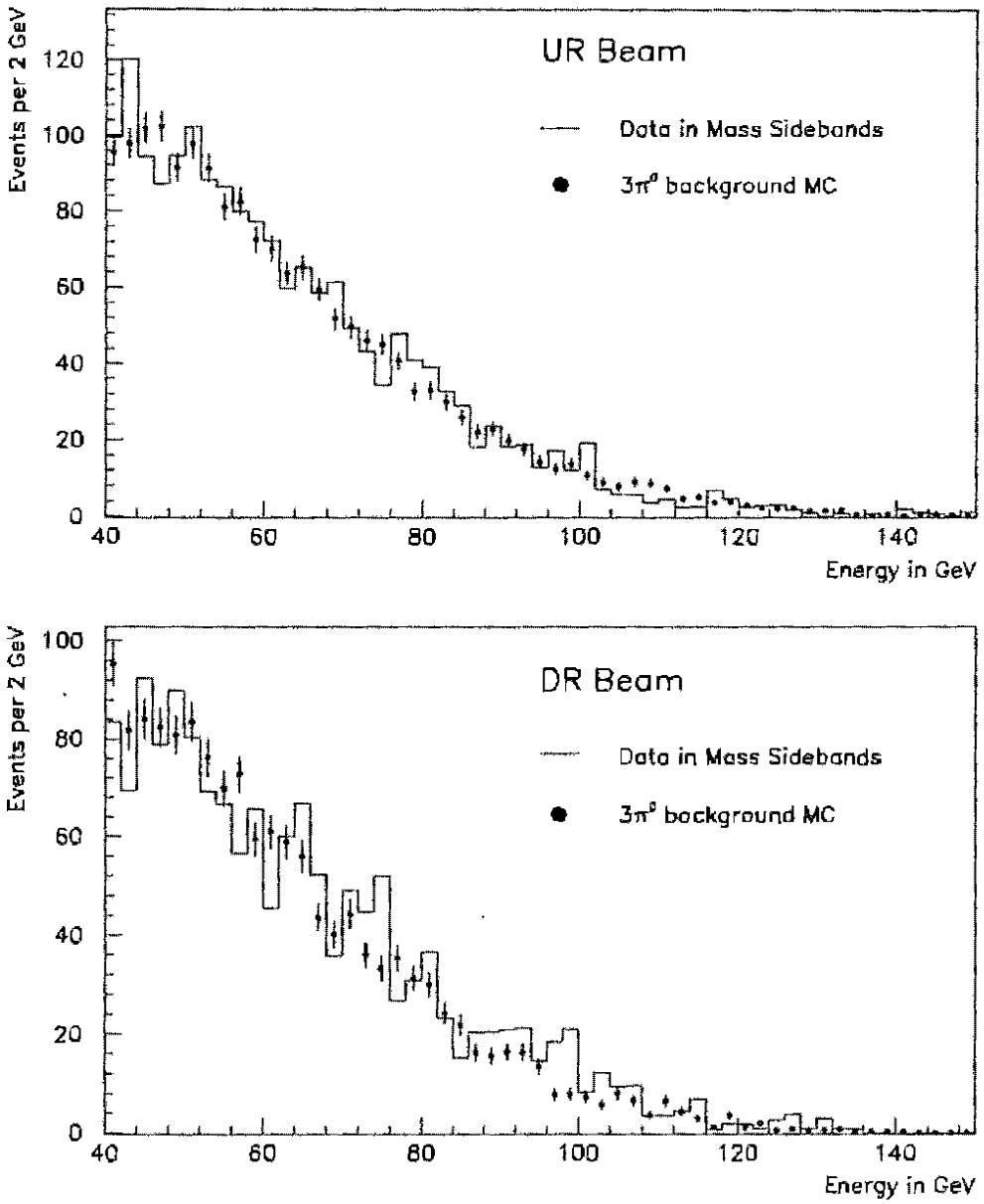

Figure 33. Energy distribution for events in the mass side bands (420 - 456 MeV/c^2 and 540 - 576 MeV/c^2). Plotted are the data and the Monte Carlo simulation of $K_L \to 3\pi^0$ background for the two regenerator beams. Only events downstream of 136 m were used. The Monte Carlo events were reweighted with a factor $(0.68 + 0.0043 \cdot E)$ with E being the sum of the four photon energies.

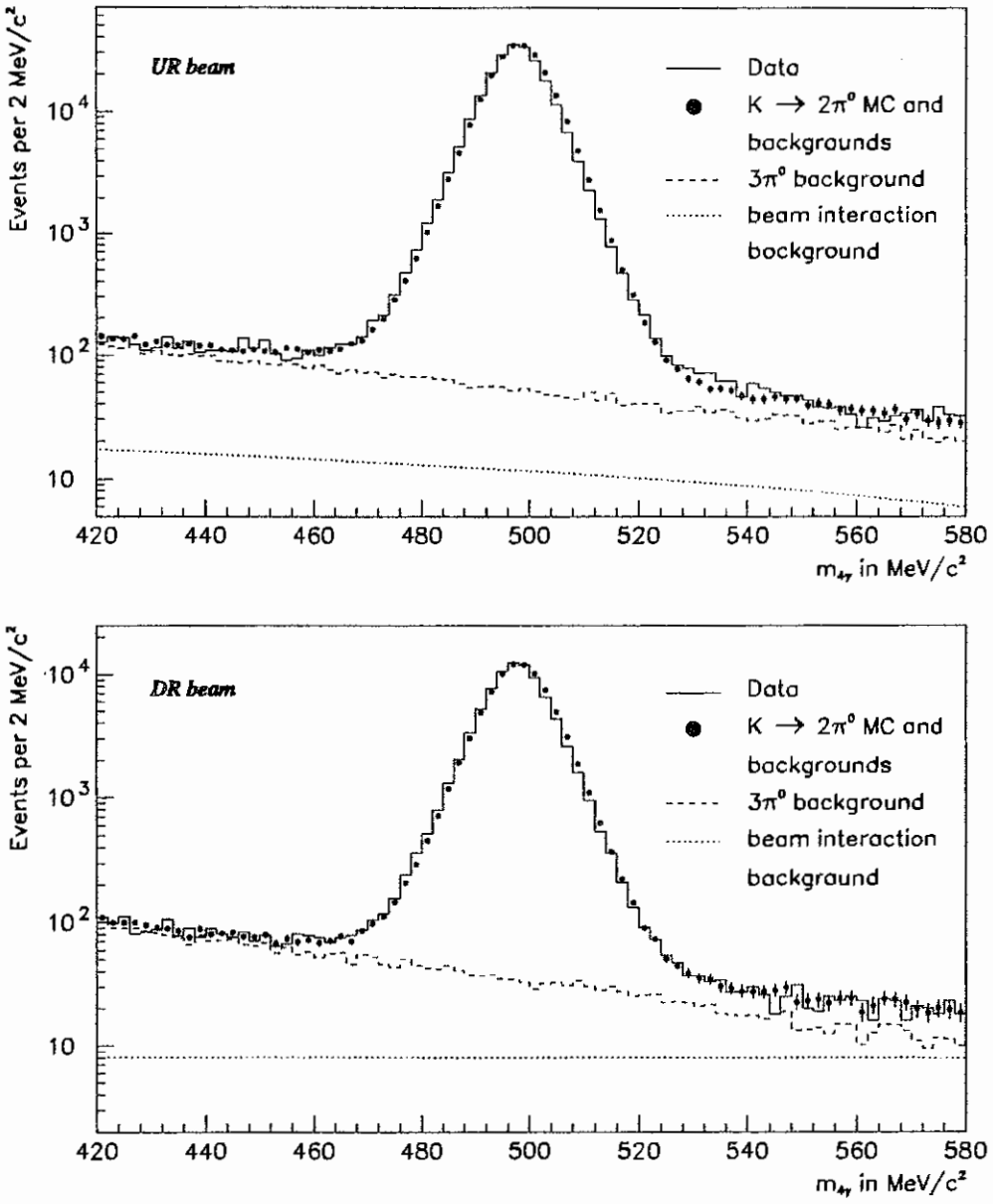

Figure 34. $m_{4\gamma}$ distributions for both regenerator beams. Events with a decay vertex between 120 m (130 m) and 152 m were used for the UR (DR) plot. Plotted are the data, the two background contributions and the sum of the two backgrounds and the signal Monte Carlo.

Table 2 lists the background levels for the different background sources and the two beams.

5.4 Background Subtraction of Scattered Kaons

Kaons could scatter diffractively or inelastically by a non-zero angle in a regenerator. In this case, there is no coherence between the different scattering centers and the decay rate is therefore proportional to N, the density of scattering centers, while it is proportional to N^2 for forward regeneration. In addition, the phase of the regeneration amplitude changes in case of diffractive or inelastic scattering, which will be discussed in more detail in chapter 7.1.2. It was therefore easiest not to include scattered kaons in the sample used to extract $\Delta\Phi$ and the other results. A cut on the ring number (transverse momentum p_T) of the kaon in the neutral (charged) mode analysis rejected most scattered kaons. The background after the cuts was estimated with a simulation.

In charged mode, the transverse momentum the kaon received in the scattering can be reconstructed with good resolution. Since the kaon scattering is the same for the charged and neutral decay mode, $\pi^+\pi^-$ decays were used to study scattering. The Monte Carlo was tuned to reproduce the scattering in the regenerators and the vacuum windows. The simulation of scattering in the scintillators T+V for data set 1 was taken from E731 (see [Gibbons 93c]). This background was small and so was its contribution to the systematic error on $\Delta\Phi$ (see chapter 10.2.2).

No tuning was necessary for the neutral mode except for the amount of background from inelastic scattering. The analysis cuts between neutral and charged mode had potentially different rejection power for inelastic events.

Fig. 35 and 36 show the ring number distributions for the UR and DR beams in slices of 2 m z bins. The agreement between the data (histogram) and simulation (solid circles) is good for both beam and all z bins.

Fig. 37 shows the composition of the background together with the data and the sum of the backgrounds as a function of ring number. Table 2 list the background fractions for the different beams. The beam interaction background and the noncoherent T+V background

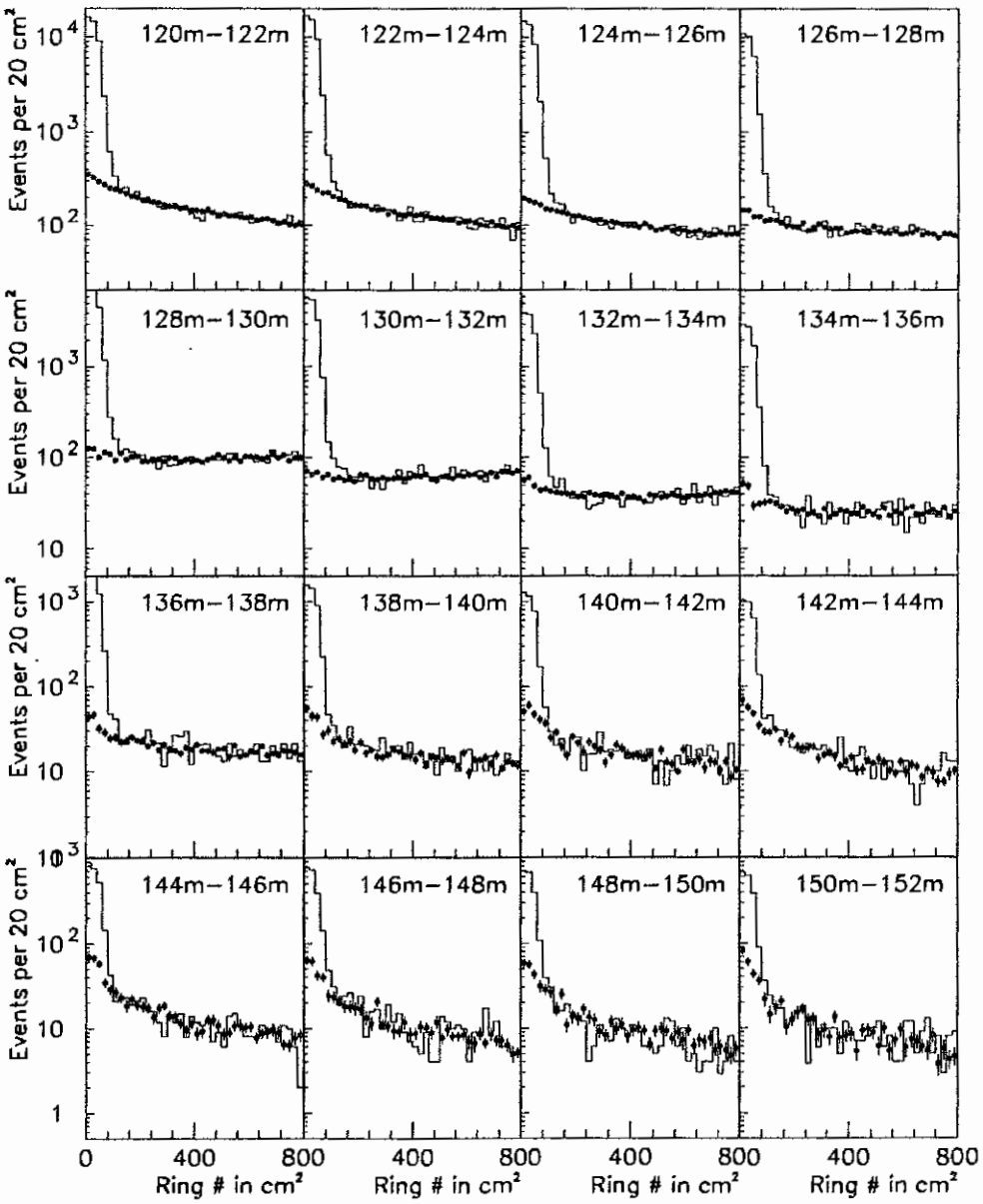

Figure 35. Ring number distributions for the upstream regenerator in z slices of 2 m. The z range each plot covers is part of the title. The data is the histogram and the simulation are the solid circles.

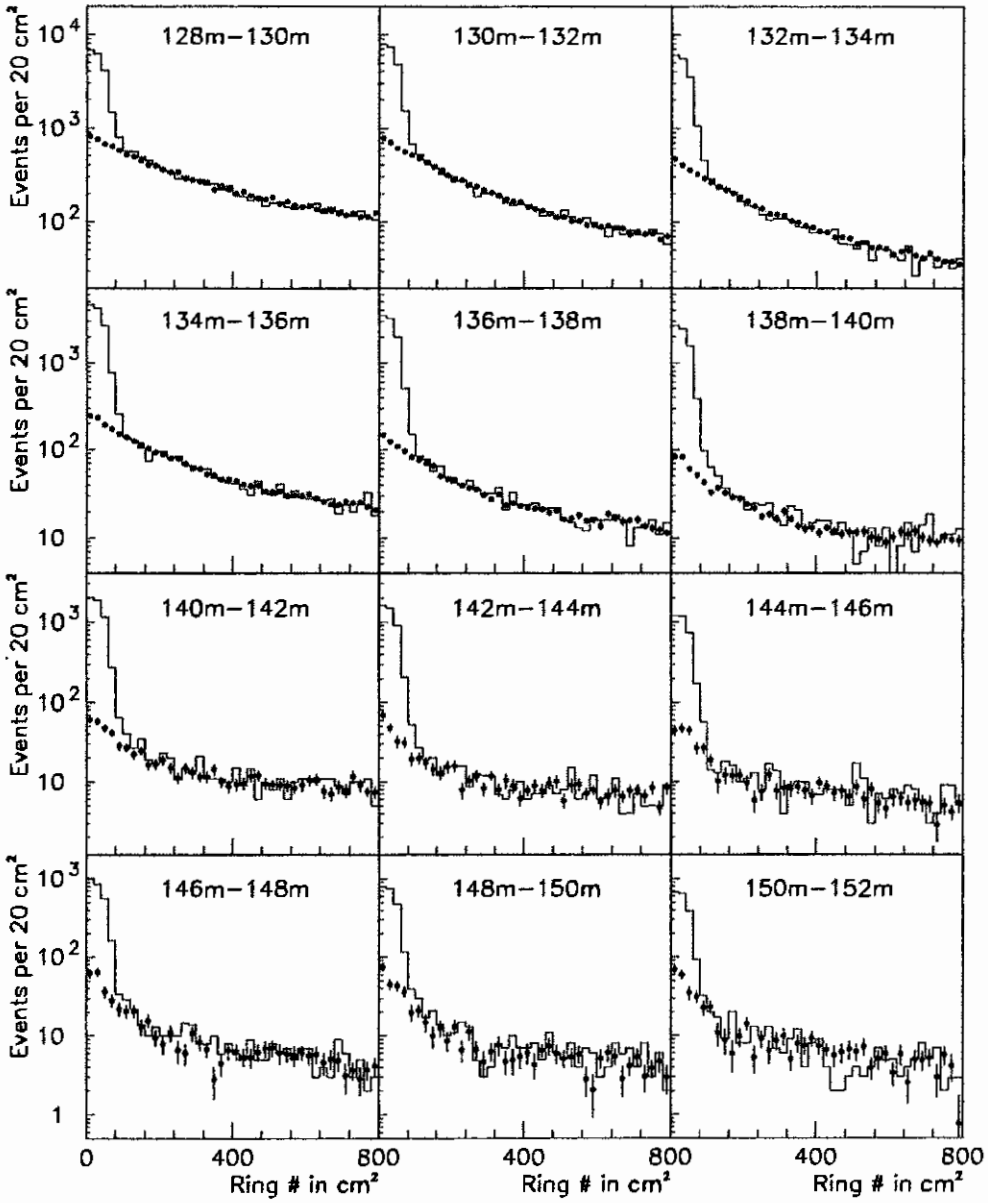

Figure 36. Ring number distributions for the downstream regenerator in z slices of 2 m. The z range each plot covers is part of the title. The data is the histogram and the simulation are the solid circles.

Table 2. Background fractions for the different sources.

	UR set 1	DR set 1	UR set 2	DR set 2
$3\pi^0$ background	0.7%	1.1%	0.7%	1.3%
beam interactions	0.1%	0.3%	0.1%	0.2%
noncoherent regenerator events	2.7%	8.8%	2.6%	9.1%
noncoherent T+V events	$< 0.1\%$	$< 0.1\%$	-	-

were negligible. The biggest background is from noncoherent regenerator events and the biggest systematic error is attributed to its simulation. The systematic error contribution however does not simply scale with the overall background fraction since the background fraction as a function of the decay vertex is more important. The total background from $3\pi^0$ decays for example is very small but strongly depended on z as is shown in Fig. 38.

5.5 Lead Glass Energy Scale

The lead glass was calibrated with electrons and the simulation was tuned to reproduce electron showers. Since photon showers have a different shower profile, a correction needed to be applied (see equation 5.3) to properly reconstruct photon energies. This correction is calculated with the EGS simulation as mentioned above. Different approximations were made during this calculation like the assumption of uniform radiation damage and it is therefore not surprising that the nonlinear response of the glass differs slightly between data and Monte Carlo. One consequence is the shift of the reconstructed kaon mass between data and Monte Carlo in Fig. 34.

This nonlinearity also causes a shift in the reconstructed decay vertex which can be observed in the position of the edge of the z distribution at the regenerator: the position of this edge depends on the absolute energy scale since the reconstructed vertex shifts if the cluster energies are scaled by a common factor (see equation 5.6). A nonlinearity will therefore shift the edge by different amounts for different kaon energies. This argument can be turned around. By comparing the edge position between data and Monte Carlo for different kaon energy bins we tried to compensate for the nonlinear response mismatch by

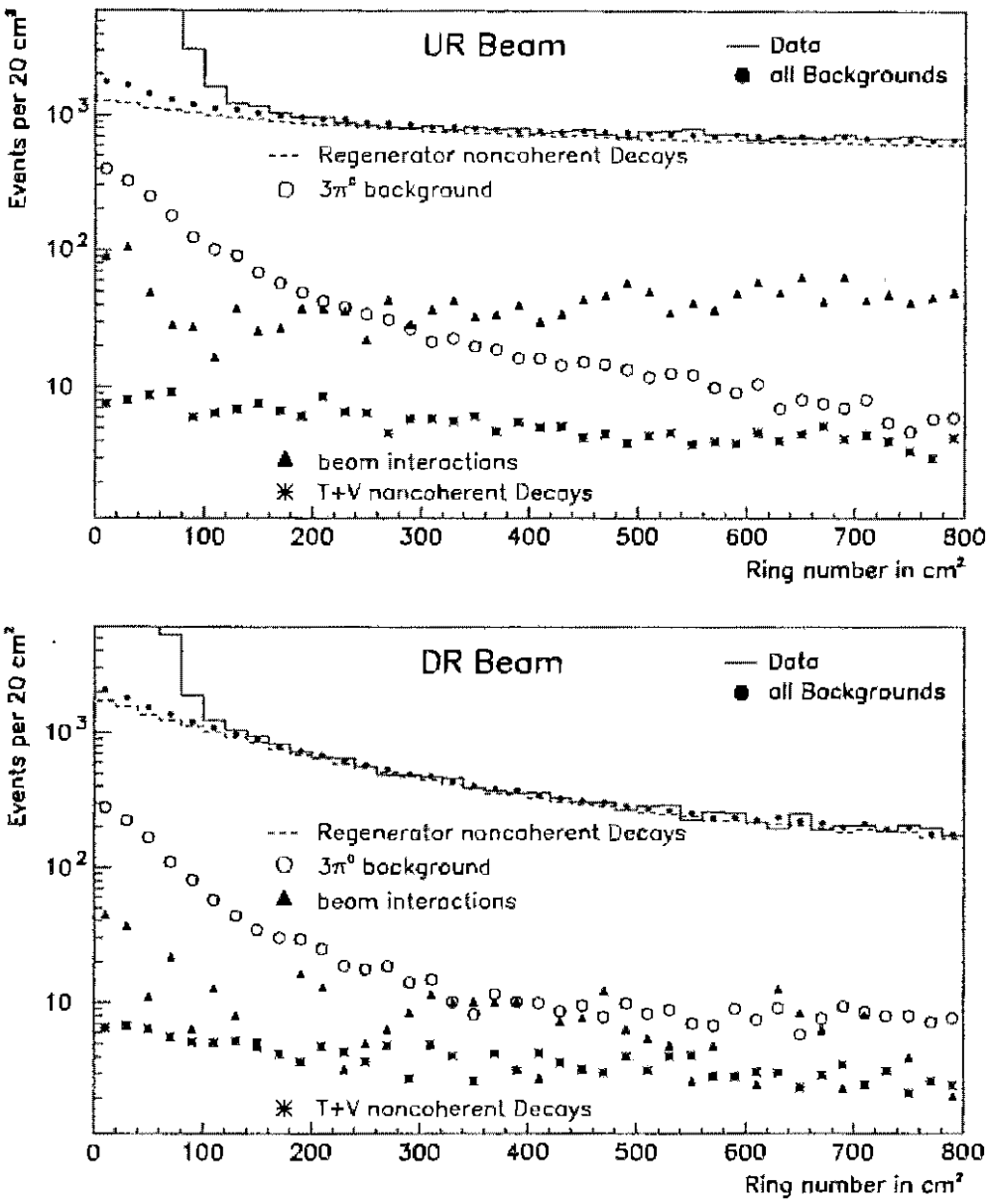

Figure 37. Composition of the background in ring numbers for both beams. All events in the (p, z) range used in the $\Delta\Phi$ fit entered the histogram. The analysis cut is at 120 cm^2.

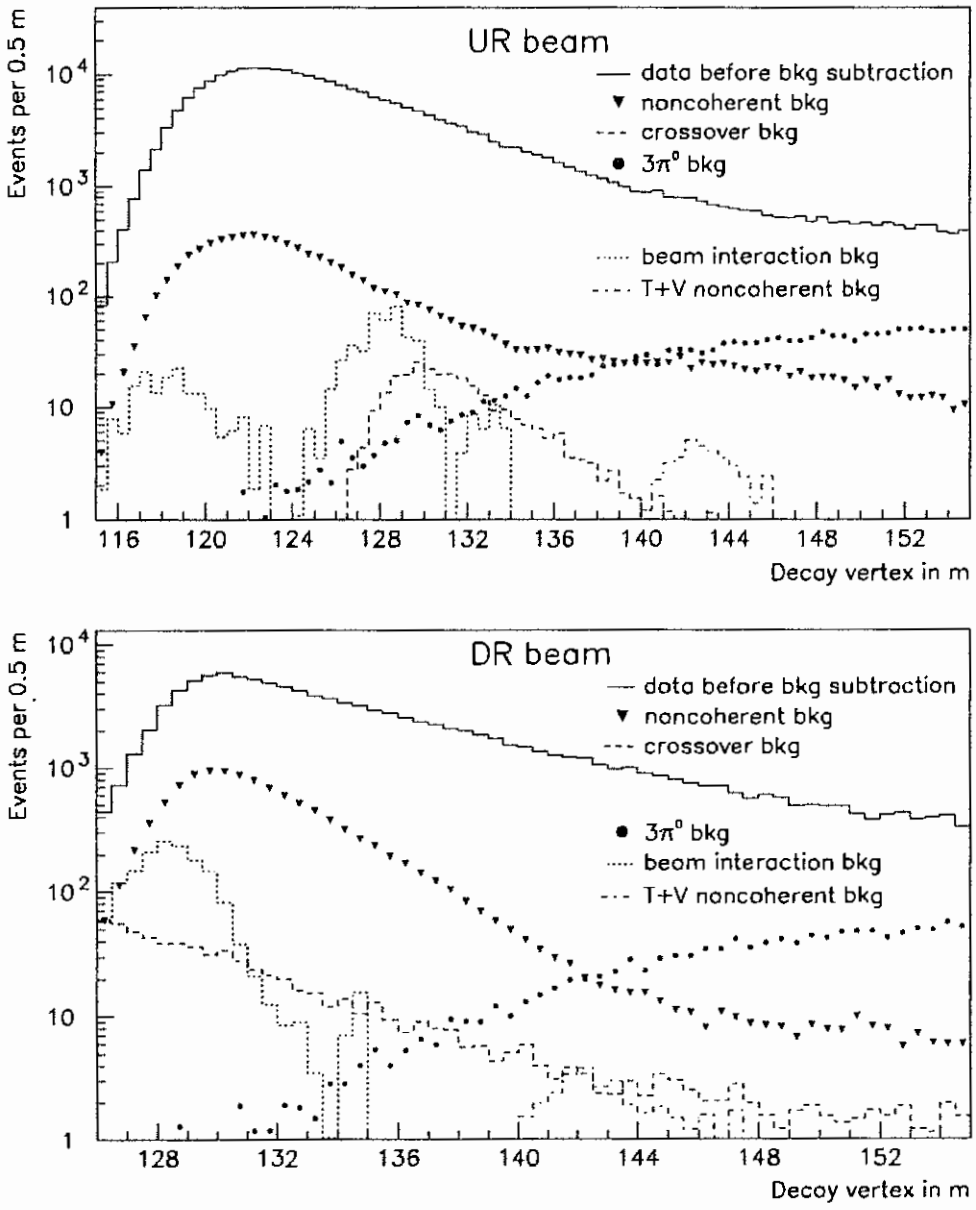

Figure 38. Decay distribution for $\pi^0\pi^0$ data and the different background contributions. The data sets 1 and 2 have been added. The "noncoherent bkg" is the background from diffractively and inelastically scattered kaon. The "crossover" background are events that scattered in one regenerator and reconstruct in the other. The "T+V noncoherent" background originates from kaons scattering in the T+V hodoscope.

rescaling the photon cluster energies. The scale factor depended on the kaon energy and was chosen to match the edge in every kaon energy bin.

E773 had two regenerators at two different locations and both edges were used for the matching. Since the data Monte Carlo mismatch depended on the light absorption and since the radiation damage increased during the run, different scales were determined for the two data sets. The scale found for data sets 1 was $(1.002 + E \cdot 10^{-5})$ and for set 2 the scale was $(1 + E \cdot 3.5 \cdot 10^{-5})$. E is the sum of the four photon energies. Fig. 63 and 64 show the decay vertex distributions between data and Monte Carlo after the matching.

In chapter 10.2.1 we will see that the edge matching procedure is a very powerful tool to compensate for the nonlinearity mismatch between data and Monte Carlo.

CHAPTER 6

Charged Mode Analysis

This chapter discusses the event reconstruction for $K \to \pi^+\pi^-$ decays, the event selection criteria and the background subtraction. A more detailed description can be found in reference [Briere 95b].

6.1 Event Reconstruction

The event reconstruction is divided into the following steps: track finding in the x and y views of the chambers, matching the x and y tracks, finding the decay vertex and calculating the track momenta and other kinematic quantities like the $\pi^+\pi^-$ mass. The drift chamber information was used primarily for this task. Because of the magnet bend in one of the views, the x view, the track finding algorithm differed for the two projections. The track finding in the x view will be described first.

The magnetic field at the chambers closest to the magnet was negligible. Therefore the path of a charged particle could be approximated by straight lines upstream and downstream of the magnet with a bend at the midplane of the magnet. Thus the track finding in the x view consisted of finding track segments upstream and downstream of the magnet and matching the segments at the bend plane.

All combinations of hit pairs and single hits in chamber one with pairs and hits in chamber two were formed, called segments. Only hit pairs for which the sum of the two drift distances (SOD) was less than 10.35 mm (= drift chamber cell size + 4 mm) are

considered (see Fig. 39). Otherwise the pair came from a track out of time relative to the trigger. A single hit in one of the chambers was allowed because of wire inefficiencies. In this case no information was available on which side of the wire the track passed and both possibilities were considered. The same way segments are found in the two downstream chambers.

Segments in the upstream chambers had to point back towards the beam since tracks originate from the beam. Valid upstream segments also had to point inside the aperture of the magnet and the vacuum window and, for data set 1, inside the DRA. Downstream segments had to point inside the magnet and the lead glass aperture. The segments upstream and downstream of the magnet were extrapolated to the bend plane. If the matching at the magnet was within 1 cm the two segments formed a track candidate. In case of a single hit, say in an upstream chamber, both possible upstream segments could match to the same downstream segment. The tracks were then ordered according to the quality of the match. If two track candidates shared hits the one with the better matching was kept and the other one was discarded. Later in the analysis the matching at the magnet was required to be within 5σ, with σ being the measured momentum dependent resolution.

In the y view a charged particle was bent very little by the magnet. Therefore hit pairs in all four chambers were used simultaneously to find track candidates. Trackfinding started with hit pairs in chambers one and four. If there were hits in at least one of the middle chambers within 1.5 cm of the line connecting the chamber 1 and 4 hits, a y track was found. At least 6 hits were required for a track in the x view but only 5 for a y view candidate (out of the possible 8). In case a hit was shared between two hit pairs the pair with the better SOD was kept and the remaining hit was treated as a single hit.

If there were more than two x or y track candidates, the number of hit pairs per track with a SOD differing by more than 1 mm from the cell size was required to be less than two to reject tracks out of time with the RF. Events with two tracks in the x and y projections and opposite charge were kept in the analysis. Fig. 40 shows the number of x and y tracks found in raw events for data sets 1 and 2. In about 75% of the events two x and y tracks were found for data set 1. The equivalent number for data set 2 is about 50%. For set 2 the

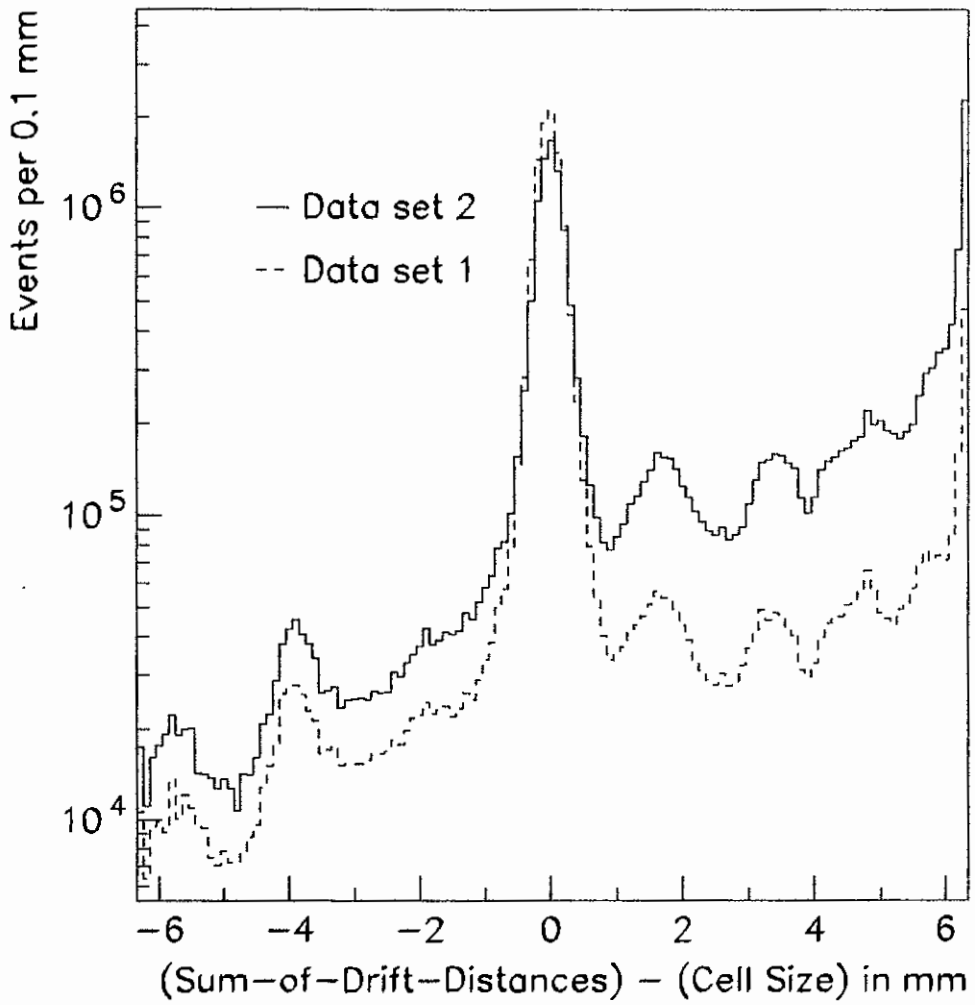

Figure 39. Sum of Drift Distances for all hit pairs from parts of data sets 1 and 2. The cell size of 6.35 mm was subtracted from the SOD. The peak at zero is due to intime hit pairs while the smaller peaks are from out-of-time pairs. Data set 2 has many more out-of-time pairs because the level 1 trigger was looser after the T+V hodoscope was removed.

trigger requirement was looser which explains the increase of the number of events without tracks.

At this point the x and y track projections of the two particles were found. The next problem was to decide what x track should be paired with a y track. By looping over all clusters in the lead glass and all x and y tracks the track-cluster distance for each combination was computed. At least one distance had to be smaller than 1.2 block sizes to match an x to a y track. In case more than one combination fulfilled this requirement, the one with the smallest distance was chosen. If no match was found the event was discarded.[1]

Finally, several corrections were applied to the fitted track positions. The drift time was corrected for the time it took the signal to travel along the chamber wire. The sag of wires in the y view was corrected for. The common stop of the TDC was in coincidence with the accelerator RF, i.e. in coincidence with the protons hitting the target. Because of the length of the proton bucket (about 1.3 nsec) there was a small jitter between the common stop and the the kaon decay time. This offset caused the SODs for all hit pairs (up to 16 in a two track event) to shift coherently. The average offset of the SODs from the nominal value could therefore be used to improve the timing of the kaon decay on an event-by-event basis.

After these corrections the track segment angles and positions are fit using the drift distances at every wire plane. For the y view separate upstream and downstream track parameters were fitted because of the small bend. The reduced χ^2 of the fit had to be smaller than 30 for each of the 8 track segments in a two-track event. For a segment with 4 hits this corresponds to a cut of about 0.7 mm on the SODs. Events with out of time tracks will be rejected by this cut (see Fig. 39).

For events with two matched tracks a vertex was calculated. The vertex was along the shortest line connecting the two tracks. In the vertex calculation the resolution of the track parameters as a function of the momentum and the amount of material the track traversed was used. If the χ^2 of the fit was larger than 30 the event was rejected.

The momentum p of each track was calculated using the expected momentum kick in

[1]Note that the cluster definition in this analysis was different from the one in the neutral mode analysis. A minimum energy of 200 MeV was required for the central block and of 500 MeV for the entire cluster. The reconstructed lead glass energy of a minimum ionizing particle was 700 MeV.

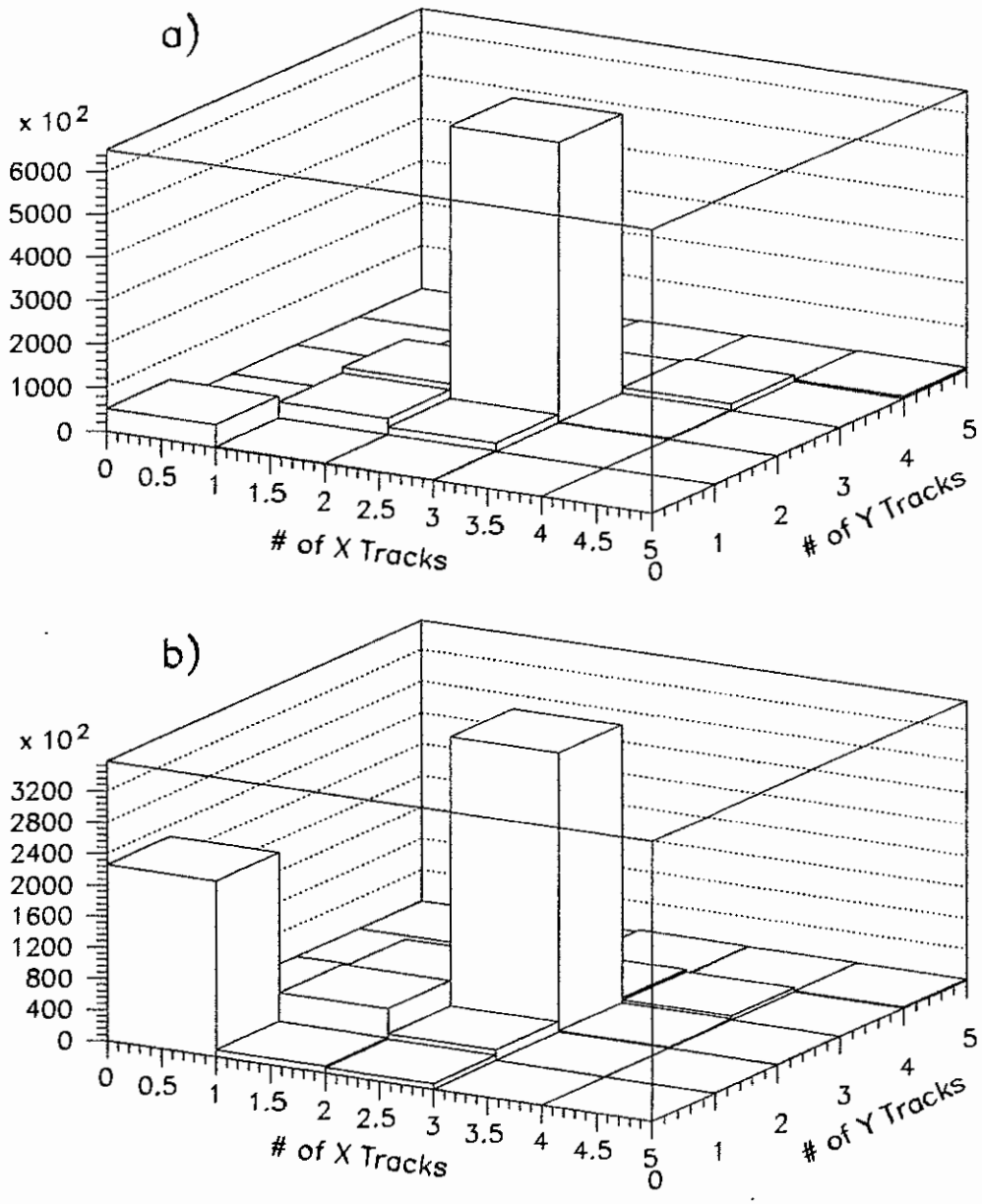

Figure 40. Number of x and y tracks found by the track finding routine for data sets 1 and 2.

the x projection Δp_x and the track angles:

$$\frac{\Delta p_x}{p} = \left| \frac{\theta_x^{up}}{\sqrt{1+(\theta_x^{up})^2+(\theta_y^{up})^2}} - \frac{\theta_x^{dn}}{\sqrt{1+(\theta_x^{dn})^2+(\theta_y^{dn})^2}} \right| \tag{6.1}$$

with $\theta_x^{up} = p_x/p_z$ being the x view track angle upstream of the magnet, etc. The momentum resolution is

$$\frac{\sigma_p}{p} = 0.005 \cdot \sqrt{1+\left(\frac{p\,[GeV/c]}{40}\right)^2} \tag{6.2}$$

Assuming the pion mass for both tracks the kaon mass and four momentum was calculated. The kaon was then propagated back from the decay vertex to the downstream face of both regenerators. In the analysis we want to know whether the kaon passed through the UR or the DR. Its positions at the regenerators was therefore required to be within a 5×5.5 cm^2 region around the regenerator centers for exactly one of them.

The initial kaon direction was determined by the vector connecting the target position with the reconstructed kaon position at the downstream face of the regenerator. The kaon could scatter in the regenerator. The transverse momentum p_T the kaon received in the scattering is then the difference between the initial kaon momentum and the momentum after the regenerator.

This completes the event reconstruction. The next section discusses the analysis cuts applied to reduce the background and to ensure a good event reconstruction.

6.2 Analysis Cuts

Most of the cuts applied can be categorized as quality cut, kinematic cuts or aperture cuts. The quality cuts ensure that the event was properly reconstructed and most of them have been mentioned in the previous section.

The aperture cuts ensured that the tracks hit only instrumented parts of the detector. As mentioned in the neutral mode analysis discussion the iron ring, the vacuum window, the table the downstream regenerator was mounted on and the photon veto VA0 were limiting apertures. For decays upstream of each of these detector elements cuts were made on the extrapolated track positions at the location of the aperture to ensure that the track did not scatter in the material.

In addition, tracks were required to hit the lead glass since the ratio of the shower energy to track momentum E/p was used to identify electrons. If one of the tracks pointed to an area of 3.2×3.2 lead glass blocks around the beam hole centers the event was discarded.[2]

The track extrapolation to the location of the muon veto plane had to be smaller than 1.2 m in x and 1.1 m in y. This ensured that muons in our sample from $K_L \to \pi\mu\nu$ decays or pion decays would hit the veto which is $2.54(x) \times 2.44(y)$ m^2 in size. If both tracks hit the glass inside the two central columns and the x projections at the glass were within 2 cm it was likely that the x-y track pairing was wrong. Those events were therefore rejected.

The kinematic cuts were applied to reduce the backgrounds from non-$\pi^+\pi^-$ decays and scattered kaons. If a cluster matched to a track E/p was required to be less than 0.8 to reduce $K_L \to \pi e\nu$ decays. Since hadron showers start deeper into the glass than electromagnetic showers less light is absorbed. The energy E can be therefore be bigger than p and some pions will fail this cut.

The minimal track momentum was 7 GeV/c to ensure that muons would have penetrated the filter in front of the muon veto plane. This reduced background from $K_L \to \pi\mu\nu$ decays. If the higher momentum track is assumed to be a proton and the proton-pion mass was within 7 MeV of the lambda mass the event was discarded.

The pion-pion mass had to be within 14 MeV of the kaon mass. This cut rejects $\pi^+\pi^-\pi^0$ decays, semileptonic decays and $K_L \to \pi^+\pi^-\gamma$ events where the photon is a direct emission photon. No cut was made on the number of clusters that did not match to tracks since additional clusters can originate from pion showers which were not simulated.

In case the photon in a $K_L \to \pi^+\pi^-\gamma$ event comes from an inner bremsstrahlung process, the $\pi^+\pi^-$ mass can be within the mass cut. These events are not treated as background since the CP violation for this decay mode has been measured by our experiment and was found to be the same as for the two-body decay modes within the errors. To be more precise, the parameter $\eta_{+-\gamma}$ which is defined as

$$\eta_{+-\gamma} = \frac{Amp(K_L \to \pi^+\pi^-\gamma)}{Amp(K_S \to \pi^+\pi^-\gamma)} \tag{6.3}$$

is expected to be equal to η_{+-} and was measured to be the same: $\eta_{+-\gamma} = (2.359 \pm 0.0074) \cdot$

[2]The beam holes have an area of 2×2 lead glass blocks and the CA covers the inner half of the blocks next to the holes, i.e. the hole and the CA cover the area of 3×3 blocks.

10^{-3} exp($i\,43.8° \pm 0.4°$) [Matthews 95a]. The acceptance for radiative decays is slightly different and the simulation of $\pi^+\pi^-$ decays therefore includes the generation of inner bremsstrahlung events by default.

As mentioned before kaons that scatter in a regenerator diffractively or inelastically are treated as background. The level of inelastic events could be reduced by a cut on the photo multiplier signals of the regenerators. These cuts are described in section 5.2. Almost all of the remaining background events were rejected by a cut on the transverse momentum. The p_T^2 had to be less than 250 MeV^2/c^2 to kept the event.

The neutral mode analysis is sensitive to accidental activity in the lead glass. In charged mode the sensitivity was due to activity in the drift chambers and trigger hodoscopes. The event could misreconstruct because of additional hits in the drift chambers or because the same wire was hit by a pion track and an accidental track. This effect was studied with two Monte Carlo samples: one with and one without accidental overlays (see section 7.5). No bias in the acceptance was observed [Briere 95b]. The more important effect was that for some events the trigger requirements were only fullfiled because of the accidental activity. To avoid any bias the trigger was simulated with the drift chamber hits on the tracks and the trigger hodoscope hits from the two tracks only. If any level 1 or level 2 requirement could not be verified by this method the event was discarded.

Finally, to reject beam interaction events with the air and vacuum windows around the two regenerators, events that have a reconstructed decay vertex between 127 m and 129 m or upstream of 118.5 m were not used in the final data sample.

Fig. 41 shows the scatter plot of the kaon mass and kaon p_T^2 for DR events. Clearly visible are the coherent peak at the kaon mass and small p_T, the events from scattered kaons and the background from semileptonic decays at low and high kaon masses. The mass cut and the cut on p_T^2 eliminate almost all the background. Fig. 42 shows for both data sets and both beams the kaon mass distributions after all cuts. The asymmetry of the mass peak for low masses around 480 MeV/c^2 in all distributions is due to radiative decays. The overall increase in the background level for data set 2 is from the additional background of semileptonic decays due to the extended decay region.

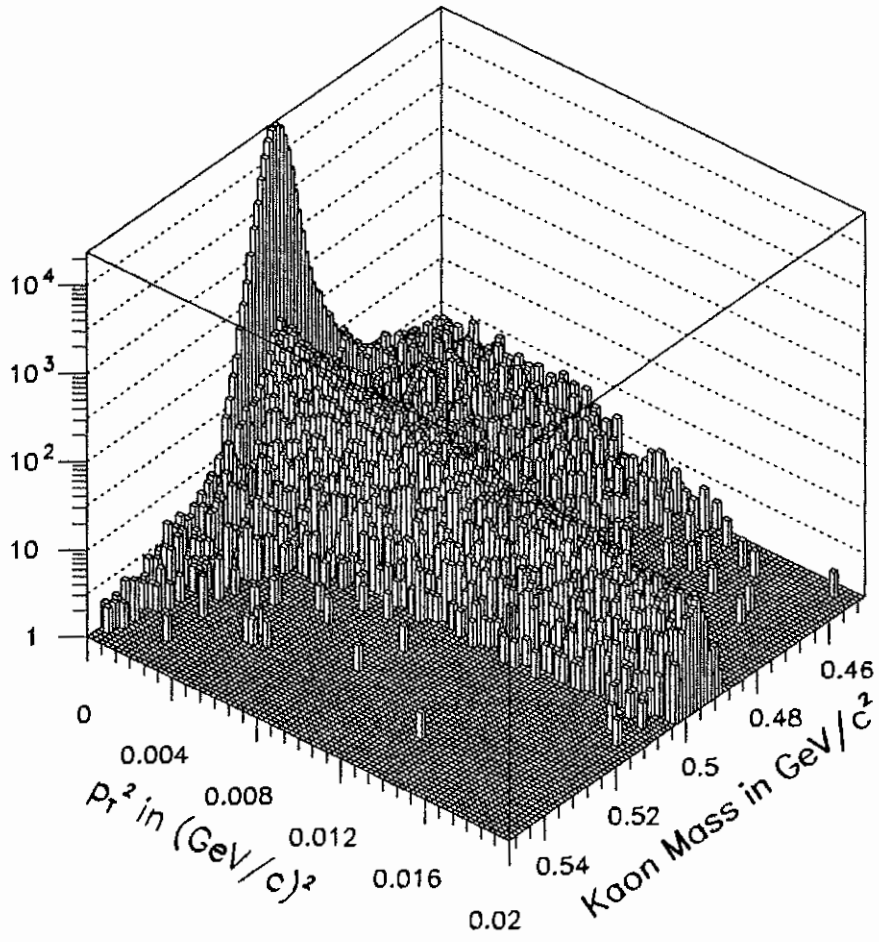

Figure 41. Scatter plot of the kaon mass and kaon p_T^2 for DR events of set 2. All cuts but the mass and transverse momentum cut have been applied.

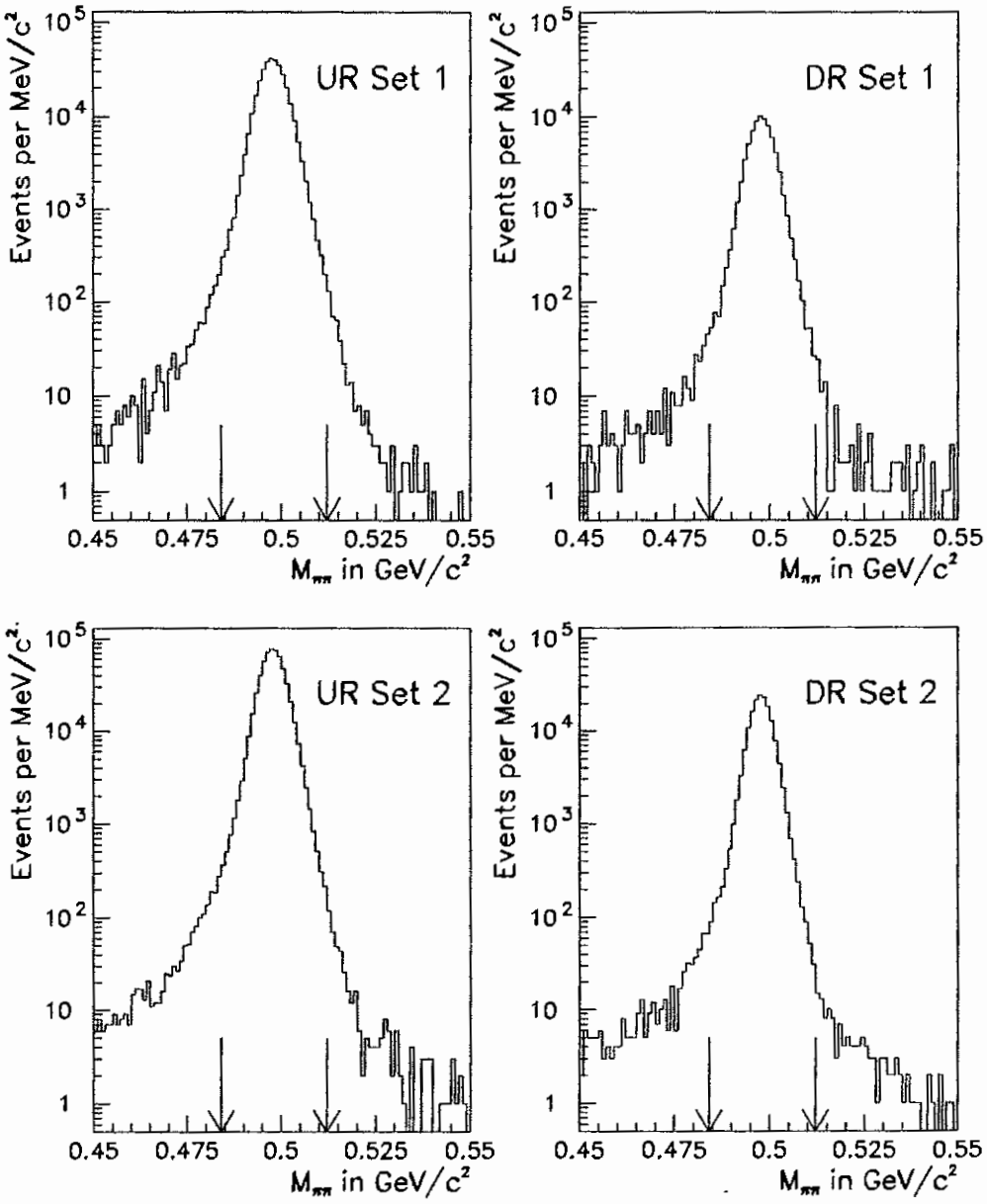

Figure 42. Reconstructed $\pi^+\pi^-$ mass for charged mode for the two beams and data sets.

6.3 Background Subtraction

The backgrounds in the charged mode after all cuts were rather small, 0.3% (0.8%) for the UR (DR). The dominant background source were noncoherent (scattered) kaon decays. Far downstream semileptonic decays become an important contribution (see Fig. 43). To determine the number of noncoherent background events a Monte Carlo prediction was used. The simulation was tuned using the observed p_T^2 distribution in charged mode for $p_T^2 > 0.004$ (GeV/c)^2. In chapter 7.1.2 the Monte Carlo modeling of this background is discussed in detail. The same parameterization is used for the neutral mode background subtraction. Section 5.3 shows that the parameterization describes the background well.

After the noncoherent decays were subtracted, the background from semileptonic decays was determined. Monte Carlo $K_L \to \pi e \nu$ events were generated and analyzed the same way as $\pi^+\pi^-$ decays except for the E/p cut. These events reproduced the main characteristics of the residual background in mass and transverse momentum and were therefore used to predict the number of background events under the coherent peak. The normalization relative to the data was taken from the mass side band and in a p_T^2 range from 0.001 (GeV/c)^2 to 0.002 (GeV/c)^2.

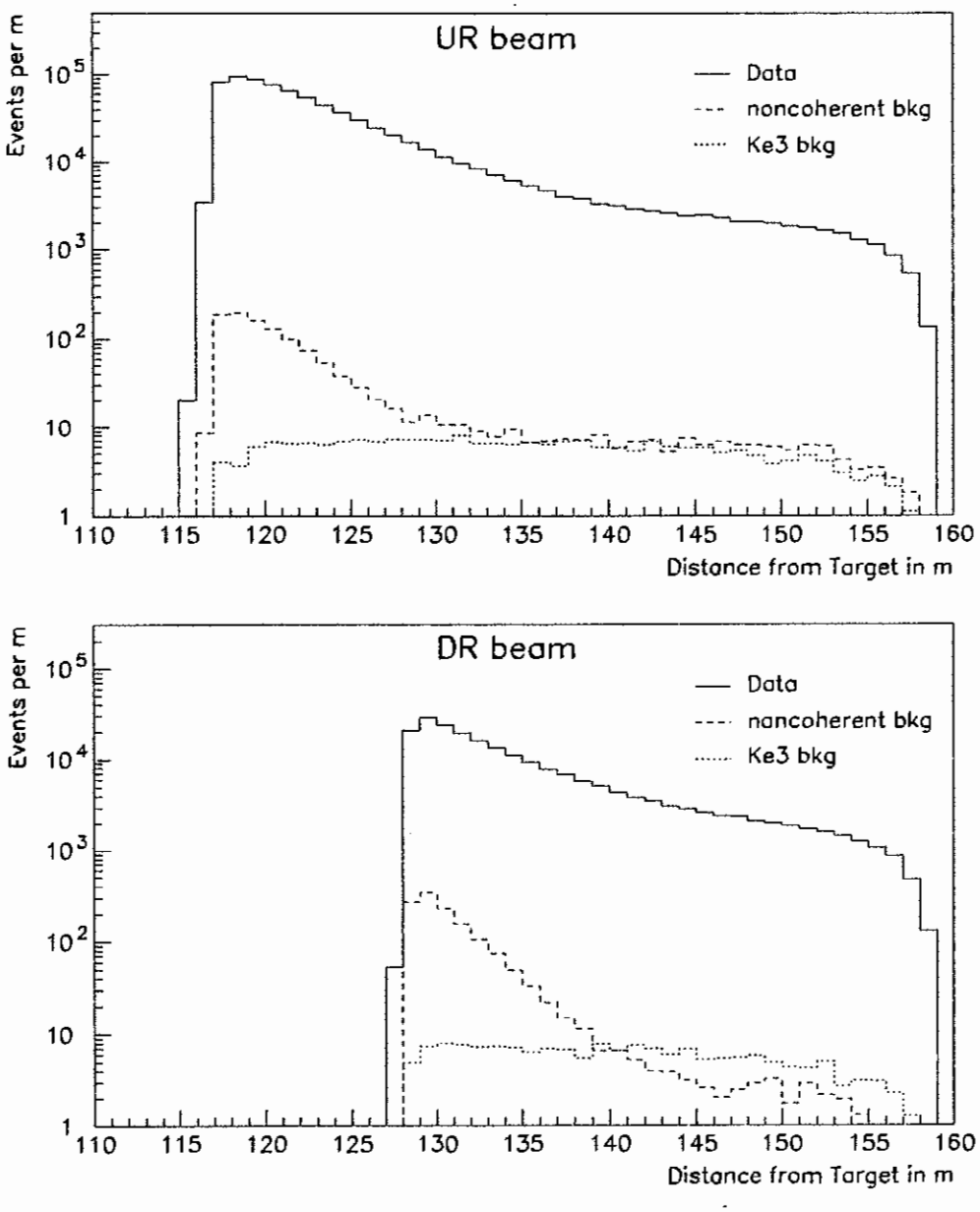

Figure 43. Decay vertex distribution for the $\pi^+\pi^-$ data, noncoherent background and background from $K_L \to \pi e \nu$ (Ke3). All distributions are for data set 2.

CHAPTER 7

The Simulation

One important step in our analysis was the correction of the data (p, z) distribution for the acceptance of the detector. A good simulation of the kaon beam and the detector response was crucial and the version of the Monte Carlo program used for this analysis utilized the detailed understanding gained in the past experiment E731. The decay modes $\pi^+\pi^-$ and $\pi^0\pi^0$ were needed to extract the result but a very powerful check of the quality of the Monte Carlo was performed by comparing the simulation of $\pi e\nu$ and $3\pi^0$ decays with the data. These K_L decay modes were independent of the regenerator simulation and the data statistics was higher than for the $\pi\pi$ modes.

This chapter discusses the important parts of the simulation: how kaon decays are generated, how the decay product interaction with the detector components were simulated and how accidental events were overlayed. At the end a comparison between data and Monte Carlo is given.

7.1 Simulation of the Kaon Decay

This section describes the simulation of the kaon decay, i.e. the generation of the kaon direction and energy, the decay vertex and the kaon scattering in the regenerators. The discussion follows the order in which these quantities were generated in the program.

7.1.1 Kaon Energy and Propagation

At the target K^0s and $\bar{K}^0$s are produced incoherently. Their momentum spectra depend on the incident proton energy and the targeting angle, i.e. the p_T of the kaon relative to the proton direction. The spectra for neutral kaons are similar to those for charged kaons which have been measured at half our proton beam energy [Malensek 81]. The ratio of the neutral kaon spectra is called the dilution factor and defined by

$$d_K = \frac{f(p) - \bar{f}(p)}{f(p) + \bar{f}(p)}. \tag{7.1}$$

with $f(p)$ and $\bar{f}(p)$ being the momentum spectra for the K^0 and $\bar{K}^0$, respectively. The CERN NA31 experiment [Carosi 90] found that

$$d_K = \frac{f^+(p) - f^-(p)}{f^+(p) + 3f^-(p)}. \tag{7.2}$$

with $f^+(p)$ and $f^-(p)$ being the charged kaon spectra. Empirically, the momentum spectrum for $\bar{K}^0$ is therefore similar to the K^- meson spectrum while the K^0 spectrum is approximated by the average of the K^+ and K^- spectra. The charged kaon spectra depend of course on the targeting angle and the incident proton energy. At the end $\Delta\Phi$ was very insensitive to d_K since the regenerators were far away from the target, i.e. the kaon beam was a pure K_L beam to a good approximation, and two parameters were floated in the fit to describe the data energy spectrum (see chapter 8).

The observed neutral kaon spectrum did not agree with this simple expectation. Based on the momentum distribution of $\pi^+\pi^-$ decays in E731 a correction (a bow of $\pm 20\%$ in our energy range) was applied to the K^0 and $\bar{K}^0$ spectra. Specific to our experiment, the targeting angles in the x and y direction were fine tuned to improve the agreement between data and Monte Carlo for $\pi^+\pi^-$ decays.

To extract our result we need to know the acceptance as a function of momentum and decay vertex, typically in 10 GeV by 2 m bins. Since the energy smearing (about 2 GeV for $\pi^0\pi^0$ decays and negligible for $\pi^+\pi^-$ decays) is much smaller than the bin size the acceptance is calculated for, events will generally be generated and reconstructed in the same energy bin. A precise simulation of the spectrum is therefore not needed for the acceptance calculation.

The simulation program starts by choosing a K^0 or $\bar{K}^0$ and the regenerator the kaon will hit (UR or DR). The relative fractions of events for the four combinations is calculated during the initialization stage by integrating the $K \to \pi\pi$ decay rate equation 7.15 over the decay vertex region, the momentum range and the targeting angle range specified. The position of the above chosen regenerator is picked randomly (upper or lower position). Then, the kaon energy and direction are chosen. Finally, the spot where the kaon is produced inside the target is chosen. The proton beam position and its width were monitored and recorded during data taking. This information and its time dependence was used to generate the kaon production point.

Next, the kaon is traced through the absorbers and the beam collimation system. The simulation includes single diffractive scattering and regeneration in the absorbers. If the kaon hits a collimator or slab the amount of material it traverses is calculated. Single diffractive scattering and absorption is simulated in this case. The scattering and absorption affect the momentum spectrum of kaons hitting the regenerators and the tails of the beam profiles. Only about 0.3% (0.4%) of the kaons have scattered far enough to miss the upstream (downstream) regenerator.

Once a kaon passes through the collimation system and reaches a regenerator its (K_S, K_L) amplitude is calculated. The amplitude at the production point is $(1,1)$ for a K^0 and $(1,-1)$ for a $\bar{K}^0$, neglecting CP violation. This amplitude is then propagated through the rest of the target, the vacuum, the absorbers, the vacuum windows, the air and the regenerator. In vacuum, the time dependence of the amplitude is given by equation 1.9. In matter this equation has an additional term due to regeneration (see equation 1.61). In the (K_S, K_L) basis the propagation is given by

$$\frac{d\,\Psi(t)}{dt} = \left\{ \begin{pmatrix} m_S - i/2\,\Gamma_S & 0 \\ 0 & m_L - i/2\,\Gamma_L \end{pmatrix} - \frac{2\pi\gamma c N}{k} \begin{pmatrix} f_{22}(0) & f_{21}(0) \\ f_{21}(0) & f_{22}(0) \end{pmatrix} \right\} \Psi(t) \quad (7.3)$$

with

$$\Psi(t) = \begin{pmatrix} K_S(t) \\ K_L(t) \end{pmatrix}, \quad (7.4)$$

$f_{22}(q^2) = (f(q^2) + \bar{f}(q^2))/2$ and $f_{21}(q^2) = (f(q^2) - \bar{f}(q^2))/2$ as defined in chapter 1.5. The factor γc originates from the variable transformation dz to $dt = dz/\gamma c$.

Thus the full kaon amplitude propagation is implemented in the simulation. The numerical values used for the scattering amplitudes in the regenerators were $f_{22}(0)/k = i16.75$ mb and

$$\frac{f_{21}(0)}{k} = 0.647\ e^{-i\,126.9^\circ} \left(\frac{p}{70\ \text{GeV}}\right)^{-0.59}\ \text{mb}. \tag{7.5}$$

f_{21} is close to the value found in our fit (see chapter 9). The value for f_{22} was calculated from total cross section measurements [Gsponer 79], its energy dependence (about 2.5% between 40 GeV and 160 GeV) is small and neglected.

7.1.2 Kaon Scattering

In chapter 5.3 the background subtraction for the neutral mode analysis was discussed. Since it was not possible to extrapolate the ring number distribution under the signal region the Monte Carlo was needed to predict the number of background events from scattered kaons. This section describes how the scattering was simulated.

Scattering in the air and vacuum window right downstream of the regenerators was negligible relative to the scattering in the regenerator itself. For UR events, scattering in the air and vacuum windows at the z position of the DR was observed in the data and therefore included in the simulation. For data set 1, the beam passed through the T+V scintillator at 141 m and scattering in the hodoscopes was simulated as well. The latter part is described in reference [Gibbons 93c].

The observed p_T^2 distributions in $\pi^+\pi^-$ decays for the downstream regenerators is shown in Fig. 2. Important characteristics of this plot is the peak at $p_T^2 = 0$ from coherently regenerated kaons, the steep exponential fall for small p_T^2 and the shallow exponential in the tail at large p_T^2. Events in the tail could be rejected by cuts on the regenerator signals (see Fig. 31) and are therefore due to inelastic interactions. The steep exponential stems from diffractively scattered kaons.

The p_T^2 distribution for inelastic events is simulated as an exponential $\exp(-a\,p_T^2)$ with the slope a being 6 $(\text{GeV/c})^{-2}$ for the DR and 4.9 $(\text{GeV/c})^{-2}$ for the UR. These numerical values and the fraction of inelastic events relative to coherent events was chosen to fit the p_T^2 distribution in $\pi^+\pi^-$ decays. The decay distribution for events with $p_T^2 > 0.15\ (\text{GeV/c})^2$,

i.e for inelastic events, was consistent with being a pure exponential with a decay time equal to the K_S life time. The Monte Carlo therefore generated a pure K_S decay distribution.

The simulation of diffractive events was more involved and differed considerably from the one used in E731. The regenerators used in E773 were shorter than the one used before which affected the p_T^2 distribution. Since the background from inelastic events was suppressed due to the active regenerators, the p_T^2 distribution for diffractive scattering could be studied easily in the data and parameterized.

As described in chapter 1.5 single diffractive scattering of a K_L in a thin regenerator is given by

$$|K_L> \rightarrow f_{22}(q^2)\,|K_L> + f_{21}(q^2)\,|K_S> . \tag{7.6}$$

with q^2 being the momentum transfer. The f_{22} term describes elastic scattering without regeneration. Its $q^2(\approx p_T^2)$ dependence can be studied with K_L decay modes or $\pi^+\pi^-$ decays many K_S life times away from the regenerators. We find that $f_{22} \propto \exp(-58\,p_T^2)$ described the $\pi^+\pi^-$ decays best for both regenerators.

The f_{21} term causes regeneration (equation 1.61). Its p_T^2 dependence was studied with $\pi^+\pi^-$ events in the DR beam close to the regenerator. An exponential $f_{21} \propto \exp(-90\,p_T^2)$ fitted the data well. The energy dependence of f_{21}/k for forward scattering is given by a power law (equation 7.5). From Regge theory we expect the power law coefficient to depend linearly on p_T^2

$$\alpha(t) = \alpha(0) + t\alpha'(0) \tag{7.7}$$

with $t \approx -p_T^2$. $\alpha(0) \approx -0.57$ is the power law coefficient which is extracted in the $\Delta\Phi$ fit (chapter 9) and $\alpha'(0)$ is the slope of the Regge trajectory in the Chew-Frautschi plot. For our regenerator material the ω is the dominant trajectory and $\alpha'(0) \approx 0.9$. The events which pass the neutral mode ring number cut have a $p_T^2 < 0.04$ (GeV/c)^2. The effect of the t dependence of α on the regeneration amplitude is therefore $(45/145)^{(0.04\text{-}0.9)} = 0.96$ over the entire energy range, i.e. negligible, and was therefore not include in the simulation. Consequently the energy spectrum for diffractive events was the same as for coherent events.

Since $|f_{22}/k| \approx 17$ mbarn $\gg |f_{21}/k| \approx 0.7$ mbarn for our regenerator at 70 GeV/c, there is a second important term contributing to the diffractively regenerated K_S amplitude: coherently regenerated K_S which subsequently scatter $K_S \rightarrow K_S$ (or $K_L \rightarrow K_L$ scattering

and subsequent coherent regeneration). The decay rate of diffractively scattered kaons downstream of the regenerator into two pions is then

$$R_{single}(p_T^2,\tau) = |(\frac{f_{21}(p_T^2)\,g(L,p)}{k} + \rho\frac{f_{22}(p_T^2)}{k})\,e^{-i\tau(m_S-i/2\Gamma_S)} + \eta\frac{f_{22}(p_T^2)}{k}\,e^{-i\tau(m_L-i/2\Gamma_L)}|^2 \tag{7.8}$$

with $\eta = \eta_{+-(00)}$ for the decay into charged (neutral) pions. $g(L,p)$ is the geometric factor in equation 1.61. For $p_T^2 = 0$ this formula reduces to

$$R_{single}(0,\tau) \propto |(x-2)\rho\,e^{-i\tau(m_S-i/2\Gamma_S)} + x\eta\,e^{-i\tau(m_L-i/2\Gamma_L)}|^2 \tag{7.9}$$

with x being the length of the regenerator in units of interaction lengths. Here equation 1.61 and the optical theorem

$$x = LN\sigma_{tot} = 4\pi\,LN\frac{\mathrm{Im}\,f_{22}}{k} \approx -i4\pi\,LN\frac{f_{22}}{k} \tag{7.10}$$

were used. L denotes the length and N is the number density of the regenerator.

In the Monte Carlo the last equation, modified by the p_T^2 dependence, was used to generate single diffractive events:

$$R_{single}(0,\tau) \propto |(x\,e^{-58p_T^2/2} - 2\,e^{-90p_T^2/2})\,\rho\,e^{-i\tau(m_S-i/2\Gamma_S)} + x\eta\,e^{-58p_T^2/2}\,e^{-i\tau(m_L-i/2\Gamma_L)}|^2 \tag{7.11}$$

From this equation one finds that a two interaction length regenerator minimizes the single diffractive scattering at $p_T^2 = 0$. This length also maximizes the K_S flux after a regenerator since $|\rho|^2 \propto x^2$ and the beam is attenuated by e^{-x}. A two interaction length regenerator was therefore chosen for the experiments E731 and E832 (KTeV).

For the upstream regenerator, which is 1.2 interaction length long, double diffractive scattering needed to be simulated. There are two terms contributing to the K_S amplitude in double diffractive scattering; coherent regeneration with elastic scattering before and after the regeneration: $f_{22}(q_1)f_{22}(q_2)\rho$; and diffractive regeneration with elastic scattering before or afterwards: $f_{21}(q_1)f_{22}(q_2)$. Here, q_1 and q_2 are the momentum transfers in the two scatterings. For the decay rate at $q_1 = q_2 = 0$ one finds

$$\begin{aligned} R_{double}(p_T^2=0,\tau) \;=\; & |(\frac{f_{21}(0)}{k}\frac{f_{22}(0)}{k}g(L,p) + \rho\frac{f_{22}(0)}{k}\frac{f_{22}(0)}{k})\,e^{-i\tau(m_S-i/2\Gamma_S)} \\ & +\eta\frac{f_{22}(0)}{k}\frac{f_{22}(0)}{k}\,e^{-i\tau(m_L-i/2\Gamma_L)}|^2 \end{aligned} \tag{7.12}$$

$$\propto \quad |(x-4)\rho\, e^{-i\tau(m_S - i/2\Gamma_S)} + x\eta\, e^{-i\tau(m_L - i/2\Gamma_L)}|^2 \qquad (7.13)$$

The p_T^2 dependence is added to the last equation as in equation 7.11:

$$R_{double}(p_T^2,\tau) \propto |(x\, e^{-29p_T^2/2} - 4\, e^{-35p_T^2/2})\,\rho\, e^{-i\tau(m_S - i/2\Gamma_S)} + x\eta\, e^{-29p_T^2/2}\, e^{-i\tau(m_L - i/2\Gamma_L)}|^2 \qquad (7.14)$$

The equations 7.11 and 7.14 determine the p_T^2 and the z distribution for diffractive events. The only other input needed to the simulation was the relative ratio of double diffractive to single diffractive events and the ratio of diffractive events to coherent events. The latter was chosen independently for the UR and DR beam to fit the number of diffractive events observed in the data. The ratio of double diffractive K_L to single diffractive K_L is given by $\frac{x}{2}\sigma_{el}/\sigma_{tot}$ with x being the length of the regenerator in units of interaction lengths and σ_{el}/σ_{tot} being the ratio of the elastic to total cross section. We find that $\sigma_{el}/\sigma_{tot} = 11\%$ fitted our data which is lower than expected.[1]

Finally, diffractive scattering off hydrogen atoms in the regenerators was also included in the simulation. The normalization relative to carbon diffractive scattering was taken from elastic cross section measurements. The slope of f_{22} was -6 $(\mathrm{GeV/c})^{-2}$ and the slope of f_{21} used in the simulation was -8 $(\mathrm{GeV/c})^{-2}$. $\Delta\Phi$ was insensitive to whether or not this background is included in the simulation.

The background simulation was most important for $K \to \pi^0\pi^0$ decays. The agreement between data and Monte Carlo was shown in a previous chapter in figures 35 and 36. Fig. 44 shows the p_T^2 distribution for $\pi^+\pi^-$ decays for data and for the simulation. The contributions from inelastic and single and double diffractive backgrounds are also plotted. The peak in the first bin from coherent events is suppressed in this plot. In the plot for the UR there is additional background in the data at $p_T^2 \approx 0.08$ $(\mathrm{GeV/c})^2$ from $K^* \to K_S\pi^0$ decays which is not included in the simulation.[2] For $p_T^2 > 0.12$ $(\mathrm{GeV/c})^2$ the background is exclusively due to inelastic events.

Due to the different length of the two regenerators and the $(x-2)$ term in the K_S

[1]The elastic carbon cross section is 25-32 mb [Schiz 80] and the total cross section is about 190 mb [Gsponer 79]. The ratio σ_{el}/σ_{tot} is therefore expected to be between 13% and 17%. The systematic effect of the level of double diffractive scattering in the simulation on $\Delta\Phi$ is however small.

[2]These events are missing in the DR beam plots because a cut on extra photons was made to reject K^* decays and this cut was more effective for the DR than for the UR.

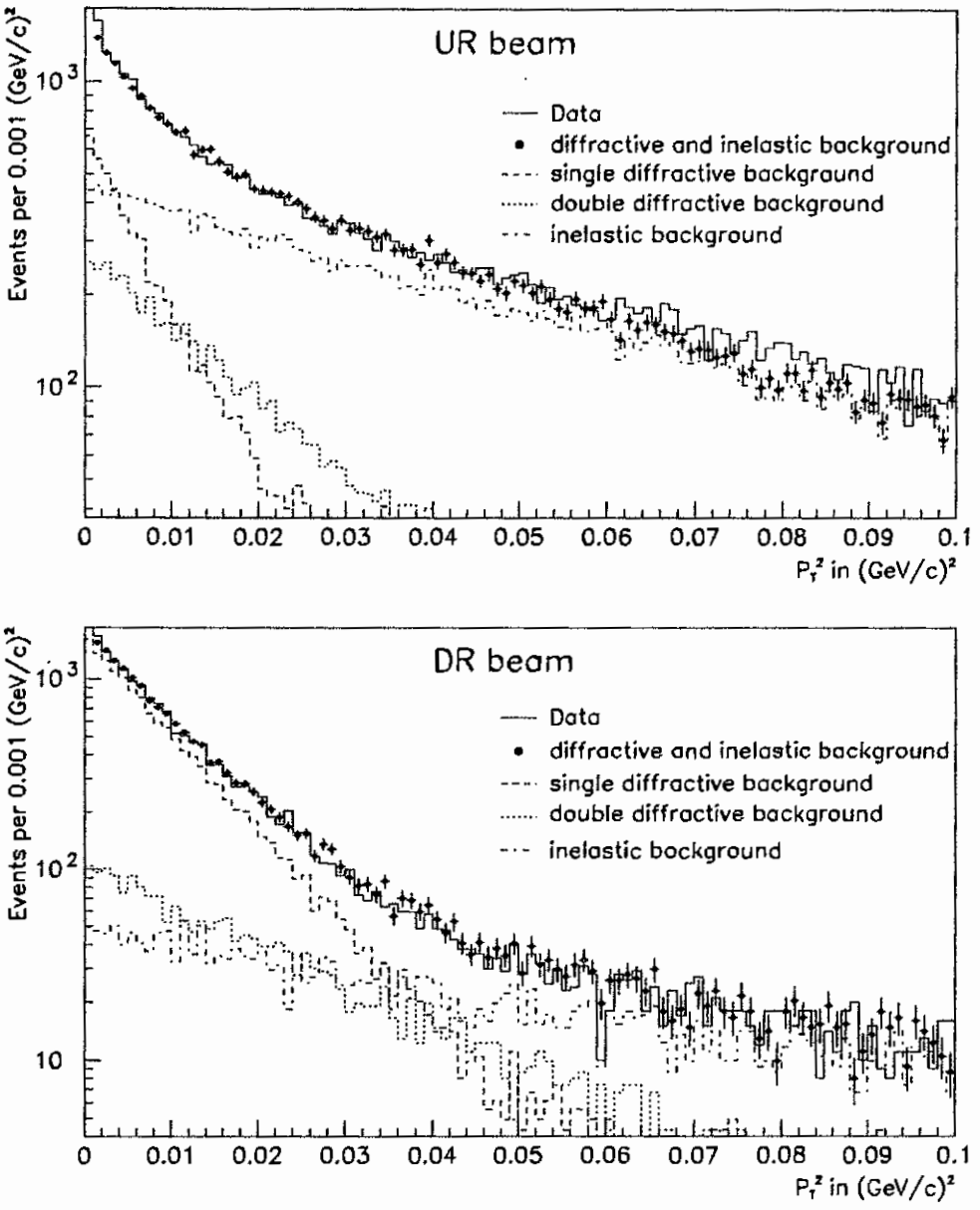

Figure 44. p_T^2 distributions of $K \to \pi^+\pi^-$ decays for data set 2 and Monte Carlo for both regenerator beams. The different contribution to the Monte Carlo from inelastic and single and double diffractive events are also plotted.

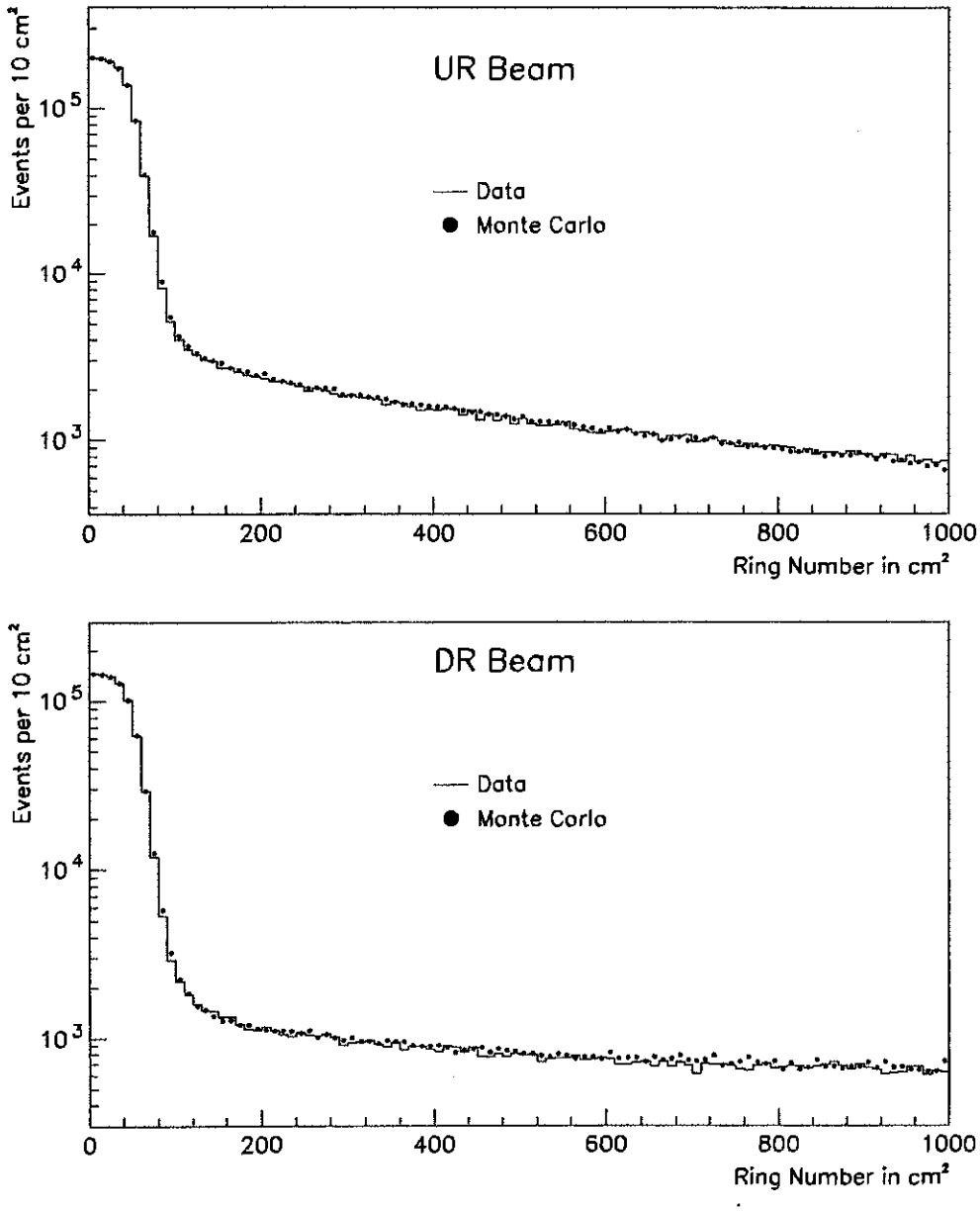

Figure 45. Ring number distributions of $K_L \to 3\pi^0$ decays for data (both data sets) and Monte Carlo for both regenerator beams.

amplitude (see equation 7.11) the level of single to double diffractive scattering changes strongly between the UR and DR. Also visible is the strong suppression of inelastic events in the DR relative to the UR. This is of course mainly due to the attenuation of the beam by the 1 K_L interaction length long shadow absorber and due to the shorter length of the DR by a factor of 3.

Fig. 45 shows the ring number distribution for data and Monte Carlo for $K_L \to 3\pi^0$. The ratio of scattered to unscattered events agree to within 4% percent between the data and the simulation. No tuning was done to simulate the level or shape of the background for this K_L decay mode which is sensitive to the f_{22} term in equation 7.11 only. This shows that the simulation, which was tuned with $\pi^+\pi^-$ decays, describes the backgrounds to the required level of accuracy. The systematic error of the background simulation will be discussed in chapter 10.2.2.

7.1.3 Kaon Decay Vertex

At this point in the program the p_T^2 was generated and the (K_S, K_L) amplitude at the beginning of the decay region was calculated. The distance from the decay point to the regenerator, z, for $2\pi^0$ decays was chosen according to

$$\begin{aligned} R(p,\tau) &= |K_S(\tau) + \eta_{00}\, K_L(\tau)|^2 \\ &= |K_S(0)|^2 e^{-\tau/\tau_S} + |\eta_{00}|^2 |K_L(0)|^2 e^{-\tau/\tau_L} + \\ &\quad |\eta_{00}||K_S(0)||K_L(0)| e^{-\tau(1/\tau_S+1/\tau_L)/2} \cos(\Delta m\tau + \Phi_{SL} - \Phi_{00}) \end{aligned} \tag{7.15}$$

with

$$\Phi_{SL} = \text{relative phase between the } K_S \text{ and } K_L \text{ amplitudes at } z = 0; \tag{7.16}$$

$$\tau = \frac{z\, m_k}{c\, p}; \tag{7.17}$$

For decays into charged pions η_{00} was replaced by η_{+-}. For $\pi^0\pi^0$ decays it was also important do generate decays upstream and inside of the regenerators. Sometimes, none of the four photons of the final state converted in the regenerator. These events were therefore accepted and could reconstruct downstream of the regenerator since the position resolution

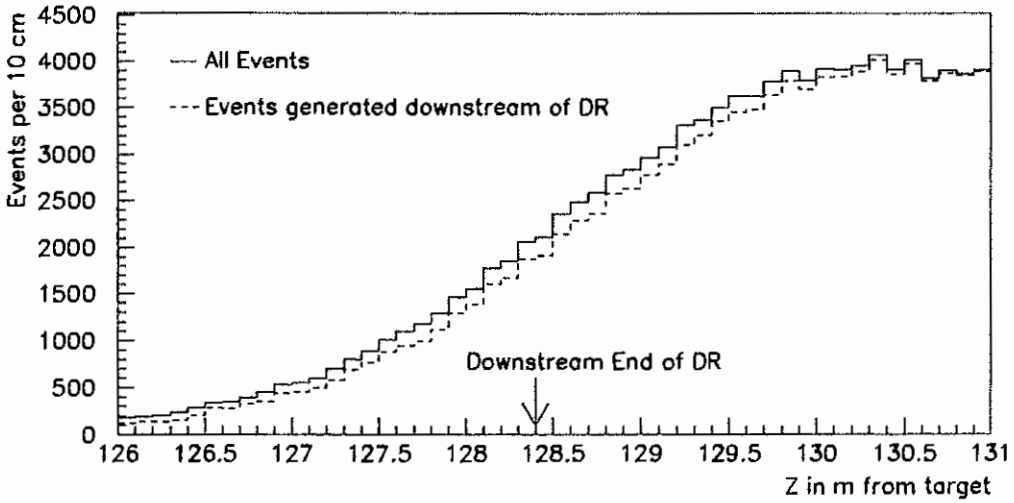

Figure 46. Reconstructed z distribution for Monte Carlo events close to the regenerator. Shown are the distributions for all decays (solid) and for decays generated downstream of the DR only (dashed).

was about 1.3 m. Fig. 46 shows the reconstructed z distribution for all Monte Carlo events close to the downstream regenerator and for the subset where the generated decay vertex is downstream of the regenerator. The difference between the two distributions is due to decays inside and upstream of the regenerator. Since the absolute energy scale of the lead glass was determined by comparing the position of the regenerator edge between data and Monte Carlo omitting the decays inside the regenerator would have shifted the edge by about 10 cm which would cause the fitted scale to shift by about 0.2%. This corresponds to a 1° change in $\Delta\Phi$. It was therefore important to include decays inside the regenerators in the simulation. Because the regenerators were active decays into charged particles inside of them were vetoed.

After the decay vertex was chosen, the decay into two neutral (or charged) pions and subsequently into photons was generated (for the $K \to \pi^0\pi^0$) according to phase space.

The decay products were then traced through the detector. If a particle left the fiducial

volume the tracing was stopped. In the following sections the response of the important detector elements to charged particles and photons is described.

7.2 Spectrometer Simulation

The spectrometer simulation consists of the simulation of the drift chamber hits and their TDC values and the bend of charged tracks by the magnet. It was sufficient to simulate the drift chamber response and the momentum kick on a rather simple level: the chamber resolution was approximated by a gaussian distribution for each plane and the tracks bend at the z position of the bend plane of the magnet according to the integrated field.

The track positions before and after the magnet were calculated and smeared according to the resolution. Wires closest to the track were found using the correct chamber offsets and rotations. The TDC value that corresponded to the distance between the track and the wire plane was looked up using the drift time - distance relation. Finally, the rate of wire inefficiencies as seen in the data was simulated. The TDC information was then written out and the event was analyzed like a real data event.

For a more detailed description see [Briere 95b].

7.3 Calorimeter Simulation

The calorimeter simulation was most important for the neutral mode analysis. The goal was to simulate the response to photons at the 0.1% level. To achieve this, the simulation was primarily tuned with electrons from $\pi e \nu$ decays.

Only electromagnetic showers are simulated in the Monte Carlo. For charged particles other than electrons 700 MeV of energy is deposited in the block the particle hit. It was found not to be necessary to simulate hadronic showers.

If an electron or photon hits the lead glass in the simulation it deposits its energy in the array. The energy of the shower and the shape of the shower, i.e. the distribution of the shower energy in the blocks of the 5×5 array around the block hit by the electron or photon, were simulated. The cluster shape is taken from a library, which consisted of 29500

electron shower profiles from a special low beam intensity data run taken without a readout threshold and from an EGS simulation for energies below 4 GeV. The profile was selected depending on the position where the particle hit the block and the shower energy.

The implanted energy for an electron shower depended on the light absorption coefficient α of the central block, the electron energy and the photon statistics of the central block. The latter is defined as the number of photoelectrons for a 1 GeV shower and was determined in a previous experiment for every block [Patterson 90]. On average there were 536 photoelectrons per GeV.

Using the generated EGS electron showers mentioned in chapter 4, the fraction x of the produced Çerenkov light reaching the end of the block was calculated as a function of energy, effective absorption α and block length $(L - t_0)$.[3] This distribution $f(x)$ for all showers was fitted to the sum of a gaussian, a low side and a high side tail (see Fig. 47 for examples and reference [Gibbons 93c] for more details):

$$f(x) = \frac{A}{\sqrt{2\pi\sigma^2}} e^{\frac{(x-\mu)^2}{2\sigma^2}} + h(x) + l(x) \tag{7.18}$$

The functional form of the high side tail was

$$h(x) = \begin{cases} 0 & \text{for } x \leq x_0 \\ a(x - x_0)\, e^{-b(x-x_0)} & \text{for } x > x_0 \end{cases} \tag{7.19}$$

with a, b and x_0 being determined by the fit. The low side tail $l(x)$ had the same functional form except $x - x_0$ was replace by $x_0 - x$. The tails in the lead glass response were due to the finite length and the absorption of the blocks. For example, if a shower develops deeper into the block the path length of the light is shorter and, for high α, less light is absorbed. This explains the increase of the high side tail with increasing α.

Once the value of the nine fitted parameters (for the gaussian and the tails) were known for every energy, absorption and block length bin, its dependence on α and $L - t_0$ was smoothened for every energy bin and the dependence on the energy was interpolated logarithmically. The light output for an electron in the Monte Carlo was then chosen according to the distribution given by equation 7.18 with the smoothened parameters. Fig. 48 shows the fitted gaussian mean and the gaussian width for 2 GeV and 22.63 GeV.

[3] The dependence on the block length was needed for the simulation of photon showers, $L - t_0$ is the reduced block length for a photon that converts at depth t_0. $t_0 = 0$ for electrons.

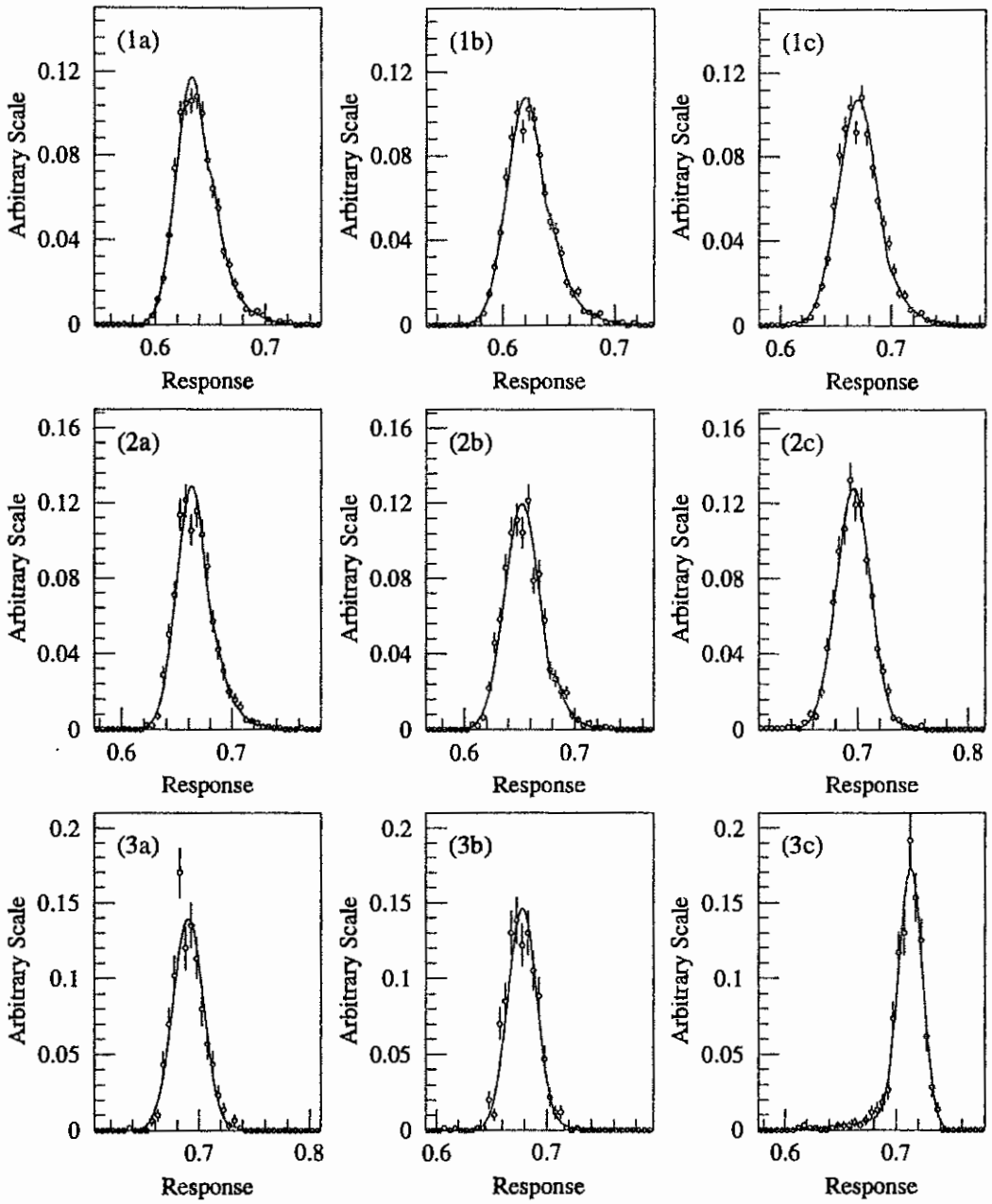

Figure 47. Fractional light output for EGS electron clusters for different energies, absorptions α and block length L. Rows 1, 2 and 3 correspond to 2, 8 and 32 GeV electrons, respectively. For column (a) α = 3.4% and L = 18.7 X_0, for column (b) α = 4% and L = 17.2 X_0 and for column (c) α = 3.8% and L = 15.7 X_0. The curve overlayed on each plot is the fit described in the text. The plots are taken from reference [Gibbons 93c].

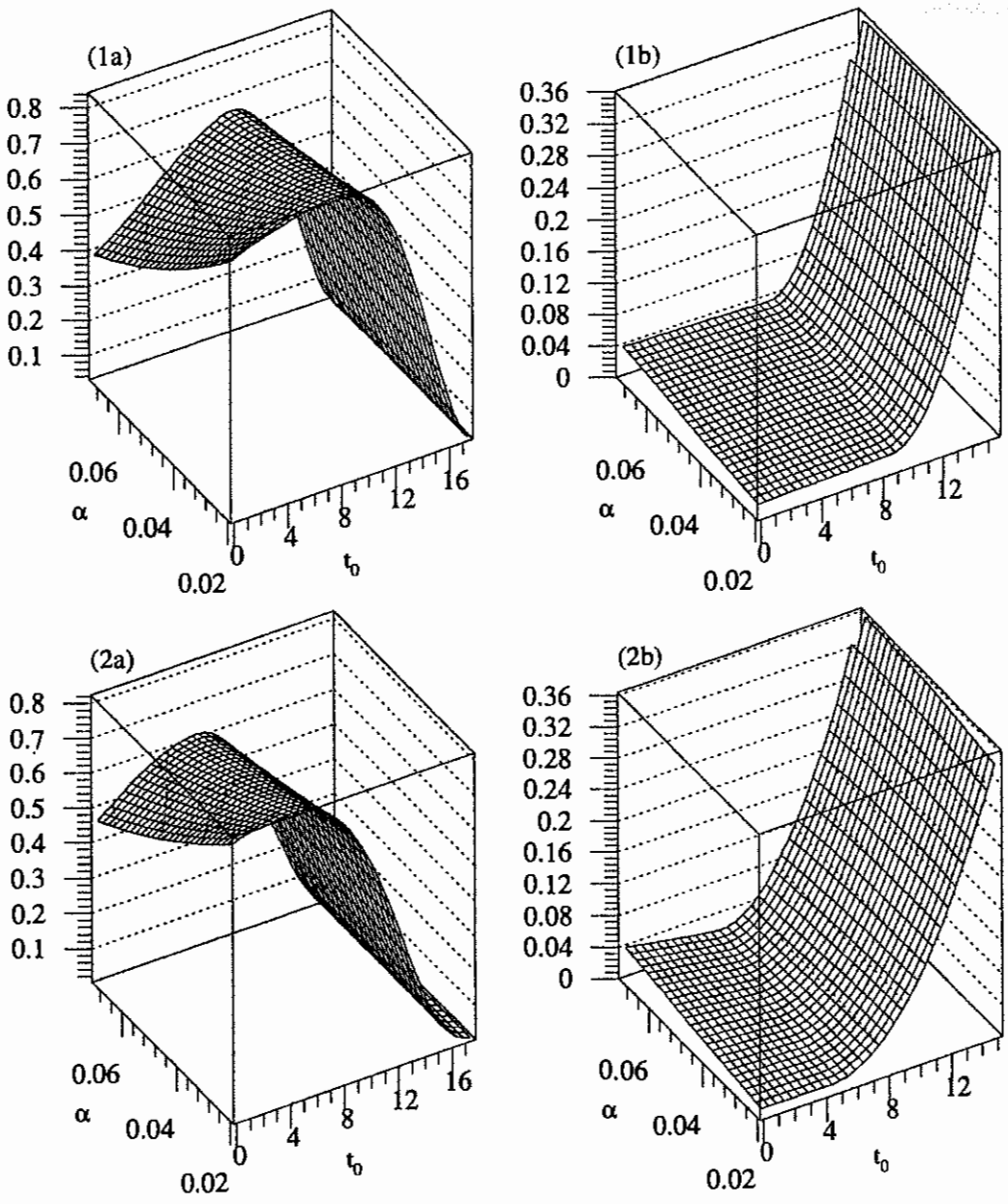

Figure 48. Gaussian mean (column a) and width (column b) of the response function defined in the text as a function of the absorption α (in units of X_0^{-1}) and conversion depth t_0 (in units of X_0). Rows 1 and 2 correspond to energies of 2 GeV and 22.63 GeV, respectively. The plots are taken from reference [Gibbons 93c].

This procedure worked from first principles and it should therefore not be surprising that the comparison between data and Monte Carlo was good, however not to the required 0.1% level. Assumptions like the uniformity of the radiation damage within a block were too simple and a bias in the calibration procedure (see chapter 4 and Fig. 20) caused the structure in the E/p versus p distribution at 20 GeV. The simulation was therefore adjusted to agree with the electron data. Some tuning was already done for E731, but because of the higher rate environment, the radiation damage in E773 was more severe and the adjustments were redone.

The tuning was done in 14 bins of α and 4 bins of energy. Fig. 49 shows the E/p distribution for data and Monte Carlo for some of these bins. The agreement after the adjustment is quite good, which of course is not surprising. Fig. 50 shows the mean and RMS(root mean square) of the E/p distribution for all blocks for data and Monte Carlo and Fig. 51 shows the same distributions broken up into three bins of α. The average agreement of the shower simulation for electrons between data and Monte Carlo is good at the 0.1% level.

Photon showers were simply the sum of two electron showers after the photon converted according to equation 5.4. Additional fine tuning was needed to compensate for the electron - photon difference not reproduced by the Monte Carlo. The regenerator edge matching was mentioned in section 5.5. It compensates for nonlinearities in the energy reconstruction. A second adjustment was used in the simulation to change the resolution of photon clusters. The absorption coefficient α of the glass block the photon hits was altered to match the average resolution between the simulation and the data to $\alpha \cdot (1 + 0.011 \cdot t_0)$, where t_0 is the conversion depth of the photon. Fig. 52 shows the best pairing χ^2 for $\pi^0\pi^0$ decays in the two regenerator beams. The Monte Carlo resolution for the UR beam is slightly better than for the data while the DR resolution is matched well. For low kaon energies the resolution in the data is slightly better, while the mean χ^2 is slightly better for the Monte Carlo at higher energies.

After the discussed steps of choosing the fractional light output, the smearing and the cluster shape, the energy for each block was digitized using the gains measured in the calibration. The ADC counts were then written out. In the analysis the Monte Carlo cluster

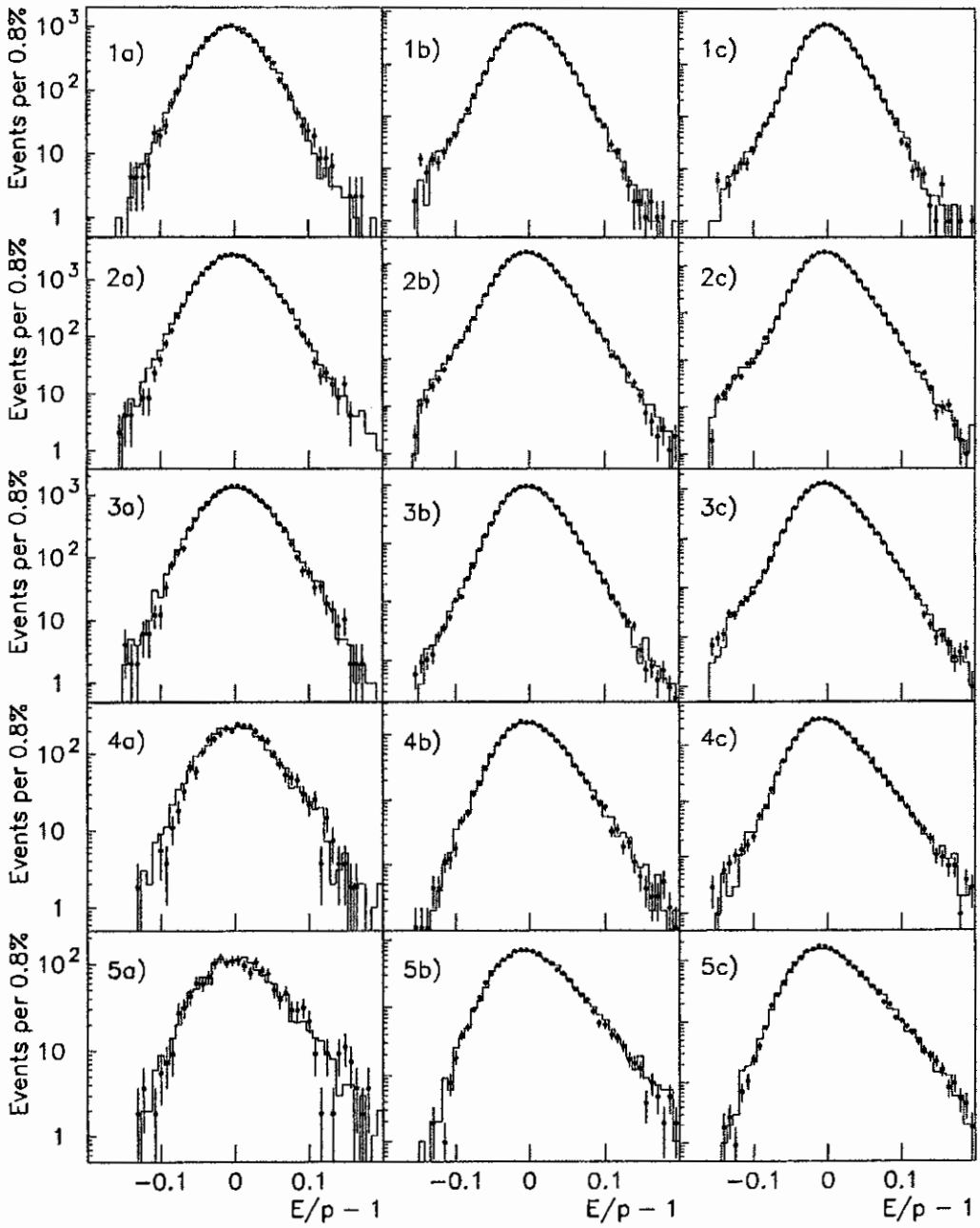

Figure 49. E/p distributions for data (histogram) and MC (dots). Shown are the overlays for energy bins 2-6 GeV (column a), 6-12 GeV (column b) and 12-20 GeV (column c). Row 1 includes blocks with absorption coefficient α from 2.8% to 3.1%. For row 2 the range is 3.5%-3.8%, row 3 4.2%-4.5%, row 4 4.8%-5.1% and for row 5 the α range was 5.5%-6.0%.

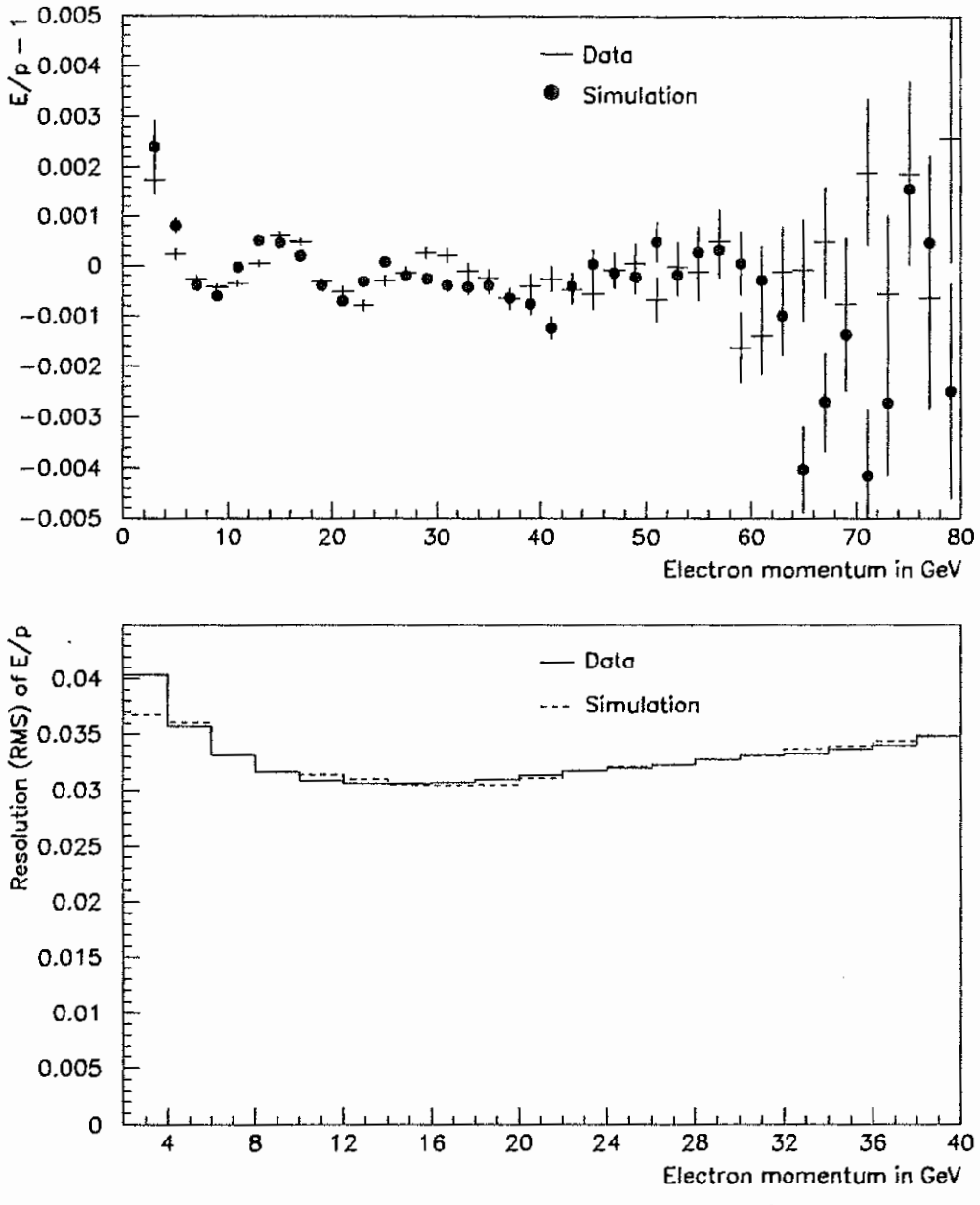

Figure 50. Mean and RMS of E/p distribution versus p for all electrons. The data are the histogram and the simulation are the dots.

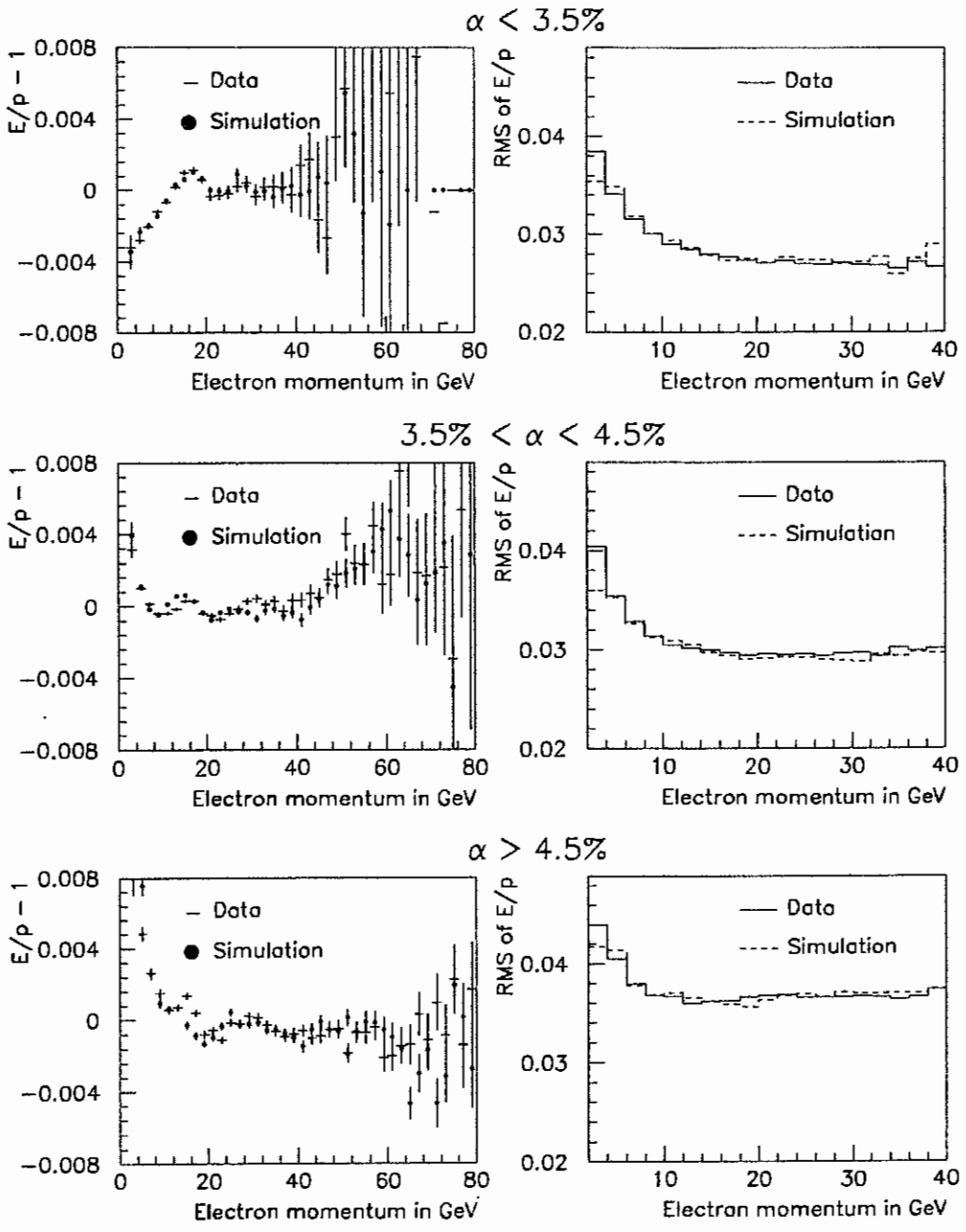

Figure 51. Mean and RMS of E/p distribution versus p for 3 α bins. Upper two plots are for blocks with $\alpha < 3.5\% X_0^{-1}$, the middle two plots are for $3.5\% X_0^{-1} < \alpha < 4.5\% X_0^{-1}$ and the lower two plot are for blocks with $\alpha > 4.5\% X_0^{-1}$.

energies were calculated and corrected the same way data clusters were reconstructed. Only the correction for the temperature shifts in the glass house (see section 5.1) was not applied.

As we will see in chapter 10.2.1 the simulation of the lead glass response will be the dominate systematic error for our $\Delta\Phi$ measurement.

7.4 Simulation of other Detector Elements

Photons that did not hit the lead glass could hit a photon veto or escape through a 'hole', i.e. hit a non instrumented part of the detector. In case a photon or electron hits a veto its energy deposition was simulated. The gains and resolutions for each of the vetoes were determined from the data. Because of the decays inside and upstream of the regenerators, photon conversions in the scintillators needed to be simulated. Conversions were also simulated for all the material in the beamline (vacuum windows, air, drift chambers and the trigger hodoscopes).

For charged tracks, multiple scattering in the above mentioned materials was simulated as well as bremsstrahlung for electrons. If a track hits a scintillator from the trigger hodoscope or photon veto the corresponding latch bit for this counter is set. This latch was then used in the trigger simulation. For the trigger hodoscope the positions and separations between the different counters was measured with data and included in the simulation. Muons from pion decays are traced through the muon filter. Scattering in the filter is approximated.

The trigger simulation was done for almost all level 1 and level 2 coincidences or vetoes. Exceptions were the hadron veto and the total energy sum of the lead glass. For all lead glass blocks above the hardware cluster finder threshold a bit was saved and the HCF algorithm was used to count the number of hardware clusters. Because the minimal energy cut on the cluster energy of 2.2 GeV was well above the HCF threshold of 1 GeV the trigger simulation was not crucial for the neutral mode analysis. For charged mode, the trigger simulation affected the acceptance since the second level trigger was sensitive to details in the track illumination.

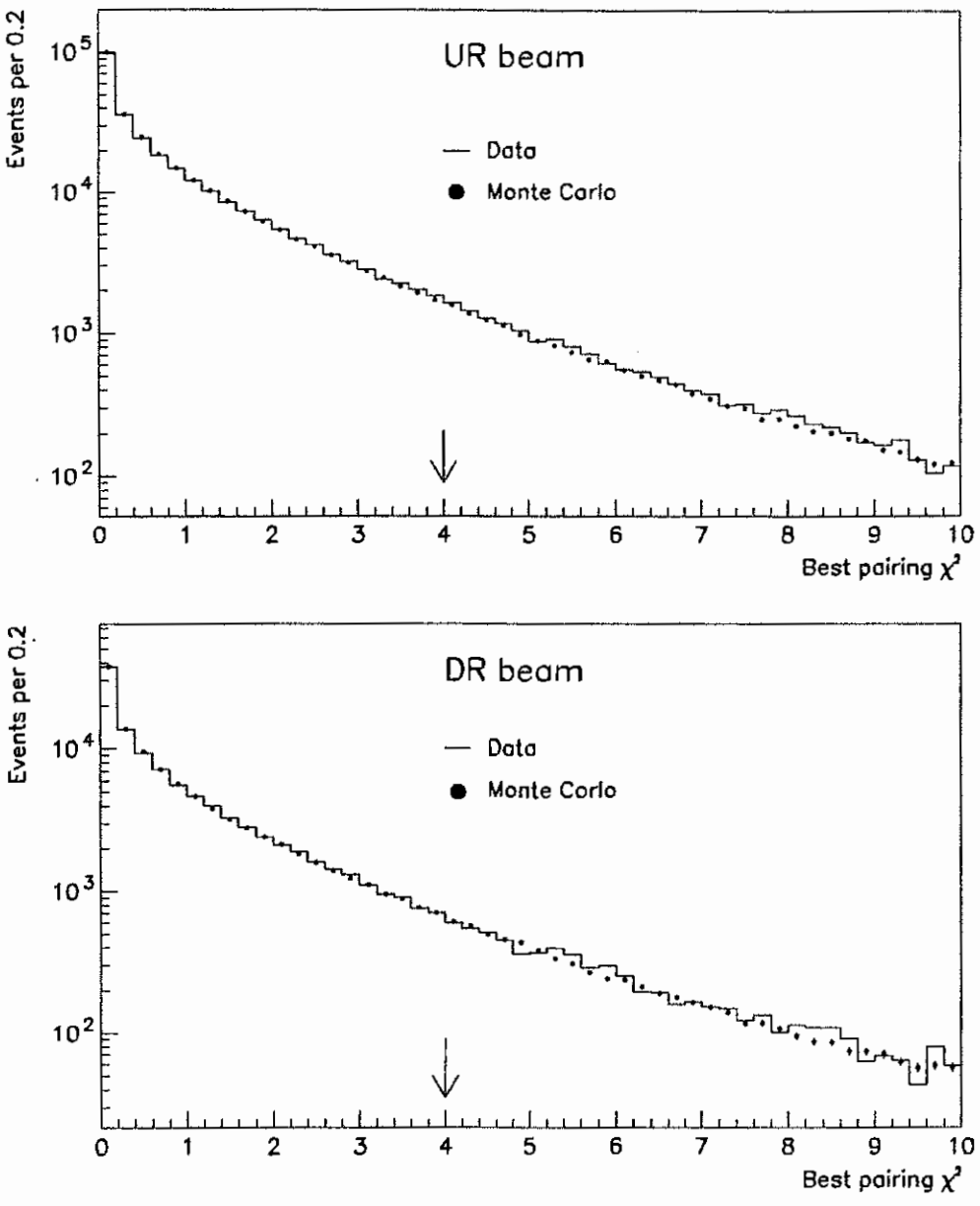

Figure 52. Pairing χ^2 of $\pi^0\pi^0$ decays for data and Monte Carlo. Shown are the overlay for the upstream and the downstream regenerator beams. The analysis cut is at 4.

7.5 Accidental Overlays

During data taking random snap shots of the detector, called accidental events, were written to tape as explained in chapter 2.9.4. To include detector activity not related to kaon decays in the simulation, the accidental events were overlayed with Monte Carlo events. The acceptance changed when overlays were included and this was especially important for the neutral mode. This section describes how the overlays were done and how well the detector activity not related to the kaon decay was simulated with this procedure.

The data taking is divided into runs of up to eight hours of beam time. As mentioned earlier, the performance of the detector changed during data taking. The Monte Carlo events were therefore generated proportional to the number of observed data events per run and accidental events from the same run number were overlayed. For the final $\pi^0\pi^0$ Monte Carlo sample with about 11 times the data statistics, every accidental event was used about 5 times for overlays.

After the kaon decay generation, particles tracing through the detector and the drift chamber and lead glass simulation, an accidental event was overlayed. To overlay discriminator outputs the logical ORs were taken. For the drift chamber, additional hits from the accidental event were written out and in case one wire had a hit in the accidental event and in the Monte Carlo event, the earlier hit was written out. For the lead glass the energies were added and then the readout threshold applied. The hardware cluster finder hits were ORed. The trigger was checked after the overlay.

With accidental hits in the drift chambers and hodoscopes, more events could pass the charge mode trigger. As explained in chapter 6.2, the analysis required however that the hits in the chambers and hodoscopes from the two charged tracks alone satisfied the trigger. This ensured that the charged mode analysis was very insensitive to the overlays. Whether accidental events were overlayed or not for the acceptance calculation did not affect the fitted value of Φ_{+-} (see [Briere 95b]). Because of CPU time constraints the final Monte Carlo sample used for the charged mode acceptance determination did not include accidental overlays.

For the lead glass the affect of accidental overlays was more important. Additional

energy from accidental events shifted the reconstructed decay vertex upstream and the resolution degraded. Accidental activity also affected cuts like the fusion cuts as discussed in chapter 5.2.

An important question is therefore, how well is the accidental activity simulated by our overlay technique? For this study $\pi^0\pi^0$ events are well suited because these events contain only electromagnetic clusters (hadronic clusters are not simulated). Upstream regenerator events with a decay vertex 2.5 m away from the regenerators and upstream of 136 m were selected to ensure that the four lead glass clusters came from a $\pi^0\pi^0$ decay.

The numbers of B and C bank counters fired are not expected to match because of the backsplash from lead glass showers as discussed in chapter 5.1. Once this effect is taken into account the average number of fired latches agree. Fig. 53 shows the number of hits in the drift chambers per event and, for hit pairs, the sum of the two drift distances (SOD). For the SOD distribution almost all pairs are due to late hits, i.e. the SOD is greater than zero. This is the case for data and Monte Carlo. The distribution of the number of drift chamber hits are very similar.

To study accidental activity in the lead glass the energy in blocks outside the 5×5 arrays around the four clusters was plotted. Fig. 54 shows the energy deposited in blocks next to the beam holes (called pipe blocks). The upper plot shows this distribution for all events. There is a big discrepancy between the data and the Monte Carlo at small energies. For the lower plot events where the center block of a photon cluster is a pipe block (pipe block cluster) are discarded. The agreement is much better. The data distribution at small energies has changed for the subset while the shape of the Monte Carlo distribution is the same in both plots. This shows that pipe block clusters often deposit a small amount of energy into other blocks around the hole.[4] The discrepancy in the upper plot is therefore due to activity from a photon shower rather than from 'accidental activity'. The cluster energy that leaks into the beam holes is not simulated in the Monte Carlo.

Fig. 55 shows the energy deposition in all blocks outside the 5×5 array of the clusters and the number of blocks per event with energies above 100 MeV. Events with a pipe block cluster are excluded. The agreement between data and Monte Carlo is good, especially

[4]This was verified by scanning events with pipe block clusters.

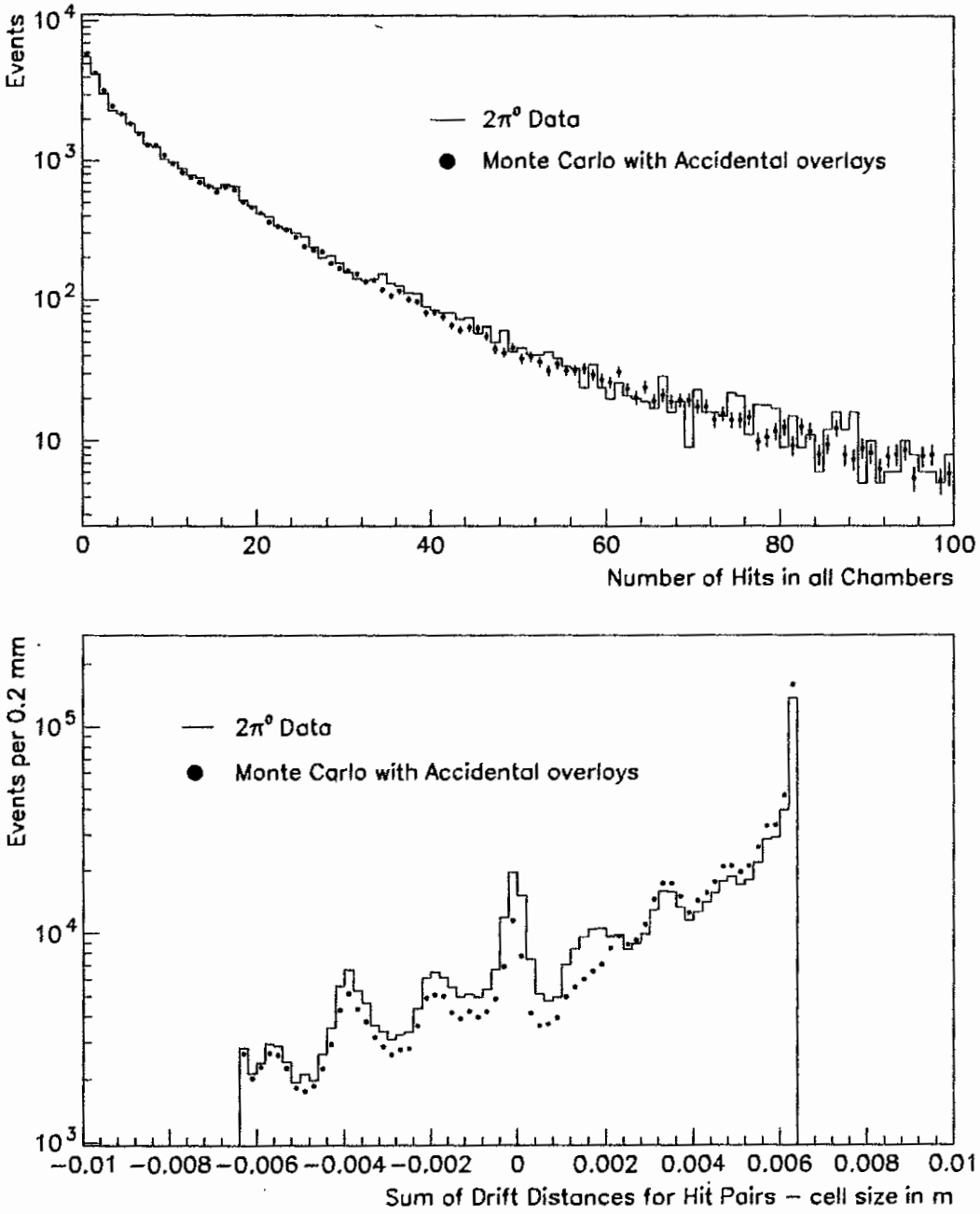

Figure 53. Number of drift chamber hits and the sum of drift distances of hit pairs for data and Monte Carlo $\pi^0\pi^0$ decays.

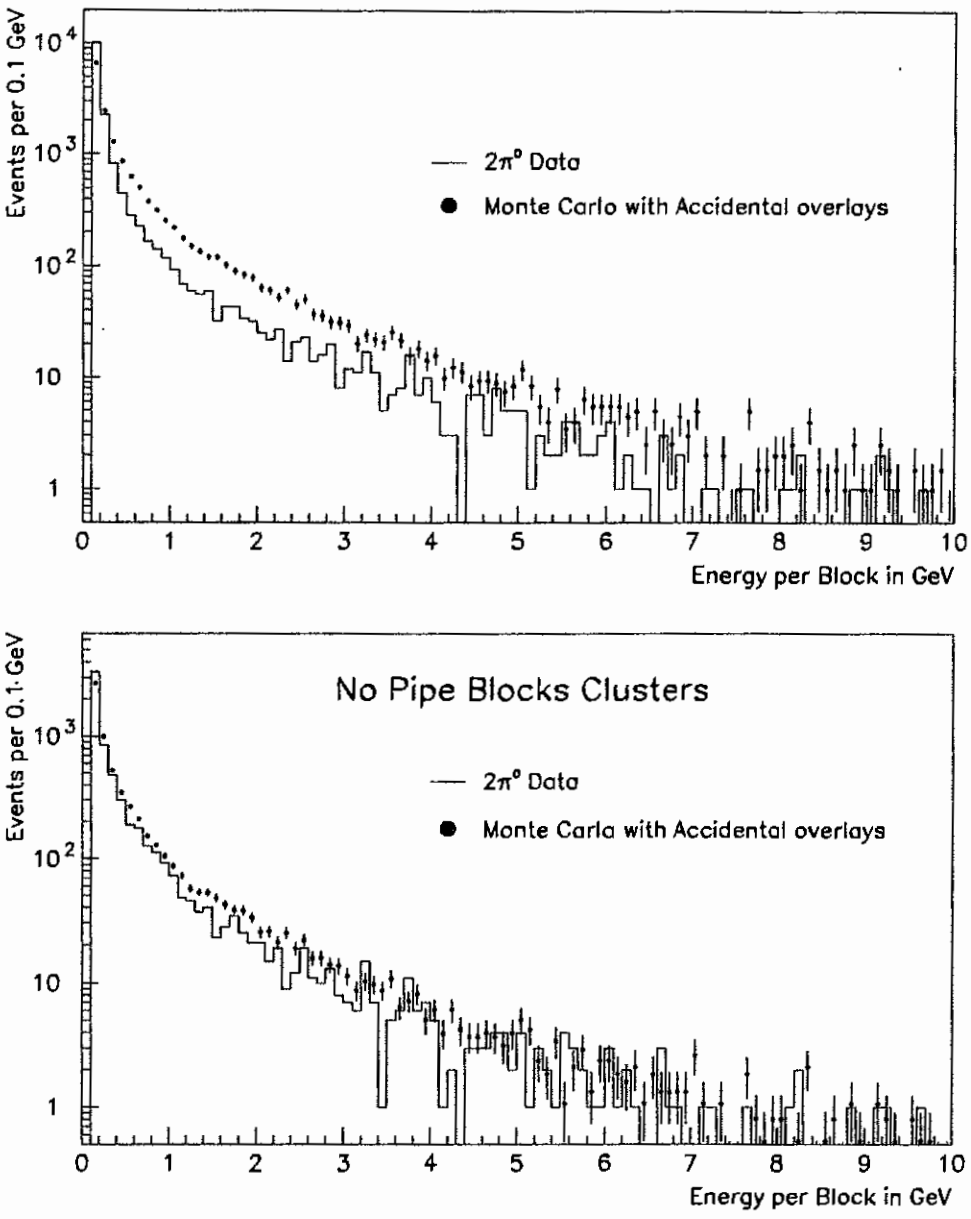

Figure 54. Lead glass block energy for pipe blocks outside the 5×5 array of the photon clusters. The upper plot shows the distribution for all events. The lower plot includes only events where the center block of all photon clusters are at least one block away from the beam holes.

considering the fact that a Monte Carlo without accidental overlay would not simulate any of these activities. Finally, Fig. 56 shows the reconstructed π^0 mass for $K_L \to \pi^+\pi^-\pi^0$ data and Monte Carlo events. The upper plot shows the overlay for Monte Carlo events without accidental overlays and the lower plot shows the overlay for Monte Carlo events with accidental overlays. Clearly, the accidental overlays are needed to describe the data and the overlays reproduces the data very well. The accidental activity in the lead glass was therefore correctly simulated in the Monte Carlo.

7.6 Neutral Mode Data - Monte Carlo Comparison

This section discusses the agreement between data and Monte Carlo for coherent $\pi^0\pi^0$ events. In previous chapters the background subtraction, the lead glass simulation and the accidental overlay procedure were described and some comparisons between data and Monte Carlo were shown. This section focuses on overlays which prove that the acceptance for $\pi^0\pi^0$ events is well simulated. All data distributions are background subtracted. Data sets 1 and 2 have been added in these plots and the Monte Carlo statistics was eleven times the data statistics.

The parameters used in the Monte Carlo generation like the power law coefficient or the kaon energy spectrum differed slightly from the fit results (see chapter 9). The Monte Carlo events are therefore reweighted by the ratio of the kaon (p, z) distributions for the two different parameter sets.

Fig. 57 shows the photon illumination for upstream regenerator events at the location of the downstream regenerator. Because of the table the DR was mounted on was a limiting aperture, cuts on the photon illumination were made which cause the sharp edges in the y view illumination. Fig. 58 shows the distribution of photon positions from the downstream regenerator beam at the vacuum window at $z = 159$ m. Both sets of plots show good agreement between the data and the simulation.

Fig. 59 shows the minimal distance between the four photon clusters for the two beams and the two regenerators. For separations smaller than 24 cm the 5×5 array around the

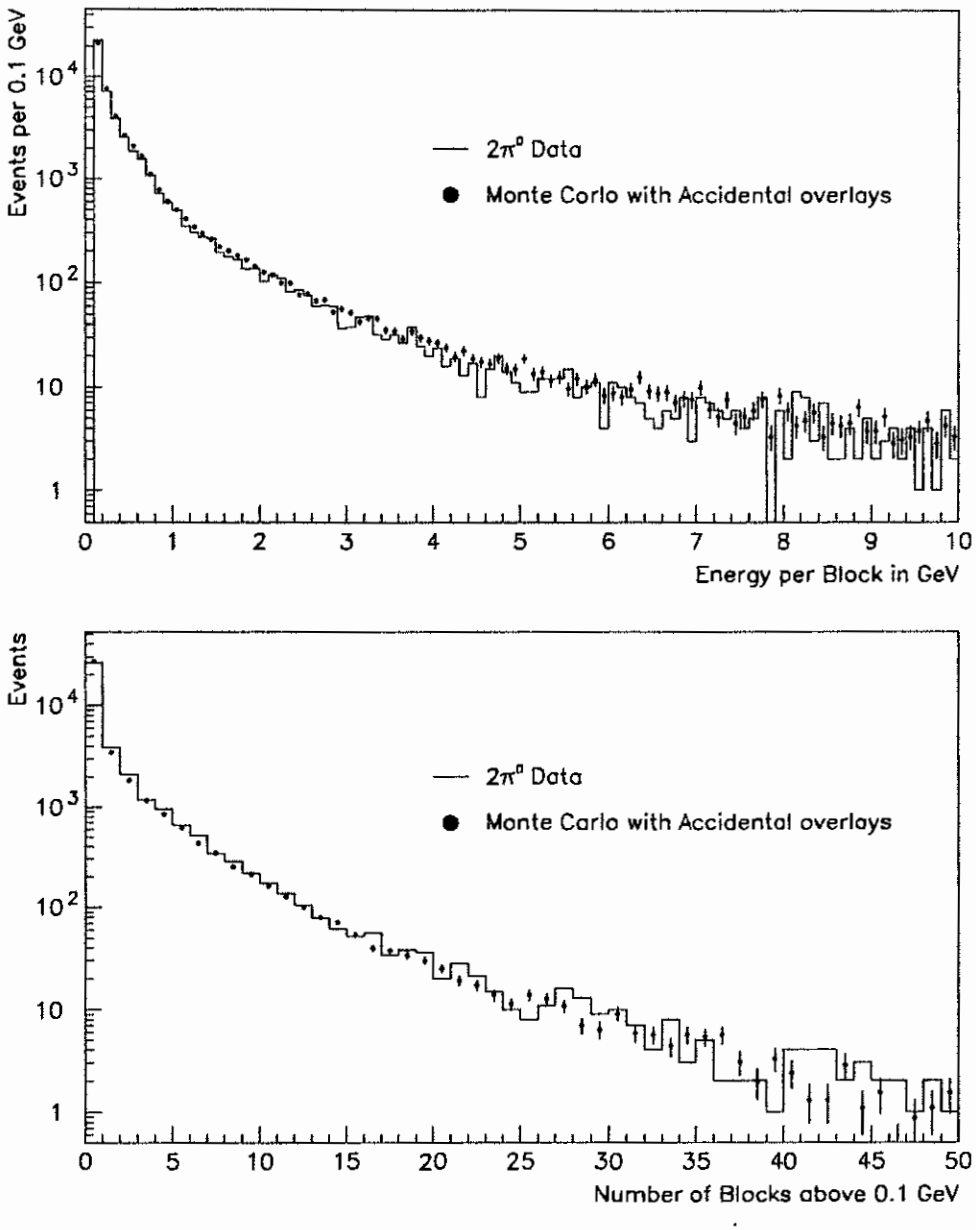

Figure 55. Lead glass block energy outside the 5 x 5 array of the photon clusters and the number of blocks with an energy above 100 MeV per event.

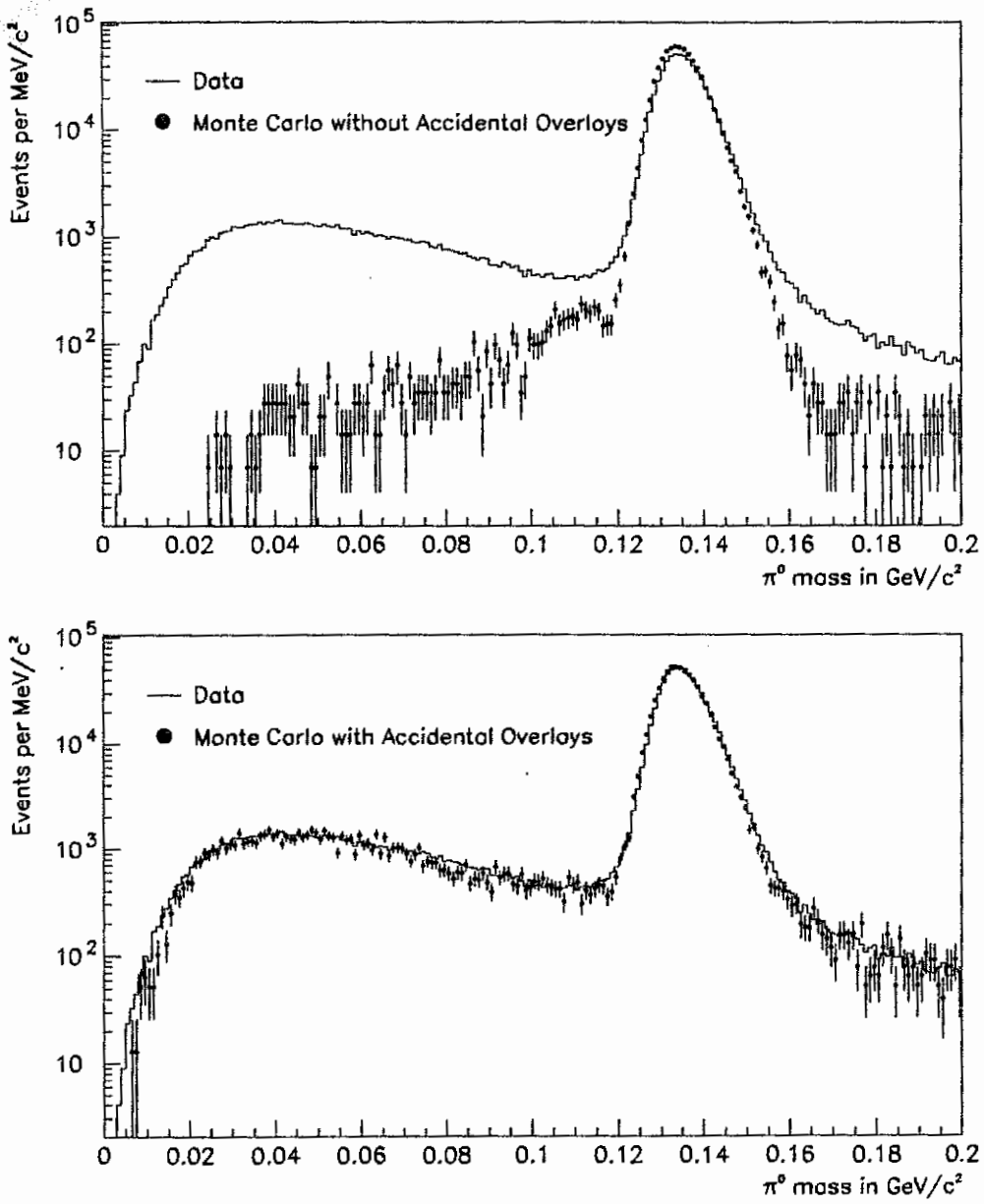

Figure 56. π^0 mass in $K_L \to \pi^+\pi^-\pi^0$ data and Monte Carlo events. The upper plot shows the Monte Carlo without overlays and the lower plot shows the overlay for Monte Carlo with overlays.

clusters overlap which affects the simulation of cuts on the cluster shape. The Monte Carlo reproduces the data.

Another test of the lead glass simulation and possible cut biases are the distributions for the minimal and maximal cluster energy in an event. Fig. 60 and Fig. 61 show these two distributions. The data and Monte Carlo distributions agree well.

Fig. 62 shows the kaon energy overlays. For the UR the agreement is very good while the ratio for the DR overlay has a 2σ slope of 3.5% over the entire energy range. Since two parameters are allowed to float in the fit to reproduce the data energy spectrum (see chapter 8) no systematic error was assigned to this disagreement.

Fig. 63 and Fig. 64 show the decay distribution for the upstream and downstream regenerator beam. The decay region used in the fit is from 120 m (130 m) to 152 m for the UR (DR) beam. The fitted slopes to the ratios of data over Monte Carlo are consistent with zero. Fig. 65 to 68 show the decay distributions for both beams in different energy intervals. The agreement is quite acceptable.

In the beginning of this chapter we argued that the K_L decay modes were powerful checks of our understanding of the acceptance. Fig. 69 shows the decay distributions for $K_L \to 3\pi^0$ decays for both beams. The ratios of the data over the Monte Carlo distribution show that the acceptance is understood at the 1% level. There is a 3σ slope in the ratio for the upstream regenerator. However the slope of 0.04% per meter is rather small and this slope will be used to estimate the systematic effect of the acceptance on the $\Delta\Phi$ measurement.

7.7 Charged Mode Data - Monte Carlo Comparison

The agreement between the simulation and the data for charged mode decays is discussed in this section. Here the most important overlays will be presented. A more detailed presentation is given in [Briere 95b]. For charged mode the plots for data sets 1 and 2 are separate because of the restricted decay region for the first data set.

In the beginning of this chapter the collimation system was mentioned. Fig. 70 shows the profile of the kaon beam at the position of the lead glass. The size of the beam is the same for data and Monte Carlo and only the y projections show a mismatch at one edge.

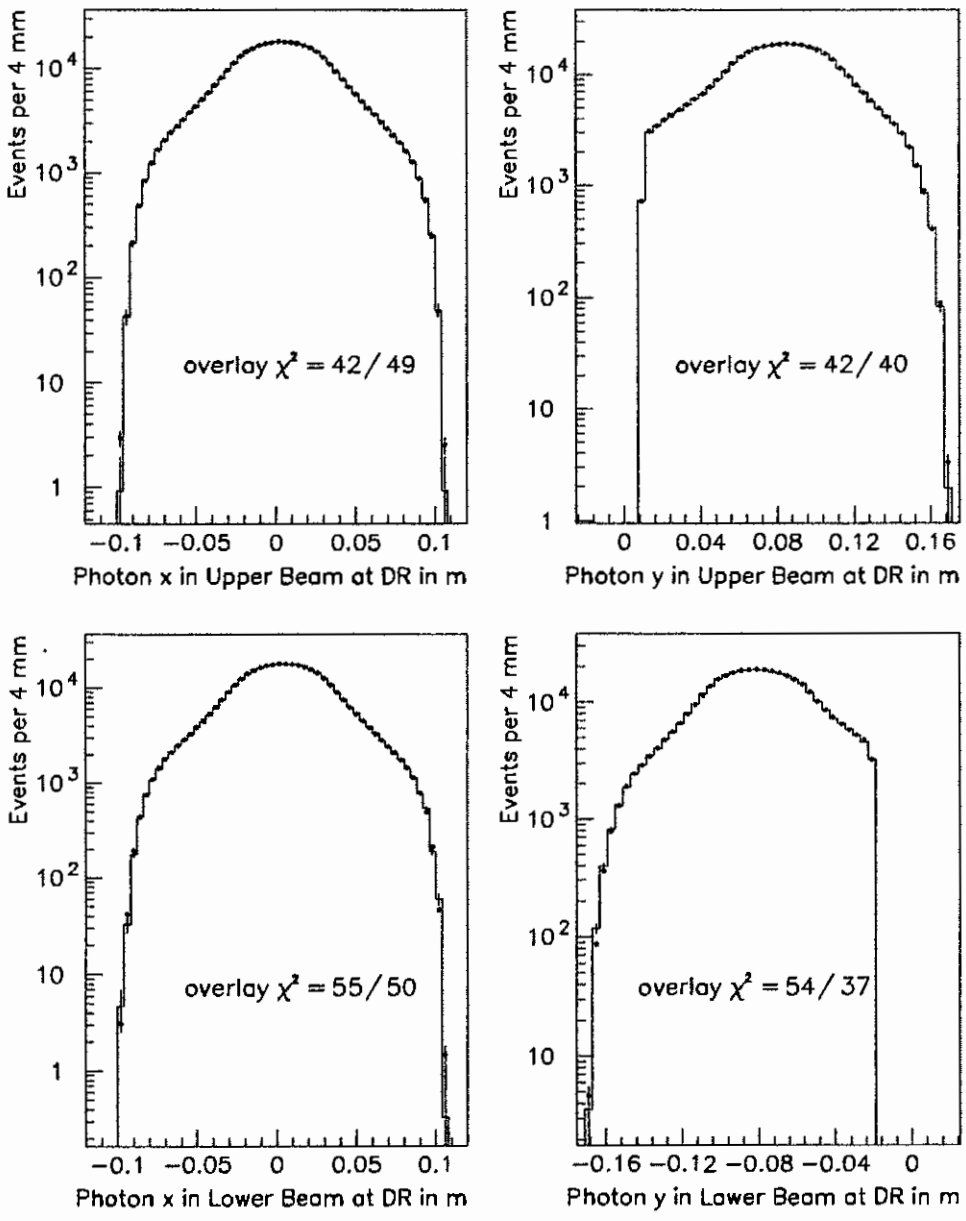

Figure 57. Photon illumination from upstream regenerator $\pi^0\pi^0$ events at the position of the downstream regenerator.

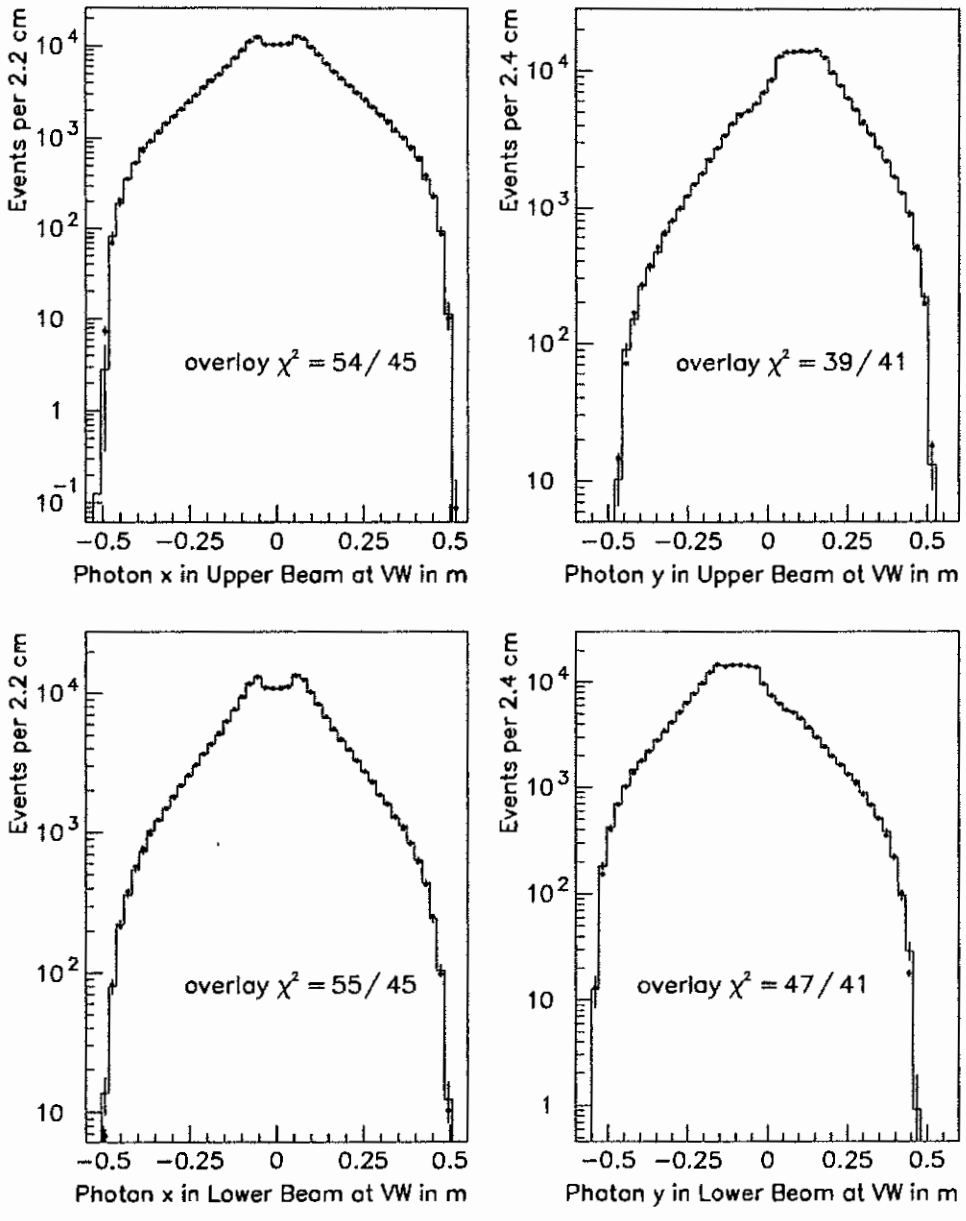

Figure 58. Photon illumination from downstream regenerator $\pi^0\pi^0$ events at the position of the vacuum window at $z = 159$ m.

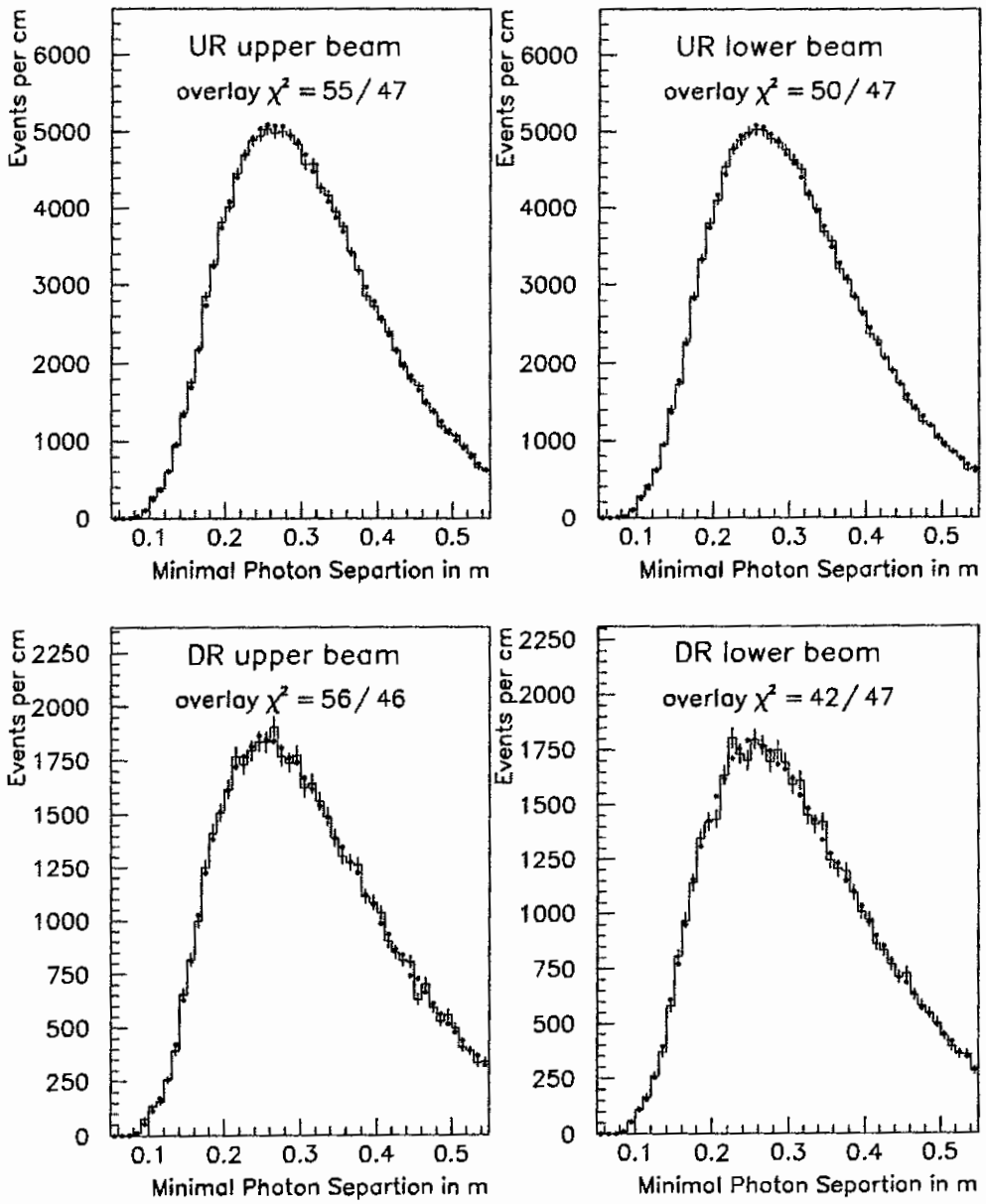

Figure 59. Minimal photon separation for $\pi^0\pi^0$ events at the lead glass. Shown are the data (histogram) and Monte Carlo (dots) for both regenerators and both beams.

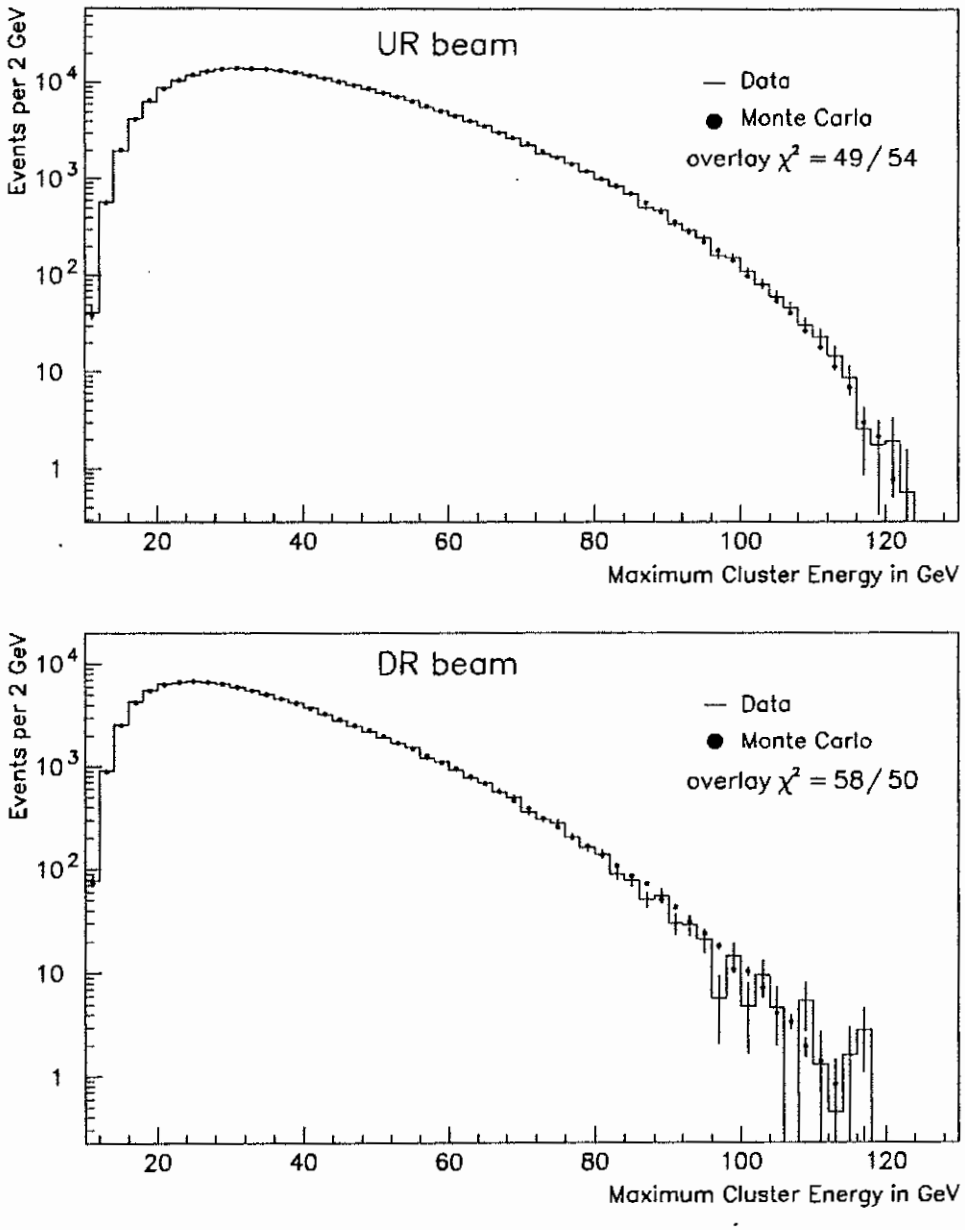

Figure 60. Distribution of maximal cluster energy per $\pi^0\pi^0$ event for data and Monte Carlo. Shown are the overlays for the UR and DR beam.

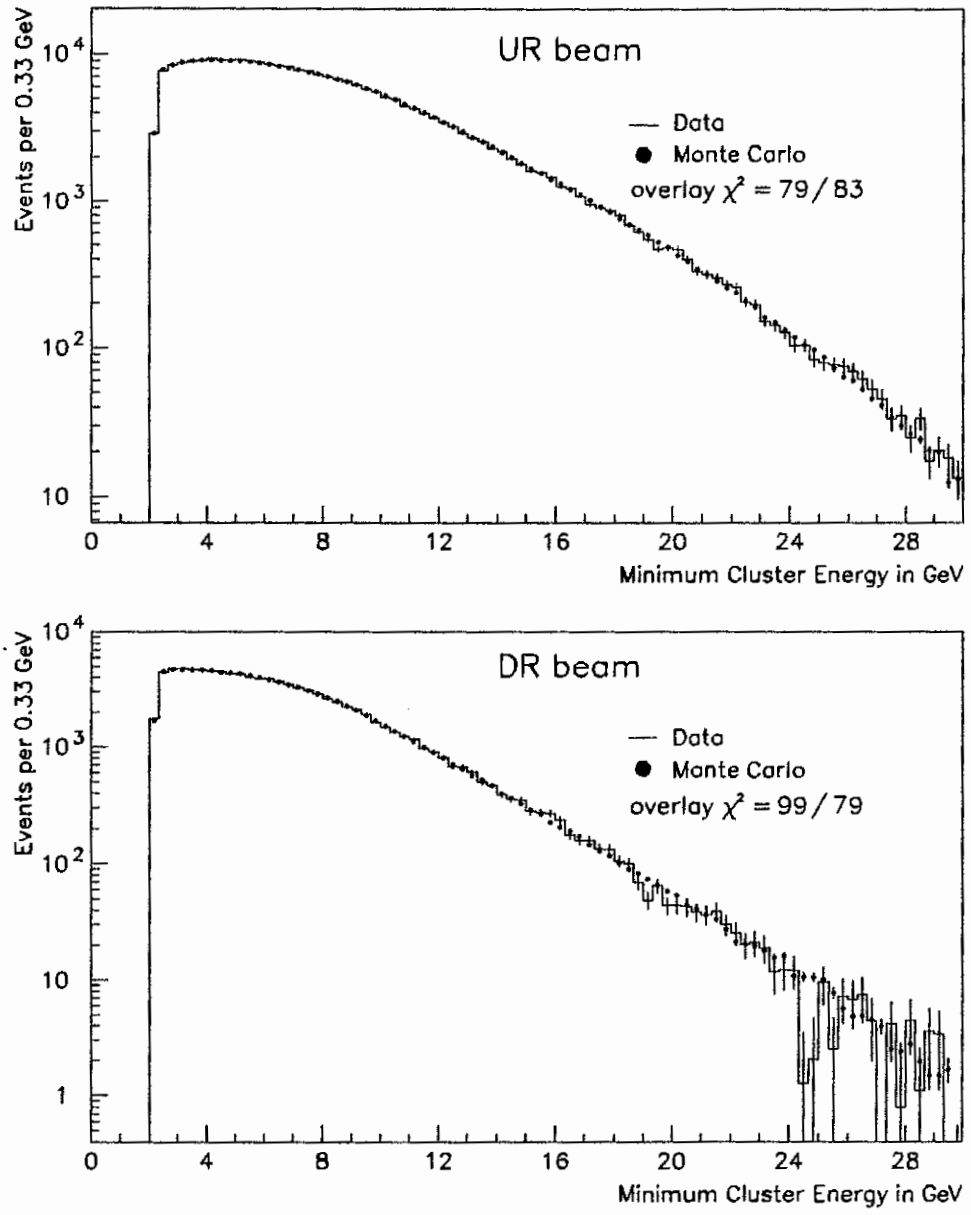

Figure 61. Distribution of minimal cluster energy per $\pi^0\pi^0$ event for data and Monte Carlo. Shown are the overlays for the UR and DR beam.

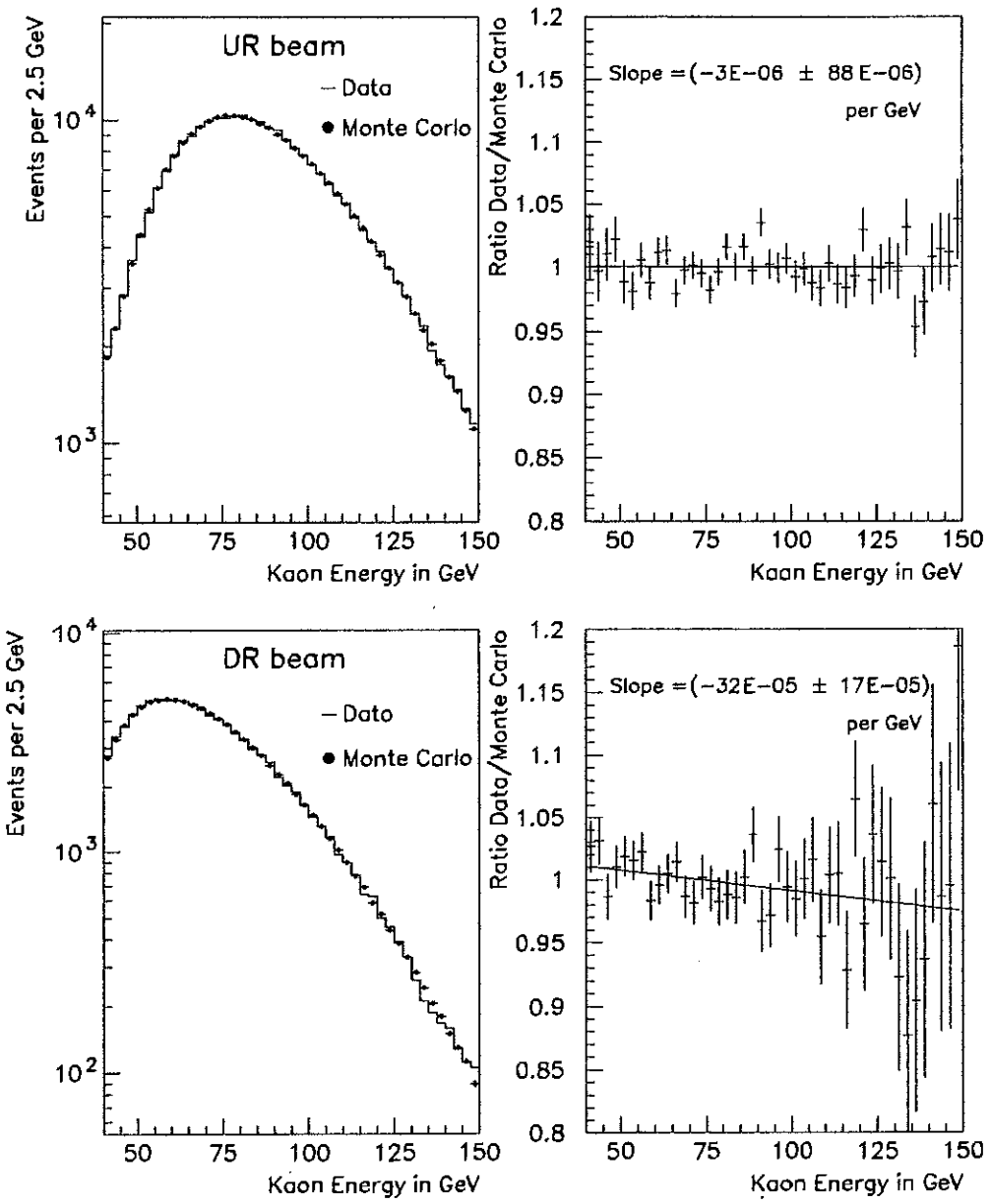

Figure 62. Energy distribution for upstream and downstream regenerator $\pi^0\pi^0$ events.

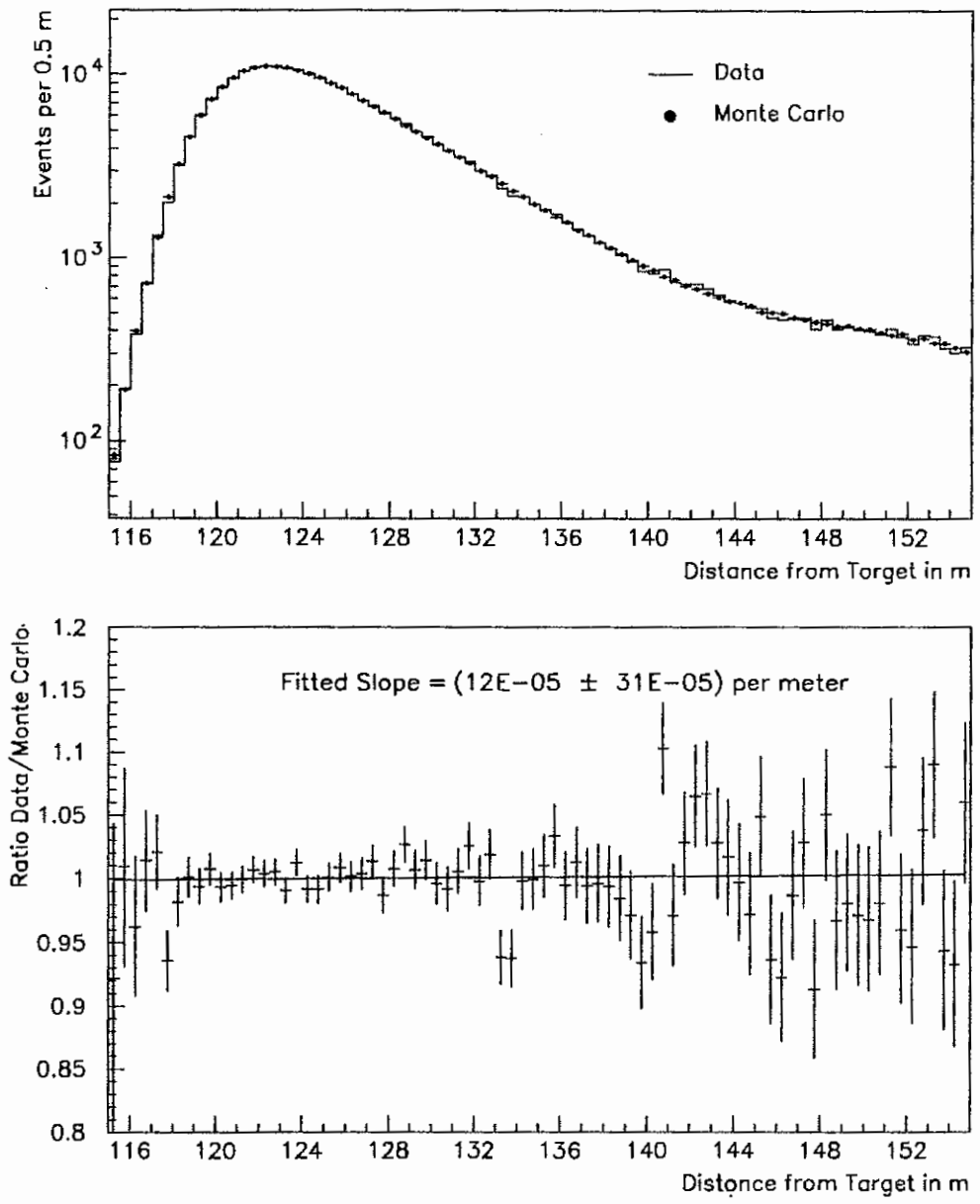

Figure 63. Decay distribution for upstream regenerator $\pi^0\pi^0$ events.

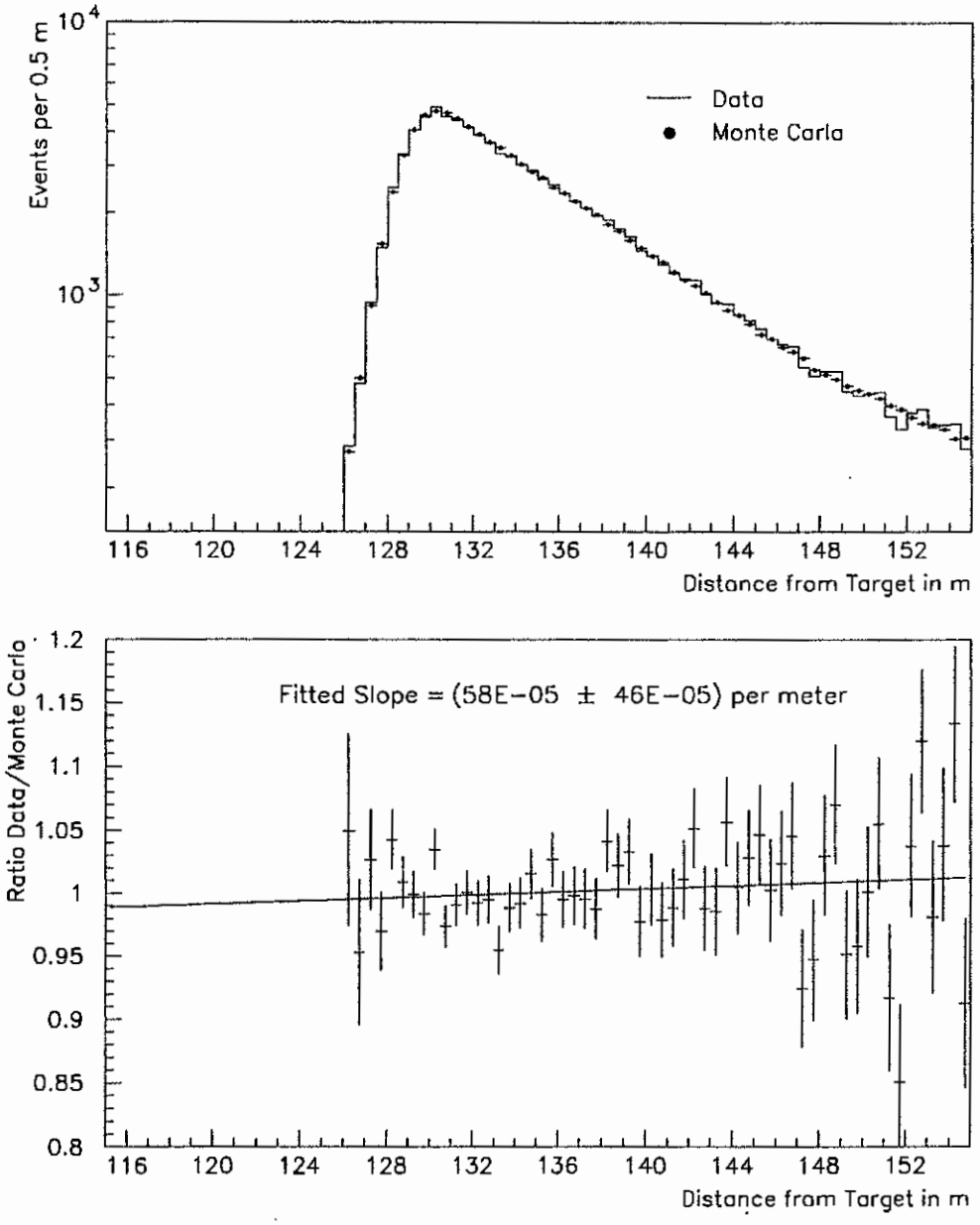

Figure 64. Decay distribution for downstream regenerator $\pi^0\pi^0$ events.

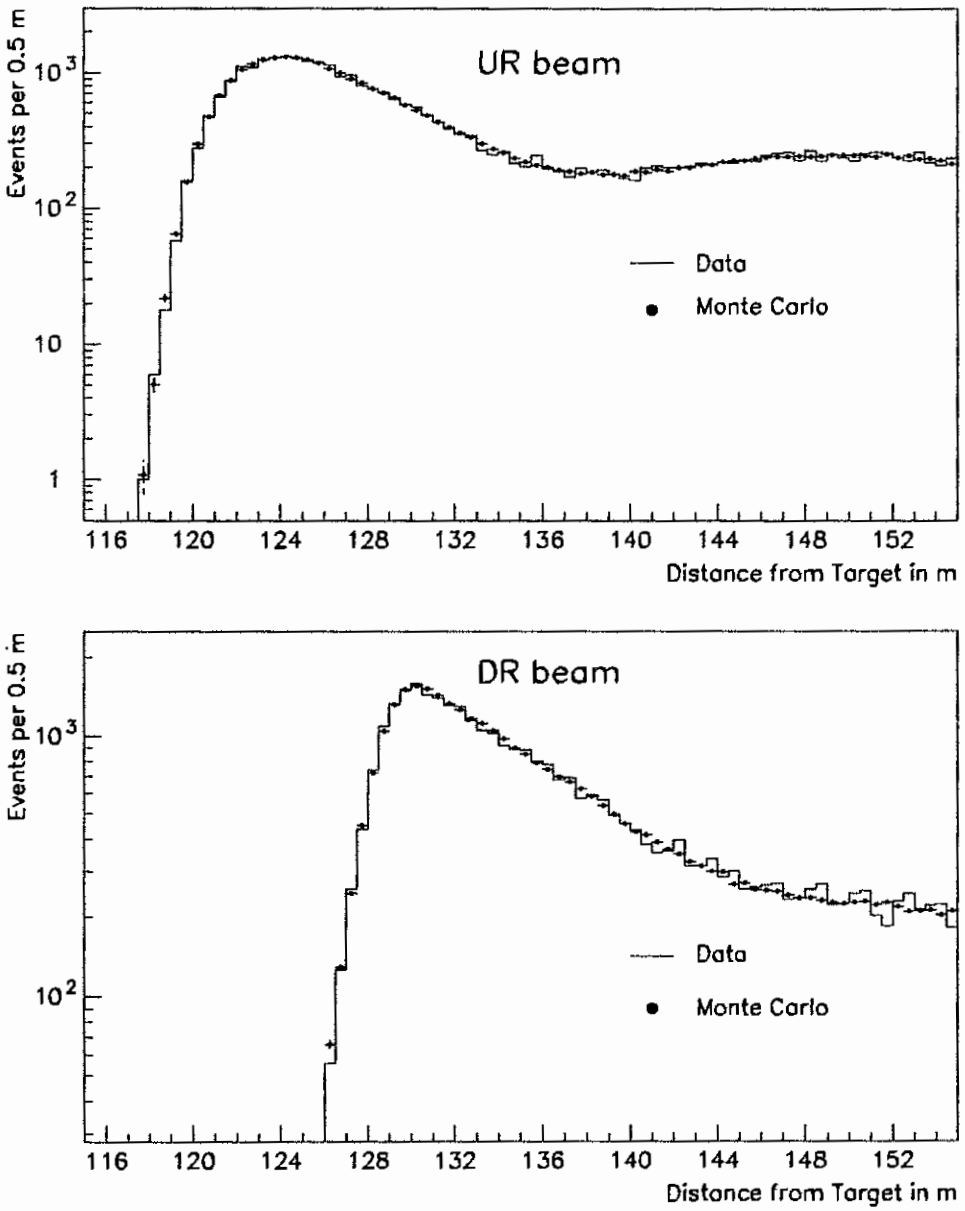

Figure 65. Decay distribution for upstream and downstream regenerator $\pi^0\pi^0$ events with kaon energy between 40 GeV and 60 GeV.

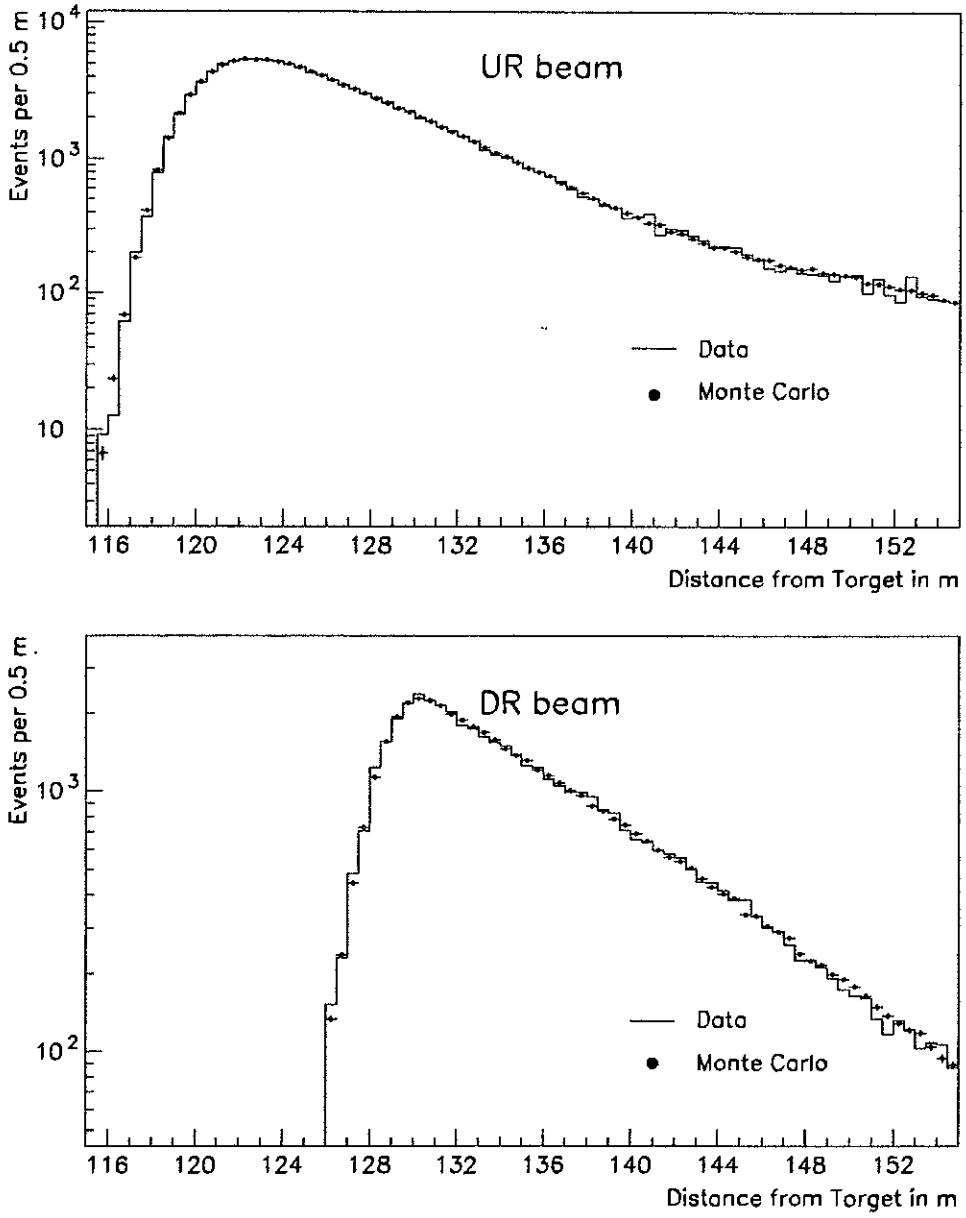

Figure 66. Decay distribution for upstream and downstream regenerator $\pi^0\pi^0$ events with kaon energy between 60 GeV and 90 GeV.

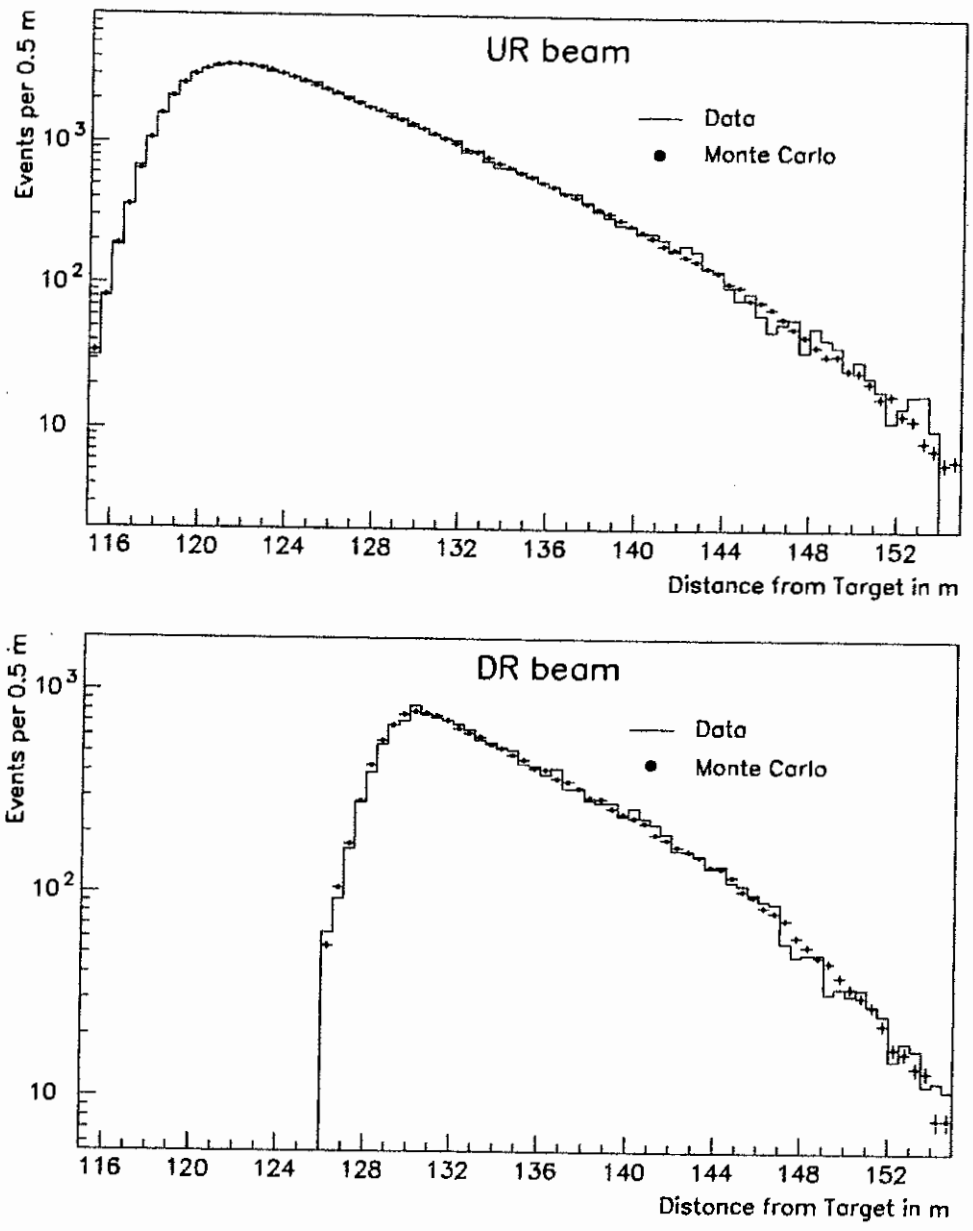

Figure 67. Decay distribution for upstream and downstream regenerator $\pi^0\pi^0$ events with kaon energy between 90 GeV and 120 GeV.

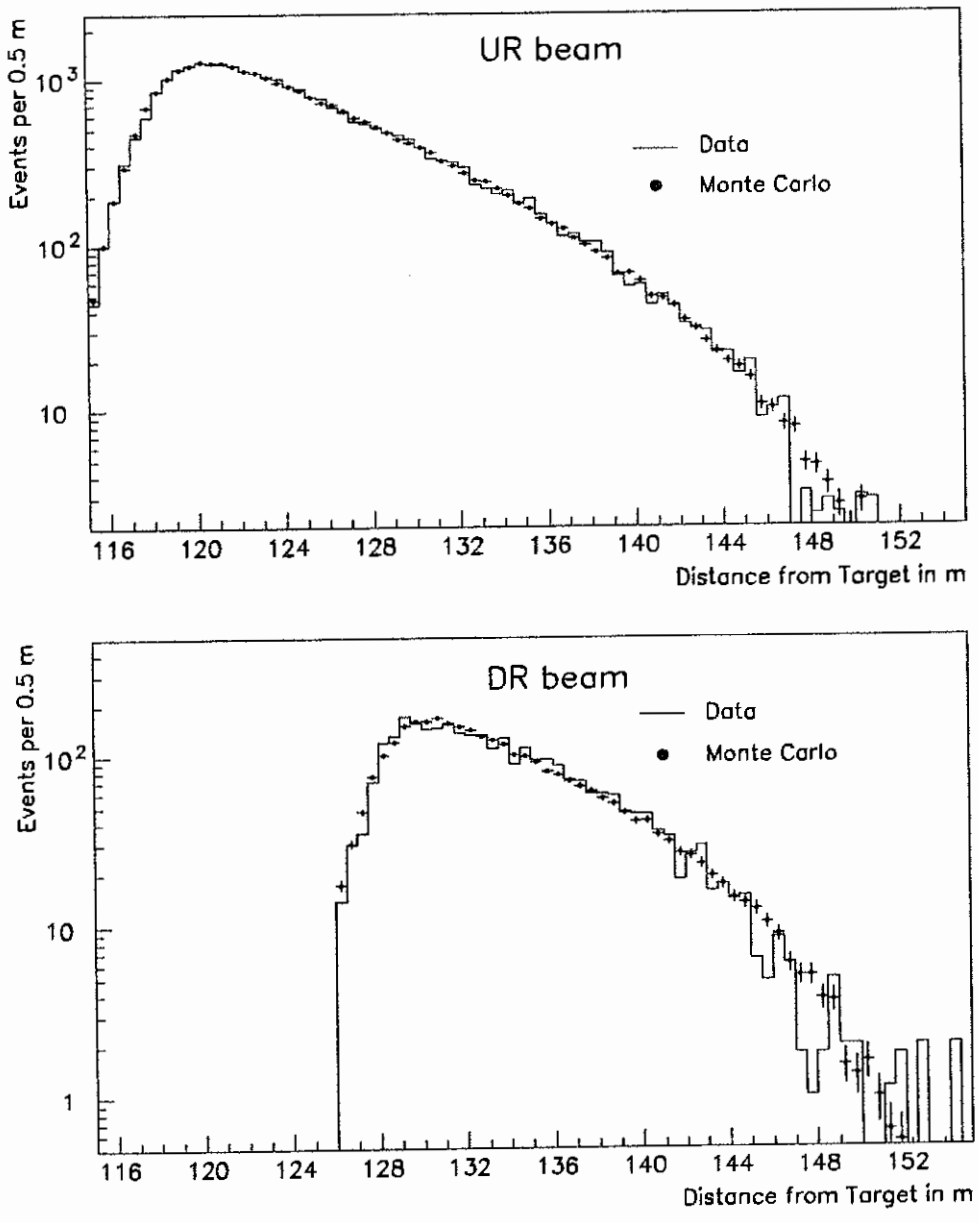

Figure 68. Decay distribution for upstream and downstream regenerator $\pi^0\pi^0$ events with kaon energy between 120 GeV and 150 GeV.

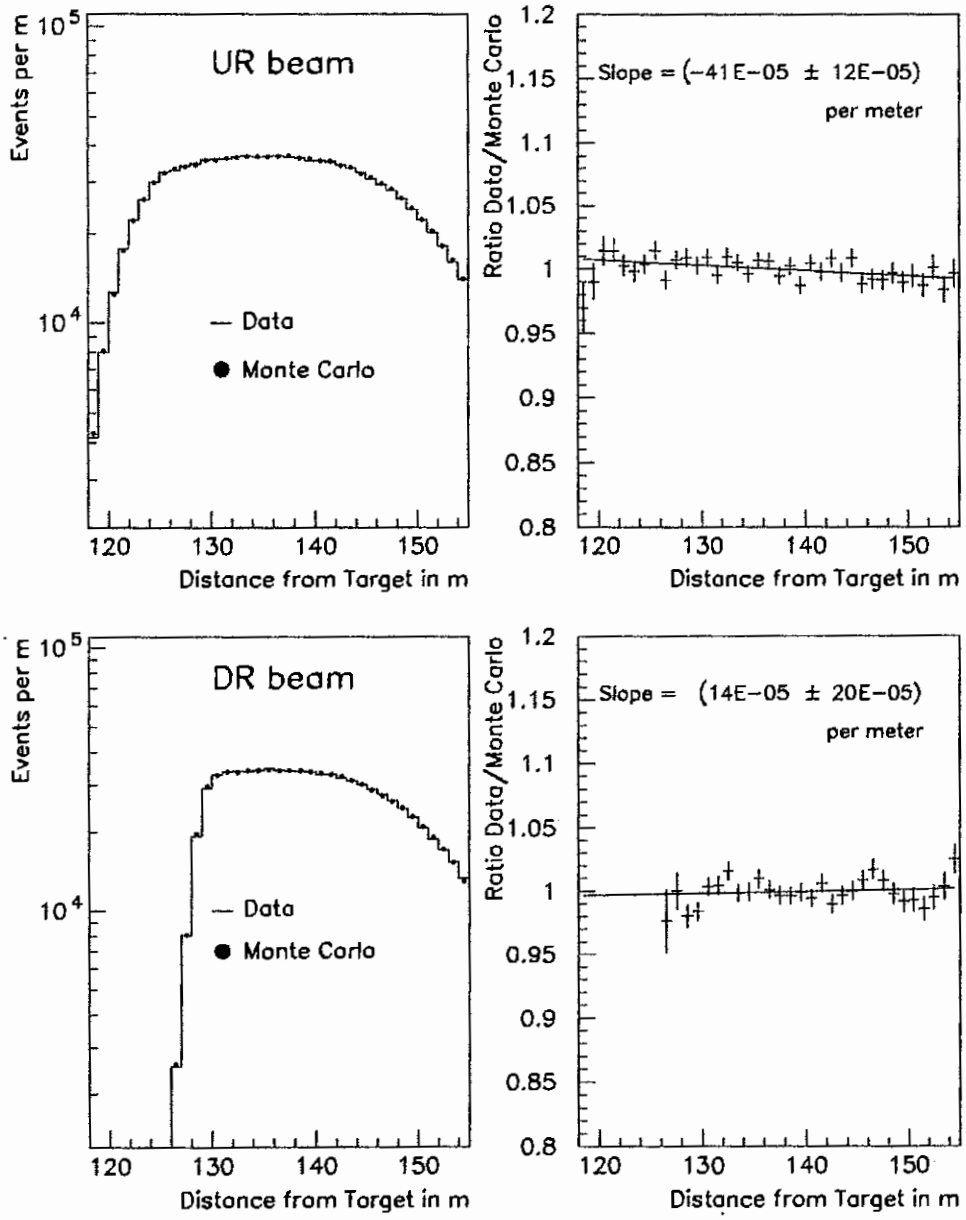

Figure 69. Decay distribution for upstream and downstream regenerator $3\pi^0$ events.

A very small fraction of the kaons are affected and the acceptance correction therefore does not depend on the details of the beam shape simulation.

Fig. 71 shows the energy overlays between data and Monte Carlo for both beams and both data sets. The agreement between data and the simulation is quite good. The overlays of the decay distributions are shown in Fig. 72 and 73 for data sets 1 and 2, respectively. In the z range used in the fitting program (from 118 m to 154 m for the UR and from 130 m to 154 m for the DR) the agreement is very good. For data set 1 the exact position of the hodoscope T+V was not know which explains the discrepancy in the last bin. The fitted region was therefore restricted to 140 m for this set (see chapter 9).

Fig. 74 and 75 show the overlays of the decay distributions for $K_L \to \pi e \nu$ decays. The data statistics for this decay mode is much higher than for the $\pi\pi$ mode and the simulation of this decay mode did not depend on the simulation of the regenerator properties (except for the amount of diffractive events). The data - Monte Carlo comparison offered therefore a powerful check of the quality of our acceptance simulation. Consequently, the systematic error from the acceptance correction can be limit by the measured slope of the ratio plots. This will be discussed in chapter 10.2.3. There is no indication for a problem with our acceptance simulation.

7.8 Summary

This chapter is the longest of the thesis. The reason is simply that our analysis depends strongly on the simulation of the detector (especially of the lead glass) and the physics of kaon propagation and scattering. In the $\Delta\Phi$ fit the data are corrected for the acceptance and the purpose of this chapter was therefore to show that this correction is understood very well. In the systematic error analysis the quality of our understanding will be quantified.

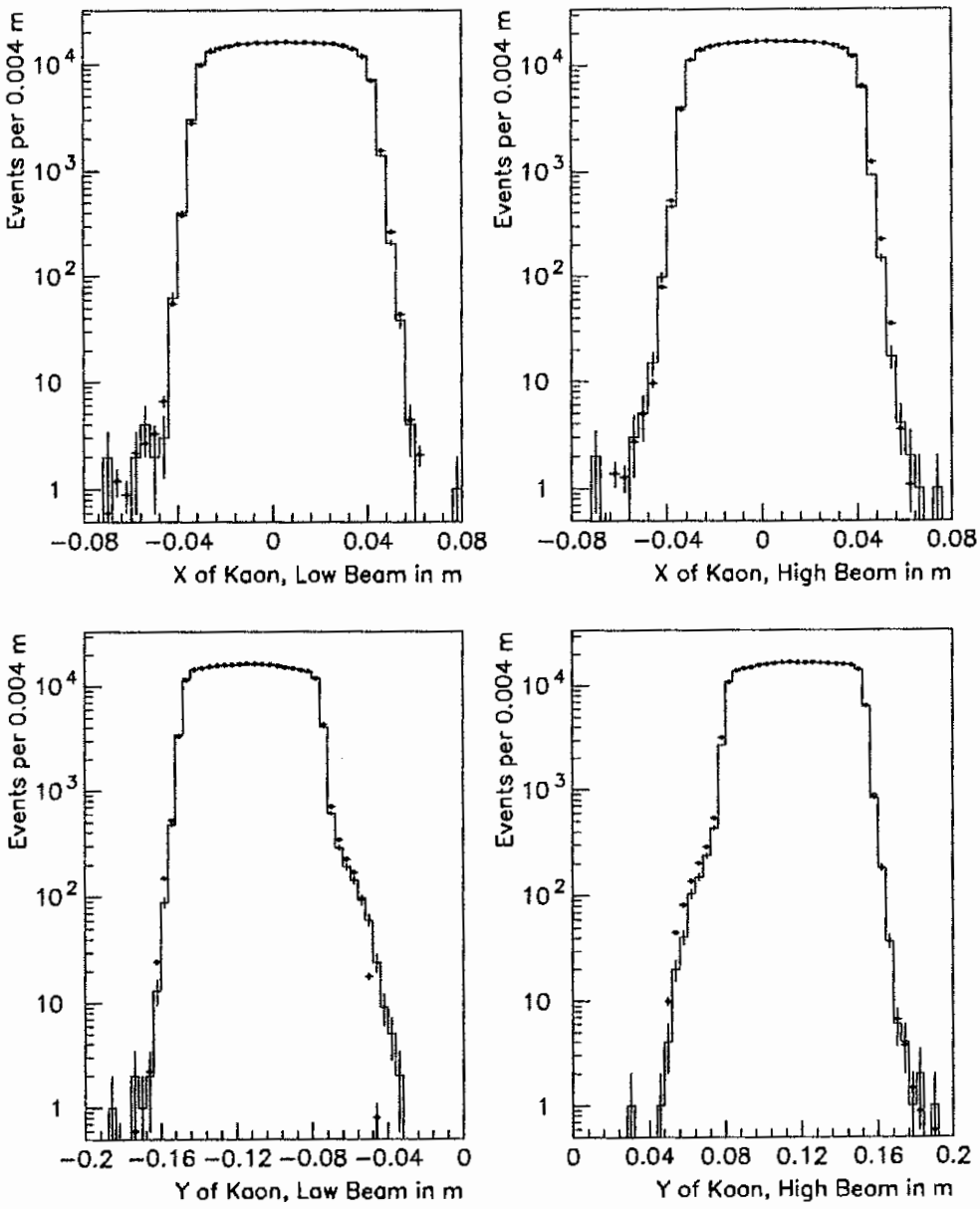

Figure 70. Projection of the kaon position in $\pi^+\pi^-$ events at the lead glass. Shown are the overlays between data (histogram) and Monte Carlo (dots) for the upper and lower beam in the x and y projection for data set 2.

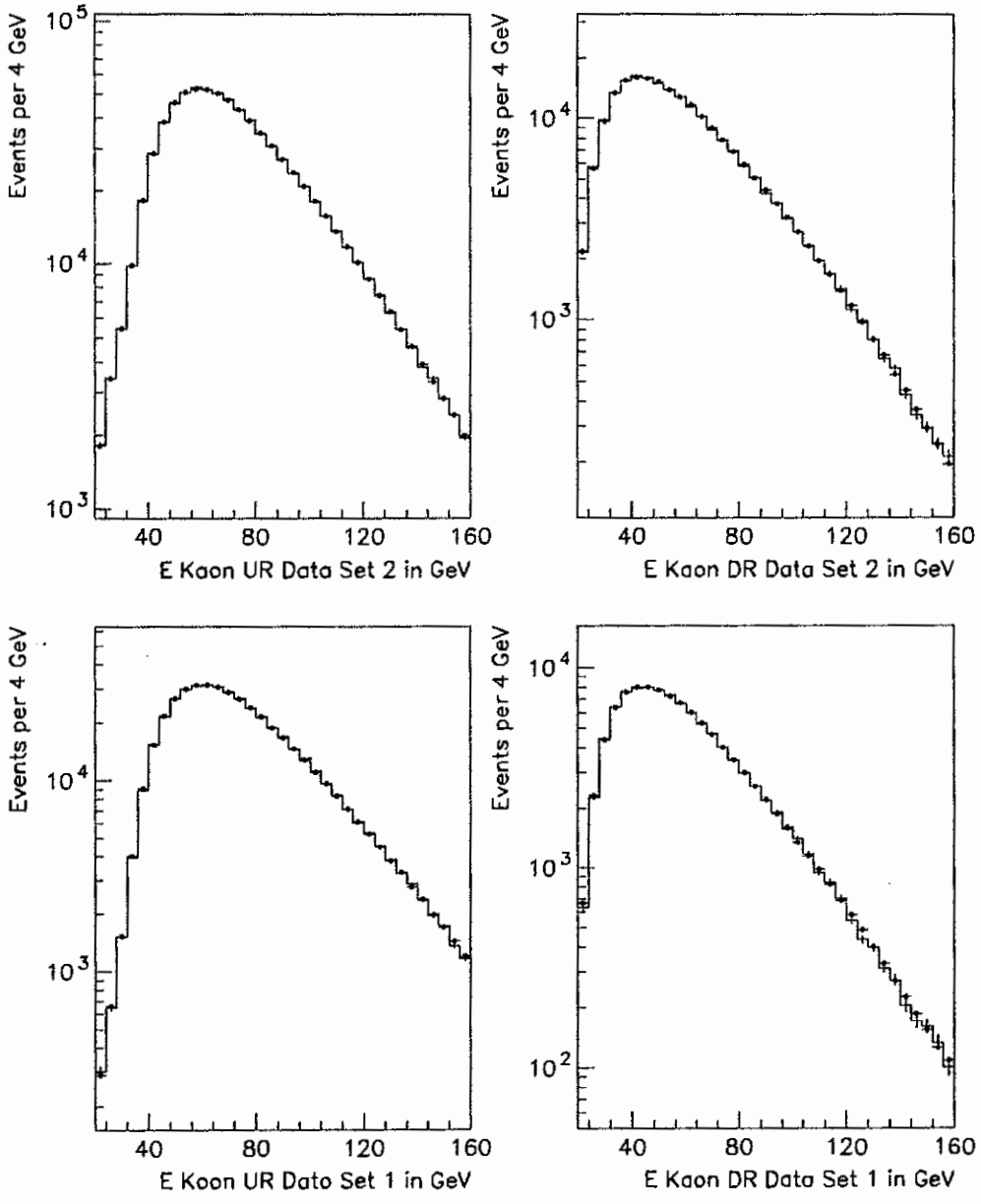

Figure 71. Kaon energy distribution for data and Monte Carlo $\pi^+\pi^-$ events for both beams and data sets. The data are the histograms and the Monte Carlo are the dots.

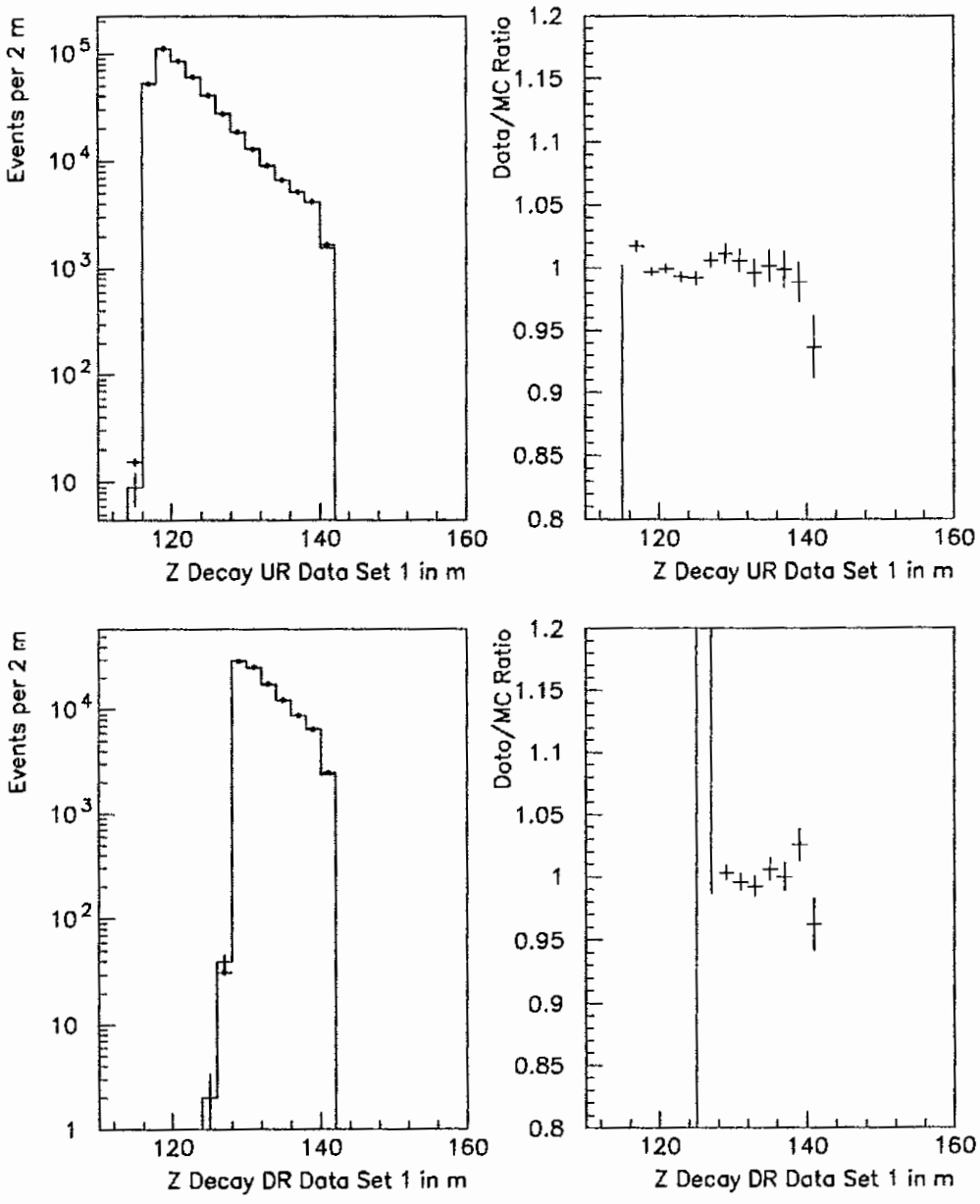

Figure 72. Decay vertex distribution for data (histogram) and Monte Carlo (dots) $\pi^+\pi^-$ events for data set 1.

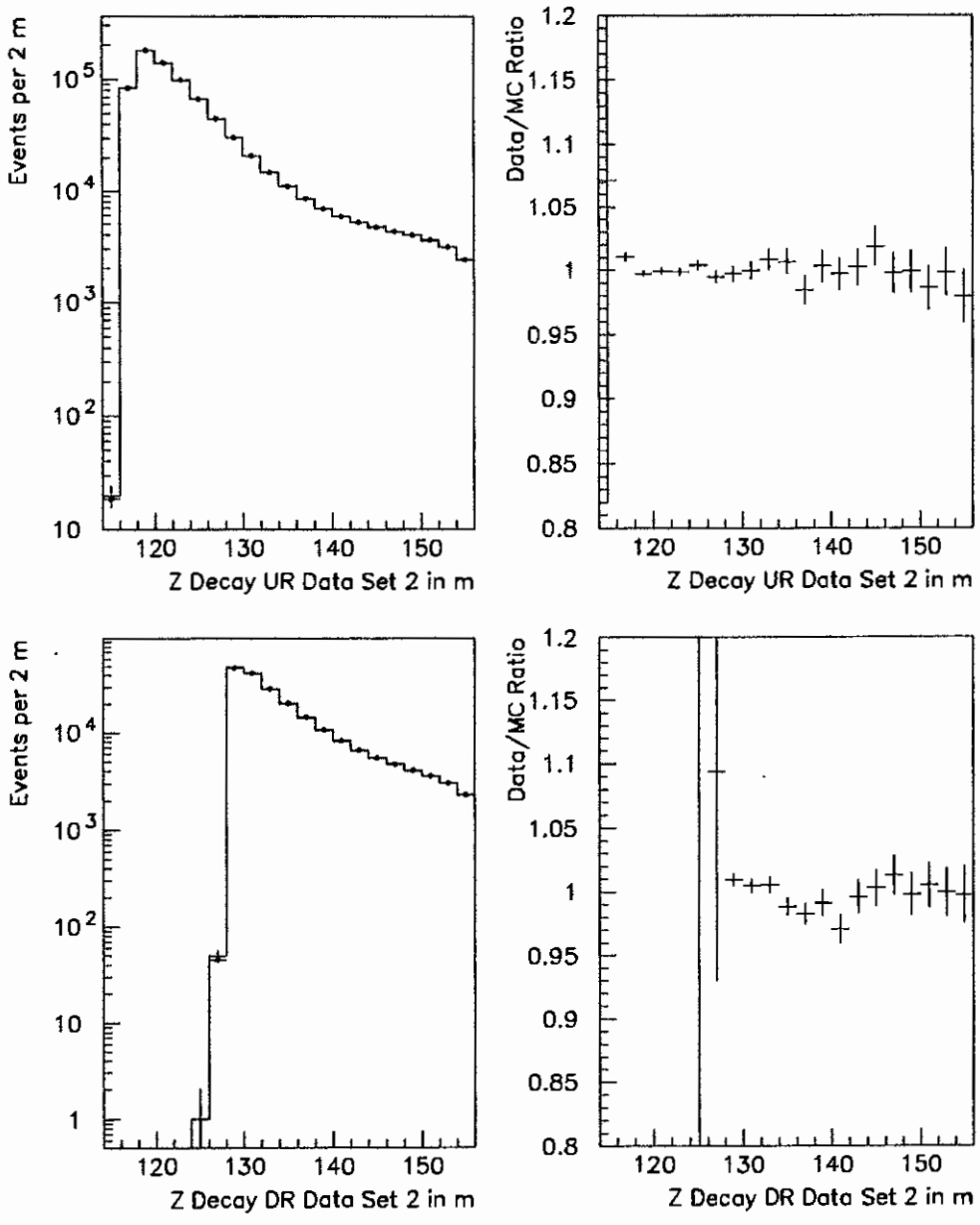

Figure 73. Decay vertex distribution for data (histogram) and Monte Carlo (dots) $\pi^+\pi^-$ events for data set 2.

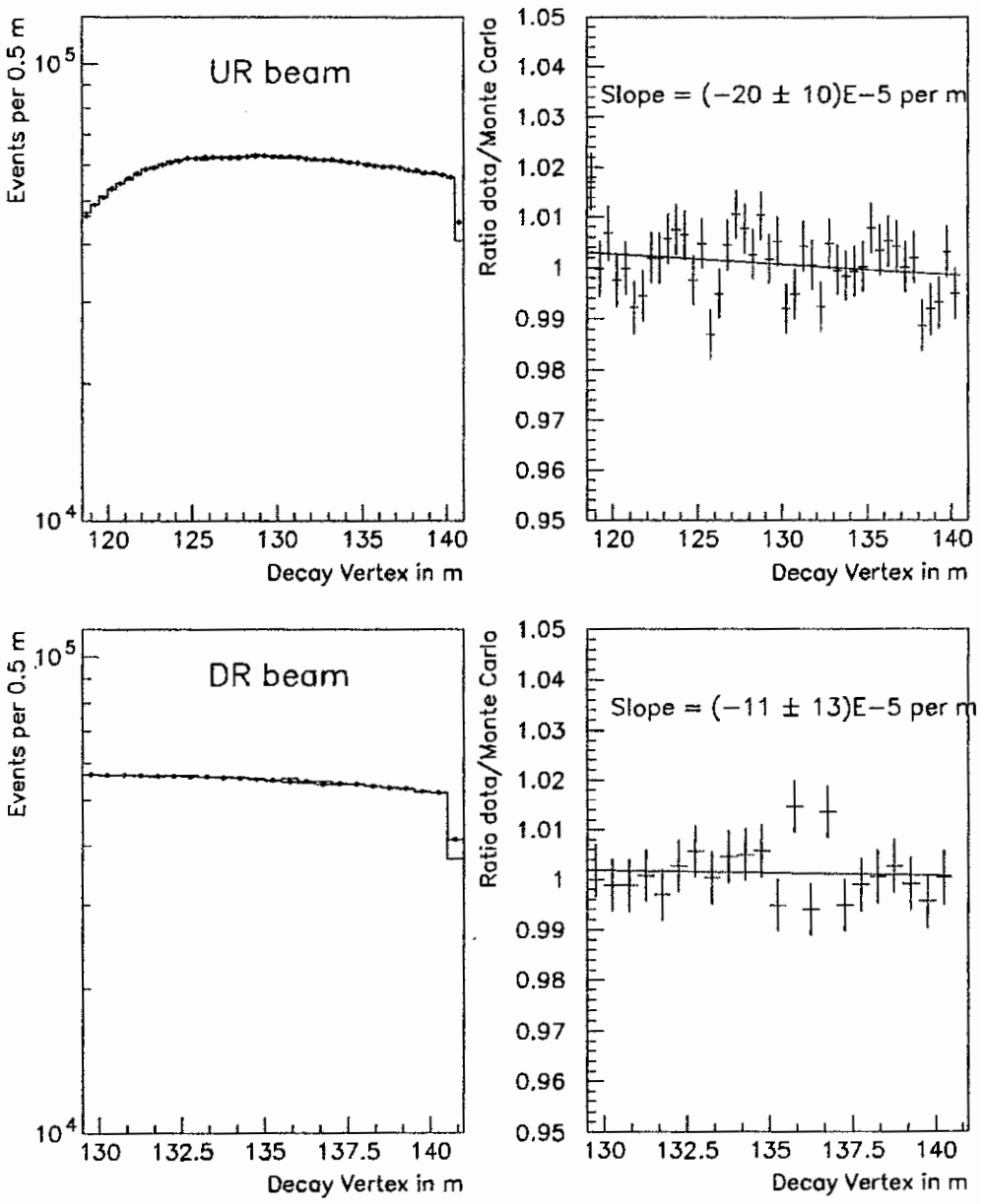

Figure 74. Decay vertex distribution for data (histogram) and Monte Carlo (dots) $K_L \to \pi e \nu$ events for data set 1. Since the position of the T+V hodoscope is not well known the data and Monte Carlo disagree in the last bin.

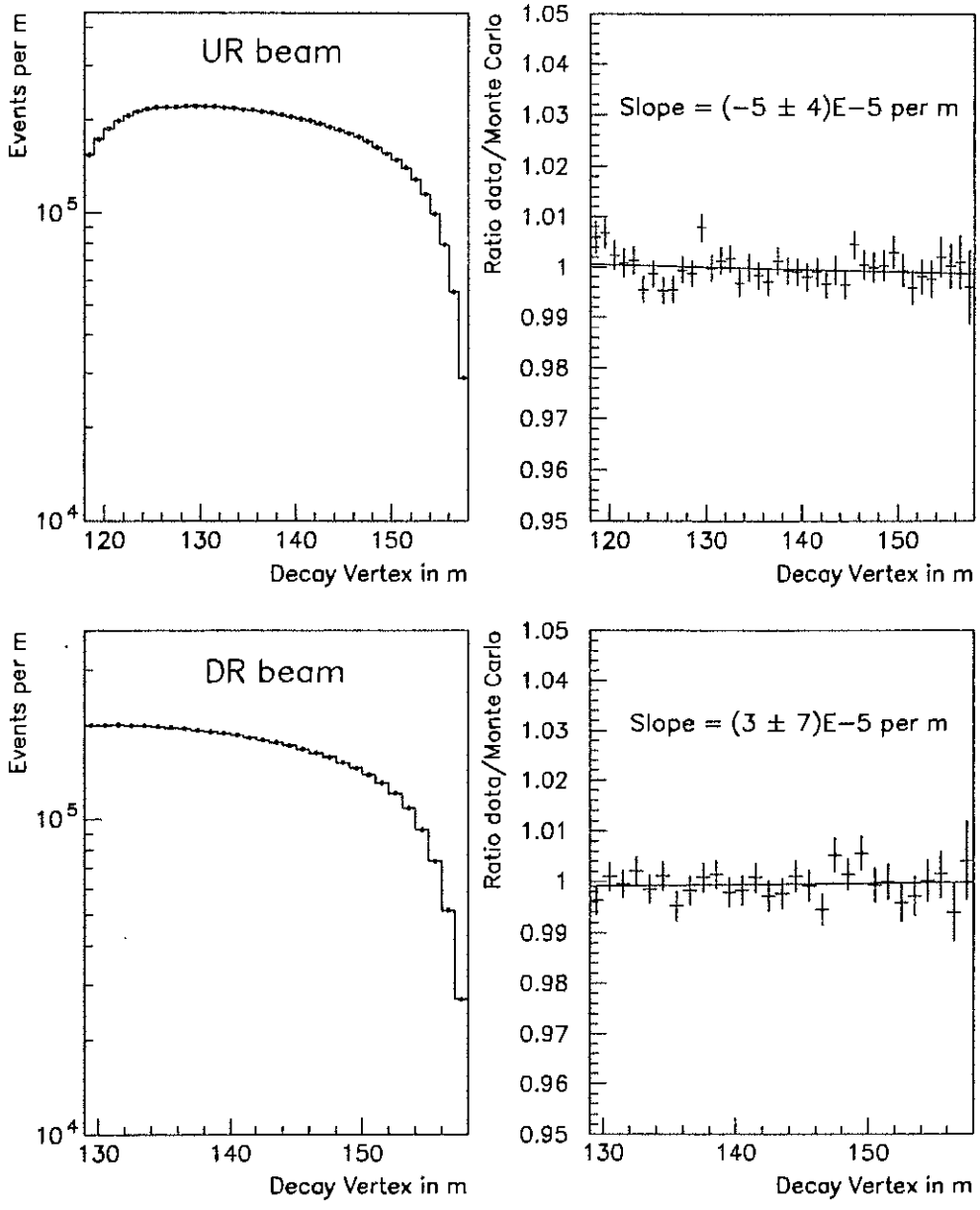

Figure 75. Decay vertex distribution for data (histogram) and Monte Carlo (dots) $K_L \to \pi e \nu$ events for data set 2.

CHAPTER 8

The Fitting Procedure

With the charged and neutral mode data the phases Φ_{+-} and $\Delta\Phi$, the K_L-K_S mass difference Δm and K_S lifetime τ_S were extracted. The background subtracted and acceptance corrected data (p, z) distributions are calculated and fitted to a predicted decay distributions which depended on the quantities we want to extract. The fit was a χ^2 fit. This chapter describes the parameters which are floated in the $\Delta\Phi$ fit and some of the technical details of the fitting program. In the fit for the other parameters only the charged mode data was used since the statistical power from the neutral mode was much smaller. The extraction of Φ_{+-}, Δm and τ_S is described in [Briere 95b].

The (p, z) distribution of the data, the backgrounds and the generated and accepted coherent Monte Carlo events for charged and neutral mode and both data sets were read in in form of histograms with 1 GeV by 0.5 m binning, called micro binning. First all histograms were rebinned to the bin sizes the fit was performed in, typically 10 GeV by 2 m. Then the backgrounds from noncoherent kaon decays and other sources were subtracted.

The background subtracted data in the upper and lower beams are added by taking the geometric sum[1] [Gibbons 93c]. If the arithmetic sum would have been used instead $\Delta\Phi$ would have changed by 0.03°.

The acceptance was calculated as the ratio of the number of reconstructed over generated coherent Monte Carlo events in every fit (p, z) bin. Because of the detector resolution some of the Monte Carlo events will reconstruct in a different (p, z) bin than the one they were

[1] If N_u and N_l is the number of events in the upper and lower beams in a fit bin, respectively, the geometric sum is $2\sqrt{N_u N_l}$.

generated in. This migration affects the acceptance calculation. Since the momentum and decay vertex distributions between data and Monte Carlo agree and the detector resolution is well simulated the migrations are correctly included in the acceptance calculation. Fig. 76 shows the acceptance for the charged and neutral mode.

The χ^2 which was minimized in the fit was defined as

$$\chi^2 = \sum_{\text{fit bins i,j}} \frac{(d(p_i,z_j) - k(p_i,z_j)\cdot a(p_i,z_j))^2}{\sigma^2} \tag{8.1}$$

Here the sum is taken over all momentum bins p_i and decay region intervals z_j and σ is given by:

$$\sigma^2 = \frac{k(p_i,z_j)\cdot a(p_i,z_j)}{b(p_i,z_j)} + k(p_i,z_j)^2 \frac{a(p_i,z_j)(1-a(p_i,z_j))}{g(p_i,z_j)}; \tag{8.2}$$

$d(p_i,z_j)$ = number of background subtracted data events in a fit bin;

$k(p_i,z_j)$ = number of kaon decays in the experiment before acceptance;

$a(p_i,z_j)$ = acceptance in a fit bin;

$b(p_i,z_j)$ = data background fraction in a fit bin;

$g(p_i,z_j)$ = number of generated Monte Carlo events in a fit bin .

The σ used in the χ^2 calculation has two contributions. The first term is due to the finite data statistics, i.e. the number of data events before the background subtraction $(= d(p_i,z_j)/b(p_i,z_j))$. The number of data events in the error calculation 8.2 was replaced by the product $(a(p_i,z_j)\cdot k(p_i,z_j))$ to avoid biasing the χ^2 by fluctuations. For example, if the number of data events fluctuates from the expected number of 49 down to 25 in one of the bins then the χ^2 contribution is $(24/7)^2 = 12$ using equation 8.2 and $(24/5)^2 = 23$ if the observed number of events were used in the error calculation[2].

The second term in equation 8.2 is the contribution from the statistical error in the acceptance calculation to the χ^2. The relative contribution of this term can be reduced by generating more Monte Carlo statistics. To estimate its contribution to the total error, the number of generated events $g(p_i,z_j)$ can be replaced by $(S\cdot k(p_i,z_j))$. S is the scale factor of the generated Monte Carlo to data statistics and is given by the ratio of the number

[2]Provided the error contribution from the second term in 8.2 is small

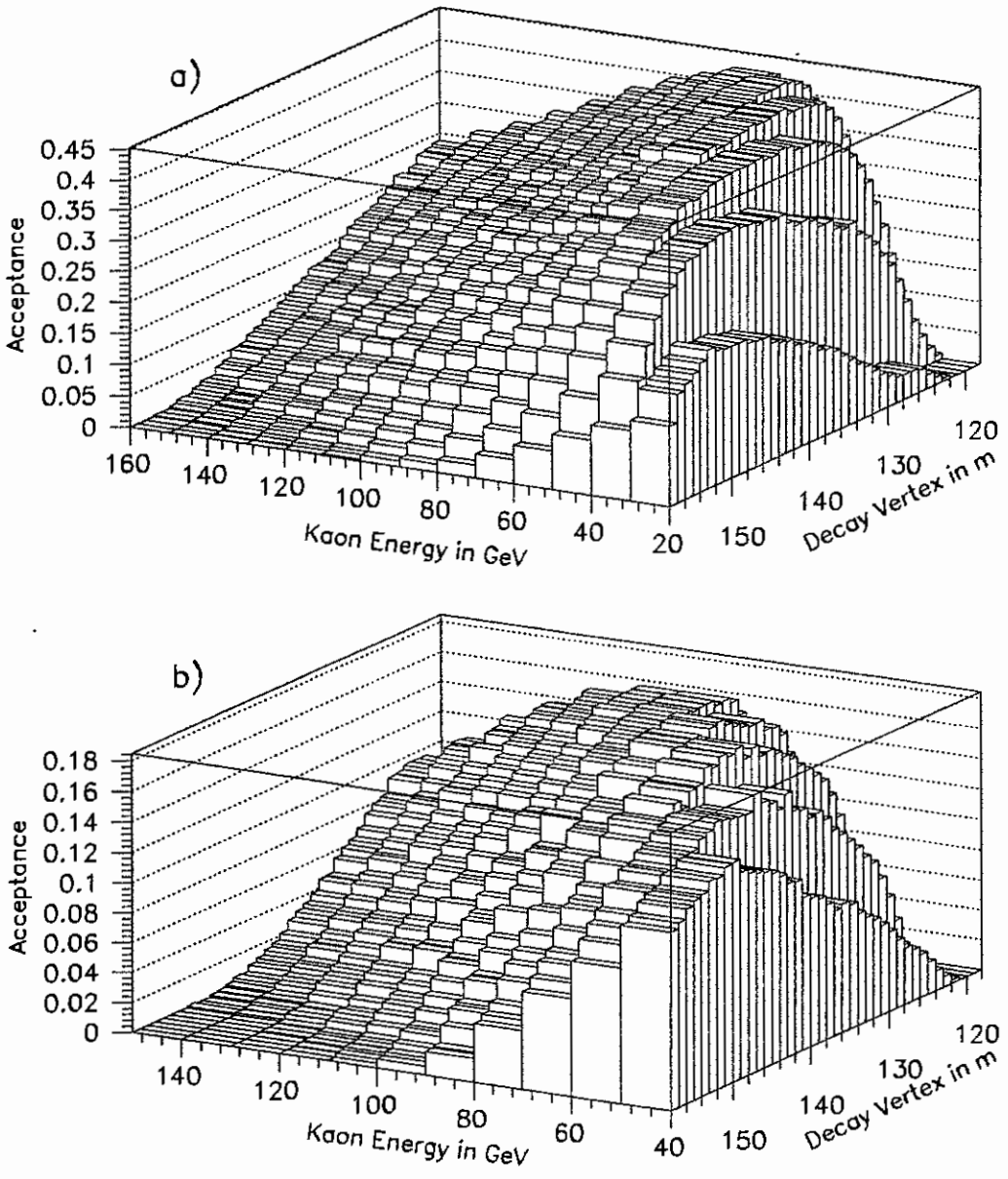

Figure 76. Acceptance as a function of decay vertex and kaon energy for charged (a) and neutral mode (b).

of accepted Monte Carlo events over the number of background subtracted data even Equation 8.2 becomes

$$\sigma^2 = k(p_i, z_j)a(p_i, z_j)(\frac{1}{b(p_i, z_j)} + \frac{1 - a(p_i, z_j)}{S}) \quad (8$$

With $S \approx 11(10)$ for our neutral (charged) mode Monte Carlo sample, the error contributi from the acceptance calculation is less than 10%. There is another advantage of having large Monte Carlo sample. The absolute level of the acceptance was not well known. If t acceptance would be lower by 10% the fitted prediction would compensate for this effe and the product would stay constant. Only the term $(1 - a(p_i, z_j))/S$ in the χ^2 calculati depends on the absolute level of the acceptance. A large value of S damps this effect.

Errors from the background subtractions are treated as systematic errors only, i.e. statistical error is assigned to the number of background events subtracted. This is on relevant for neutral mode since the background fractions were smaller than a percent charged mode.

In the remainder of this chapter the calculation of the number of predicted even $k(p_i, z_j)$ in every fit bin is discussed. Ingredients to this calculation and floated paramete are:

- The kaon energy spectra incident on the regenerators were calculated the same wa they were determined for the Monte Carlo. For the spectra of K^0 and $\bar{K}^0$ at the targ the same parameterization and targeting angles were chosen as in the simulatio program. Since the data and Monte Carlo energy spectra agree this was a goo approximation.

  Two effects altered the spectra of the kaons between the target and the regenerator In the experiment kaons within an opening angle of about ± 0.2 mrad around th targeting angle reached the detector and the spectra depend on this angle. Kaon also scattered in the absorbers and the average scattering angle decreased linearl with the kaon momentum. The correction of the two effects to the spectrum relativ to a pencil beam at a constant targeting angle without scattering was calculated wit the Monte Carlo by generating a large number of kaons with the regular condition and with a pencil beam. The ratio of the two spectra is shown in Fig. 77 and

4th order polynomial was fit to this distribution. In the $\Delta\Phi$ fit the energy spectrum was then determined by propagating the energy spectrum at the target with a fixed targeting angle to the regenerator and multiplying this spectrum by the 4th order polynomial.

Since we have no independent way to determine the energy spectrum, except by comparing the data we are fitting with the Monte Carlo, two parameters were floated in the fit to compensate for our ignorance. [3] The kaon flux was modified by a quadratic factor $A \cdot E_{kaon} + B \cdot E_{kaon}^2$, with A and B being determined by the fit.

- The prediction $k(p_i, z_j)$ has to fit the absolute number of observed charged and neutral mode data events in the UR and DR beams and for data sets 1 and 2. Therefore 5 flux normalization factors were floated in the fit: two independent normalizations for the UR beam flux in the two data sets for charged mode, two factors for the relative neutral to charged mode normalization for sets 1 and 2 and one normalization for the DR over UR flux which was the same for both sets and both modes.

- The K^0 and $\bar{K}^0$ states were propagated through all the material in the beam line to the regenerators using the correct kaon propagation formula in equation 7.3. The (K_S, K_L) amplitude after the regenerator depends primarily on the regeneration properties of the scintillator $CH_{1.1}$.[4] As explained in chapter 1.5 $(f - \bar{f})/k$ can be parameterized as:

$$\frac{f-\bar{f}}{k} = s(p) \cdot \left|\frac{f-\bar{f}}{k}\right|_{70\ \mathrm{GeV/c}} \left(\frac{p\ [GeV/c]}{70\ GeV/c}\right)^{\alpha} e^{-i\pi(2+\alpha)/2} \qquad (8.4)$$

  $s(p)$ is the complex correction due to the screening effects. Its calculation is described in reference [Briere 95b]. In the fit, $|(f - \bar{f})k|_{70\mathrm{GeV/c}}$ and α for carbon were floated while the regeneration off hydrogen is taken from reference [Bock 79].

- Once the (K_S, K_L) amplitude at the downstream face of the regenerator was known

[3] In the previous experiment E731 the vacuum beam was used to predict the kaon energy spectrum incident on the regenerator. The ignorance in our experiment had a large impact on the statistical and systematic error of Φ_{+-} [Briere 95b].

[4] At high energies, the K_S amplitude from the target does not completely decay away and adds to the amplitude downstream of the regenerator.

the decay rate into $\pi^0\pi^0$ and $\pi^+\pi^-$ as a function of proper time τ was given by equation 7.15.

The parameters describing the kaon decay in this formula are τ_L, τ_S, Δm, η_{00} and η_{+-}. τ_L and τ_S were taken from PDG for all fits [PDG 94]. The charged mode data was used to fit for Δm and in the $\Delta\Phi$ fit, Δm was fixed to the averaged values from E731 and E773 [Briere 95b]. The phase Φ_{+-}, the phase difference $\Delta\Phi = \Phi_{00} - \Phi_{+-}$ and $|\eta_{00}/\eta_{+-}|$ were floated in the fit described here. Note that the decay rate did not depend on the absolute value of η_{+-}, only on the ratio $|\rho/\eta|$. Since we fit for $|\rho|$, i.e. $|(f-\bar{f})/k|_{70GeV}$ and α, we fix $|\eta_{+-}|$ to the PDG value of 0.002275 [PDG 94].

The above equation 7.15 is the decay rate in vacuum. However, vacuum windows and air were in the decay region and caused regeneration. In the calculation of the the decay rate downstream of, say the vacuum window behind the regenerator, the (K_S, K_L) amplitude was therefore first propagated with equation 7.3 through the window and then equation 7.15 could be applied. Decay rates inside the regenerators are not calculated in the fitting program.

The total decay rate is the sum of the rates for an initial K^0 and an initial $\bar{K}^0$ with the relative weight according to the different spectra.

- Hadronic showering in the lead glass was not modeled in the Monte Carlo. Charged pions could therefore fail the E/p cut in the data but not in the simulation. In addition, the probability for a pion to fail this cut will depend on the pion momentum and the absorption coefficient of the lead glass block the pion hits. This loss can therefore affect the reconstructed energy spectrum for charged pions. To allow for an energy dependent acceptance difference between neutral and charged mode two parameters were floated, which multiplied the neutral mode kaon flux by $A \cdot E_K + B \cdot E_K^2$.

In total, 14 parameters were floated in the $\Delta\Phi$ fit. To calculate the prediction in a fit bin for given values of these parameters, the decay rate 7.15 was analytically integrated over the z range of the bin. This integral was calculated in 1 GeV momentum steps and multiplied with the momentum dependent kaon flux factors and the normalizations mentioned above.

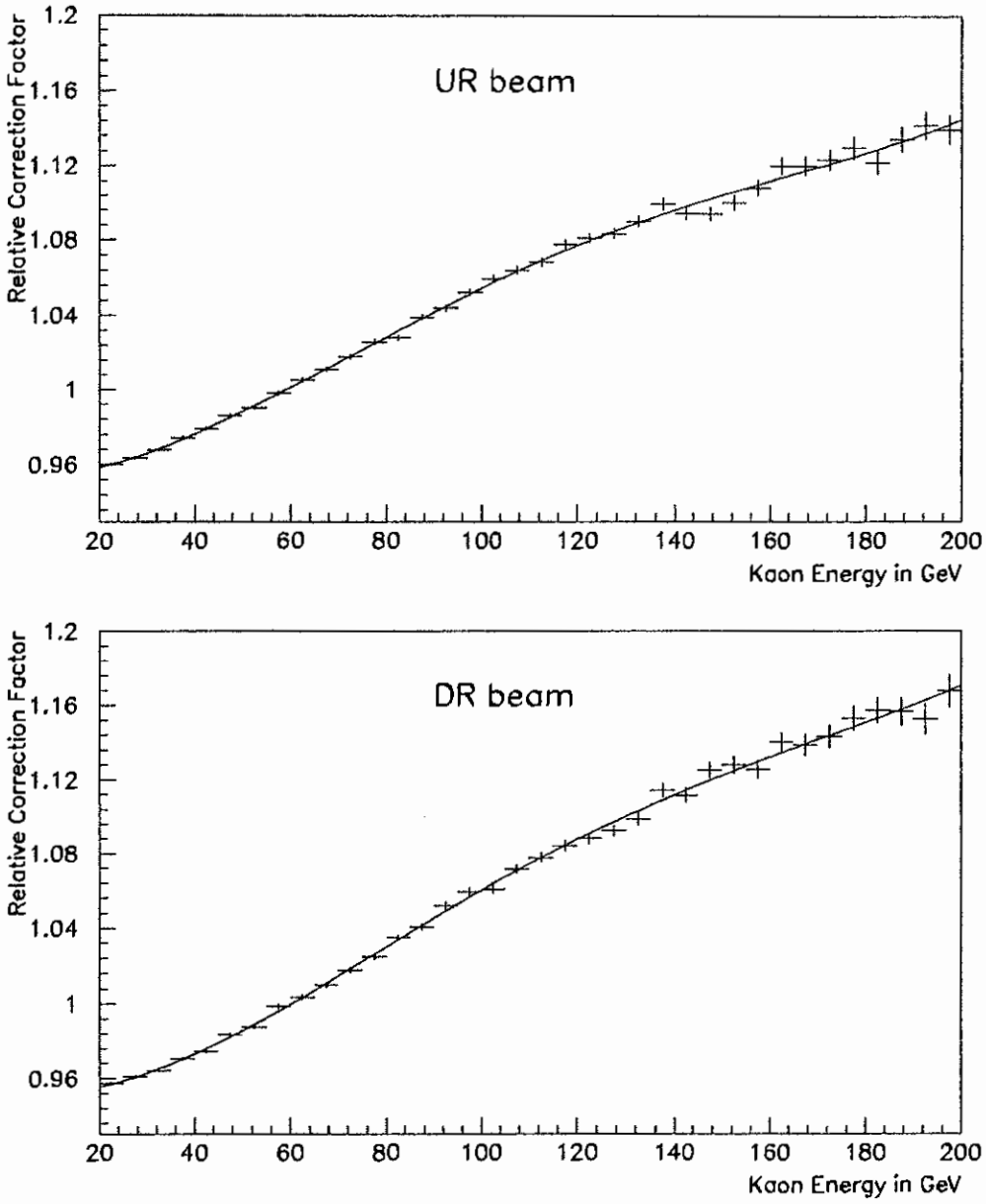

Figure 77. Correction to the 'pencil beam' kaon spectra for the UR and DR as a function of the kaon energy. The curve is a fit to a 4th order polynomial.

Each of these products is the prediction at a given momentum. The sum of ten of these terms for the momenta p to $p+10$ GeV gives the prediction in a 10 GeV momentum interval

Once the prediction was calculated in all fit bins, the sum in equation 8.1 could be performed. Bins with fewer than 10 data events after the background subtraction were excluded from the χ^2 calculation. The CERN library program MINUIT found the parameter values for which the χ^2 was minimized and the program MINOS was used to calculate the errors. In the next chapter the fit results are discussed.

CHAPTER 9

The Result

The previous chapters discussed the entire path of the data analysis. It took three years and the participation of several post-docs and graduate students to accomplish this task, and of course the understanding of the detector gained in the previous experiment E731. At the end, it was most rewarding to put the pieces together and fit the data for the first time for the physics parameters we want to extract. Especially the plots showing the interference between the K_L and K_S decay amplitudes are very beautiful. Fig. 78 and 79 show the decay distribution into neutral and charged pions for two energy intervals and the two regenerators. Plotted are the background subtracted and acceptance corrected data distributions and the predictions as extracted from the final fit with and without the interference term of equation 7.15. Clearly visible is the minimum of the decay rate in the lower kaon energy bins and the contribution from the interference term to the total rate is significant for most of the decay region.

The fit that extracted the final result was performed in the momentum range from 20 GeV/c to 160 GeV/c for charged mode and 40 GeV/c to 150 GeV/c for neutral mode. The bin size was 10 GeV/c. The region for $\pi^+\pi^-$ decays used in the fit was from 118 m (130 m) to 154 m for the UR (DR) beam.[1] For data set 1 the fit range was restricted to 140 m because a hit in the hodoscope T+V at 141 m was a requirement for the charged mode trigger. The decay region from 127 m to 129 m and upstream of 118.5 m was excluded in

[1]The UR was positioned 117.14 m downstream of the target and the DR was at 128.42 m.

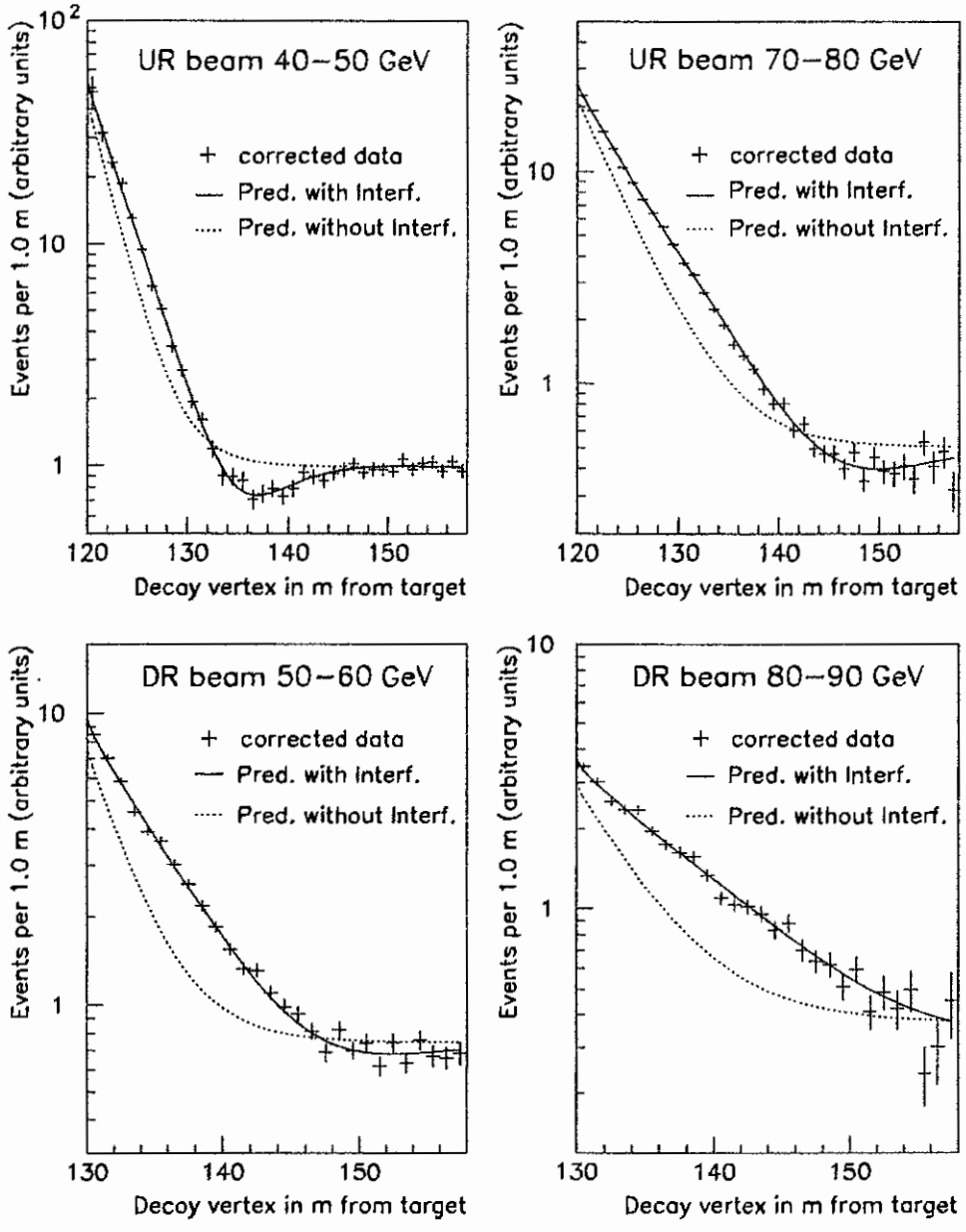

Figure 78. Background subtracted and acceptance corrected decay distribution for $\pi^0\pi^0$ decays in different energy bins. Overlayed are the predictions with and without the interference term. Data sets 1 and 2 have been added in these plots.

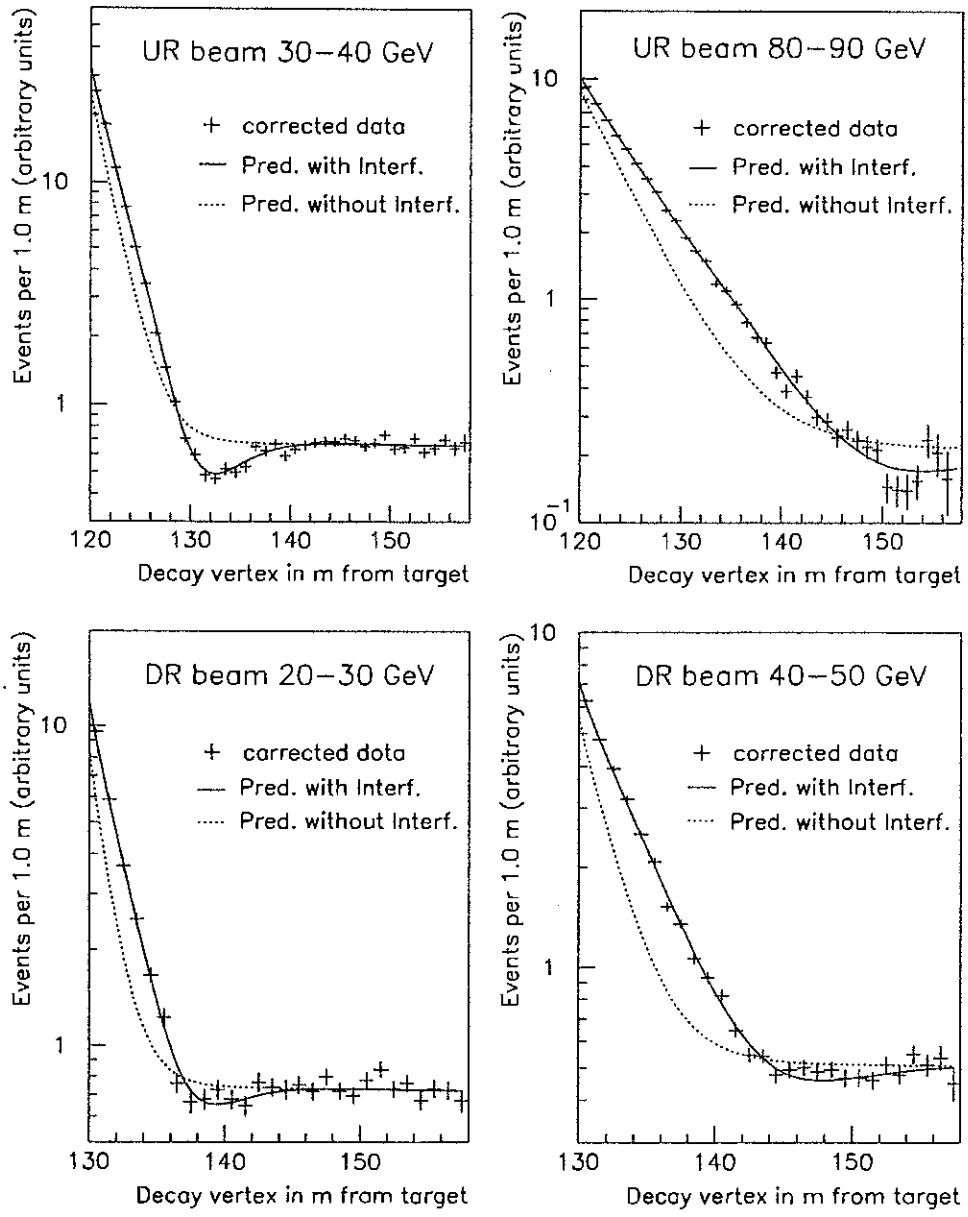

Figure 79. Background subtracted and acceptance corrected decay distribution for $\pi^+\pi^-$ decays in different energy bins. Overlayed are the predictions with and without the interference term. Only data set 2 is used in these plots because of the shorter decay region in charged mode for set 1.

the UR beam analysis because of the background contamination from beam interactions in the vacuum windows and air.

In neutral mode the fitted decay region extended from 120 m (130 m) to 152 m for the UR (DR) beam for both data sets. The bin size was 2 m for both modes and data sets. Table 3 lists the number of data events after the background subtraction used in the fit.

In both modes the beginning of the decay region started downstream of the regenerators, i.e. no attempt was made to fit the sharp rising edge of the decay rate next to the regenerators. This edge is sensitive to the simulation of the glass resolution and multiple scattering in the vacuum windows and air and the uncertainties in our Monte Carlo would have resulted in a larger systematic error.

The fit result with the statistical error and the dependence on Δm and τ_S is

$$\Delta\Phi = 0.62^\circ \pm 0.71^\circ - 0.030^\circ \frac{(\Delta m - 0.5282 \cdot 10^{10}\hbar s)}{0.0030 \cdot 10^{10}\hbar s} - 0.009^\circ \frac{(\tau_S - 0.8926 \cdot 10^{-10} s)}{0.0012 \cdot 10^{-10} s} \quad (9.1)$$

This fit also yields:

$$|\frac{f(0) - \bar{f}(0)}{k}|_{70\ \mathrm{GeV/c}} = (1.214 \pm 0.006)\ \mathrm{mb} \quad (9.2)$$

$$\alpha = -0.560 \pm 0.007 \quad (9.3)$$

$$\Phi_{+-} = 43.40^\circ \pm 0.56^\circ \quad (9.4)$$

$$|\frac{\eta_{00}}{\eta_{+-}}| - 1 = -0.012 \pm 0.007 \quad (9.5)$$

with $|(f - \bar{f})/k|$ and α parameterizing the regeneration amplitude ρ for carbon (see equation 1.61 and [Briere 95b]). The errors are statistical only.

The fit value for Φ_{+-} is consistent with the result from the charged mode of $43.53^\circ \pm 0.58^\circ$. Note that the statistical error on Φ_{+-} improves a little when the neutral mode data is added. This improvement is however offset by the increase in the systematic error from the lead glass simulation.

Note that $|\eta_{00}/\eta_{+-}|$ can be related to $\mathrm{Re}(\epsilon'/\epsilon)$ which was measured by E731 ($\mathrm{Re}(\epsilon'/\epsilon) = (7.4 \pm 5.9) \cdot 10^{-4}$ [Gibbons 93a]) and NA31 ($\mathrm{Re}(\epsilon'/\epsilon) = (23 \pm 6.5) \cdot 10^{-4}$ [Barr 93]) by $\mathrm{Re}(\epsilon'/\epsilon) \approx (1 - |\eta_{00}/\eta_{+-}|)/3 = (39 \pm 23) \cdot 10^{-4}$ (statistical error). Since this quantity depends on the neutral mode data a problem in the lead glass simulation or background subtraction

could have shifted the central value and made it inconsistent with the E731/NA31 results. There is no hint for such a problem.[2]

In the previous chapter the possible bias of the charged mode energy spectrum by the E/p cut was discussed. Two fit parameters were added to allow for a energy dependent difference between the charged and neutral mode acceptance. These factors multiplied the neutral mode flux by $(1 + A \cdot E_{kaon} + B \cdot E_{kaon}^2)$. The fit results are $A = (4.4 \pm 6.1) \cdot 10^{-4}$ and $B = -(7.6 \cdot \pm 33.6) \cdot 10^{-7}$. Both numbers are consistent with zero, i.e. the acceptance bias is small.

The χ^2 of the fit is 1192 for 1150 degrees of freedom, which is 0.9σ high. Table 4 shows the number of fit bins and the χ^2 contributions from each of the eight data subsets. All subsets contribute about evenly to the total χ^2.

The global correlation coefficient for $\Delta\Phi$ is 80% and the correlation with $|\eta_{00}/\eta_{+-}|$ is the largest. Fig. 80 shows the correlation between the the two parameters in our fit.

If the neutral mode data alone are used to fit for $|(f - \bar{f})/k|_{70}$, α and Φ_{00} we find:

$$|\frac{f(0) - \bar{f}(0)}{k}|_{70 \text{ GeV/c}} = (1.234 \pm 0.012) \text{ mb} \quad (9.6)$$

$$\alpha = -0.542 \pm 0.021 \quad (9.7)$$

$$\Phi_{00} = 42.7^\circ \pm 1.6^\circ \quad (9.8)$$

The χ^2 of the fit is 535 for 526 degrees of freedom. The errors are much larger than for the fit to the charged and neutral mode data which shows that $|(f - \bar{f})/k|_{70}$ and α in our combined fit are determined mainly by the charged mode data. The results from the fit to the neutral mode data only are consistent with the values found in the combined fit.

Note that the central value for $\Phi_{00} = \Delta\Phi + \Phi_{+-}$ has shifted relative to the combined fit by -1.3°, which is however due to a shift in the regeneration phase Φ_ρ: the phase in the interference term of the decay distribution depends on $\Phi_\rho - \Phi_{00}$ and $\Phi_\rho \propto -i\pi\alpha/2$ (see equation 8.4). α changed by $+0.018$ relative to the combined fit, i.e. Φ_ρ changed by -1.6° and $\Phi_\rho - \Phi_{00}$ changed by $+0.3^\circ$ only.

If Δm and τ_S are extracted with the neutral mode data we find:

[2] If we wanted to measure $|\eta_{00}/\eta_{+-}|$ in our experiment the decay regions used in the fit would have to include the regenerators to reduce the systematic error. Then the photon conversions inside the regenerators would have to be modeled extremely well.

Table 3. Number of data events after background subtraction used in the fit.

data set	number of events
charge mode, UR beam, set 1	333434
charge mode, UR beam, set 2	573480
charge mode, DR beam, set 1	70746
charge mode, DR beam, set 2	153009
neutral mode, UR beam, set 1	70566
neutral mode, UR beam, set 2	146614
neutral mode, DR beam, set 1	24579
neutral mode, DR Beam, set 2	50427

Table 4. Contributions to the number of fit bins and the χ^2 from the two beams, modes and data sets.

data set	number of fit bins	χ^2
charge mode, UR beam, set 1	153	140
charge mode, UR beam, set 2	246	255
charge mode, DR beam, set 1	70	86
charge mode, DR beam, set 2	161	174
neutral mode, UR beam, set 1	159	157
neutral mode, UR beam, set 2	165	144
neutral mode, DR beam, set 1	103	125
neutral mode, DR Beam, set 2	107	110
total	1164	1192

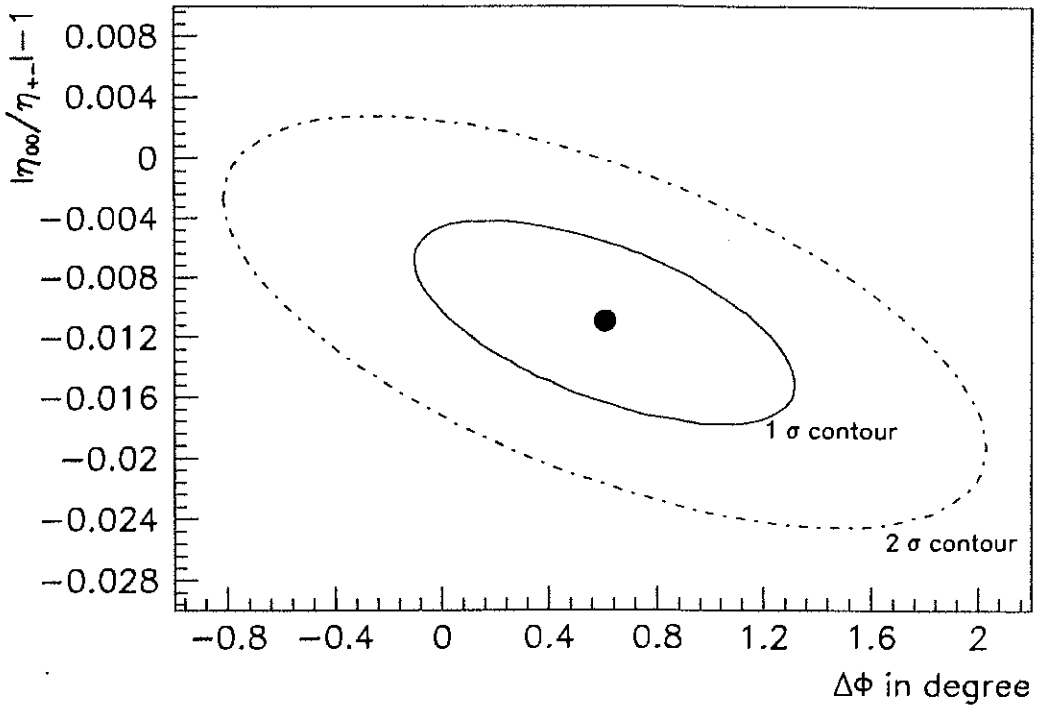

Figure 80. Correlation between $\Delta\Phi$ and $|\eta_{00}/\eta_{+-}| - 1$ in our fit. The dot corresponds to the fitted values with the lowest χ^2 while the ellipses are the 1σ and 2σ contours.

$$\Delta m = (0.5292 \pm 0.0054) \cdot 10^{10} \hbar s \tag{9.9}$$

$$\tau_S = (0.8916 \pm 0.0033) \cdot 10^{-10} s \tag{9.10}$$

The errors are statistical errors only and Φ_{00} is set to the superweak phase in the fit (see equation 1.56). The same fit to the charged mode data yields:

$$\Delta m = (0.5288 \pm 0.0026) \cdot 10^{10} \hbar s \tag{9.11}$$

$$\tau_S = (0.8941 \pm 0.0014) \cdot 10^{-10} s \tag{9.12}$$

Again, the results from neutral and charged mode are consistent while the statistical error of the neutral mode data is much bigger than for the charged mode data. Adding the neutral

mode data in the determination of Δm and τ_S therefore reduced the statistical error very little.

In the following two chapters the systematic error calculation for $\Delta\Phi$ is discussed and the conclusion is presented. However, the main conclusion of the analysis can be drawn at this point already: $\Delta\Phi$ is consistent with zero. We found therefore no evidence for a violation of the CPT symmetry.

CHAPTER 10

Checks and Systematic Errors

This chapter describes the sensitivity of the $\Delta\Phi$ result on our understanding of the calorimeter, the background subtraction and the acceptance for the charged and neutral mode decays. For example, how does the answer change if the number of subtracted diffractive background events is increased by 10%? From such studies the systematic error will be determined.

In addition, several checks of the answer are discussed, e.g. $\Delta\Phi$ should not depend on the cut thresholds chosen in the analysis or the size of the (p, z) bins used in the fit.

10.1 Checks of the Result

The checks of the $\Delta\Phi$ result can be divided into two classes: consistency checks between fit results from different data subsets and sensitivity of $\Delta\Phi$ to changes in the analysis cuts.

Table 5 lists the results of the $\Delta\Phi$ fits from subsets of the data. The results from the UR and DR beam, data sets 1 and 2, and the two different energy fit ranges are statistically independent of each other and all results are consistent with each other. This is not surprising, since the χ^2 contributions from each set as listed in table 4 shows that all subsets are fitted equally well with the set of parameters from the combined fit.

Several cuts have been tightened to study the $\Delta\Phi$ sensitivity to the thresholds chosen in the analysis. The following list describes the cuts considered for neutral and charged

Table 5. $\Delta\Phi$ results for different data subsets. The result for each subset is statistically independent from that of its complimentary set. In the fits listed in the last two lines the energy range is split: the low energy range spans from 20 GeV to 70 GeV for charged and for 40 GeV to 80 GeV for neutral mode. The high energy range interval is from 70 GeV to 160 GeV in charged mode and 80 GeV to 150 GeV in neutral mode.

subset	$\Delta\Phi$	fit χ^2/d.o.f.
UR beam	$0.11° \pm 1.03°$	693/710
DR beam	$2.12° \pm 2.56°$	481/428
data set 1	$-0.12° \pm 1.26°$	492/473
data set 2	$0.73° \pm 0.86°$	674/667
low energy range	$0.86° \pm 0.87°$	444/430
high energy range	$-0.04° \pm 1.26°$	725/706

mode and tables 6 and 7 lists the fit result, respectively. The new analysis requirements were applied to the data, the signal and the background Monte Carlos.

- The ring number cut was tightened from 120 cm^2 to 60 cm^2 which reduces the background level and therefore checks the subtraction of noncoherent kaon decays.
- The mass cut was changed from ± 24 MeV/c^2 around the kaon mass to ± 13 MeV/c^2. This reduces the level of $K_L \to 3\pi^0$ background and tests the lead glass resolution.
- Events where the central block of one of the clusters was next to a beam hole were excluded from the analysis. These pipe blocks experienced the worst radiation damage during the experiment.
- Events with a maximal cluster energy above 60 GeV were excluded. This tests biases due to nonlinearities or cluster shape cuts.
- The minimal cluster energy cut was tightened from 2.2 GeV to 3.2 GeV and 4 GeV to test possible nonlinear responses at small energies.
- Cuts on the limiting apertures of the DR table and the iron ring were tightened. This tests the simulation of the outer acceptance edge.

- The kaon energy range for neutral mode was reduced from 50 GeV to 140 GeV.
- In neutral mode, the upper limit of the decay region was reduced to 148 m and 146 m. The decay region excluded is sensitive to the $3\pi^0$ background subtraction.
- The start of the fit region for neutral mode was shifted from 120 m to 122 m for the UR beam and from 130 m to 132 m for the DR beam.
- The upper limit of the decay region for charged mode was restricted to 150 m.
- The start of the fit region for charged mode was shifted from 118 m to 120 m for the UR beam and from 130 m to 132 m for the DR beam.
- The momentum region in charged mode was restricted to 40 GeV/c to 150 GeV/c.

For all checks the change in the answer is either small or insignificant. In case the minimal cluster energy threshold was changed from 2.2 GeV to 4.0 GeV the absolute change of the answer and the significance were largest. In earlier stages of the analysis the shift in the answer was even larger and we therefore looked for possible problems with the lead glass simulation. When the data were broken up into four sets $\Delta\Phi$ changed by $+1.1\sigma$, $+3\sigma$, -1.3σ and $+1.1\sigma$ for the sets when the cut was tightened. The subsets behaved quite differently indicating that a statistical fluctuation in the data is responsible for the effect.

We also generated four Monte Carlo samples, used one as fake data and the remaining three to calculate the acceptance. One of the samples behaved similar to the data: if this sample was taken as fake data the answer shifted by more than 2σ when the cut was tightened. We checked whether a nonlinear response of the lead glass (like adding 50 MeV to every cluster energy in the simulation, see Fig. 84) or a mismatch between the data and Monte Carlo resolution at low energies could explain the dependence of the answer on the cut threshold. Non of the studies however changed the sensitivity of $\Delta\Phi$ on the cut value. If the cut was tightened even further to 6 GeV, $\Delta\Phi$ changed in the opposite direction such that the answer was close to the standard fit. We concluded that the sensitivity of $\Delta\Phi$ on the minimum cluster energy threshold is not due to a systematic effect.

Finally, the z bin size was changed from 2 m to 1 m for charged and neutral mode. This almost doubled the number of degrees of freedom. For neutral mode the bin width was

Table 6. $\Delta\Phi$ results after tightening some of the analysis cuts in the *neutral* mod analysis. The first column lists the cut and how it was tightened. The second column list the fraction of data events lost because of the change in the cut. The third and fourth colum list $\Delta\Phi$ and the change relative to the standard fit. The last column gives the statistica significance of the shift by assuming the error and the central value of the standard fit i the average of the fits from two data subsets: the events left after the cut is tightened an the complementary set consisting of events lost due to the shift in the cut threshold.

analysis cut changed	event loss	$\Delta\Phi$	change in $\Delta\Phi$	σ
ring number cut, 60 cm^2	5.4%	$0.68° \pm 0.72°$	0.07°	0.6
mass cut, 13 MeV/c^2	4.4%	$0.70° \pm 0.72°$	0.09°	0.7
aperture cuts	8.6%	$0.60° \pm 0.74°$	0.01°	0.04
pipe block cut	15.5%	$0.79° \pm 0.89°$	0.18°	0.3
max. cluster energy, 60 GeV	10.4%	$0.57° \pm 0.74°$	0.14°	0.2
min. cluster energy, 3.2 GeV	10.3%	$0.84° \pm 0.75°$	0.65°	1.0
min. cluster energy, 4 GeV	20.0%	$1.26° \pm 0.80°$	0.65°	1.8
energy region 50 to 140 GeV	7.5%	$0.66° \pm 0.76°$	0.07°	0.6
decay region ends at 148 m	2.3%	$0.39° \pm 0.74°$	0.22°	1.1
decay region ends at 146 m	3.7%	$0.48° \pm 0.75°$	0.13°	0.5
decay region starts 2 m downstr	18.6%	$0.87° \pm 0.76°$	0.26°	1.0

Table 7. $\Delta\Phi$ results after tightening some *charged* mode analysis cuts. The meaning of the columns are the similar as in the previous table.

analysis cut changed	event loss	$\Delta\Phi$	change in $\Delta\Phi$	σ
decay region ends at 150 m	3.4%	$0.70° \pm 0.72°$	0.09°	0.8
decay region starts 2 m downstr	25%	$0.43° \pm 0.74°$	0.26°	0.9
energy region 40 to 150 GeV	9.0%	$0.31° \pm 0.73°$	0.3°	1.7

comparable to the vertex resolution and the fit therefore depended on the modeling of the lead glass energy resolution. The fit result was $\Delta\Phi = 0.63^\circ \pm 0.71^\circ$ and the χ^2 was 2345 for 2185 degrees of freedom.

10.2 Systematic Error

The neutral mode analysis depends strongly on the energy reconstruction of the calorimeter. The understanding of the lead glass response is therefore the dominant source of the systematic error. To estimate its influence we analyzed the sensitivity of $\Delta\Phi$ to changes in the absolute energy scale, the nonlinear response of the glass and the calorimeter resolution simulation. In every study the Monte Carlo cluster energies were modified and the acceptance was recalculated. The fitted $\Delta\Phi$ was then compared to the standard fit result. Other contributions to the systematic error originate from the background subtraction and the acceptance correction.

10.2.1 Lead Glass Systematics

The regenerator edge matching procedure was used to find the absolute energy scale of the calorimeter (see section 5.5). To estimate how well this can be determined we studied the z overlays between data and Monte Carlo as a function of the variation in the scale. For example, when all cluster energies were increased by 0.08% for Monte Carlo events the edge of the decay distribution at the regenerators moved upstream relative to the data as shown in Fig. 81. These overlays should be compared to Fig. 63 and 64. The difference between the edge position for data and Monte Carlo is clearly visible and we choose this scale to limit the uncertainty in the edge matching. If the acceptance is calculated using the Monte Carlo with the scaled cluster energies the fit result for $\Delta\Phi$ changes by $\approx 0.45^\circ$. This shift is taken as the systematic error on the determination of the absolute energy scale.

The regenerator edge matching was also used to compensate for the nonlinear response of the calorimeter since the energy scale factor was calculated as a function of the kaon energy. For data set 2 the scale factor was $(1 + \alpha E_{kaon})$ with $\alpha = 3.5 \cdot 10^{-5}$. (see section 5.5). To

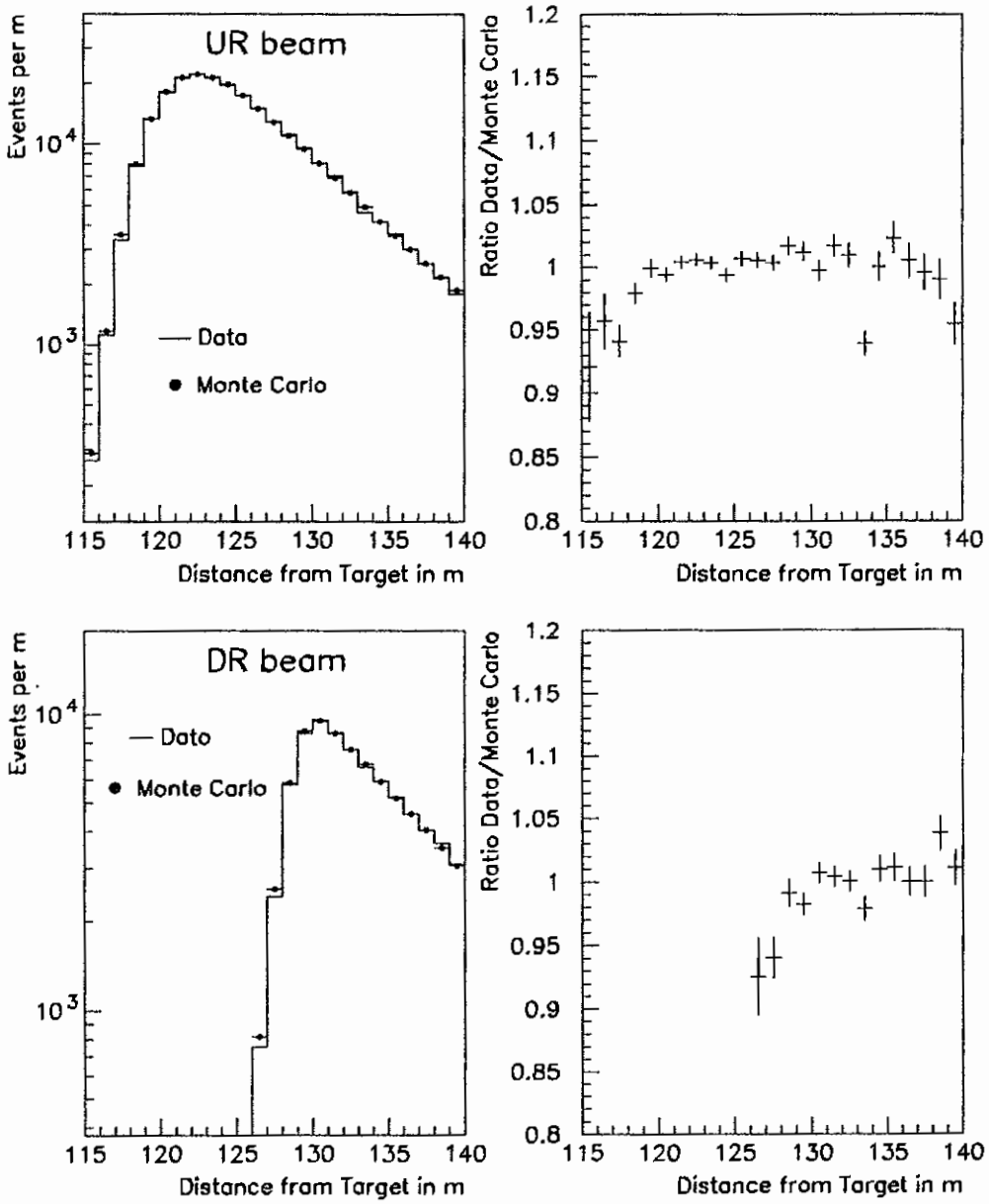

Figure 81. Decay distributions for $\pi^0\pi^0$ events and the ratio of the overlays after th energy scale of the Monte Carlo was changed by 0.08%. The position of the rising edge a the location of the regenerators is shifted between the data and the Monte Carlo after th scaling.

estimate the sensitivity of $\Delta\Phi$ to the uncertainty in the nonlinear lead glass response, our result was compared to the one we would have gotten without the nonlinear part αE in the scale factor. The average kaon energy E_{avg} was about 80 GeV and the average scale factor was therefore $\alpha E_{avg} \approx 0.3\%$. In the study the Monte Carlo cluster energies were therefore multiplied by $(1.003 - E_{kaon} \cdot 0.003/E_{avg})$. This scale factor therefore does not shift the average kaon energy and the overall position of the regenerator edge for the Monte Carlo but removes the nonlinearity introduced by the edge matching. We find that $\Delta\Phi$ changes by 0.4° in this study.

Two additional studies were performed to estimate the systematic from the nonlinear response. In one test, 50 MeV was added to every cluster energy in the Monte Carlo. This corresponds to a coherent shift by 1 ADC count for all blocks and would have been clearly visible in accidental events (see Fig.23). Fig. 82 shows how the position of the upstream regenerator edge moves in this case. After the edge matching procedure was applied to the Monte Carlo (with the 50 MeV shift in the cluster energy) the overlay agreed much better (see Fig.83). Before the edge is matched, $\Delta\Phi$ changed by $+2.1°$; after the edge matching $\Delta\Phi$ changed by $-0.31°$ relative to the standard fit. The edge matching was therefore very successful in taking out the nonlinearity introduced by the 50 MeV energy shift. The overlay χ^2 for the distribution of the minimal cluster energy (Fig.61) changed from 79 over 83 degrees of freedom to 163 for the UR beam (see Fig 84). Fig. 85 shows the E/p versus p distribution for electron. The dashed curve shows, how these points would be affected by a 50 MeV shift in the energy. Such an energy shift is therefore ruled out.

In the third study of the nonlinear lead glass response every cluster energy in Monte Carlo events was rescaled by a factor $(1 + 0.0004 \cdot E_{cluster})$. Whereas the 50 MeV energy shift has mainly affected low energy clusters this scale factor is biggest at high energies. The dotted line in Fig. 85 shows how this scaling would affect the E/p distribution for electrons. For $\pi^0\pi^0$ decays the mean of the reconstructed four photon mass shifts when this nonlinear scaling is applied. Recall that the mean of the mass distribution is shifted between data and Monte Carlo (see Fig. 34) which indicates that the nonlinear response of the lead glass is not simulated correctly. For the data the means are 497.4 MeV/c^2 and 497.3 MeV/c^2 for the UR and DR beams, respectively. The equivalent numbers for the Monte Carlo are

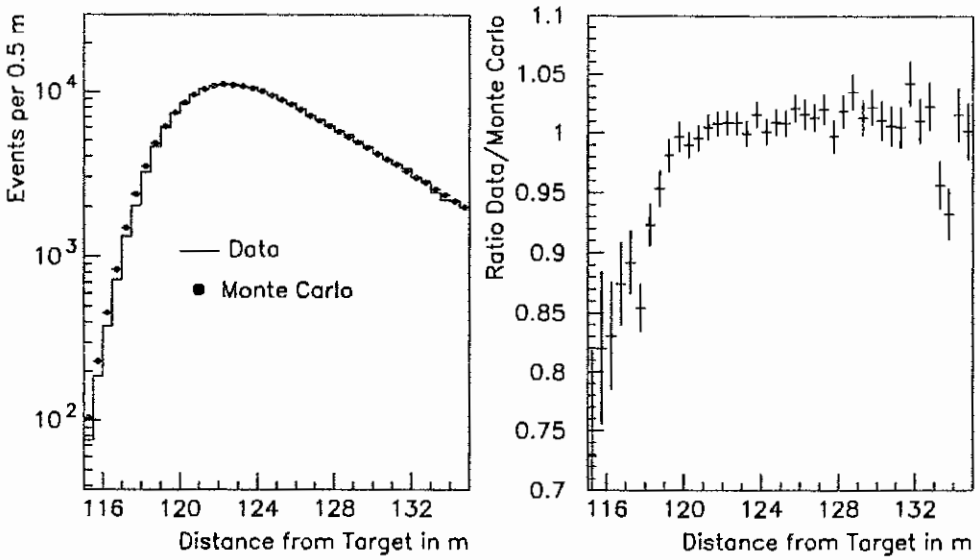

Figure 82. Decay distributions for UR $\pi^0\pi^0$ events and the ratio of the overlays a
50 MeV was added to every Monte Carlo cluster energy.

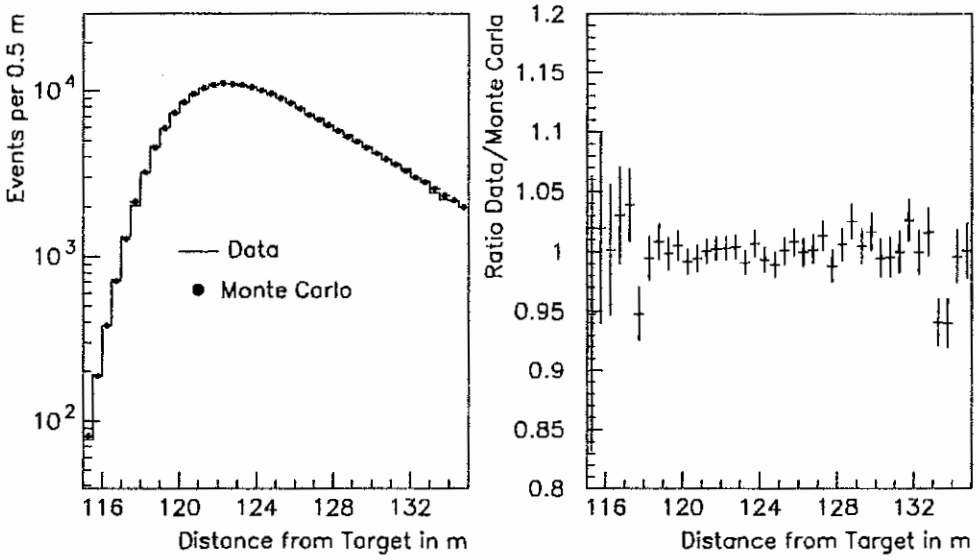

Figure 83. Decay distributions for UR $\pi^0\pi^0$ events and the ratio of the overlays af
50 MeV was added to Monte Carlo cluster energies and the regenerator edge position w
matched.

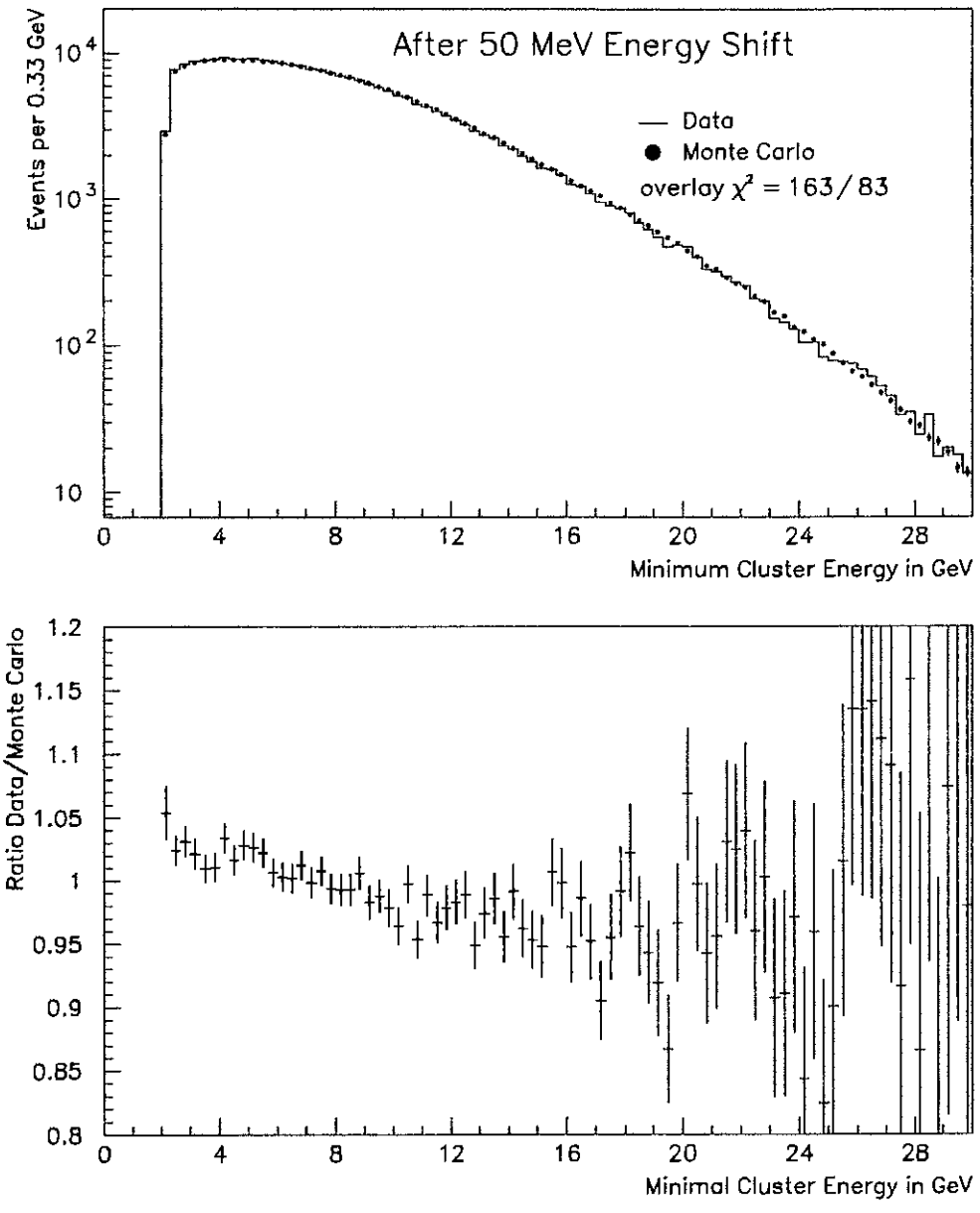

Figure 84. Minimum cluster energy distribution for the UR beam after 50 MeV wa added to Monte Carlo cluster energies. The bottom plot shows the ratio of the data ove the Monte Carlo distribution.

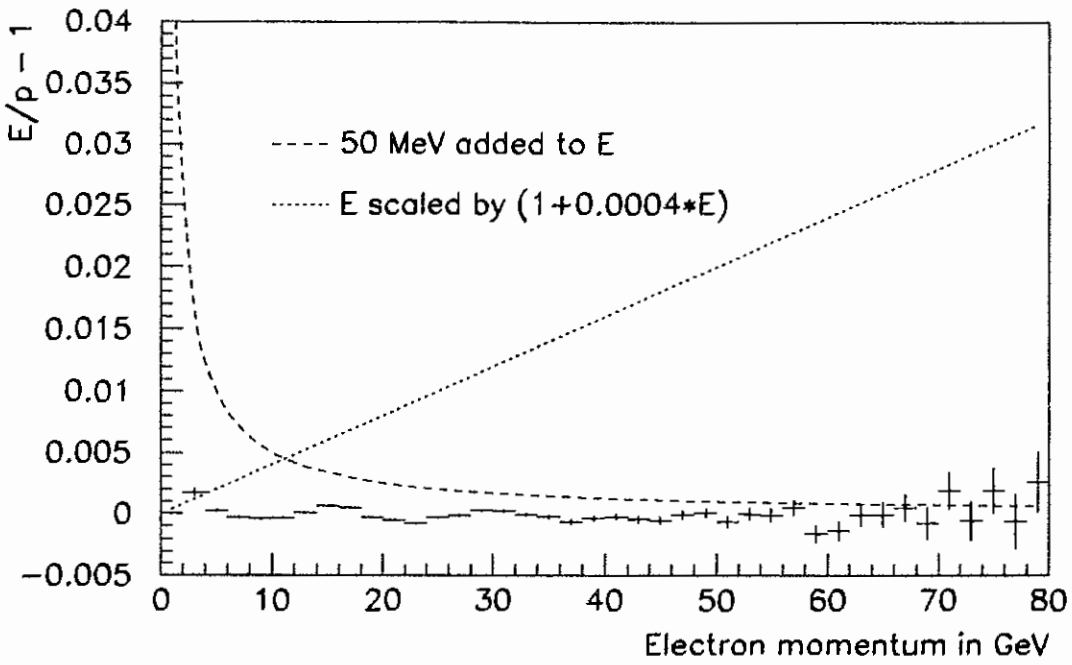

Figure 85. E/p versus p distribution for electrons. Overlayed are curves how E/p would look if 50 MeV is added to the cluster energy and if the cluster energies are rescaled by $(1 + 0.0004 \cdot E)$. Note that in practice the effects would be less dramatic since the calibration procedure would correct for some of the nonlinearities by finding a different absorption constant α.

497.7 MeV/c^2 and 497.5 MeV/c^2. After the energy scaling the means become 498.7 MeV/c^2 and 498.2 MeV/c^2 for the UR and DR, respectively. A 0.3 MeV/c^2 discrepancy between data and Monte Carlo became a 1.3 MeV/c^2 discrepancy after the scaling. The residual nonlinearity between data and Monte Carlo should therefore be much smaller than the one introduced by this scale factor.

As in the previous case of the 50 MeV energy shift, the regenerator edge matching was able to compensate for most of the nonlinearity (see Fig. 86). The fit result before the matching was applied had shifted by +3.6° relative to the standard fit while the shift was only +0.4° after the matching. From the three studies an error of 0.3° was chosen to limit the systematic from the nonlinear response simulation of the lead glass.

To study the sensitivity of $\Delta\Phi$ on the simulation of the calorimeter resolution, every cluster energy for Monte Carlo events was smeared by scaling the energy with a random number chosen under a gaussian distribution with width σ of 1.5% and a mean of one.

Whereas the average resolution in the Monte Carlo is slightly better than the data resolution (RMS of $m_{4\gamma}$ is 5.99 MeV/c^2 for data and 5.97 MeV/c^2 for the Monte Carlo in the UR beam) the resolution of the Monte Carlo events degraded to 6.21 MeV/c^2 after the energies were smeared out. Fig. 87 shows the decay vertex overlay for downstream regenerator events after the energy smearing. The additional smearing affects the shape of the regenerator edge and shows the mismatch in the resolution between the two distributions. After the edge matching was performed $\Delta\Phi$ changed by 0.25° (relative to the standard fit) For the systematic error analysis the contribution from the resolution simulation was estimated to be 0.2°.

Adding the errors from the absolute energy scale determination, the nonlinearity simulation and the resolution simulation in quadrature yields 0.58° as the total systematic error due to the lead glass simulation.

10.2.2 Background Subtraction Systematics

Three different backgrounds were subtracted as described in chapter 5.3. The smallest background was the beam interaction background. If the number of subtracted events changed by 50% of itself $\Delta\Phi$ changed by 0.1°. This was used to estimate the systematic error contribution from this background.

The background from $K_L \rightarrow 3\pi^0$ decays strongly depends on the decay vertex and energy (see Fig. 38). As mentioned in chapter 5.3 the energy distribution did not match between data and the simulation. The background Monte Carlo events were weighted with $(0.68 + 0.0043 \cdot E_{kaon})$. $\Delta\Phi$ changes by 0.25° when this scale factor is applied. Since the origin of the mismatch is not known the full size of the effect was chosen as the systematic error from the $3\pi^0$ background subtraction.

The background from noncoherent kaons decays was the largest. The systematic error contribution does not scale with the size of the background since the shape of the (p, z) distribution is important. The background from scattered kaons consisted mainly of inelastically and diffractively scattered kaons at the regenerators. Smaller contributions originate from scattering in the vacuum windows and air and scattering in the T+V hodoscope. The

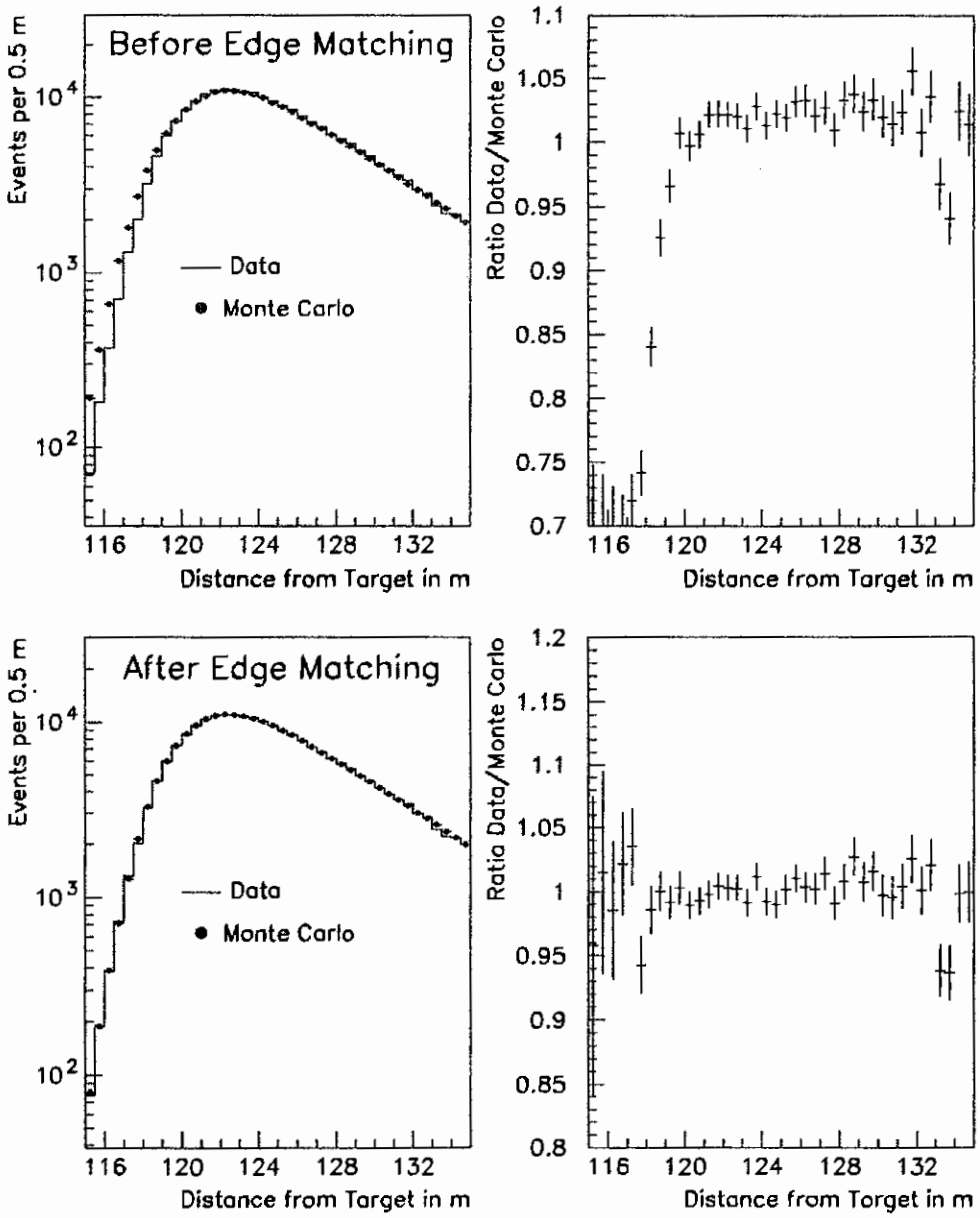

Figure 86. Decay vertex distribution of $\pi^0\pi^0$ events for the upstream regenerator beam after the Monte Carlo cluster energies were scaled by $(1 + 0.004 \cdot E_{cluster})$. Shown are the distributions before and after the regenerator edge was matched and the ratios of data over Monte Carlo.

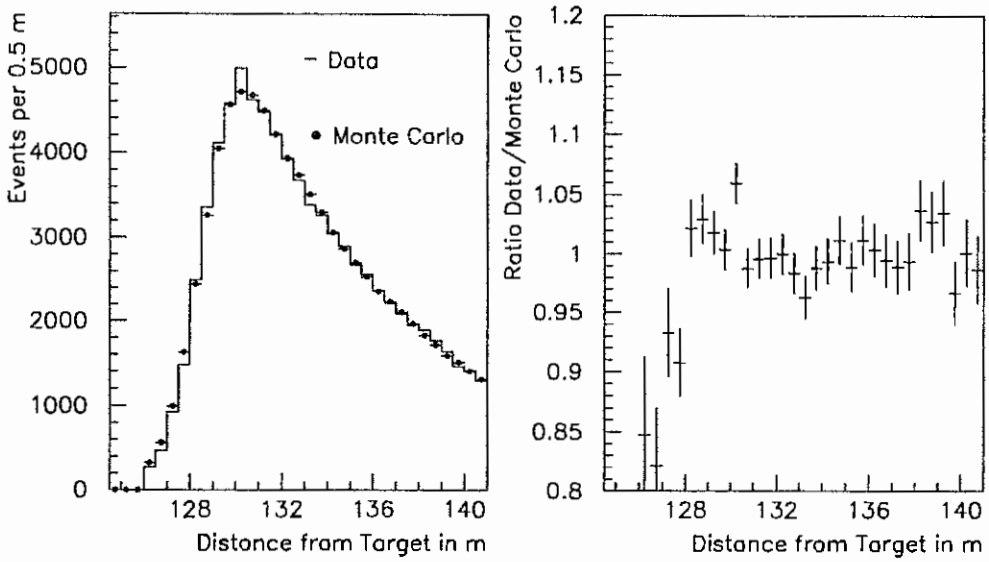

Figure 87. Decay vertex distribution of $\pi^0\pi^0$ events for the downstream regenerator beam after the Monte Carlo cluster energies were smeared.

effects of the last two background on $\Delta\Phi$ are quite small. If the level of events that scattered in T+V was doubled $\Delta\Phi$ changed by 0.05°. Not subtracting scattering events in the vacuum window for the UR beam (at the z position of the DR) changes $\Delta\Phi$ by 0.02°.

Another negligible component in the background subtraction comes from the kaons that scatter diffractively off hydrogen atoms. If the level of events included in the simulation was set to zero $\Delta\Phi$ changes by 0.04°.

Scaling the number of subtracted regenerator inelastic events by 130% changes the answer by 0.1°. Fig. 88 shows the ring number data/Monte Carlo overlay for UR $\pi^0\pi^0$ events after the scaling. Obviously, a 30% error on the number of inelastic events can be ruled out.

The ratio of diffractive to coherent events is the same for charged and neutral mode events. For the systematic error analysis the charged mode p_T^2 distributions could therefore be used to limit a possible bias in the simulation. Fig. 89 shows the p_T^2 overlay after the level of diffractive events have been scaled by 1.1 and 1.05 for the UR and DR beam,

respectively. The discrepancy between the shifted Monte Carlo and the data distributi is clearly visible. After the scaling the answer changes by 0.34°.[1]

Other checks on the background subtraction of diffractive events include a change the ratio of double over single diffractive events by 33% and changing the energy and dec vertex distributions of the background events.

From the above studies the systematic error from the background subtraction of no coherent events was estimated to be 0.3°. To summarize, the total systematic from background subtractions is 0.4° which was calculated by adding in quadrature 0.3° (nonc herent subtraction), 0.25° ($3\pi^0$ background) and 0.1° (beam interaction background).

No separate systematic error was assigned to the charged mode background subtractio The background level was much smaller than for the neutral mode data and the backgrour in both modes was dominated by diffractive and inelastic events, hence correlated. Tl additional background from $K_L \to \pi e \nu$ decays was much smaller than the background fro scattered kaons [Briere 95b] and the systematic error contribution was therefore neglecte

10.2.3 Other Systematics

Fig. 69 shows the overlay of the data and Monte Carlo decay distributions for $K_L \to 3\pi$ events. The fitted slope for the UR beam is $(0.041 \pm 0.0012)\%$ per meter. To estimat the affect on $\Delta\Phi$ from such a slope the acceptance was scaled by a z dependent facto $(1 + (z - 135\text{m}) \cdot 0.001)$. Consequently, $\Delta\Phi$ changed by 0.22°.

The acceptance depends on the apertures of the detector. The inner acceptance edge i defined by the CA (see chapter 2.6) and the position of the CA was found with the dat using the measured position of electrons as described in chapter 3. Statistically, the CA position was determined to better than 0.1 mm. To study the effect of this inner aperture on the acceptance, the CA size was increased by 1.5 mm in the Monte Carlo. This resulted in a shift of $\Delta\Phi$ by 0.13°. From these two studies a systematic error of 0.2° was assigned to the acceptance simulation in neutral mode.

[1]The sensitivity stems mainly from the DR beam since the level of noncoherent background is about a factor of 3.5 higher than for the UR beam.

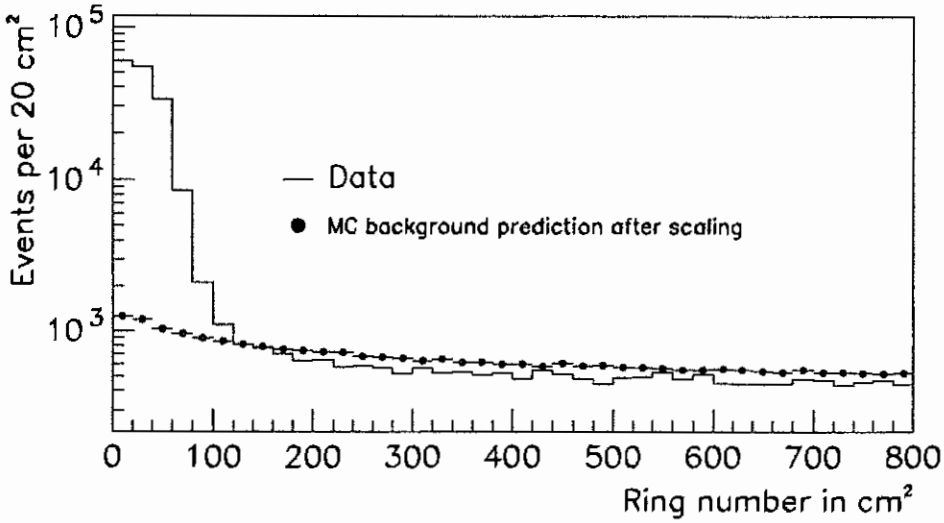

Figure 88. Ring number distribution for UR regenerator $\pi^0\pi^0$ decays after the level of inelastic events was rescaled by 1.3.

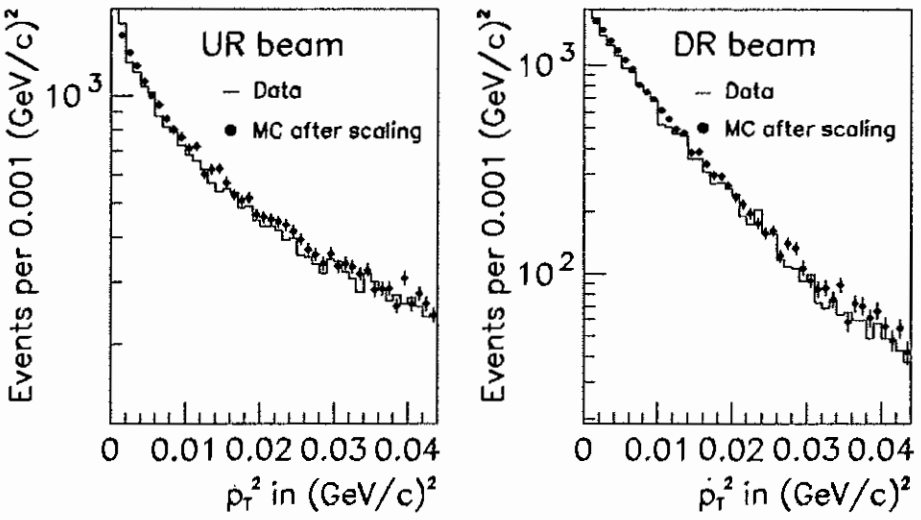

Figure 89. p_T^2 for UR and DR regenerator $\pi^+\pi^-$ decays after the level of diffractive events was rescaled by 1.1 and 1.05 for the UR and DR Monte Carlo, respectively.

Table 8. Contributions to the systematic error

source	systematic error
lead glass simulation	0.58°
background subtraction	0.40°
neutral mode acceptance	0.20°
charged mode acceptance	0.13°
screening correction	0.07°
total	0.75°

The charged mode acceptance systematic was evaluated similarly. The calculated ceptance was scaled by $(1 + \alpha(z - 135\text{m}))$ with $\alpha = 3.3 \cdot 10^{-4}$ m^{-1}. Consequently, Δ changed by 0.13°. In Fig. 75 and 74 the decay distribution overlays for $K_L \to \pi e\nu$ dec are plotted. The ratio plots show no evidence for an acceptance problem causing a slope $3.3 \cdot 10^{-4}$ m^{-1}.

The $\Delta\Phi$ analysis was quite insensitive to the phase Φ_ρ of the regeneration amplitu ρ since the charged and neutral mode interference distributions depend on the differe of the regeneration phase and the phase of η, $\Phi_\rho - \Phi_\eta$. For the phase difference $\Delta\Phi$ $(\Phi_\rho - \Phi_{+-}) - (\Phi_\rho - \Phi_{00})$, the phase of ρ drops out. However the screening effects caus deviation from a pure power law behavior of ρ as discussed in reference [Briere 95b]. T affects $\Delta\Phi$ slightly. To estimate the systematic effect from the screening calculation shift of the fit result by 0.07° for different inelastic screening corrections was taken.

Table 8 list all sources of systematic errors considered. Adding all contribution quadrature yields 0.75°.

CHAPTER 11

Conclusion

The final result for $\Delta\Phi$ with the statistical and systematic error is

$$\Delta\Phi = 0.62^\circ \pm 0.71^\circ(stat) \pm 0.75^\circ(syst) \tag{11.1}$$

and its Δm and τ_S dependences are small and given in equation 9.1. Adding the statistical and systematic errors in quadrature gives $\Delta\Phi = 0.62^\circ \pm 1.03^\circ$ which is currently the most precise measurement of $\Delta\Phi$. The phase difference is consistent with zero and shows therefore no evidence for a CPT symmetry violation. However we cannot definitively rule out CPT violation since $\Delta\Phi$ depends on the difference of two amplitudes $(\epsilon' - a\omega/\sqrt{2})$ and both terms are in general CPT violating.

As mentioned in section 1.2 we also performed a second test of the CPT invariance. We measured

$$\begin{aligned}\Phi_{+-} = 43.53^\circ \pm 0.58^\circ(stat) \pm 0.49^\circ(syst) \quad &+ \quad 0.52^\circ \frac{(\Delta m - 0.5282 \cdot 10^{10}\hbar s)}{0.0030 \cdot 10^{10}\hbar s} \\ &- \quad 0.33^\circ \frac{(\tau_S - 0.8926 \cdot 10^{-10} s)}{0.0012 \cdot 10^{-10} s}\end{aligned} \tag{11.2}$$

This phase should be compared to the superweak phase defined in equation 1.56 which depends on Δm and τ_S. Our results for these parameters are

$$\tau_S = (0.8941 \pm 0.0014(stat) \pm 0.0009(syst)) \cdot 10^{-10} s \tag{11.3}$$

$$\Delta m = (0.5297 \pm 0.0030(stat) \pm 0.0022(syst)) \cdot 10^{10}\hbar s^{-1} \tag{11.4}$$

and after averaging with the E731 results:

$$\tau_S = (0.8935 \pm 0.0012) \cdot 10^{-10} s \qquad \text{E731/E773} \qquad (11.$$

$$\Delta m = (0.5282 \pm 0.0030) \cdot 10^{10} \hbar s^{-1} \qquad \text{E731/E773} \qquad (11.$$

Using our average Δm and $\tau_S = (0.8926 \pm 0.0012) \cdot 10^{-10}$ s from [PDG 94] $\Phi_{sw} = 43.37°$ $0.17°$ which agrees well with our measurement of Φ_{+-}. The second CPT test shows therefo also no evidence for a violation of the symmetry.

In the τ_S fit Φ_{+-} was fixed to the superweak phase and Δm was floated. For all oth fits τ_S was fixed to the PDG central value to avoid the circular argument of first assumi CPT in the τ_S fit and then using the result to test CPT symmetry. In the Δm fit Φ_{+-} w floated because both quantities are highly correlated.

As for $\Delta\Phi$ our result for Φ_{+-} is the most precise single measurement. The next mo precise measurements being from E731. The above results are described in detail in tl thesis of Roy A. Briere [Briere 95b].

In the remainder of this chapter I will discuss other $\Delta\Phi$ measurements, give limits o CPT violating quantities as extracted from our data and briefly mention other ongoin efforts to test CPT.

There were 6 measurements of Φ_{00} or $\Delta\Phi$ prior to ours which are listed in table 9. Th three earlier measurements were all consistent with zero and had rather large error bar The result from reference [Christenson 79] is $\Delta\Phi = 12.6° \pm 6.2°$. This is important sinc it is inconsistent with zero at the 2σ level and therefore hints a CPT violating effect. Thi result motivated special runs at CERN and Fermilab (this experiment) to measure $\Delta\Phi$.

The two most recent and most precise measurements, namely ours and E731's, hav common systematic errors from the lead glass simulation. These correlations have to b considered when the two results are averaged. The error contributions to the E731 (our result are: $1.0°(0.71°)$ from the statistical error, $0.32°(0.03°)$ from the dependence on τ_S an Δm, $0.5°(0.58°)$ from the "lead glass" systematic error and $0.5°(0.47°)$ from the uncorrelate systematic error sources.

After correcting the E731 central value for the Δm and τ_S used in our fit we get:

$$\Delta\Phi = -1.7° \pm 1.16°(uncorr) \pm 0.5°(corr) \qquad \text{E731} \qquad (11.7$$

$$\Delta\Phi = 0.62° \pm 0.85°(uncorr) \pm 0.58°(corr) \qquad \text{E773} \qquad (11.8$$

Table 9. Previous measurements and the current result of Φ_{00} or $\Delta\Phi$.

reference	publication year	Φ_{00}	$\Delta\Phi$
[Chollet 70]	1970	$51° \pm 31°$	-
[Wolff 71]	1971	$38° \pm 25°$	-
[Barbiellini 73]	1973	-	$7.6° \pm 18°$
[Christenson 79]	1979	$55.7° \pm 5.8°$	-
[Carosi 90]	1990	$47.1° \pm 2.8°$	-
[Gibbons 93a]	1993	-	$-1.6° \pm 1.2°$
this result	1995	-	$0.62° \pm 1.03°$

To estimate the common systematic error the two lead glass systematic errors are averaged with a weight according to the total errors for each measurement, giving 0.55°. The uncorrelated errors for each experiment are then averaged and the common error 0.55° is added in quadrature. The two central values are averaged according to their total error. This yields:

$$\Delta\Phi = -0.30° \pm 0.88° \qquad \text{avg. E731/E773} \tag{11.9}$$

Averaging this with the NA31 result $\Delta\Phi = 0.2° \pm 2.9°$ [Carosi 90], which was corrected for its Δm and τ_S dependence, yields

$$\Delta\Phi = -0.26° \pm 0.84° \qquad \text{avg. NA31/E731/E773} \tag{11.10}$$

This angle can now be used to calculate $\eta_{00} - \eta_{+-}$:

$$\eta_{00} - \eta_{+-} = |\eta_{+-}|e^{i\Phi_{+-}} \left(\frac{|\eta_{00}|}{|\eta_{+-}|} \cos\Delta\Phi - 1 + i\frac{|\eta_{00}|}{|\eta_{+-}|} \sin\Delta\Phi \right) \tag{11.11}$$

$$\approx |\eta_{+-}|e^{i\Phi_{+-}} \left(\frac{|\eta_{00}|}{|\eta_{+-}|} - 1 + i\frac{|\eta_{00}|}{|\eta_{+-}|}\Delta\Phi \right) \tag{11.12}$$

In the last step $\Delta\Phi \ll 1$ was used. With the E731's result for $\mathrm{Re}(\epsilon'/\epsilon)$ [Gibbons 93c][1]

[1] The result and the statistical error was taken from table 20 of the reference since CPT conservation was not assumed in the fits listed. The systematic error ($2.9 \cdot 10^{-4}$) was taken from the standard analysis of $\mathrm{Re}(\epsilon'/\epsilon)$ which assumes CPT invariance.

$$\frac{|\eta_{00}|}{|\eta_{+-}|} = 0.9988 \pm 0.0022 \tag{11.13}$$

we find

$$\eta_{00} - \eta_{+-} = |\eta_{+-}| e^{i\Phi_{+-}} \{(-0.0012 \pm 0.0022) - i\,(0.005 \pm 0.015)\} \tag{11.14}$$

In chapter 1.2 we derived equation 1.50

$$\begin{aligned} \eta_{00} - \eta_{+-} &= -3(\epsilon' - a\omega/\sqrt{2}) = -\frac{3}{\sqrt{2}} \frac{\mathrm{Re}A_0(\mathrm{Re}B_2 + i\mathrm{Im}A_2) - \mathrm{Re}B_0\mathrm{Re}A_2}{\mathrm{Re}A_0(\mathrm{Re}A_0 + i\mathrm{Im}B_0)} e^{i(\delta_2 - \delta_0)} \\ &= -\frac{3}{\sqrt{2}} \frac{\mathrm{Re}A_0\mathrm{Re}B_2 - \mathrm{Re}B_0\mathrm{Re}A_2}{\mathrm{Re}A_0(\mathrm{Re}A_0 + i\mathrm{Im}B_0)} e^{i(\delta_2 - \delta_0)} - \\ &\quad \frac{3}{\sqrt{2}} \frac{\mathrm{Im}A_2}{\mathrm{Re}A_0 + i\mathrm{Im}B_0} e^{i(\pi + \delta_2 - \delta_0)} \end{aligned} \tag{11.15}$$

Here, A_k and B_k are the CPT conserving and violating amplitudes in the isospin $I = k$ channels, respectively. Since $(\pi + \delta_2 - \delta_0) = 48^\circ \pm 4^\circ$ [Chell 93] and $\Phi_{+-} \approx 44^\circ$ the second term of the last equation is almost parallel to η_{+-}. The first term, which is purely CPT violating, is therefore perpendicular to η_{+-}. From equation 11.14 the CPT conserving part of $\eta_{00} - \eta_{+-}$ is then $|\eta_{+-}|(0.0012 \pm 0.0022)$ and the CPT violating part is $|\eta_{+-}|(0.005 \pm 0.015)$. The experimental precision on the CPT conserving part is much better.

Following the argument in [Barmin 84] the resulting limit for the CPT violating parameters can be compared to the decay width difference into two pions for charged kaons and the charged kaon lifetime difference. Using their assumption for the CPT violating amplitudes $|\mathrm{Re}B_0\mathrm{Re}A_2| < |\mathrm{Re}B_2\mathrm{Re}A_0|$ and neglecting all $\mathrm{Im}B_k$ terms (which are CP conserving and CPT violating), the last equation and 11.14 yields

$$\frac{\mathrm{Re}B_2}{\mathrm{Re}A_2} = \frac{\mathrm{Re}B_2}{\omega \mathrm{Re}A_0} = \frac{\sqrt{2}}{3\omega} |\eta_{+-}| \Delta\Phi = (1 \pm 4) \cdot 10^{-4} \tag{11.16}$$

where $\omega \approx 1/22$ and $|\eta_{+-}| = 2.27 \cdot 10^{-3}$ have been used [PDG 94]. This can be related to the decay width difference for charged kaons:

$$\begin{aligned} \frac{\Gamma(K^+ \to \pi^+\pi^0) - \Gamma(K^- \to \pi^-\pi^0)}{\Gamma(K^+ \to \pi^+\pi^0)} &= \frac{|A_2 + B_2|^2 - |A_2^* - B_2^*|^2}{|A_2 + B_2|^2} \\ &= \frac{2\mathrm{Re}(A_2 B_2^*) + 2\mathrm{Re}(A_2^* B_2)}{|A_2|^2} \approx \frac{4\mathrm{Re}B_2}{\mathrm{Re}A_2} \end{aligned} \tag{11.17}$$

since $\mathrm{Im}A_2 \ll \mathrm{Re}A_2$ ($\epsilon' \ll \omega$). The current experimental limit is

$$\frac{\Gamma(K^+ \to \pi^+\pi^0) - \Gamma(K^- \to \pi^-\pi^0)}{\Gamma(K^+ \to \pi^+\pi^0)} = (8 \pm 12) \cdot 10^{-3} \tag{11.18}$$

The indirect limit as derived from equation 11.16 is $(4 \pm 14) \cdot 10^{-4}$ which is an order of magnitude more precise than the above direct measurement.

If one assumes that the only CPT violating effects in charged kaon decays are in the decays into two pions one finds $\Gamma(K^+ \to \text{all}) - \Gamma(K^- \to \text{all}) = \Gamma(K^+ \to \pi^+\pi^0) - \Gamma(K^- \to \pi^-\pi^0)$ and for the lifetime differences equation 11.16 yields:

$$\frac{\Gamma(K^+ \to \text{all}) - \Gamma(K^- \to \text{all})}{\Gamma(K^+ \to \text{all})} = \frac{\Gamma(K^+ \to \pi^+\pi^0) - \Gamma(K^- \to \pi^-\pi^0)}{\Gamma(K^+ \to \text{all})} \tag{11.19}$$

$$= 4\text{BR}(K^+ \to \pi^+\pi^0)\frac{\text{Re}B_2}{\text{Re}A_2} = (0.8 \pm 3)\cdot 10^{-4} \tag{11.20}$$

This should be compared to the direct experimental limit $(\tau^+ - \tau^-)/\tau^+ = (11 \pm 9) \cdot 10^{-4}$. Again, our indirect limit constraints possible CPT violations better than the direct test.

We can also extract information about the CPT violating terms in the mass matrix. From equations 1.47 and 1.48 we get

$$\frac{2}{3}\eta_{+-} + \frac{1}{3}\eta_{00} = \epsilon - \Delta + a \tag{11.21}$$

where Δ parameterizes CPT violation in mass matrix and a parameterizes CPT violation in the $I = 0$ decay amplitude. In our following discussion we assume $a = 0$. Since CPT violating effects are small, if they exist at all, $|\Delta| \ll |\epsilon|$. It is therefore easiest to measure $\Delta_\perp$, the component of Δ that is perpendicular to ϵ. From above equation we find

$$\Delta_\perp \approx |\eta_{+-}|(\frac{2}{3}\Phi_{+-} + \frac{1}{3}\Phi_{00} - \Phi_{sw}) = |\eta_{+-}|(\Phi_{+-} + \frac{1}{3}\Delta\Phi - \Phi_{sw}) \tag{11.22}$$

Here we used the fact that the phase of ϵ is very close to the superweak phase. From the definition of Δ, equation 1.24, we find

$$|\Delta_\perp| = \frac{1}{2}\frac{|M_{11} - M_{22}|}{|i\Delta m - \Delta\Gamma/2|} = \frac{1}{2}\frac{|m_{K^0} - m_{\bar{K}^0}|}{\Delta m}\sin\Phi_{sw} \tag{11.23}$$

with m_{K^0} and $m_{\bar{K}^0}$ being the mass of the K^0 and $\bar{K}^0$, respectively. Using the combined result for $\Delta\Phi$ (equation 11.10) and our results for $\Phi_{+-} = 43.53^\circ \pm 0.97^\circ$ and $\Phi_{sw} = 43.37^\circ \pm 0.17^\circ$ we get $\Phi_{+-} - \Phi_{sw} + \Delta\Phi/3 = 0.07^\circ \pm 0.96^\circ$. Here, the correlated Δm and τ_S dependence

of $\Phi_{+-} - \Phi_{sw}$ was taken into account. This yields $|\Phi_{+-} - \Phi_{sw} + \Delta\Phi/3| < 1.58°$ at the 90% confidence limit.[2] The limit on the mass difference is then

$$\frac{|m_{K^0} - m_{\bar{K}^0}|}{m_{K^0}} = \frac{2\Delta m}{m_{K^0} \sin \Phi_{sw}} |\eta_{+-}||\Phi_{+-} - \Phi_{sw} + \Delta\Phi/3| < 1.3 \cdot 10^{-18} \tag{11.24}$$

which is an impressive test of CPT invariance. The precision is of course mainly due to the small value of $\Delta m = 0.5282 \cdot 10^{10} \hbar s^{-1} = 3.477 \cdot 10^{-12} MeV/c^2$.

Above results can also be used to decompose η (or, to be more precise, a linear combination of η_{00} and η_{+-}) into a T violating (and CPT conserving) and CPT violating (and T conserving) part. This discussion uses the equation 9.142 of reference [Sachs 87]:

$$Z^e = e^{i\Phi_{sw}}(i\,\mathrm{Im}\{e^{-i\Phi_{sw}} Z\} - \Sigma) \tag{11.25}$$

$$Z^o = e^{i\Phi_{sw}}(\mathrm{Re}\{e^{-i\Phi_{sw}} Z\} + \Sigma) \tag{11.26}$$

where Z^e (Z^o) are the CPT (T) violating parts of $Z = (\eta_{00} + C\eta_{+-})/(1 + C)$ and $C = |Amp(K_S \to \pi^+\pi^-)|^2/|Amp(K_S \to \pi^0\pi^0)|^2 = 2.19 \pm 0.02$. In above equation Σ stands for

$$\Sigma = \frac{1}{\Gamma_S \sqrt{1 + (2\Delta m/\Gamma_S)^2}} \sum_{f \neq 2\pi} Amp(K_S \to f)\, Amp(K_L \to f)^* \tag{11.27}$$

where the sum is over all final states f except over the 2π modes. Because of the arguments used for the derivation of equation 1.56 Σ is expected to be very small. With the recently improved upper limits on $\eta_{+-0} < 0.06$ and the violation of the $\Delta S = \Delta Q$ rule ($|x| < 0.04$) [CPLEAR 95] the upper limit on Σ is dominated by the experimental limit on $|\mathrm{Im}(\eta_{000})| = 0.02 \pm 0.18$ [Barmin 83].

$$|\Sigma| < \frac{\Gamma_L}{\Gamma_S \sqrt{1 + (2\Delta m/\Gamma_S)^2}} BR(K_L \to 3\pi^0) |\mathrm{Im}(\eta_{000})| = 8 \cdot 10^{-5} \tag{11.28}$$

For the real and imaginary parts of $Ze^{-i\Phi_{sw}}$ one finds

$$\mathrm{Re}(Ze^{-i\Phi_{sw}}) \approx |\eta_{+-}| = (2.27 \pm 0.02) \cdot 10^{-3} \tag{11.29}$$

$$\mathrm{Im}(Ze^{-i\Phi_{sw}}) \approx \frac{|\eta_{+-}|}{1 + C}\{(\Phi_{+-} - \Phi_{sw})(1 + C) + \frac{|\eta_{00}|}{|\eta_{+-}|}\Delta\Phi\} = (0.3 \pm 3.8) \cdot 10^{-5} \tag{11.30}$$

[2] Averaging our value of Φ_{+-} and E731's does not significantly reduce the error because of the large correlated dependences on Δm and τ_S.

here equation 11.13, $\Delta\Phi = -0.26^\circ \pm 0.84^\circ \ll 1$ and $(\Phi_{+-} - \Phi_{sw}) = 0.16^\circ \pm 0.92^\circ \ll 1$ have been used.[3] This leads to

$$|Z^e| < 1.0 \cdot 10^{-4} \quad (11.31)$$

$$|Z^o| = (22.7 \pm 0.2) \cdot 10^{-4} \quad (11.32)$$

at the 90% C.L. Consequently, the CPT violating part of Z is very small and the data are consistent with Z being purely T violating.

Other experiments that test CPT symmetry in the neutral kaon system have collected data recently or are in preparation. The CPLEAR collaboration will soon publish their result of Φ_{+-}. In addition, this experiment is expected to make the first direct observation of T violation. In the near future the collaborations KTeV and NA48 at FNAL and CERN, respectively, will collect new data to measure ϵ'/ϵ, Φ_{+-}, $\Delta\Phi$, Δm and τ_S. Especially for the KTeV experiment a $\Delta\Phi$ measurement with a precision better than 0.3 degree is expected.

In Frascati, Italy, an electron-positron storage ring is under construction which will produce Φ mesons. This meson decays into $K_L + K_S$ with a branching ratio of 34%. The final state is $|K_L(\vec{p})\rangle|K_S(-\vec{p})\rangle - |K_L(-\vec{p})\rangle|K_S(\vec{p})\rangle$. The K_L and K_S states will then decay independently with decay times t_1 and t_2, respectively. By measuring the decay rate as a function of the time difference $t_1 - t_2$ for decays into the same and different final states single CPT violating amplitudes can be measured directly rather than a combination of them [Buchanan 92].

Note that only KTeV will be able to significantly improve the experimental precision on $\Delta\Phi$. The NA48 experiment has a very short decay region which compromises their ability to measure the interference term. For the other two experiments mentioned the kaon energies are much lower and the reconstruction of $K \to \pi^0\pi^0$ events is therefore very difficult.

When the Υ4S (Υ5S) resonance decays into two neutral B_d (B_s) mesons the same quantum mechanical state as for the Φ decay is created [Colladay 95, Kobayashi 92]. Since the B meson lifetime is about a factor of 70 smaller then the K_S lifetime and since the B_S and B_L lifetimes are very similar it is experimentally more challenging to test CP symmetry in B meson decays. Currently there are several experiments under construction to observe

[3] The correlated Δm and τ_S dependences of $\Phi_{+-} - \Phi_{sw}$ are taken into account.

CP violation and test the CPT invariance in the B system: at SLAC in the US, at KEK in Japan and at DESY in Europe [Schlein 93, Lohse 94]. All experiments are expected to take data by the year 2000.

Even though one might argue that the neutral K and B meson systems are premier places to look for symmetry violations because of the interferometric measurements there are other experimental efforts to test CPT. One example is the APEX experiment at Fermilab which tries to detect antiproton decays in the antiproton accumulator [Geer 94]. The ultimate expected lifetime sensitivity is approximately 10^7 years.

The neutral kaon system is a very interesting quantum mechanical system which plays an important role in the understanding of symmetry violations and therefore our understanding of particle physics. Our experiment performed two very sensitive tests of the CPT invariance and found no indication for a symmetry violation.

REFERENCES

[Adler 93] R. Adler et al., Nucl. Phys. **A558**, 437 (1993)

[Barbiellini 73] G. Barbiellini et al., Phys. Lett. **B43**, 529 (1973).

[Barmin 83] V.V. Barmin et al., Phys. Lett. **128B**, 129 (1983)

[Barmin 84] V.V. Barmin et al., Nucl. Phys. **B247**, 293 (1984), **B254**, 747(E) (1985).

[Barr 93] G.D. Barr et al., Phys. Lett. **B317**, 233 (1993).

[Bock 79] G. Bock et al., Phys. Rev. Lett. **42**, 350 (1979)

[Briere 95a] R.A. Briere and B. Winstein, to be published in Phys. Rev. Lett.

[Briere 95b] R.A. Briere, Ph.D. Thesis, University of Chicago (1995), unpublished.

[Buchanan 92] C.D. Buchanan et al., Phy. Rev. **D45**, 4088 (1992)

[Carosi 90] R. Carosi et al., Phys. Lett. **B237**, 303 (1990).

[Chell 93] E. Chell and M.G. Olsson, Phys. Rev. **D48**, 4076 (1993).

[Chollet 70] J.C. Chollet et al., Phys. Lett. **B36**, 658 (1970).

[Christenson 64] J.H. Christenson, J.W. Cronin, V.L. Fitch and R. Turlay, Phys. Rev. Lett. **13**, 138 (1964).

[Christenson 79] J.H. Christenson et al., Phys. Rev. Lett. **43**, 1209 (1979).

[Colladay 95] D. Colladay and V.A. Kostelecky, Phys. Lett. **B344**, 259 (1995).

[CPLEAR 95] Results from the CPLEAR collaboration, presented by O. Behnke at the German Physical Society (DPG) Meeting 1995 in Mainz and by C. Touramanis at the Moriond Conference 1995

[Cronin 81] J.W. Cronin, Rew. Mod. Phys. **53**, 373 (1981)

[Ellis 92] J. Ellis, N.E. Mavromatos and D.V. Nanopoulos, CERN-TH-6755/92 preprint, hep-th/9212057 in Los Alamos preprint library.

[Gabrielse 95] G. Gabrielse et al., Phys. Rev. Lett. **74**, 3544 (1995).

[Garwin 57] R.L. Garwin, L.M. Lederman and M. Weinrich, Phys. Rev. **105**, 1415 (1957).

[Geer 94] S. Geer et al., Phys Rev. Lett. **72**, 1596 (1994)

[Gell-Mann 55] M. Gell-Mann and A. Pais, Phys. Rev. **97**, 1387 (1955).

[Gibbons 93a] L.K. Gibbons et al., Phys. Rev. Lett. **70**, 1199 (1993).

[Gibbons 93b] L.K. Gibbons et al., Phys. Rev. Lett. **70**, 1203 (1993).

[Gibbons 93c] L.K. Gibbons, Ph.D. Thesis, University of Chicago (1993), unpublished.

[Good 61] R.H. Good et al., Phys. Rev. **124**, 1223 (1961).

[Gsponer 79] A. Gsponer et al., Phys. Rev. Lett. **42**, 9 (1979)

[Hawking 75] S.H. Hawking, Commun. Math. Phys. **43**, 199 (1975).

[Huet 95] P. Huet and M.E. Peskin, Nucl. Phys. **B434**, 3 (1995).

[Fitch 65] V.L. Fitch, R.F. Roth, J. Russ and W. Vernon, Phys. Rev. Lett. **15**, 73 (1965) and Phys. Rev. **164**, 1711 (1967).

[Friedman 57] J.I. Friedman and V.L. Telegdi, Phys. Rev. **105**, 1681 (1957).

[Jackson 75] J.D. Jackson, Classical Electrodynamics, John Wilney & Sons, New York, 1975.

[Jost 57] R. Jost, Helv. Phys. Acta **30**, 409 (1957)

[Kleinknecht 73] K. Kleinknecht, Fortschritte d. Physik **21**, 57 (1973)

[Kleinknecht 94] K. Kleinknecht and S. Luitz, Phys. Lett. **B336**, 581 (1994)

[Kobayashi 92] M. Kobayashi and A.I. Sanda, Phys. Rev. Lett. **69**, 3139 (1992).

[Kostelecky 94] V.A. Kostelecky and R. Potting, IUHET 265 preprint, hep-ph/9501341 in Los Alamos preprint library, accecpted by Phys. Rev. D.

[Lee 56] T.D. Lee and C.N. Yang, Phys. Rev. **104**, 254 (1956).

[Lee 57] T.D. Lee, R. Oehme and C.N. Yang, Phys. Rev. **106**, 340 (1957).

[Lipkin 95] H.J. Lipkin, WIS-95-1-PH preprint, hep-ph/9501269 in Los Alamos preprint library.

[Lohse 94] T. Lohse et al., HeraB Proposal, DESY-PRC 94/02

[Lüders 54] G. Lüders, Kgl. Danske Videnskab Selskab. Mat. Fys. Medd. **28**, 1 (1954).

[Nakada 93] T. Nakada, Lepton-Photon Symposium, AIP Conference Proceedings No. 302 (1993), Preprint PSI-PR-93-18.

[Nelson 85] W.R. Nelson, H. Hirayama and D.W.O. Rogers, SLAC-Report-265, 1985

[Malensek 81] A.J. Malensek, FNAL-Report FN-341 (1981)

[Matthews 95a] J.N. Matthews et al., to be published in Phys. Rev. Lett.

[Matthews 95b] J.N. Matthews, Ph.D. Thesis, Rutgers University, 1995, unpublished.

[McFarland 94] K.S. McFarland, Ph.D. Thesis, University of Chicago, 1994, unpublished.

[Pais 55] A. Pais and O. Piccioni, Phys. Rev. **100**, 1487 (1955)

[Papadimitriou 90] V. Papadimitriou, Ph.D. Thesis, University of Chicago, 1990, unpublished.

[Patterson 90] J.R. Patterson, Ph.D. Thesis, University of Chicago, 1990, unpublished.

[Pauli 55] W. Pauli, p. 30 in "Niels Bohr and the Development of Physics", W. Pauli, ed., McGraw-Hill, New York, 1955.

[PDG 94] Particle Data Group, L.Montanet et al., Phys. Rev. **D50**, 1173 (1994).

[Sachs 87] R.G. Sachs, The Physics of Time Reversal, The University of Chicago Press (1987)

[Schiz 80] A. Schiz et al., Phys. Rev. bf D21, 3010 (1980)

[Schlein 93] P.E. Schlein, ed., Beauty '93, Nucl. Phys. **A333**, (1993)

[Schubert 70] K.R. Schubert et al., Phys. Lett. **B31**, 662 (1970)

[Schwingenheuer 95] B. Schwingenheuer, R.A. Briere et al., to be published in Phys. Rev. Lett.

[Streater 64] R.F. Streater and A.S. Wightman, "PCT, Spin and Statistics, and All That", Benjamin Cummings, Reading 1964.

[Strominger 93] A. Strominger, Phys. Rev. **D48**, 5769 (1993)

[Wigner 32] E. Wigner, Göttinger Nachrichten, Math. Naturw. Klasse **32**, 546 (1932)

[Winstein 93] B. Winstein L. Wolfenstein, Rev. Mod. Phys. **65**, 1113 (1993).

[Wolff 71] B.Wolff et al., Phys. Lett. **B36**, 517 (1971)

[Wu 57] C.S. Wu et al., Phys. Rev. **105**, 1413 (1957).

[Wu 64] T.T. Wu and C.N. Yang, Phys. Rev. Lett. **13**, 381 (1964).

[Wolfenstein 64] L. Wolfenstein, Phys. Rev. Lett. **13**, 562 (1964) 1244 (1975).